Measurement of the Top Quark Pair Production Cross Section and Simultaneous Extraction of the W Heavy Flavor Fraction at $\sqrt{s} = 7$ TeV with the ATLAS Detector at the LHC

Dissertation

zur Erlangung des mathematisch-naturwissenschaftlichen Doktorgrades
"Doctor rerum naturalium"
der Georg-August-Universität Göttingen

vorgelegt von

Adam Roe

aus New York City, NY, USA

Göttingen, 2012

Referent: Prof. Dr. Arnulf Quadt
Korreferent: PD Dr. Jörn Große-Knetter

Tag der mündlichen Prüfung: 22. März 2012

Measurement of the Top Quark Pair Production Cross Section and Simultaneous Extraction of the W Heavy Flavor Fraction at $\sqrt{s} = 7$ TeV with the ATLAS Detector at the LHC

von

Adam Roe

The top quark pair production cross section, $\sigma_{t\bar{t}}$, is measured in the semileptonic channel in two datasets using a binned profiled likelihood template fit to data to discriminate the signal, $t\bar{t}$, from its main background, the production of a W-boson in association with jets (W+jets). Templates in the first analysis are derived from a four variable flavor-sensitive discriminant to measure $\sigma_{t\bar{t}}$ in $\int \mathcal{L}\, dt = 35$ pb^{-1}. A similar but flavor-insensitive discriminant is then used to measure $\sigma_{t\bar{t}}$ in $\int \mathcal{L}\, dt = 0.7$ fb^{-1}. A third analysis is presented which simultaneously fits the fractions of $t\bar{t}$ and W+jets events in which heavy flavor jets are produced, using a single flavor-sensitive distribution in the $\int \mathcal{L}\, dt = 0.7$ fb^{-1} dataset. Experimental precision of the top quark pair production cross section surpasses the theoretical uncertainty. No significant deviations from predictions are found but the results are higher than expectation.

Post address:
Friedrich-Hund-Platz 1
37077 Göttingen
Germany

II.Physik-UniGö-Diss-2012/04
II. Physikalisches Institut
Georg-August-Universität Göttingen
April 2012

It would be so nice if something made sense for a change!

– *Alice in Wonderland*, Lewis Carroll

Contents

1 Introduction

The title of this thesis proposes to measure the top quark pair production cross section at the Large Hadron Collider using the ATLAS experiment, that is, to determine experimentally the rate of one of the many possible outcomes in a high-energy proton-proton collision. The precise meaning of this task and understanding of possible results warrants discussion.

Much interpretation is done. What is truly measured is the energy deposited by, or momentum of, particles which in fact are the decay remnants of the particles of interest. In some cases, the particles which are measured are several steps away along a decay chain. Using our knowledge of interactions of particles with matter built over the past hundred years, we can associate these primal measurements – a charged particle's trajectory through a tracker, a deposit of energy in a calorimeter – with specific particles, making the first leap necessary. Such traces left across the detector allow for the reconstruction of a single physical object: an electron, muon, or a jet (coming from a quark, for instance).

The neutrino has posed experimentally and philosophically challenging questions since its proposal in 1930, and in the present collider environment, their detection not feasible [1]. In certain recent experiments designed specifically for neutrino detection, it has proved only to be a technical challenge: the small probability of a neutrino interacting with matter has lead to the use of extraordinary masses in experiments, so large in fact that experiments are even using Antarctica or the Mediterranean Sea as a part of their detector. In such experiments, the neutrino is no more abstract than the nucleus was in the gold foil experiment [2, 3]. This is not the case here, where the neutrino here is signified by an absence of direct signal in the detector.

Let us presume that the necessary departure from positivism caused by the high powered abstractions of our scope are not problematic. The association of the particles with a parent from which they have decayed is, to some extent, the issue at hand in this thesis. The particles observed in a single collision event are collectively known as the final state. The signal under study is pairs of top quarks produced in collision. Both top quarks decay into a W boson and a b-quark, where one W subsequently decays into a charged lepton and a neutrino while the other decays into two quarks. Each of the four quarks present forms a jet, which can be observed. A typical final state in the measurements presented here is therefore four jets, a charged lepton (electron or muon) and large missing energy (a neutrino). Events here are identified using the lepton, naturally dividing the semileptonic channel further according to lepton flavor, e+jets and μ+jets. Those are further subdivided by the number of jets in the event, since it may have more or less than four.

There are several other mechanisms known in the Standard Model which can create this final state. In this thesis, the results are obtained assuming that those and only those processes contribute to the data sample. Beyond the production of $t\bar{t}$, the main process which can create the same final state is the direct production of a W boson in association with jets. Smaller contributions are expected from other electroweak processes.The signal as well as these background processes are modeled using Monte Carlo (MC) simulation [4]. The tools which implement basic theoretical predictions as MC are known as generators.

The production of a multijet final state in which one of the objects is misidentified as an isolated, prompt lepton also creates the same experimental final state. This process is difficult to

model as it is fundamentally an effect of experimental limitation, arising from a false assignment of the measured energy and momentum. The rate of the underlying physical process in a given energy range is naturally very high, so much so that even a small rate of lepton misidentification can cause a significant contribution from this process to the selected data sample.

On an event-by-event basis, it is impossible to distinguish the various physical processes from one another. In other words, if a single event with such final state is observed, one cannot say definitely which of those physical process occured in the proton-proton collision. There are many ways to use the observed events in a measurement, but two will be focused on in particular in this discussion. One can take for granted the presence of the background processes and attempt to establish an excess of events in the form of a signal, as has been done in the first paper from ATLAS measuring top pair production cross section, $\sigma_{t\bar{t}}$ [5]. The theoretical assumptions would then be that the full number of events is described by the SM and that $\sigma_{t\bar{t}}$ is the only unknown, that branching ratios for the decays of the processes involved including top quarks are known, and that differential predictions in the form of MC can model the percentage of the process which will be observed (acceptance and efficiency). Such a cut-and-count method was used to establish the signal in that first paper. This is not precisely the route followed in this thesis.

In the analyses presented, differential theoretical predictions are used to discriminate the mechanisms which produce the final state under study, effectively allowing one to claim, for a given event, that it is more likely to arise from a certain physical process or another, but certainly not allowing a definitive statement of origin on an event-by-event basis.

Taking a relatively traditional approach, one may ask what hypothesis we are testing. The naive answer may be "The Standard Model". The first papers published using the cut-and-count method with early data already showed that the observed cross section is in the same range as predictions, albeit with a large experimental uncertainty [5, 6]. Yet it is extremely difficult to make a precise prediction for a production cross section in proton-proton collisions for the process of interest here. This difficulty is due mostly to the complications of the theory of the strong force, Quantum Chromodynamics (QCD), and partially to our lack of knowledge of the proton. Predictions are done with QCD using perturbation theory, approximating it by a series expansion around the strength of the force. One must always choose to which order it will be expanded, where higher-order corrections are typically of less importance and harder to calculate. A more precise measurement, such as those presented here, does not therefore test the Standard Model in general but rather tests specific predictions made with it at a given precision.

Different signal models exist, one of which has to be assumed, even though none of them is a priori more correct than another. The degree of theoretical knowledge becomes a relatively large uncertainty at the level of precision currently available.

The best differential predictions available and implemented in MC simulation are at second order, Next to Leading Order (NLO), while non-differential "inclusive" cross section predictions are approaching one order more of precision, known as approximate NNLO. For the production of $t\bar{t}$ we use NLO kinematics for the core process with approximate NNLO normalization[1]. Most of the background processes are only available at one order lower, that is, LO kinematics with NLO normalization. The hypothesis may then be that "QCD NLO kinematics and NNLO rate predict the behavior of top quark pairs produced in proton-proton collisions at the LHC".

This hypothesis itself raises several questions. Are NLO kinematics for the process well predicted? Is approximate NNLO well defined? Does it make sense to combine NLO kinematics with NNLO inclusive predictions? What would be the implications if the result of the analysis is not compatible with the hypothesis?

[1] Throughout this thesis, the kinematics present in NLO MC generators will be referred to simply as "NLO" and the inclusive approximate NNLO predictions as "NNLO"

There are two main NLO MC generators available for the prediction of $t\bar{t}$ which will be used in this thesis. They are hitherto equally valid[2]. Considering the reliance on this to make predictions, be it for calculating signal acceptance or for more complete kinematics as in these analyses, one could use one and not the other and test the hypothesis using a single generator. The hypothesis then becomes "QCD NLO kinematics as predicted by Generator X and NNLO rate predict the behavior". It could of course be tested for the other as well. What is done here instead is that one generator is taken to be the baseline and the other is used to evaluate potential bias as a systematic uncertainty. Doing so thereby retains the more general hypothesis of testing NLO kinematics, taking the two generators as representative of the difference. One of three analyses presented in this thesis includes the possibility to learn if one or the other is favored as a model of the data.

A study has been undertaken to examine the uncertainty on acceptance of the signal process at NLO. The ratio of the fiducial cross section to the fully inclusive cross section is defined[3]. The fiducial cross-section is calculated using truth-level kinematic cuts corresponding to those in the analysis. The theoretical prediction for both the inclusive and fiducial cross sections are varied within their uncertainty, by the standard method of changing the renormalization and factorization scales by a factor of 2, and the change in the ratio is observed. We have learned that the effect of the scale variation on this ratio is in fact rather dependent on the number of jets considered in the analysis. Requiring at least four jets, as is often done in such analyses, yields a difference in the ratio of as much as 10 %. Only by requiring at least three jets are the migration effects mitigated, and the change in the ratio becomes $\approx 2\,\%$. In the analyses presented here, at least two or three jets are required, so the ratio is well defined. This simple study indicates that using NLO predictions for precisely measuring $\sigma_{t\bar{t}}$ cannot be done without the inclusion of events with a 3-jet final state in addition to those with higher jet multiplicities.

There are various approximate NNLO predictions for $\sigma_{t\bar{t}}$. Any measurement in the range of about 140-180 pb would be found to be consistent[4]. In other words, one can consider approximate NNLO predictions for $m_{\text{top}} = 172.5\,\text{GeV}$ to be about $158 \pm 18\,\text{pb}$, about a 12 % uncertainty. Of the various approximate NNLO predictions available, a single value is used for comparison throughout this thesis, but it is important to know that there are other estimations available. The NLO MC simulation is normalized to the NNLO cross section using a non-differential "k-factor", in essence assuming that the ratio $\sigma(\text{NLO})/\sigma(\text{NNLO})$ is not phase-space dependent. This is not necessarily a physically sound assumption, however doing so allows for comparison with the most precise theoretical results available. Normalizing the MC simulation to theoretical predictions using non-differential k-factors will be done throughout this thesis.

The results presented here find final uncertainties on the top pair production cross section in the range of 6-13 %. The experimental uncertainty is therefore smaller than the theoretical, and in fact by now a huge portion of the experimental uncertainty is due to theoretical dependence. What then, would be the implications, if the measurement does not agree with the theoretical predictions? First and foremost, it would in fact be difficult for them *not* to agree given the interdependence of theory and experiment. If they are not in perfect agreement either – which

[2] An excellent, hot-off-the press review of methods and differences is available in [7]. The two generators used here are MC@NLO[8, 9] and POWHEG[10]. A very interesting comparison of them can be found in [11], which highlights the differences between the two and related issues.

[3] MCFM [12] is used for the numerator while the denominator uses Hathor [13] evaluated at NLO. Details of this study are given in Appendix C of [14].

[4] The prediction used by the ATLAS collaboration and throughout this thesis is $\sigma_{t\bar{t}}=164^{+11}_{-16}\,\text{pb}$ [13]. Other predictions such as $\sigma_{t\bar{t}}=154^{+15}_{-14}\,\text{pb}$ exist as well[15]. It should be noted that the latter value uses a slightly higher value for m_{top}, suppressing the cross section. About half of the discrepancy between the predictions seems to be numerical choices including the mass difference and the other half methodological.

they also cannot be, except by chance – predictions which do not agree may be tweaked, at which point they cease to be predictions and become descriptions. If the measurements are a bit wider off the theoretical mark, it could easily be claimed that higher order predictions are needed. This is the essence of the hypothesis: if a discrepancy is found, it is not with the underlying theory itself but rather with the best available predictions using the theory. The theory of QCD is not being tested here, but rather the precision of the estimates using it are. This is all the more so the case in the measurement of the production of W bosons with associated heavy flavor jets, whose theoretical uncertainty is on the order of 50-100 %, meaning a measurement would have to be nearly an order of magnitude different from predictions to bring into question our understanding of the underlying physical processes. In this case, it is rather that theoretical predictions need experimental input than that precision predictions are being tested.

1.1 The Scientific Process

Never before has scientific collaboration on the scale of the LHC and its experiments been undertaken: the two main experiments each have nearly three thousand active scientists who are taken to be the authors of the papers published by the respective collaboration. The size of the collaborations implies a necessary departure from certain tenets of traditional science. The scientific work is considered to be truly collaborative, as evidenced by the fact that papers are published by the collaboration and not individuals. A great deal of input from the collaboration is used in any physics analysis. More than 100 papers have been published by the ATLAS collaboration at time of writing, all of which have an author list of about 3,000 physicists listed alphabetically. To qualify as an author one must meet basic criteria intended to show continued dedication to the collaboration, such as periodically taking part in the acquisition of data or monitoring of the detector. The author of this thesis has contributed in particular to the real-time monitoring of the pixel subsystem of the experiment, both in developing software used in monitoring and doing so.

The data are recorded centrally, with a handful of physicists sitting in the control room at a given time in charge of the process. Algorithms to process the raw data are also run centrally, and the data are made available to the entire collaboration. Physicists self-organize into groups, some of which are responsible for a part of the detector or given final state observable particle, while others are organized by topic of underlying physical interest. These group calibrate the detector, maintain reconstruction algorithms, estimate uncertainties, and make general recommendations.

The work described in this thesis relies on the ATLAS collaboration. The details of object definition and uncertainty described in Chapter 4 are common to those studying the top quark and to some extent the entire collaboration. The author has contributed to a handful of topics, in particular to the definition of the electron and in optimizing kinematic cuts in the e+jets channel in the context of reducing the fake contribution.

An additional effect of the size of the collaborations is that any analysis undergoes an extensive internal review by the collaboration prior to submission to a journal. In ATLAS, the process of publishing a paper goes through many steps, first receiving approval from the related group before being sent for collaboration-wide review. This is followed by a final sign-off from the collaboration leadership before being submitted to a journal. It is generally assumed that any paper submitted by one of the large collaborations will be published. A streamlined version of this process exists for "preliminary" results, in particular for international conferences. The standards required to be met for the paper publication procedure are generally higher than those for a preliminary result.

The measurement of the top pair production cross section using the 2010 data which is presented in Chapter 7 of this thesis was first shown by the collaboration at the Moriond QCD and High Energy Interactions conference [16]. After ten months of review, this work was submitted by the collaboration as a paper to Physics Letters B [17]. In the meantime, a similar analysis using a significantly larger dataset recorded in the first half of 2011 was performed and presented by the collaboration at the Lepton Photon conference [18], presented in Chapter 8. The final analysis in this thesis presented in Chapter 9 has not been subjected to the approval procedure and is therefore not in any way an official result from ATLAS.

In addition to the structure of the collaboration described, the analysis team is often comprised of a few people working very closely together. In the case of the analysis methodology presented in Chapter 6, the concept was developed by a team of a few students, including the author, and postdocs, working together. The publicly presented analyses themselves are the product of direct work from this small group of researchers. It is somehow natural for no more than a few people to work together intensely, constantly. On this scale agreement can be reached that satisfies the concerns of those involved without formal procedure. This is where, absent the shackles of politics, scientific rigor is truly achieved.

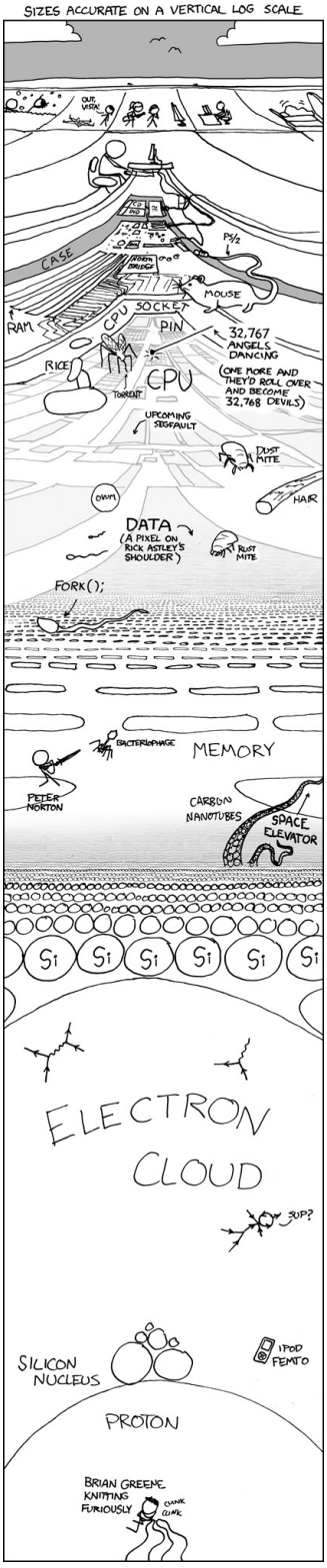

Depth. "The Planck length is another thousand or two pixels below the comic."[19]

2 Theoretical Background

An overview of current knowledge of fundamental particles and their interactions will be given here. The special case of the top quark, the object under study in this thesis, will be discussed. The theoretical predictions for top quark pair production cross section in collisions at the LHC will be reviewed, along with predictions for W+jets production, in particular with heavy quark jets in the final state.

2.1 The Standard Model of Particle Physics

The Standard Model of Particle Physics (SM) contains our state-of-the-art knowledge of experimentally fundamental particles and their interactions. Six quarks and six leptons (all spin 1/2 fermions) are the building blocks of matter while four known force carriers (spin 1 bosons) are the quanta of their interactions. Our knowledge of the properties and interactions of these particles has been built over the last hundred years through experiment and interpreted in the framework of quantum field theory (QFT), the relativistic field theory of quantum mechanics. The Standard Model as it is currently conceived of will be reviewed here.

The quarks and leptons are understood as three generations each of 2 quarks and 2 leptons. The traditional arrangement of these three generations follows the historical development of their discovery which, for reasons of energy requirements, follows the increasing rest mass of the particle (except for possibly in the case of neutrinos). Each generation is composed of an "up-type" quark with electric charge $Q = +2/3$ and a "down-type" quark with $Q = $-1/3, as well as a charged lepton with $Q = $-1 and an electrically uncharged neutrino. All particles have antimatter partners with opposite quantum numbers but identical mass.

In our current understanding, these particles are fundamental: there is no evidence that any of them can be broken into constituents and they are treated with the same mechanisms in QFT. The properties of these particles are not identical, giving rise to their varied behavior.

In moving from one generation to the next, the two things which change are the mass of the particle and its "flavor" which is described by its name. The three generations can be arranged as

$$\begin{pmatrix} u & \text{(up)} \\ d & \text{(down)} \end{pmatrix} \quad \begin{pmatrix} c & \text{(charm)} \\ s & \text{(strange)} \end{pmatrix} \quad \begin{pmatrix} t & \text{(top)} \\ b & \text{(bottom)} \end{pmatrix}$$

$$\begin{pmatrix} \nu_e & (e \text{ neutrino}) \\ e & \text{(electron)} \end{pmatrix} \begin{pmatrix} \nu_\mu & (\mu \text{ neutrino}) \\ \mu & \text{(muon)} \end{pmatrix} \begin{pmatrix} \nu_\tau & (\tau \text{ neutrino}) \\ \tau & \text{(tau)} \end{pmatrix}$$

The fermion masses are free parameters in the SM and are of great interest. They are measured experimentally and input to the theory. Using the lagrangian formalism, the Dirac equation describing a free spin-1/2 particle of mass m with wave function ψ can be written as [20]:

$$\mathcal{L}_{\text{free}} = \bar{\psi}(i\partial\!\!\!/ - m_f)\psi$$

The mass of a particle affects its behavior strongly. In part this is due to considerations of energy: a heavier particle will decay into lighter particles if it is possible. The lightest particles

are thus stable; the material found in the Periodic Table of Elements can be understood as being built of the first generation of particles. The mass also affects particles in more subtle ways, due to the extraordinarily large range of masses present: the neutrinos have masses below 2 eV[1] [21] while the top quark has a mass of hundreds of GeV [22], thereby spanning at least eleven orders of magnitude. An example of the difference in particle behavior caused by the magnitude of the particle masses is the relatively recent discovery of neutrino oscillations amongst flavor states [23]. This implies that neutrinos do indeed *have* mass, but so far only mass differences have been measured and upper limits on the mass have been set [24, 25, 26, 27]. The phenomenon of neutrino oscillation is not itself a physical interaction but exists naturally in the theory of particles. One may ask therefore if other particles oscillate as well. Recent work has shown that other particles – the charged leptons, for instance – could in principle oscillate as well, but that the mass difference between the generations is so much larger than for the neutrinos that observation is not particularly feasible [28]. It is the small mass difference (squared) amongst the generations which causes observable oscillations in the neutrino system.

The Interactions of Particles in the Standard Model

There are four known fundamental forces of nature – electromagnetic, weak, strong, and gravitational – each governing the interactions of particles based on their properties, the electric charge, weak isospin, color charge, and mass, respectively. All except for gravity are understood in the context of QFT and are a part of the SM. The electromagnetic and weak interactions are known to be different low-energy manifestations of the same force, the electroweak force. The SM therefore describes two fundamentally different forces, electroweak and strong, using QFT. The quantum field theory of electromagnetism will be considered first, then electroweak unification and the symmetry breaking into weak and electromagnetic forces, and finally the theory of the strong force will be discussed.

Renormalization

An essential concept in QFT is renormalization, a consequence of which is that fundamental parameters become a function of energy. Renormalization dictates the dependence of a parameter on energy. An example which will be further discussed is that the coupling of a force is $\alpha = \alpha(Q^2)$, where Q^2 is an energy scale relevant to the process (such as energy transfer). Sometimes the bare coupling will be written as g, which is related to α by $g = 4\pi\alpha$.

Electromagnetism and Quantum Electrodynamics

The strength of the electromagnetic interaction is proportional to the electric charge, q. Its exchange boson, the excitation of its quantum field, is the photon, γ. The photon is a massless, spin-1 particle. The coupling of the field is the electric charge,

$$\alpha_{\mathrm{EM}} = q_e^2 \approx \frac{1}{137}.$$

The charge of the electron is therefore a fundamental parameter in the SM. Quantum Electrodynamics (QED) predicts very precisely the dependence of many observables on α_{EM}.

[1] In natural units, $\hbar = c = 1$, will be used throughout. In these units, energy, momentum, and mass are all expressed in units of energy.

The electromagnetic interaction is symmetric under global $\mathrm{U}(1)_q$ transformations, corresponding to conservation of electric charge. The electromagnetic field is quantized, and the lagrangian for a particle of charge Q can then be written as

$$\mathcal{L}^{\mathrm{EM}} = -\frac{1}{4}F^{\mu\nu}F_{\mu\nu} - i\alpha_{\mathrm{EM}}Q\bar{\psi}\gamma^5 A_\mu\psi$$

in the Lorentz gauge, where A_μ is the electromagnetic vector potential and $F_{\mu\nu}$ is the electromagnetic field strength tensor, defined as $F_{\mu\nu} \equiv \partial\mu A_\nu - \partial\nu A_\mu$. Together with the Dirac terms for the interacting particles in question (as shown in 2.1), the lagrangian for Quantum Electrodynamics is specified.

The Weak Force and Electroweak Theory

The weak interaction was first proposed as a four-point interaction by Fermi to explain nuclear decay. A dimensionful coupling constant was proposed to describe the interaction, now measured to be $G_F \sim 10^{-5}$ GeV^{-2} [29]. This was an effective theory; the units are incorrect for it to be a fundamental constant. Understanding of the interaction after the discovery of parity violation lead to the inclusion of "handedness" into the weak theory [30], and eventually the unification of the electromagnetic and weak forces into the electroweak force.

The left handed state or a right handed state of a particle is defined by the chiral projection operators, such that $\psi_{\mathrm{left}} = \frac{1}{2}(1-\gamma_5)\psi = L\psi$ and $\psi_{\mathrm{right}} = \frac{1}{2}(1+\gamma_5)\psi = R\psi$. Each of the doublets of quarks or leptons is a left-handed weak isopsin doublet, while the right-handed particles are singlets. The symmetry of the weak interaction is $\mathrm{SU}(2)_L$ where L stands for "left". A three-component field W_μ is introduced which corresponds to this symmetry. The weak field strength tensor has a form similar to the electromagnetic field strength tensor, except that the generators of SU(2) yield a non-Abelian term, physically representing self-coupling amongst the gauge bosons. The tensor is then defined as

$$F^a_{\mu\nu} \equiv \partial\mu W^a_\nu - \partial\nu W^a_\mu - g_W f^{abc} W^b_\mu W^c_\nu.$$

The symbol f^{abc} is the generator of the symmetry group; physically it implies self-coupling amongst the exchange bosons with the coupling g_W. For the SU(2) group, f^{abc} is the fully-antisymmetric tensor ε_{abc}. The symmetry of $\mathrm{SU}(2)_L$ cannot, however, be exact: it would imply three massless gauge bosons mediating the force, which do no exist. The conundrum is solved by proposing the unification of electromagnetism and the weak force, known as electroweak unification [31, 32, 33]. This proposed symmetry still has the awkward issue that it must be broken. Before symmetry breaking, the field lagrangian can be written as:

$$\mathcal{L}^{\mathrm{electroweak}}_{\mathrm{field}} = -\frac{1}{4}F^a_{\mu\nu}F^{\mu\nu}_a - \frac{1}{4}F^{\mu\nu}F_{\mu\nu}.$$

Here the three-index tensor represents the "pure" weak fields W_μ while the two-index tensor has the same form as the electromagnetic field. In order to incorporate electromagnetism, hypercharge Y is defined, which is a combination of both the electric charge and the weak isospin component (I), defined as $Y = 2(Q - I)$. The charge symmetry of electromagnetism becomes hypercharge. The unification of the electromagnetic and weak forces into a single theory means that electroweak symmetry can be understood to be $\mathrm{SU}(2)_L \otimes \mathrm{U}(1)_Y$.

The breaking of this symmetry is proposed to give mass to the quanta of the field W_μ, and in the process must therefore preserve only the simple electric charge symmetry and the massless photon field, a process which can be understood as $\mathrm{SU}(2)_L \otimes \mathrm{U}(1)_Y \rightarrow \mathrm{U}(1)_q$ [34]. Through

the process of electroweak symmetry breaking, the fields mix by simple rotation which can be parameterized as an angle, known as the weak mixing angle, θ_{W}. The theory therefore predicts three massive bosons and one massless: two neutral, the familiar massless γ as well as the massive Z^0, and two charged, $W^{\pm}$. The mixing of these fields relates the masses of the heavy bosons by θ_{W} and to G_F to identify a dimensionless coupling by

$$M_W^2 = \frac{g^2}{4\sqrt{2}G_F \sin^2\theta_{\mathrm{W}}},\ M_Z^2 = M_W^2/\cos^2\theta_{\mathrm{W}}.$$

The weak force is therefore not weak compared to electromagnetism because of a small coupling but rather because of the large mass of its interacting bosons.

The electroweak symmetry breaking mechanism in the SM has an additional consequence which is the prediction of an additional boson, the scalar Higgs boson [35, 36]. The electroweak theory has been extremely successful in general, but the Higgs boson – whose mass is not predicted by the theory – has eluded discovery for nearly fifty years. The collaborations at the LHC have made extraordinary progress in the search and indeed have ruled out its existence over nearly the complete mass range, save for $115 < m_H < 127$ GeV [37, 38]. If the SM Higgs exists, it must be in that mass range; if it does not exist, something else must be responsible for electroweak symmetry breaking. Electroweak theory is too successful for most physicists to doubt the theory in general and therefore expect *an* electroweak symmetry breaking mechanism even if the Higgs boson is not found. Accordingly there are few if any paradigm shifting approaches to this problem, rather, another mechanism (of which there are many) would be fit into the theory.

The Strong Force: Quantum Chromodynamics

To a great extent the force under study in this thesis is the strong force, elucidated through the theory of Quantum Chromodynamics (QCD). It is the dominant force amongst protons and their constituents in collision at the LHC. There are three "color charges" which are conserved in the theory, making it $\mathrm{SU}(3)_{color}$ symmetric. Eight gluon fields are required to describe the interactions predicted by the generators of the group. All matter which interacts via the strong force is known as hadronic, hence the name "Large Hadron Collider" (Large refers to the size of the accelerator, not the hadrons).

Particles which are color charged (e.g. quarks) interact via the massless, spin-1 gluon, g. Quarks experience a phenomenon known as color confinement: only color-neutral particles are stable. This can be accomplished by pairing two quarks together which are color-anticolor and therefore form a 2-quark state known as a meson, such as the pion. It can also be constructed out of one quark of each color (following the analogy of stage lights) to form a three-quark state known as a baryon, of which the proton and neutron are examples. Searches for hadronic matter with more than 3 quarks have been performed, and indeed evidence for such states has recently emerged [39]. In order to conserve color, gluons must carry color charge as well.

The field strength tensor is written with the same form as for the weak interaction, however the coupling constant is that of the strong force, g_s, and the generators of the SU(3) group are different. As in the weak interaction, the non-Abelian term predicts the self-interaction amongst gluons, both as a 3-gluon interaction and as a 4-gluon interaction. In electroweak theory the large mass of the bosons mitigates effects from such self-interaction terms, while in QCD the gluon being massless leads to low energy divergences in the theory. The coupling also implies the possibility of a bound gluon state known as "glueballs", a bound state with no valence quarks,

which has not been observed [40]. The lagrangian for QCD is then written as [41]

$$\mathcal{L}_{\text{QCD}} = \sum_{\text{quarks}} \bar{\psi_a}(i\not{\partial} - m_f)_{ab}\psi_b - \frac{1}{4}F^a_{\mu\nu}F^{\mu\nu}_a + \mathcal{L}_{\text{gauge fixing}},$$

where the roman indices specify color charge and $F^a_{\mu\nu}$ is the strong force field strength tensor.

The coupling constant in QCD, $\alpha_s(Q^2)$ is renormalized as in the other theories, predicted by the beta function of QCD, $\beta(\alpha_s)$. This can be expanded around $\alpha_s(Q^2)$, currently known up to a precision of α_s^5 [42, 43]:

$$\beta(\alpha_s(Q^2)) \equiv Q^2\frac{\partial\alpha_s(Q^2)}{\partial Q^2} = -\beta_0\alpha_s^2 - \beta_1\alpha_s^3 - \beta_1\alpha_s^4 - \beta_1\alpha_s^5 + O(\alpha_s^6)$$

The constants β_i are expressed by simple formulae depending on the number of quark flavors present, N_f. At first order, for instance, $\beta_0 = 11 - 2/3 \times N_f$, implying that β_0 is positive for $N_f < 16$ and therefore that the β function as a whole is negative [44, 45]. For the six known quark flavors, β stays negative to all known orders. The energy dependence is also found to be logarithmic; at leading order $\alpha_s \sim 1/\ln(Q^2/\Lambda^2_{QCD})$, where the "scale" of QCD, Λ_{QCD}, has been introduced. At energies near or below Λ_{QCD}, the perturbative approach breaks down. The fact that the coupling decreases logarithmically with increasing energy leads to the extraordinary property known as asymptotic freedom: high-energy quark becomes free from the strong force[2]. The theory of QCD predicts this running, but an input value for α_s is needed. The most precisely measured value comes from measurements at the Z-mass pole, recently combined to [48]:

$$\alpha_s(M_Z) = 0.1184 \pm 0.0007.$$

This can be translated into a value for the scale of the theory, $\Lambda_{QCD} = 213 \pm 9\,\text{MeV}$. Above this scale, as in the hard interaction of protons considered in this thesis, perturbative QCD is valid.

Standard Model Summary

The Standard Model of Particle Physics can be summed up as a lagrangian with many different components describing the fundamental particles and their interactions, which have been sketched out here. Perturbative expansion around the coupling constants of the forces can be used to make predictions for observations in a collider environment using the Feynman rules. The examples most relevant to this thesis will be discussed in Section 2.3. A wealth of predictions have been made with these theories which have been tested, in some cases to great precision, with rare discrepancy. The Standard Model accounts for a great deal of observed phenomena and has successfully made a number of predictions. It certainly does not answer all of our questions and there are many "Beyond the Standard Model" theories to tackle them, but to date there is no accepted, coherent view of any particles or interactions aside from those mentioned here.

[2] This is such an impressive result that it warranted not only a Nobel Prize but also a reference on popular television[46, 47].

2.2 The Top Quark

Amongst the particles discovered, the top quark stands out for its exceptionally large mass. Apart from its mass (and flavor of course) it is indistinguishable from the up and charm quarks, but the mass is so much larger that its behavior is unique amongst the quarks. Theoretically, the large mass means that it often enters into loop calculations at different orders of magnitude than other quarks, in particular into Higgs mass loop corrections. A particle's coupling to the Higgs field is proportional to its mass, thus the top quark, being the most massive known particle, has the strongest known coupling to it. Furthermore the mass of the top quark is of the same order of magnitude as the scale of electroweak symmetry breaking, raising the intriguing possibility that the top quark plays a special role in it.

Prediction and Discovery of the Top Quark

The top quark had been widely expected to exist since the discovery of the bottom quark in 1977, needed in order to complete the third generation quark doublet [49]. The third generation of quarks was in fact predicted by the work of Kobayashi and Maskawa amongst others, who extended the then 2×2 Cabibbo matrix into the now familiar 3×3 CKM matrix in order to account for CP-Violation in the weak interaction, work for which the Nobel Prize in Physics was recently awarded [50, 51]. Searches for the top quark, at CERN's Large Electron Positron Collider (LEP) in particular, placed lower limits on the mass of the top quark before it was discovered [52]. To do so, its expected mass was determined based on precision measurements of parameters at the Z-pole interpreted within the framework of the Standard Model.

In 1995, the top quark was discovered by the CDF and DØ Collaborations at Fermilab's Tevatron in pair production [53, 54]. More recently, in 2009, both collaborations have observed the production of a single top quark [55, 56], found to be consistent with SM expectations. The progress of the direct search limits and indirect SM constraints on m_{top} are shown over time in Figure 2.1, along with the early measurements at the Tevatron, consistent with expectations. The discovery of the top quark and the fact that its mass was found to be consistent with global fits to data predicted it are true feats of the Standard Model.

Properties of the Top Quark

A wealth of measurements of top quark properties have been undertaken at the Tevatron, a tradition which the LHC is continuing. At the time of writing the most precise measurements of the top quark properties still come from the Tevatron, some of which will be discussed here. Top pair production cross section at the Tevatron will be discussed in the next section. A more complete review of property measurements can be found, for instance, in [21].

The top quark is expected to decay almost entirely as $t \to Wb$, since other quark flavor decays are suppressed by tiny off-diagonal CKM Matrix elements and by larger mass differences. This can be tested by measuring the ratio R_{b}, defined as $R_{\text{b}} = \Gamma(t \to Wb)/\Gamma(t \to Wq)$, where $q = d, s, b$. The ratio has been measured by both the CDF and DØ collaborations and combined (externally) to obtain [57, 58, 21]:

$$R_{\text{b}} = 0.99^{+0.09}_{-0.08},$$

which is dominated by the more precise DØ measurement. Given that measurements of R_{b} are consistent with 1, the top quark is assumed to *always* decay as $t \to Wb$ in this thesis. The measurement of R_{b} can be used as one of the inputs to measure the total width of the top quark,

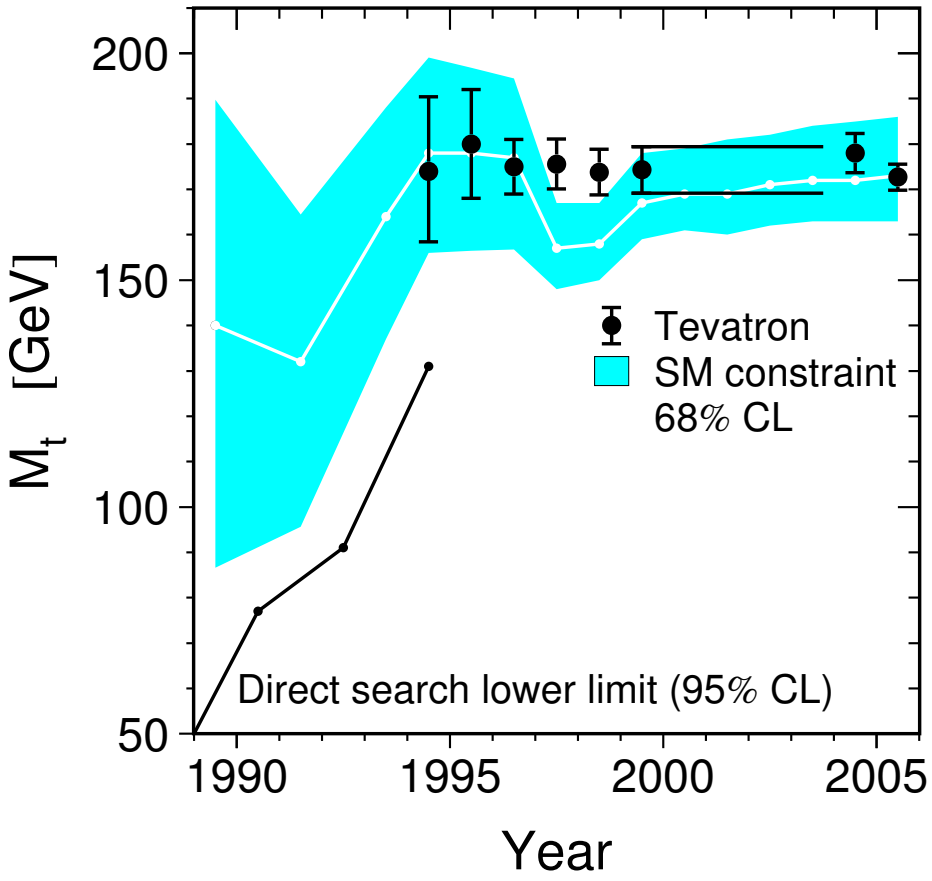

Figure 2.1: The development of knowledge of the top quark mass over time. The black line is the direct search limit, and the shaded area is the 68% confidence level for the mass based on a global fit of precision electoweak data interpreted within the SM. The actual measurements from the first decade of the Tevatron's measurements of the top quark, beginning in 1995, are shown. Image from [52].

Γ_{top}, determined by DØ to be [59]:

$$\Gamma_{\text{top}} = 1.99^{+0.69}_{-0.55}\,\text{GeV}.$$

Using the uncertainty principle [60], this implies that the lifetime of the top quark is

$$\tau_{\text{top}} = 3.3^{+1.3}_{-0.9} \times 10^{-25}\,\text{s},$$

which is in agreement with theoretical predictions. The characteristic timescale of QCD can also be calculated as well using Λ_{QCD}, to be

$$\tau_{\text{QCD}} = 3.1 \pm 0.7 \times 10^{-24}\,\text{s}.$$

The fact that the lifetime of the top is shorter than the characteristic timescale of QCD means that it decays before hadronization, the only quark to do so. This preserves much information in the final state which is generally lost for the lighter quarks [61]. This behavior has lent itself to extremely precise measurement of many of the top quark properties, in particular its mass. The current average of the top quark mass from Tevatron experiments is $m_{\text{top}} = 173.2 \pm 0.9\,\text{GeV}$ [22]. For practical purposes, the top quark is assumed to have a mass of $m_{\text{top}} = 172.5\,\text{GeV}$ throughout this thesis, and the cross section will be quoted as such.

Decay of the Top Quark and the $t\bar{t}$ Final State

These properties of the top quark have profound experimental significance. That the top quark cannot hadronize before it decays combined with the fact that it decays into a W boson and a b-quark yields an extremely identifiable final state. In contrast to the top quark, b-quarks are relatively long lived; they hadronize and often travel a distance measurable in the detector before decay. Independent how the W is produced, it can decay as either $W \to q\bar{q}$ or $W \to l\nu$. Excluding the third generation of quarks ($m_{\text{top}} > m_{\text{W}}$), a W can decay hadronically into quarks of the first or second generation, ignoring CKM suppressed decays. These contributions are each enhanced by a color factor of three since the weak force is colorblind. A leptonically decaying W can decay into all three generations. The branching ratio for each of these nine channels is approximately equal, $1/9 \approx 11\,\%$. More precise numbers for the W branching ratio can be found in [21].

After the decay of $t\bar{t}$, three possible combinations of W decay are named "all-hadronic" when both decay as $W \to q\bar{q}$, "dileptonic" when both decay as $W \to l\nu$, or "semileptonic" when one W decays hadronically and the other leptonically. A simple probability calculation shows that the all-hadronic channel is the most likely final state and the dilepton channel is the least. The semileptonic channel, which accounts for about 30 % of the decays of top quark pairs, is studied in this thesis. It should be noted that the τ lepton decays further within the detector and is not explicitly considered in these analyses. Accordingly, a decay chain like $W \to \tau\nu$ followed by $\tau \to \mu\nu$ is considered as a leptonic W decay, though if the τ decays as $\tau \to q\bar{q}$ it is considered hadronic.

2.3 Cross Section Predictions at Hadron Colliders

Precise predictions of cross sections at a hadron collider are a difficult task, though great strides have been made in recent years. Knowledge of both the interactions at play and the structure of the proton are essential in this task. Cross section predictions generally done first as a kinematically inclusive cross section before being calculated differentially. The latter is then used in a MC generator to make kinematic predictions. Predictions for both top quark pair production cross section and W boson in association with jets will be discussed here.

Production Cross Section Calculations: The Main Idea

The effort of using a QFT in the SM to calculate for the cross section of a process is done by a perturbative expansion in coupling constant, technically achieved by using the Feynman rules for the interaction in question. In the case of quark pair production at the LHC, the strong force is hugely dominant, so the interaction studied is QCD. A more complete explanation can be found in [41], for instance.

The process of deriving a production cross section begins with the probability for a quantum mechanical transition of state, described by Fermi's Golden Rule, relating the transition amplitude of a process to the sum of contributing matrix elements squared, $|\mathcal{M}|^2$, integrated over phase space. The perturbation expansion of QCD is used to approximate $|\mathcal{M}|^2$. The other essential input to such a prediction is knowledge of the proton structure. Fermi's rule relates the transition probability from a given state to another; in our case the final state desired is clear but the initial state is not.

The proton is composed of partons – quarks and gluons. At rest, the proton can be described by comprising two u quarks and one d quark, known as the valence quarks. At low energies, the three valence quarks together carry about half of the proton's longitudinal momentum. As a proton is accelerated, what is known as the particle "sea" develops. The sea consists of low p_{T} partons which carry a fraction of the proton's longitudinal momentum. As the energy is increased, the sea partons carry more and more of the proton's longitudinal momentum while the valence quarks carry less and less. More than fifty years of experimental research have lead to a decent understanding of the distribution of the fraction of energy carried by each parton in the energy range accessible at the LHC, known as the Parton Distribution Function (PDF). The fraction of longitudinal momentum carried by the interacting partons, denoted x for each, determines the effective energy of the collision.

The total cross section for the production of a pair of particles of mass m in a proton-proton process as a function of the center-of-mass collision energy $\sqrt{s}$ is

$$\sigma_m(\sqrt{s}) = \sum_{i,j} \int dx_1 dx_2 \; \hat{\sigma}_{ij}(Q^2, m^2, \mu^2) f_1^i(x_1, \mu,) f_2^j(x_2, \mu).$$

The functions f_1^i and f_2^j are the PDF for each of the two protons, the parton i from the first proton carries a momentum fraction x_1 and from the second parton j a fraction x_2. Here, $\hat{\sigma}$ is the partonic cross section for the process in question which is calculated by summing the squares of the contributing matrix elements. The integral runs from a characteristic low scale, such as Λ_{QCD}, to the maximum which is kinematically permissible. Contributions below the integral bounds lie in a regime where perturbative QCD breaks down and are handled by the PDF. This is known as factorization, which is an essential tool in making predictions. The parton momentum transfer in the collision is $Q^2 \equiv x_1 x_2 s$. All partons considered in the PDF are summed over. The theoretical maximum of Q^2 is in s itself, if the parton from each proton in question happens to carry the full momentum of its proton, a very unlikely situation due to the distribution of momentum amongst the partons. An example of a PDF is shown in Figure 2.2 at two different Q values for the CTEQ6M set [62], similar to the PDF sets used in this thesis. The renormalization scale, μ, is essential for predictions but is not a physical parameter; $\sigma(\sqrt{s})$ should therefore in principle be independent of it, however in practice this is not the case. The choice of μ is arbitrary, but often taken by convention to be the mass of the particle in question. To asses any systematic uncertainty on a theoretical prediction caused by this choice, μ is often varied by a factor of 2 up and down.

Inclusive Calculations

After making use of factorization, the parton cross section, $\hat{\sigma}$, must be evaluated. Following [63], the threshold for production is introduced as a parameter, $\rho \equiv 4m^2/Q^2$, which is essential in assessing the magnitude of contributions. The parton cross section $\hat{\sigma}$ for heavy quark pair production can be written as

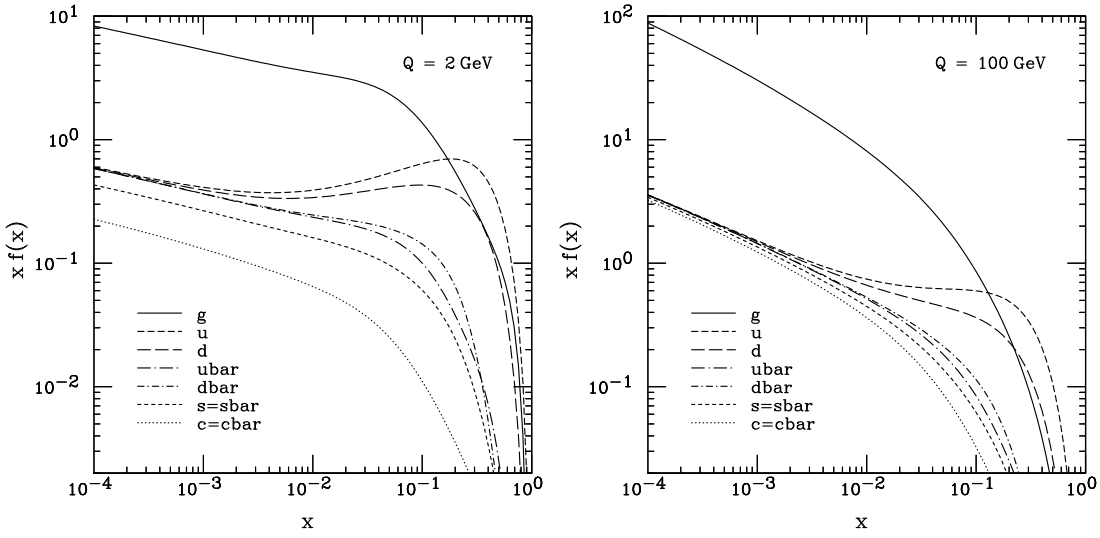

Figure 2.2: The CTEQ6M parton distribution functions, showing the fraction of energy (x) carried by a specific parton type, from [62]. It is shown at two energies, $Q = 2$, 100 GeV. One can see that gluons dominate the PDF over most the range of x.

$$\hat{\sigma}(Q^2, m^2, \mu^2) = \frac{\alpha_s^2(\mu^2)}{m^2} f_{ij}(\rho, \frac{\mu^2}{m^2}),$$

where the functions f_{ij} correspond to the various contributing processes and i, j are the incoming partons. An expansion around $\alpha_s(\mu^2)$ is therefore needed in order to calculate $\hat{\sigma}$. The functions f_{ij} can be expanded in (μ^2/m^2), as

$$f_{ij}(\rho, \frac{\mu^2}{m^2}) = f_{ij}^0(\rho) + 4\pi\alpha_s(\mu^2)\Big[f_{ij}^1(\rho) + \bar{f}_{ij}^1(\rho)\ln(\frac{\mu^2}{m^2})\Big] + O(\alpha_s^2),$$

The functions f_{ij}^0 are the leading order contribution for heavy quark pair production when summed over initial state partons, f_{ij}^1 is next to leading order (NLO), and so on. Keeping in mind the equation is a part of the partonic cross section, the leading-order term in the cross section is of order α_s^2 as expected. Leading order production of a quark pair is by either quark-antiquark annihilation or by gluon fusion, shown in the Feynman diagrams in Figure 2.3. Calculations of such terms for heavy quarks were necessitated by the discovery of the massive charm quark via observation of the $c\bar{c}$ bound state, the J/Ψ meson, in 1974 [64, 65]. The leading order functions f_{ij}^0 for heavy quarks were calculated a few years later [66, 67]. This was done both as a function of Q^2 and of m_{quark}, therefore applicable not only to the original case-study of charm pairs in electron-positron annihilation but also to top pairs in proton collisons. It was then established that both the gluon fusion and quark-antiquark annihilation processes contributed to $c\bar{c}$ production and therefore $q\bar{q}$ production for heavy quarks in general. At LHC energies, the gluon fusion process is expected to dominate over quark annihilation. In the expansion of f_{ij}, terms which are multiplied by a logarithm in μ^2/m^2 are gathered as $\bar{f}_{ij}$, such that the NLO term $\bar{f}_{ij}^1$ shown. These terms are of higher order but are affected by a logarithmic factor and can therefore be of more importance than other terms of the same order. Calculations of these terms are often carried out in place of the full calculation at that order, known as the "leading log" approximation. Complete calculations at NLO (α_s^3) were carried out in the late 1980's [63].

In the years since, approximate NNLO (α_s^4) calculations have become available for heavy quark pairs in general and top quark pairs in particular [68, 69, 70].

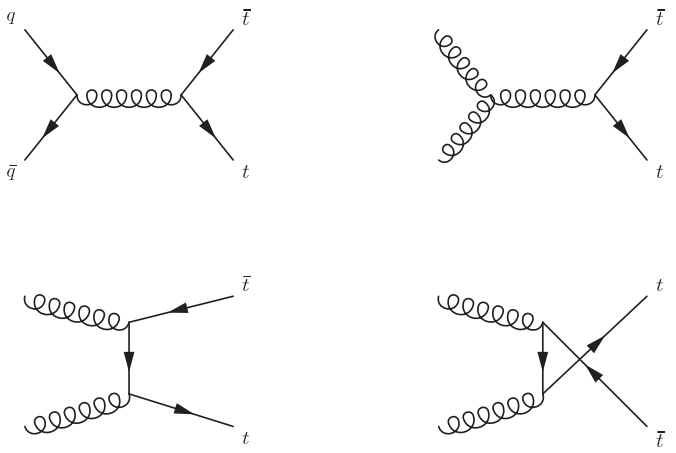

Figure 2.3: The Feynman diagrams entering the matrix element calculation for QCD $t\bar{t}$ production in proton collisions at leading order. The two mechanisms are quark-antiquark annihilation (upper left) and gluon fusion (other three). The latter dominates at LHC energies.

The Top Quark Pair Production Cross Section

The predictions for the top quark pair production cross section currently available come in two forms: an inclusive cross section and a differential cross section. In the analyses presented here, differential cross section predictions in the form of NLO MC is to model the kinematics of top quark pairs but the total cross section used for expectations is the best available approximate NNLO prediction. The MC simulation will be discussed more in Section 5.1. For inclusive $\sigma_{t\bar{t}}$, Hathor is used with the CTEQ6.6 PDF set [13, 62]. The renormalization and factorization scales are taken to be m_{top} in both the MC simulation and the inclusive calculation. In the MC simulation as throughout this thesis, $m_{\text{top}} = 172.5\,\text{GeV}$ is used. A prediction of

$$\sigma_{t\bar{t}} = 164.6^{+11.5}_{-15.8}\,\text{pb}$$

is taken to be the inclusive cross section for $t\bar{t}$ production in pp collisions at $\sqrt{s} = 7\,\text{TeV}$.

The first measurements of $\sigma_{t\bar{t}}$ were performed at Fermilab's Tevatron, a $p\bar{p}$ collider with a center-of-mass energy of $\sqrt{s} = 1.8\,\text{TeV}$ at the time. These first measurements by the CDF and DØ collaborations accompanied the announcement of the discovery of the top quark [53, 54]. They have since been refined to a much greater accuracy at $\sqrt{s} = 1.96\,\text{TeV}$. The latest and most precise result measures $\sigma_{t\bar{t}} = 7.50 \pm 0.48\,\text{pb}$ from CDF in about $5\,\text{fb}^{-1}$ of data, achieving a relative uncertainty of 6.4 % [71]. The DØ collaboration measures $\sigma_{t\bar{t}} = 7.56^{+0.63}_{-0.56}$ [72]. Both measurements agree with approximate NNLO QCD calculations for the process at the Tevatron, which predicts $\sigma_{t\bar{t}} = 7.46^{+0.66}_{-0.80}\,\text{pb}$ [71].

In 2010, the ATLAS and CMS collaborations both published measurements of $\sigma_{t\bar{t}}$ in proton-proton collisions at a center-of-mass energy of $\sqrt{s} = 7$ TeV in about $3\,\text{pb}^{-1}$ of data [5, 6]. ATLAS measured $\sigma_{t\bar{t}} = 145^{+52}_{-41}\,\text{pb}$, a total uncertainty of 30-40 %. This served to establish the signal at this energy and showed already that there are no enormous surprises in the rate of $t\bar{t}$ production. This measurement, along with the corresponding CMS measurement, is shown

in Figure 2.4 together with the measurements from the Tevatron at proton-antiproton collision energies of $\sqrt{s} = 1.8$ and 1.96 TeV. The theoretical prediction for the dependence of $\sigma_{t\bar{t}}$ on the center-of-mass energy for both types of collisions is shown as well. This essentially represents the knowledge of $\sigma_{t\bar{t}}$ at $\sqrt{s} = 7$ TeV before the work presented in Chapters 7 and 8 was undertaken.

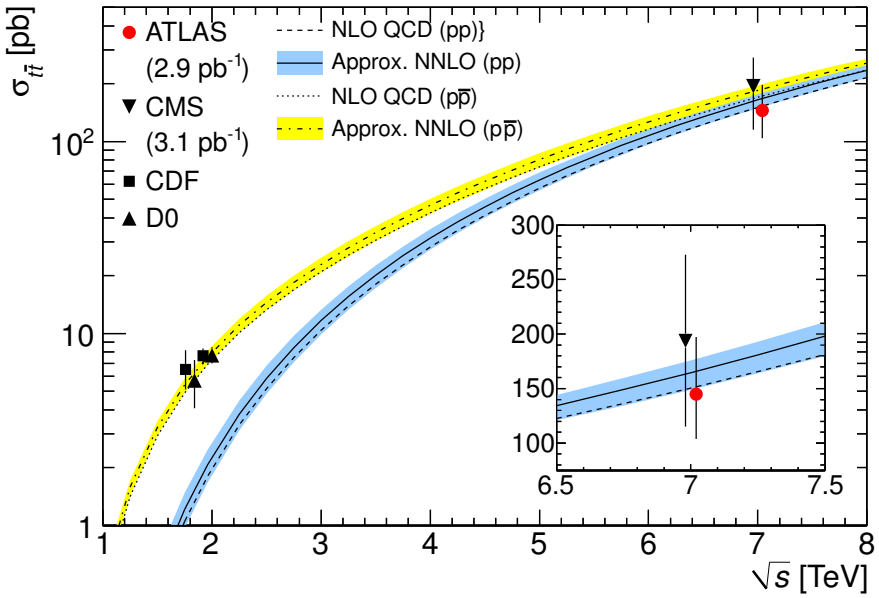

Figure 2.4: The top pair production cross section as a function of center-of-mass collision energy, as of late 2010. Measurements from the Tevatron at $p\bar{p}$ collision energies $\sqrt{s} = 1.8$ and 1.96 TeV are shown along with the results from the very first $3\,\text{pb}^{-1}$ of data from LHC pp collisions at $\sqrt{s} = 7$ TeV. The error bars on the measured $\sigma_{t\bar{t}}$ values represent the sum of all uncertainties. Theoretical predictions shown are from Hathor[13], with the uncertainty band corresponding to scale and PDF uncertainties.

The Production of W+jets

The production of a W boson with associated jets yields the same final state objects as in the decay of top quark pairs. The predictions for the cross section of this process are significantly more complicated because it is higher order in α_s, often involving more partons in the matrix element calculation. Since two of the analyses in this thesis make use of the assumption that every top quark decays as $t \to Wb$, the production of W+jets where one or two of the jets are from heavy quark decays is of importance.

The basic process for W production is $q\bar{q}' \to W$ and yields only the direct decay products of the W in the final state. The LO Feynman diagram is shown in Figure 2.5, together with a contribution to the W+1 jet final state. Leading order predictions for the W/Z+2 jets cross section were first completed in the mid-1980's and by now W+4 jets is available at NLO [73, 74, 75]. The LO to NLO k-factor corrections for W+jets are in the range of 1.5-2.0 [75], motivating both the need for special experimental care and for more precise calculations. In the analyses here, the W+jets contribution will be determined in each jet bin separately, with a constraint of

$\Delta\sigma \sim 50\,\%$, however the kinematics used to describe it will be LO as no higher order simulation is available as of yet.

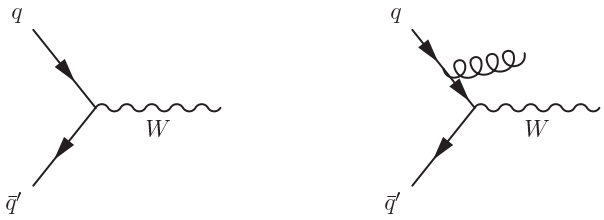

Figure 2.5: The LO Feynman diagram for exclusive W production in proton-proton collisions which is from quark annihilation (left), together with an example of initial state gluon radiation off of one of the incoming quarks, a LO contribution to the W+1-jet final state (right).

The final states of particular interest in such calculations are W plus a heavy quark pair, $W{+}b\bar{b}$ and $W{+}c\bar{c}$, as well as W plus a single heavy quark, $W{+}b/\bar{b}$ and $W{+}c/\bar{c}$. These are calculated as an N-jet final state where one or two of the jets is heavy flavor. The main contributing Feynman diagrams are shown in Figure 2.6 [76]. The calculations for either b or c in the final state are quite similar in principle.

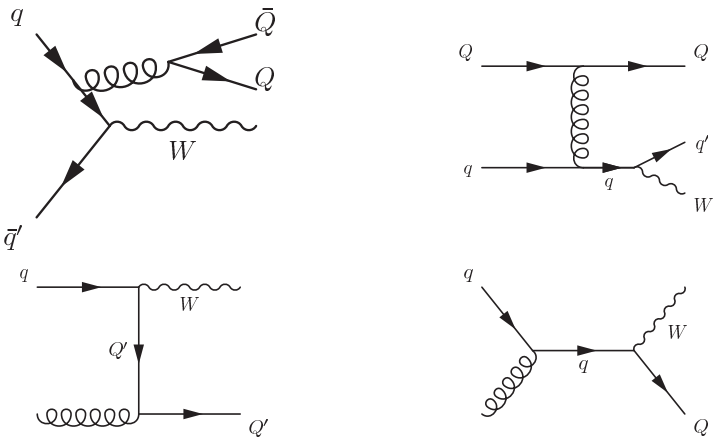

Figure 2.6: The dominant Feynman diagrams for W production in association with heavy-flavor jets, where $Q = c, b$. The dominant mechanism for heavy flavor pair production is a radiated gluon splitting to $Q\bar{Q}$ (top left). For single production of a heavy flavor jet, the main mechanisms are either a heavy parton directly from the PDF (top right) or a flavor-changing weak current to produce the heavy flavor quark along with the W (bottom row). The latter dominates for $W + c$ production, with an s-quark in the initial state. The PDF contribution dominates for $W + b$ production due to CKM suppression of the $s \to Wb$ vertex and the as of yet immeasurably small top quark component of the proton PDF. Initial and final state gluon radiation in any of these processes can produce additional jets.

There are two mechanisms to produce of a single heavy quark jet: there is either a flavor changing (weak) current to produce both the W and the heavy quark or there is a heavy parton in the initial state. The LO Feynman diagrams for these two processes are shown in Figure 2.6.

The production of charm is enhanced with respect to bottom due to the strange component of the PDF, where the process $sg \to Wc$ is favored due to V_{cs} in the CKM matrix [77]. By comparison, production of a b-quark in the final state by the same mechanism would require a top quark in the PDF, a process so thoroughly negligible it is not considered. A $s \to Wb$ vertex is therefore necessary for that process to produce a single b-quark, which is CKM suppressed. The main contribution to the production of a b-quark in association with a W is therefore expected to contain a b-quark coming directly from the PDF. The large b mass suppresses this contribution from the PDF as well.

The prediction of $W + c$ has begun to reach NLO accuracy. Results show that it is a non-negligible portion of the inclusive W+jets production cross section[76]. Interest in the suppressed $W + b$ is in great part due to the recent observation of single top quark production which has the same final state [55, 56], making $W + b$ an essential background to understand for that measurement, if of a small magnitude. Indeed the process has been measured by ATLAS and found to have a central value larger than expected but consistent with predictions nonetheless [78, 79].

The main mechanism for heavy quark pair production in association with a W comes from gluon splitting, $g \to Q\bar{Q}$ [80]. These predictions for W+$b\bar{b}$ and W+$c\bar{c}$ have reached NLO precision [81, 80, 82]. There is particular interest in W+$b\bar{b}$ due to the possibility to observe a Higgs boson in the $H \to b\bar{b}$ decay channel, where a Higgs is produced along with a W. This would lead to W+$b\bar{b}$ final state as well, making direct production of W+$b\bar{b}$ a background to the Higgs search in this final state, thereby necessitating its precise prediction [80].

In the analyses presented here, most processes are normalized to theoretical predictions, while some are normalized to measurements from within ATLAS where available. The W+jets background and in particular the heavy flavor content is normalized to measurements. In general, the heavy flavor content is treated as a ratio of events containing a certain jet configuration in the final state to all other jet configurations, as found in the MC.

To quantify the heavy flavor content in data with respect to the MC, the ratio $f_{\mathrm{W_{HF}}}$ is defined, such that

$$f_{\mathrm{W_{HF}}} \cdot \left(\frac{\sigma(W{+}Q\bar{Q})_{\mathrm{incl.}}}{\sigma(W{+}2\ \mathrm{jets})_{\mathrm{incl.}} - \sigma(W{+}Q\bar{Q})_{\mathrm{incl.}}} \right)_{\mathrm{MC}} = \left(\frac{\sigma(W{+}Q\bar{Q})_{\mathrm{incl.}}}{\sigma(W{+}2\ \mathrm{jets})_{\mathrm{incl.}} - \sigma(W{+}Q\bar{Q})_{\mathrm{incl.}}} \right)_{\mathrm{Measured}},$$

where $Q = b, c$. The denominator has all 2-jet (inclusive) configurations *except* for the processes considered in the numerator, which are those containing a pair of heavy flavor jets. A value $f_{\mathrm{W_{HF}}} = 1$ is therefore the expectation before measurement. It should be noted that the $W + b$ process is technically included in the numerator of the definition, although only the contribution with a PDF b-parton is considered[3]. The process is mathematically assumed to scale with W+$b\bar{b}$ and W+$c\bar{c}$, but no physical sensitivity to the process expected.

Similarly, f_{Wc} is defined, such that

$$f_{\mathrm{Wc}} \cdot \left(\frac{\sigma(W{+}c/\bar{c}{+}\mathrm{jet})_{\mathrm{incl.}}}{\sigma(W{+}2\ \mathrm{jets})_{\mathrm{incl.}} - \sigma(W{+}c/\bar{c}{+}\mathrm{jet})_{\mathrm{incl.}}} \right)_{\mathrm{MC}} = \left(\frac{\sigma(W{+}c/\bar{c}{+}\mathrm{jet})_{\mathrm{incl.}}}{\sigma(W{+}2\ \mathrm{jets})_{\mathrm{incl.}} - \sigma(W{+}c/\bar{c}{+}\mathrm{jet})_{\mathrm{incl.}}} \right)_{\mathrm{Measured}}.$$

Note that the denominators are not the same in the definition of $f_{\mathrm{W_{HF}}}$ and f_{Wc}; in the former case the $W + c$ process is included while $W + b\bar{b}$ and $W + c\bar{c}$ are excluded, and vice-versa.

[3] This process with a PDF b-parton is so small that it is not even mentioned whether or not it is indeed simulated in the manual for the MC generator used, ALPGEN [83, 84]. The author of the generator claims, however, that it is calculated. The other processes, which require a flavor-changing interaction, are found in ALPGEN for c-quarks but not b-quarks, because the author 'didn't think it would have a large cross section'.

The analysis in Chapter 7 is flavor-sensitive and treats the uncertainty on $f_{\mathrm{W_{HF}}}$ and f_{Wc} as a systematic uncertainty in the determination of $\sigma_{t\bar{t}}$. The analysis in Chapter 8 is almost entirely insensitive to flavor effects. For the final analysis presented in Chapter 9, the fractions $f_{\mathrm{W_{HF}}}$ and f_{Wc} are measured simultaneously with $\sigma_{t\bar{t}}$.

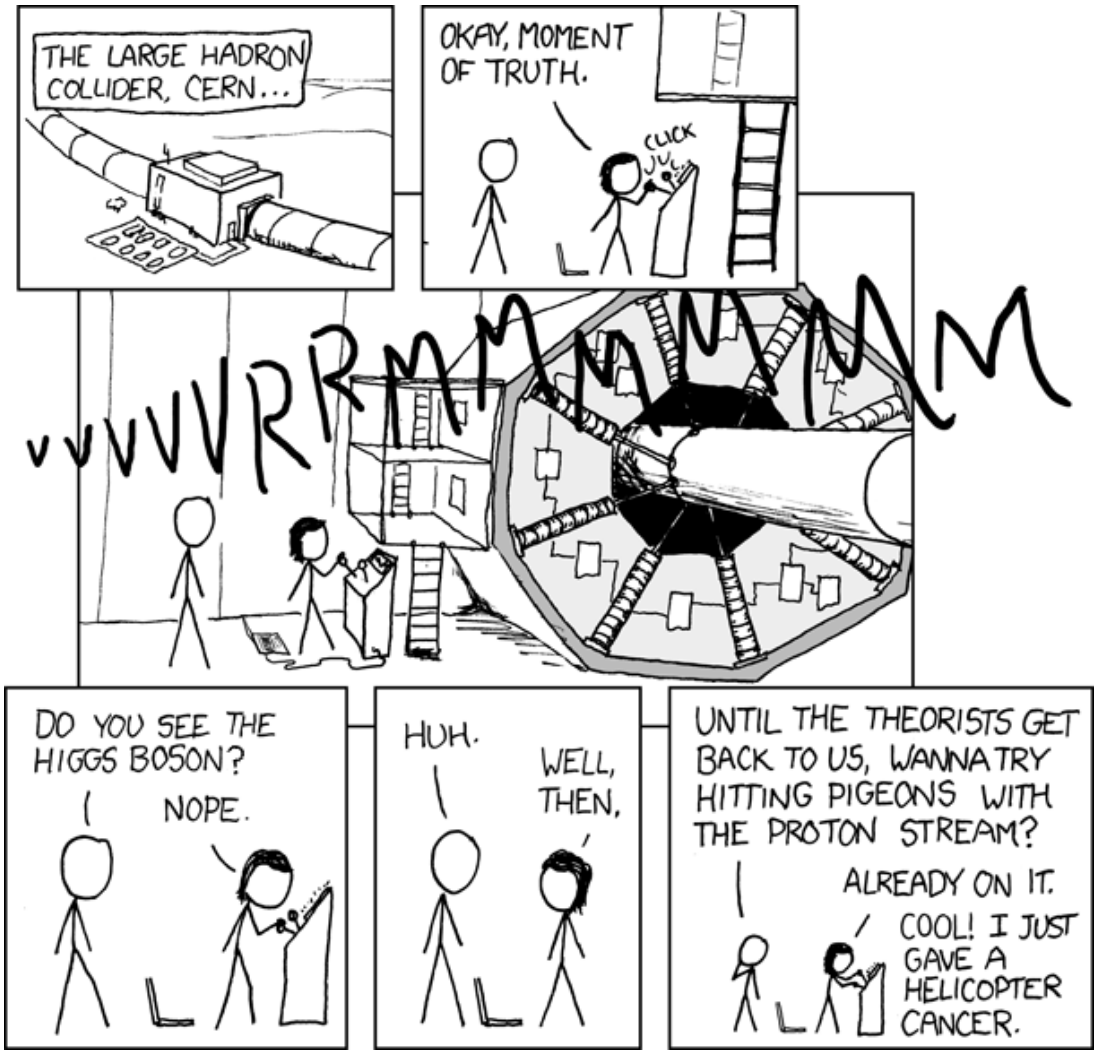

Large Hadron Collider. "When charged particles of more than 5 TeV pass through a bubble chamber, they leave a trail of candy."[19]

3 Experimental Environment

The data analyzed in this thesis are high energy proton-proton collisions produced by he Large Hadron Collider (LHC) and recorded by the ATLAS detector, at CERN in Geneva, Switzerland. The accelerator and the detector will both be described here.

3.1 The LHC Accelerator

The LHC is a proton-proton (pp) collider which began successful operation in autumn 2009, and has been improving its performance since. The LHC is 27 km in circumference, built in the tunnel originally used by the LEP collider, about 100 m below the surface of the earth in the bedrock of the Alps. Four main experiments are built in caverns at the level of the accelerator, each one at an interaction point where the beams of protons are brought into collision. Each beam consists of huge numbers of protons, organized first into "bunches" – about 10^{11} protons, packed as densely as possible – spaced at intervals of 50 ns [85] (about 15 m). These bunches are organized into "trains", which are groups of bunches, typically 8 or 12 bunches long during 2011. The trains are separated by a longer distance from one another. A theoretical maximum of 2,808 bunches in the LHC at once is possible, which would require a spacing of only 25 ns[85]. So far, a maximum of 1,380 – the maximum with 50 ns spacing – has been achieved[86].

Protons being accelerated go through a chain of many steps, beginning with a bottle of hydrogen gas and ending with the LHC [85]. Hydrogen molecules are dissociated in an electric field, breaking H_2 into hydrogen atoms and stripping the electrons away. A magnetic field is applied to bend the positively charged H^+ (that is, the proton) in the direction opposite from the electrons. The protons are accelerated in a linear accelerator up to 50 MeV, then injected into the Proton Synchrotron Booster (PSB), which subsequently accelerates protons to 1.4 GeV. They are then accelerated up to 450 GeV in the Super Proton Synchrotron (SPS) after passing through the 25 GeV Proton Synchrotron (PS) accelerator. At an energy of 450 GeV, protons are injected into the LHC, where they are accelerated to their final collision energy.

The LHC has 1,232 bending dipoles which make up the core of the accelerator, as well as a system of quadrupole, sextupole, and octupole magnets used to bring the proton beams into collision at the interaction points, at the center of each detector. The LHC's accelerator chain is shown in Figure 3.1. At the time of writing, the LHC has operated in three stages of energy: first at 450 GeV per beam, then at 1.18 TeV, and finally an operational energy of 3.5 TeV. All data analyzed in this thesis are recorded at 3.5 TeV per beam, providing a center-of-mass energy of $\sqrt{s} = 7$ TeV. A visualization of the very first collision event recorded by ATLAS, at $\sqrt{s} = 900$ GeV, is shown in Figure 3.2 alongside one of the first di-jet events recorded by ATLAS at $\sqrt{s} = 7$ TeV, four months later.

The LHC can also be used as a heavy ion accelerator for lead ion collisions, where each nucleon present achieves the highest energy deliverable by the accelerator, so far 3.5 TeV / nucleon. Given the density of a bound nucleus, an ion beam brought to these energies behaves very differently in collision than bunches of protons, allowing for study of low-p_T, high multiplicity events (in contrast to the proton physics program, which focuses on the opposite). The heavy-ion physics

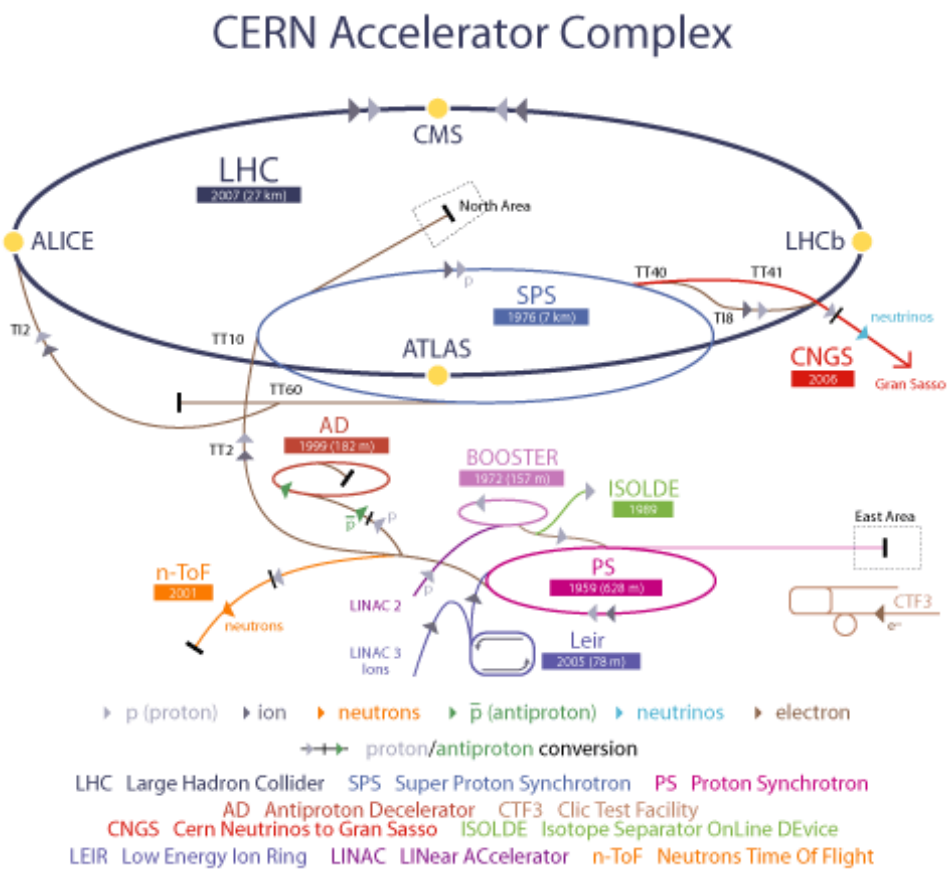

Figure 3.1: The CERN accelator complex, including the LHC. The trajectory of a proton can be followed from the LINAC to the Booster and PS, then on to the SPS and finally the LHC. Image from [87].

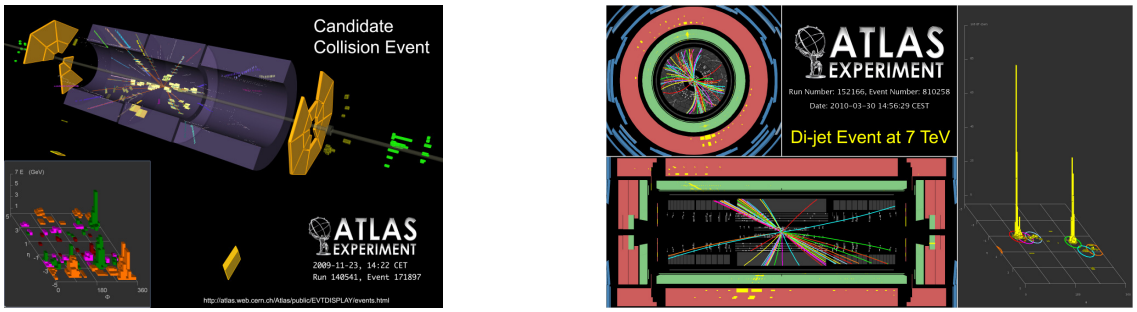

Figure 3.2: The first collision provided by the LHC recorded by the ATLAS detector, at $\sqrt{s} =$ 900 GeV, on 23 November 2009 (left). Soft hadronic activity can be seen. di-jet event recorded by ATLAS during the first $\sqrt{s} = 7$ TeV collision fill on 30 March 2010 (right). Images from [88] and [89].

program at the LHC has proved successful, both for the special-purpose ALICE detector designed precisely for heavy ion collisions and for the multi-purpose detectors, CMS and ATLAS.

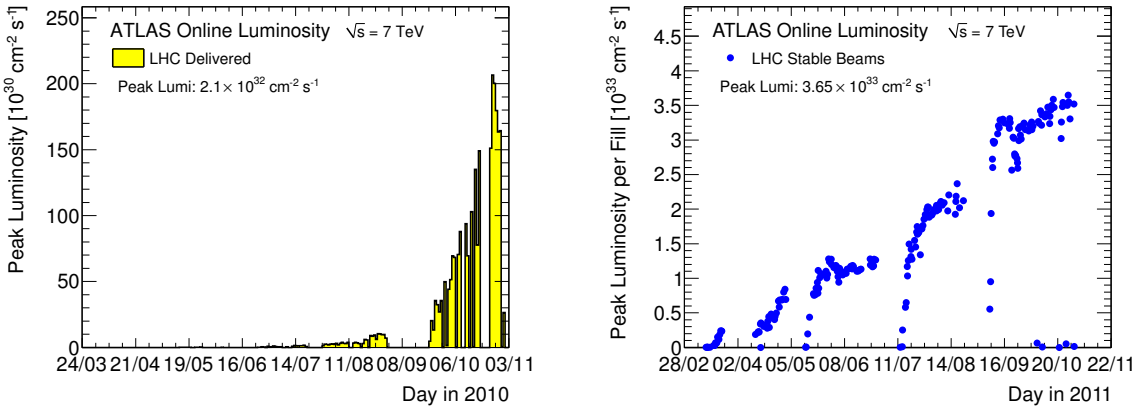

Figure 3.3: The peak instantaneous luminosity delivered to ATLAS by the LHC in 2010 (left) and 2011 (right). One can see a clear increase over time, as the LHC improved its performance. The y-scale on the right plot is three orders of magnitude higher than on the left plot. Images from [90].

Proton Beam Data Delivered at $\sqrt{s} = 7$ TeV

To quantify the amount of data delivered by a collider, the instantaneous luminosity $\mathcal{L}$ is defined, a measure of particle flux from two sources per unit time:

$$\mathcal{L} = fn\frac{N_1 N_2}{A}\ \mathrm{cm}^{-2}\,\mathrm{s}^{-1}.$$

Here, N_1 and N_2 are the number of particles in each bunch, n is the number of bunches in each beam, f is the revolution frequency and A is the cross-sectional area of the beams. Peak luminosities on the order of $\sim 10^{33}\,\mathrm{cm}^{-2}\,\mathrm{s}^{-1}$ have already been achieved at the LHC, just one order of magnitude lower than the design [85, 90]. The time-integrated luminosity, $\int \mathcal{L}\,dt$, has the units of inverse cross-section, and indeed is directly proportional to the number of events (N) expected for a given physical process, by a factor of the cross section σ:

$$N = \sigma \times \int \mathcal{L}\,dt.$$

Measuring the cross section σ of the $t\bar{t}$ process is the goal of this thesis, and the uncertainty on the measurement goes down with an increasing amount of data (for a simple counting experiment the statistical uncertainty goes as $\sqrt{N}$, thus the relative uncertainty goes as $1/\sqrt{N}$). It is therefore in the interest of such measurements to collect more luminosity, and, in the interest of time, the highest instantaneous luminosity possible. Given that the accelerator has already been built – defining the revolution frequency and the cross-sectional area of the beams – luminosity can be increased by stuffing more protons into a given bunch, putting more bunches into the accelerator at once and by running for a longer time. The peak instantaneous luminosity delivered to ATLAS as a function of the day in both 2010 and 2011 is shown in Figure 3.3, and the integrated luminosity delivered by the LHC to ATLAS and recorded by ATLAS is shown in Figure 3.4. One can see there increasingly higher peak instantaneous luminosities, an effect of both adding bunches over time and adding protons to each bunch. Work has been done in order to calibrate the measurement of the integrated luminosity recorded by ATLAS and to estimate its uncertainty [91, 92]. An uncertainty of 3.4 % on its magnitude is used for 2010, with a slightly increased uncertainty of 3.7 % in 2011.

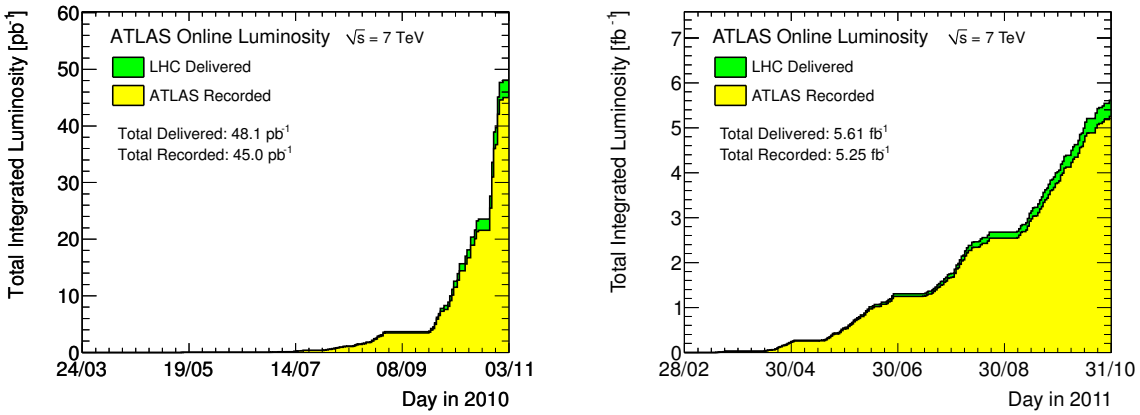

Figure 3.4: The integrated luminosity delivered to ATLAS by the LHC and recorded by ATLAS, both in 2010 (left) and 2011 (right). The amount of data recorded has grown rapidly over time since the LHC has begun delivering pp collisions. The y-axis of the plot on the right is three orders of magnitude larger (units of fb^{-1}) than that of the left-hand plot (pb^{-1}). Images from [90].

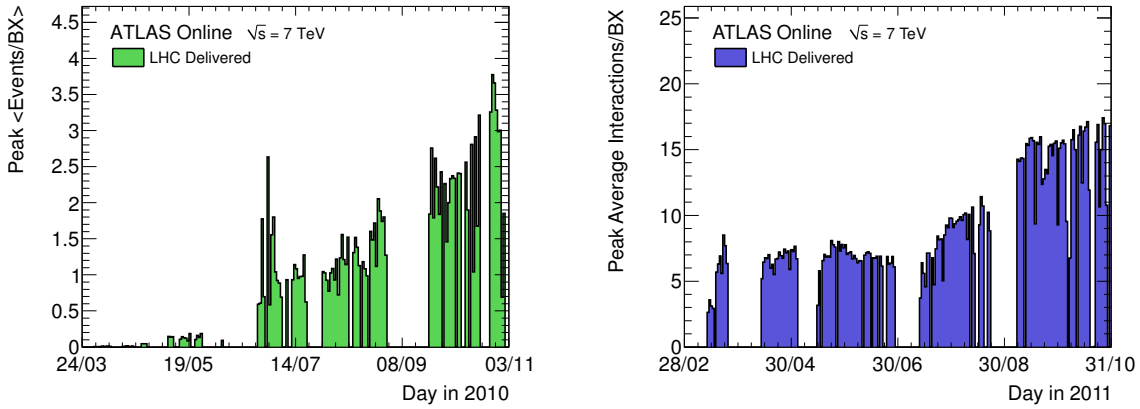

Figure 3.5: The peak of the average number of interactions per bunch crossing, $< \mu >$, shown per luminosity block (60 or 120 s of data taking) as a function of time in 2010 (left) and 2011 (right). One can see clearly how this is correlated with the instantaneous luminosity, shown in Figure 3.3. Images from [90].

Increasing instantaneous luminosity does however come with an experimental challenge, known as "pileup". The interaction of partons in a proton-proton interaction is a statistical process, whose chance of occurring is increased by increasing the number of protons present. Nothing prevents several parton-parton interactions from occurring in one crossing of the proton beams, indeed such "multiple interactions" are the norm. The average number of parton interactions per bunch crossing, $< \mu >$, is shown for the data recorded in 2010 and 2011 in Figure 3.5. The experimental challenges this poses will be discussed in Section 4.1.

3.2 The ATLAS Experiment

The ATLAS (A Toroidal LHC ApparatuS) detector is one of the two multi-purpose detectors at the LHC. It is located at interaction point 1, just across the street from the main entrance to CERN. ATLAS is built following a "traditional" detector design, with an inner tracking detector to measure charged particle's trajectory, followed by calorimeters to measure both electromagnetic and hadronic interactions, all surrounded by a designated muon tracking system. A schematic view of the entire detector can be seen in Figure 3.6. The outer muon system also resides in a magnetic (toroidal) field that has eight-fold symmetry around the beam pipe. A smaller toroidal magnetic system, also with eight-fold symmetry and staggered with respect to the barrel magnets, is used for the outermost regions of ATLAS. The complete design of the ATLAS detector is laid out in [93, 94].

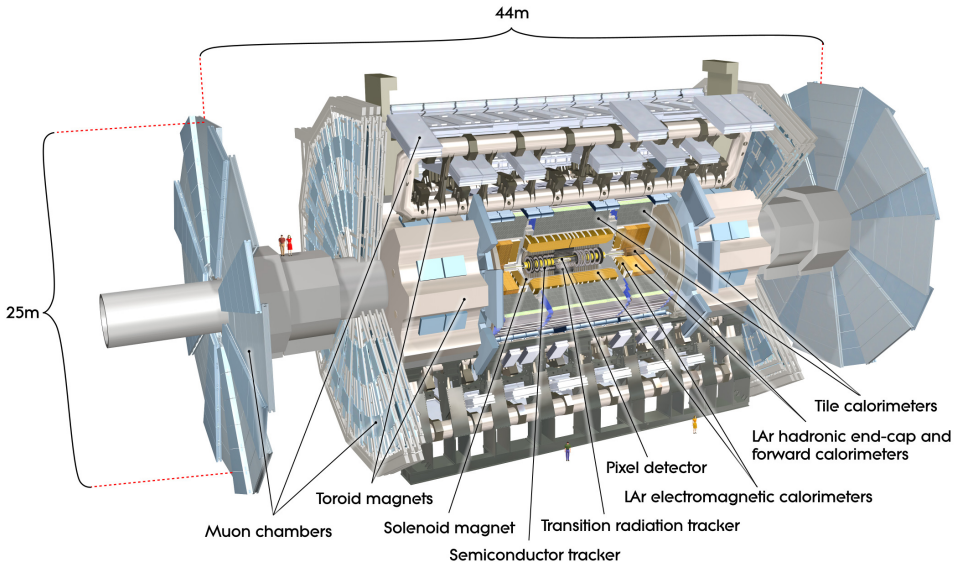

Figure 3.6: A schematic view of the ATLAS detector. From inside to out, the inner detector is made up of the pixel detector, the SCT, and the TRT, which reside in a 2 T solenoidal magnetic field. The various calorimeter systems (LAr and Tile) are found beyond that. The outermost layer of the detector is the muon system, present both in the barrel region and making up the two "wheels" beyond the main body of the detector, situated in a toroidal field. Image from [95].

Coordinate System

The ATLAS detector uses a right-handed coordinate system. The $+x$ direction points from the interaction point towards the center of the LHC, while the $+y$ direction points skywards. The beam travels along the z-axis, making the x-y plane transverse to it. Most often, polar coordinates are used. The azimuthal angle ϕ is measured in the $x - y$ plane, where transverse kinematic definitions including transverse momentum (p_{T}), transverse energy (E_{T}), and missing transverse energy ($E_{\mathrm{T}}^{\mathrm{miss}}$) are defined. The rapidity angle θ is defined as the angle from the beam axis, and the pseudorapidity η, defined as

$$\eta \equiv -\ln \tan(\theta/2),$$

is generally used. A very useful quantity for measuring the distance between two objects in the detector, ΔR, is defined as

$$\Delta R \equiv \sqrt{\Delta\phi^2 + \Delta\eta^2}.$$

Two different coordinate system definitions are used, "detector" and "physics". In detector coordinates, the physical center of ATLAS is taken to be the origin of coordinates. Object selection is based on the physical limitations of the detector and therefore uses the detector coordinate system. In physics coordinates, the reconstructed primary vertex of the event is taken to be the origin of coordinates. Higher order corrections to reconstruction, such as an object's p_{T}, are often taken into account using physics coordinates. It should be noted, however, that the beam spot of the LHC is significantly more accurate in z than it was at the Tevatron, making the distinction between physics and detector coordinates less critical than there.

Inner Detector

The ATLAS inner detector is designed to precisely reconstruct the trajectory of charged particles in a 2 T solenoidal field over a range of hundreds of MeV to a couple of TeV [95]. The extremely precise pixel detector is closest to the beamline is, followed by the silicon strip tracker (SCT). This is in turn surrounded by the transition radiation tracker (TRT), a dedicated system for distinguishing pions from electrons. The inner detector covers up to $|\eta| < 2.5$, making it physically about 7 m long and 2.3 m in diameter. A plan view of one quadrant of inner detector can be seen in Figure 3.7.

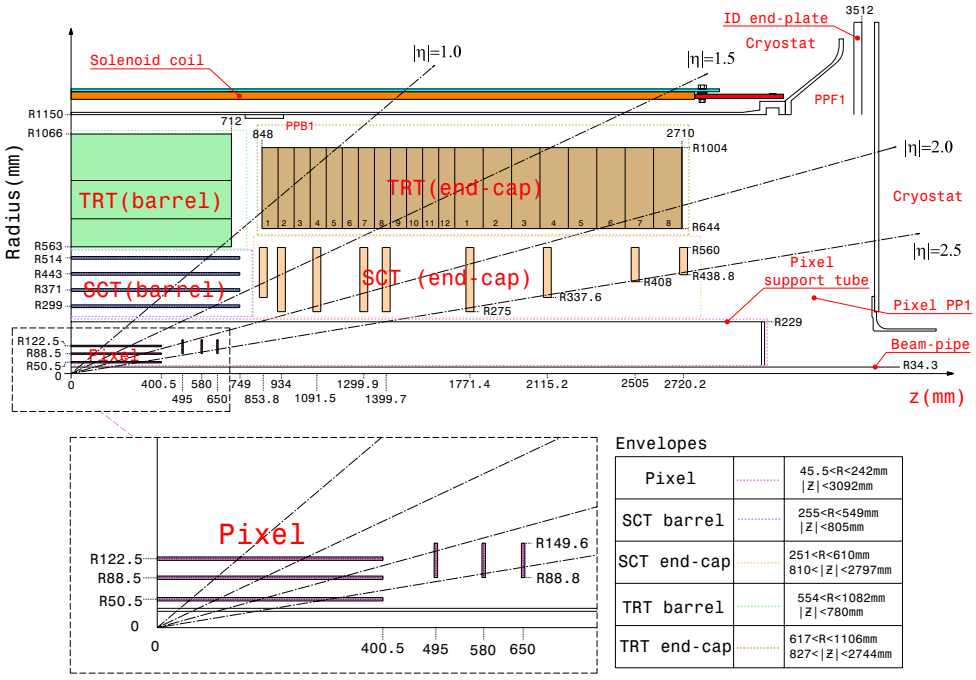

Figure 3.7: A plan view of one quadrant of the inner detector, with an enlargement of the pixel detector on the bottom. From inside to outside, the inner detector consists of the Pixel Detector, SCT, and TRT, all residing in a 2 T solenoidal magnetic field. Image from [95].

The pixel subsystem is at the core of the ATLAS detector. Each pixel sensor is a 50×400 μm^2 chip, with a total of 80.4 million readout channels in the entire system. The pixel detector is laid

out in three concentric layers in the barrel region, with three endcaps on either side. The design is such that a charged particle should always cross three layers of the pixel detector, aiding in precise reconstruction of the track's trajectory and offering redundancy in case of a hardware failure. In particular, the system is used in determining the location of a track's vertex, useful in distinguishing primary vertices from secondary. The closest layer, known as the b-layer, is about 50 mm from the interaction point, just outside the beam pipe's vacuum. As the name suggests, it is designed to be able to identify the path of charged particles precisely enough to reconstruct the displaced decay vertex of a long-lived hadron, resultant from the production of a b-quark in a hard interaction. The pixel detector's calibration and functioning is crucial to the b-tagging algorithms which will be discussed in Section 4.4. Since there is very little material in between the interaction point and the b-layer, it is also extremely useful for distinguishing electrons from photons. The latter can convert in the detector, often after passing through the b-layer without leaving a hit there. Early measurements of the material in the pixel system and beampipe, as well as particle energy loss per unit length, are shown in Figure 3.8.

The SCT system is a silicon strip detector, arranged with a geometry similar to that of the pixel system, covering a physically larger area to have the same η coverage. It is made up of about 6.3 million channels. The silicon strip technology is less precise than the digital pixel system but also significantly less expensive, allowing it to cover a larger area. A typical prompt lepton track will have at least five hits in the SCT. Together with the pixel detector, these two silicon detectors allow for precise track reconstruction.

The TRT surrounds the SCT with $|\eta| < 2.0$. It consists of about 300,000 drift tubes, 36 of which should be crossed by most particles. While so many hits are in general useful for refining tracking in general, it is dedicated to distinguishing electrons from hadrons (pions in particular). The high-threshold hits in the TRT signify photons radiated by an electron as it crosses from one material to another, allowing for this discrimination. The three inner detector subsystems together allow for precise tracking of charged particles in general as well as measuring crucial properties which aid the separation of certain types of particles from others.

Calorimeters

The ATLAS calorimeter is a set of several systems designed to be optimal for object reconstruction over a very wide momentum range, from tens of MeV to a few TeV [98, 95]. Generally, there is an inner electromagnetic (EM) calorimeter and an outer hadronic calorimeter. All components are sampling calorimeters. Calorimetry begins just after the inner detector's solenoid.

The EM calorimeter is a lead-liquid-argon design (LAr), extending out to $|\eta| < 3.2$, with a presampler (PS) in the range $|\eta| < 1.8$ [95]. The granularity of barrel EM calorimeter reaches a fineness of 0.003×0.01 ($\Delta\eta \times \Delta\phi$) in the first of the three samplings (excluding the PS) and 0.025×0.025 in the second. The granularity of the EM endcap changes over η, with its finest granularity the same as the barrel's first sampling. A schematic of the highly efficient accordion design of the calorimeter is shown in Figure 3.9.

The barrel of the hadronic calorimeter consists of plastic scintillators in iron absorber plates (Tile) within $|\eta| < 1.7$. The first of the two out of thrsee samples have a granularity of 0.1×0.1 while the third is coarser in η, $\Delta\eta = 0.2$. The hadronic calorimeter endcaps are again LAr technology due to the radiation hardness necessary to be robust against increased particle flux, covering $1.5 < |\eta| < 3.2$. The granularity is 0.1×0.1 for $1.5 < |\eta| < 2.5$, and 0.2×0.2 for $2.5 < |\eta| < 3.2$. The forward calorimeters cover the outermost range, $3.1 < |\eta| < 4.9$, with a granularity of 0.2×0.2, following again the LAr technology.

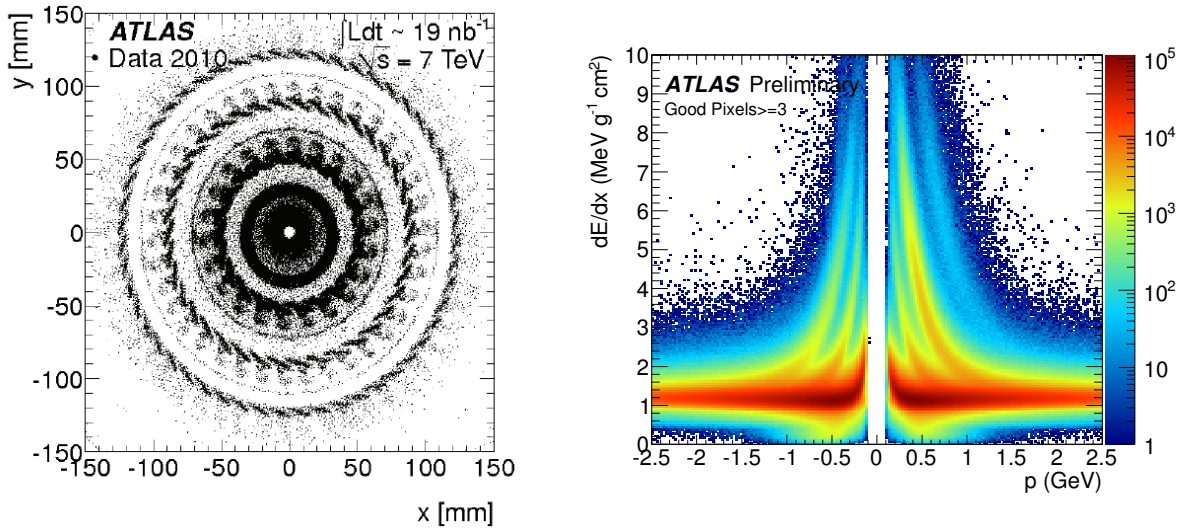

Figure 3.8: Early measurements using the pixel detector. The reconstructed position of secondary vertices in very early data, reflecting the material present (left). Image from [96]. Viewing from outside inwards, one can see the three layers of the the pixel detector, and then the beam pipe itself. The stopping distance of particles is shown as a function of their momentum (right), from [97]. The various "stripes" in the plot correspond to different particles.

Muon System

The ATLAS muon system uses several different types of chambers, in particular two types with fast readout and coarse granularity used for triggering and two types with slower readout and finer resolution for precision muon tracking [95]. The Monitored Drift Tubes (MDT) are the precision chambers over much of the system, while Cathode Strip Chambers (CSC) are used in the highest-radiation setting. The precision chambers cover up to $|\eta| < 2.7$, where the innermost chambers in the region $2.0 < |\eta| < 2.7$ are CSCs and the rest are MDTs. The muon trigger system uses Resistive Plate Chambers (RPC) in the barrel region up to $|\eta| < 1.05$ and Thin Gap Chambers (TGC) in the endcap region, covering $1.05 < |\eta| < 2.4$.

The Muon system sits in a toroidal field with a maximum bending power of 7.5 Tm perpendicular to the muon trajectory. Three toroids are used, each of which consist of eight coils, arranged symmetrically around the beam axis. Two of the toroids are for the endcaps, rotated at 22.5° with respect to the barrel toroid, shown in Figure 3.9.

Trigger and Data Acquisition

The trigger system in ATLAS decides in near-real time ("online") whether or not to record a given event. It is designed in three levels which have access to increasing amounts of information, known as Level 1 (L1), Level 2 (L2), and the Event Filter (EF) [95]. Overall, the rate is reduced to 2-300 Hz, from its initial rate which changes depending on the accelerator's conditions (the LHC's design a ∼1 GHz collision rate). The L1 trigger system runs on hardware distributed throughout the detector, using coarse-grained information from specific systems: the dedicated muon trigger chambers, specific sections of the calorimeter, and parts of the SCT. In running its algorithm, the L1 trigger identifies "Regions of Interest" (RoI) in $\eta \times \phi$ where a potential physical object is present. The L1 trigger passes ∼ 100 kHz events to centralized L2 software,

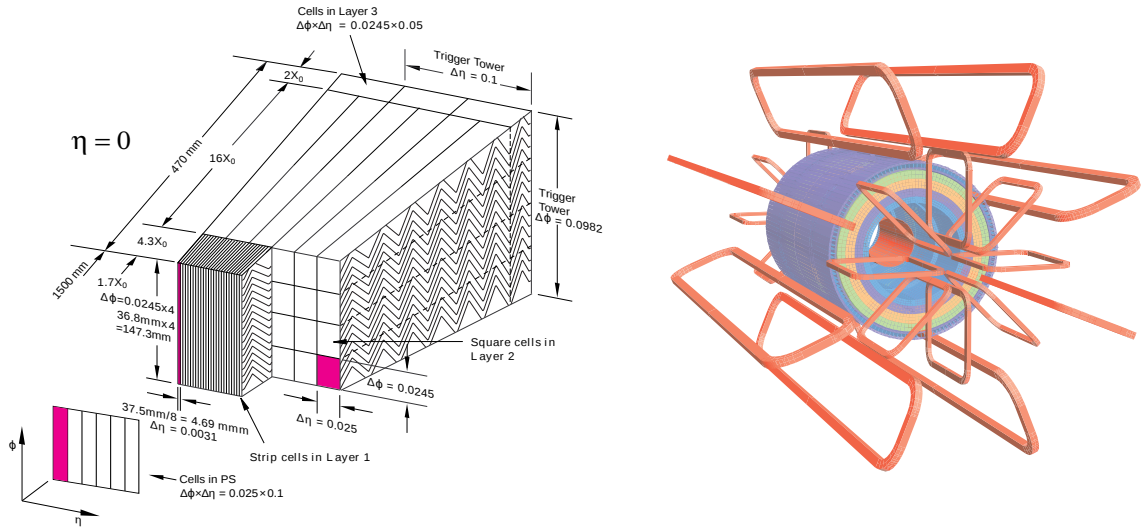

Figure 3.9: Elements of the ATLAS detector design. The electromagnetic calorimeter's accordion design (left). The design of the ATLAS magnet system is shown (right). The inner cylinder is the solenoidal magnetic in which the inner detector sits. The muon system's barrel toroid surrounds that, and a smaller toroid for the muon endcap system (the "wheels") can be found on either end. Images from [95].

which uses full detector readout for the RoIs in reconstruction algorithms which are simplified with respect to those run offline. This is done in order to better determine whether or not a physical object is indeed present. Several kHz of events pass the L2 selection for processing by the EF. The EF runs the full ATLAS reconstruction software in the online environment in order to fully reconstruct the event. This is time intensive but has the advantage of being nearly identical to the algorithms used in a physics analysis. The EF chooses 2-300 Hz of events to be written out for permanent storage, to be considered for analysis.

The data acquisition system of the experiment is intertwined with the trigger system. The heart of the data acquisition (DAQ) system are the Readout Drivers (RODs), which are subdetector specific but are used throughout ATLAS [95]. RODs are essentially the detector readout electronics, which do their job after an L1 trigger accepts an event, and function as a buffer to hold the data throughout the process of the trigger decision. The RODs send information for a given RoI to the L2 trigger upon its request, and, if selected, send the information on to the EF. In the calorimeter, front end boards (FEB) perform the analog to digital signal processing necessary before sending information onwards.

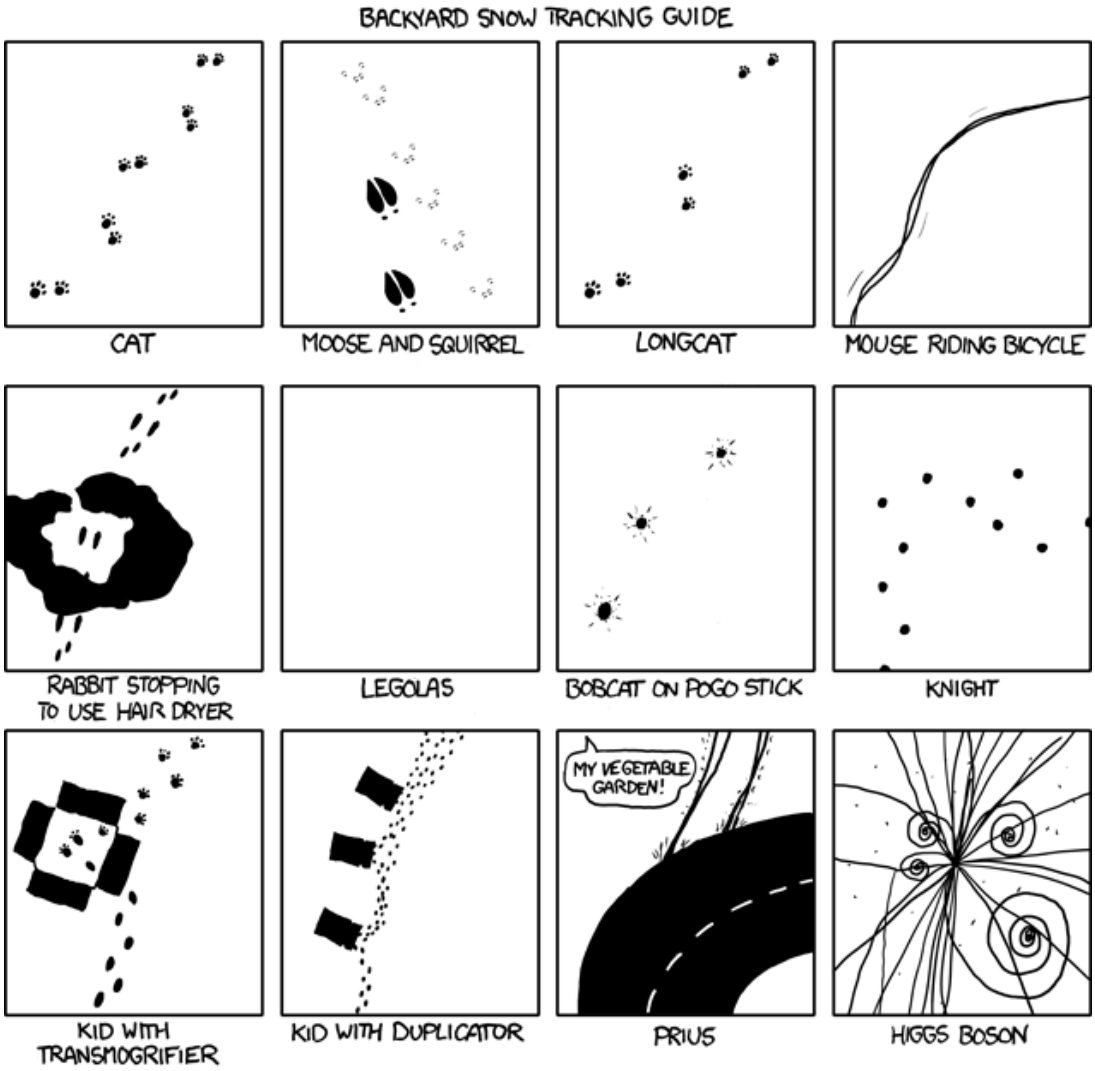

Snow Tracking. "I suppose that's more accurately a hare dryer."[19]

4 Reconstruction and Definition of Physical Objects

The association of primary measurements in the detector with physical objects is described here, a process applied identically to the MC simulation and the data. Imperfect simulation can give rise to discrepancies, which are understood and calibrated as best as possible. The reconstruction process and the associated systematic uncertainties in analyses are discussed.

The selection of events is described here as well. There are two main steps in the selection procedure. The first is to determine which events can be considered for analysis at all: those which have been triggered by an appropriate object and those in which we expect to have objects that can be well reconstructed. This is discussed in Section 4.1. Once an event is deemed to be analyzable, the objects present in the event are reconstructed and selected as described in Section 4.2. Special attention is paid to the b-tagging algorithms used for identifying heavy-quark hadrons in Section 4.4, which will be later used in Chapters 7 and 9.

For a $t\bar{t}$ pair which decays semileptonically, the end of the decay chain is two b-quarks, two light quarks, an electron (e) or muon (μ), and a neutrino. Quarks are not observed directly but are reconstructed as jets, and the neutrino is not measured directly but quantified in terms of missing transverse energy in the event, $E_{\mathrm{T}}^{\mathrm{miss}}$. The selection of events from the recorded data sample reflect the expectation of observing a final state consistent with the semileptonic decay products of a pair of top quarks. The lepton flavor is used to classify events into lepton channels, called either "e+jets" or "μ+jets". There are certain differences between the requirements in the two channels, which will be noted.

Not all semileptonic $t\bar{t}$ events are observed; the efficiency of observation is modeled with MC simulation which will be described in the next chapter. If a charged lepton is not observed the event is not used. The expectation of four jets in the final state means that it is not improbable for one jet to be lost. Furthermore, radiation effects mean that it is not unlikely for an additional jet to be observed. Accordingly, the analyses are further divided in "jet multiplicity bins", according to the number of jets present in the event. The analyses in Chapters 7 and 8 use the 3-jet exclusive bin, 4-jet exclusive bin and 5-jet inclusive bin, while the analysis in Chapter 9 adds the 2-jet bin but uses the 4-jet bin inclusively.

This thesis contains analyses using two separate datasets, one recorded in 2010 totaling $\int \mathcal{L}\,dt = 35$ pb^{-1} and one recorded in 2011 comprising $\int \mathcal{L}\,dt = 0.7$ fb^{-1}. Accordingly, certain conditions differing the data between the datasets, which require small changes to event and object definitions. Unless otherwise noted, the statements apply equally to both lepton channels in both datasets.

4.1 Event Level: Data Streams, Triggers, and Event Cleaning

In order to ensure that events considered are those in which proper reconstruction of physical objects can be done, a handful of event-wide requirements are put in place.

Good Run List

The main work of requiring that an event can be considered for analysis is done by the Good Run List (GRL) mechanism, which is applied to all recorded data events in order to preselect those in which protons are being collided and the entire detector is performing as expected. An example of a situation where an event would not be considered is if a crucial section of the detector has been temporarily switched off due to a high-voltage trip. Good data quality for all relevant detector subsystems is required (those described in Section 3.2, with the general exception of calorimetry beyond $|\eta| > 2.5$). Additional checks ensure that each type of physical object needed in the analysis is well behaved in the data, also included in the GRL. Because of the necessity to veto a second lepton, the muon channel analysis must always be able to reconstruct electrons and vice-versa.

Trigger

A trigger is required to fire for an event to be recorded by the detector, as described in Section 3.2. A balance must be found between the bandwidth available to the detector and the requirements for the physics analysis. The expectation of a lepton present in the event provides a clean trigger (as opposed to jets, for instance, which pose enormous experimental challenges. See for instance [99]). The lowest possible thresholds and quality are used at every turn, for two reasons. Foremost, the algorithms run online for the trigger are not identical (at L1 in particular) to those run in the full "offline" reconstruction for the analysis; having a looser selection at the trigger means that more events will be available to the offline algorithms, thereby increasing efficiency in the turn-on region. The best example of this is the p_{T} of the object, for which a trigger has a turn-on. A 15 GeV electron trigger will be fully efficient for offline electrons by about 18 GeV, due to the differences in the algorithms. Furthermore, looser criteria in the definition of the online object is necessary for the methods used to estimate the contributions due to fake leptons, to be discussed in detail in Chapter 5. In general, looser requirements online mean a higher rate of triggered events.

As the LHC delivered higher and higher instantaneous luminosity throughout the periods analyzed here, the trigger requirements had to be tightened. Several triggers have been used depending on when the data was taken, all of which have thresholds for both quality and p_{T} sufficiently lower than the leptons in the analysis at hand. Of note is that the electron trigger rate for the last trigger used in 2010 was predicted to be too high for the 2011 conditions, necessitating raising the trigger threshold from 18 to 22 GeV. The offline cut in the analysis was adjusted accordingly. All triggers used for μ are in their efficiency plateau by p_{T}>20 GeV. A trigger simulation in the MC is used, and it is required to have been fired for MC events as well. Small differences between the simulation of the trigger and its real performance have been observed, giving rise to a systematic uncertainty discussed for each lepton separately.

Calorimeter Cleaning

Two phenomena which affect the calorimeter have occured which affect reconstruction capabilities; these are not accounted for by the GRL. Non-physical high-energy bursts in individual cells in the electromagnetic calorimeter have been observed. These bursts cause a "jet" to be reconstructed and greatly affect the $E_{\mathrm{T}}^{\mathrm{miss}}$ calculation. Events in which such a burst occurred are identified by requiring a certain "quality" of all jets, by checking the timing associated with it, fractions of energy found in the EM versus hadronic calorimeter, and other such sanity checks. If any jet with $p_{\mathrm{T}} > 10$ GeV in an event fulfills the criteria signifying that it came from such a

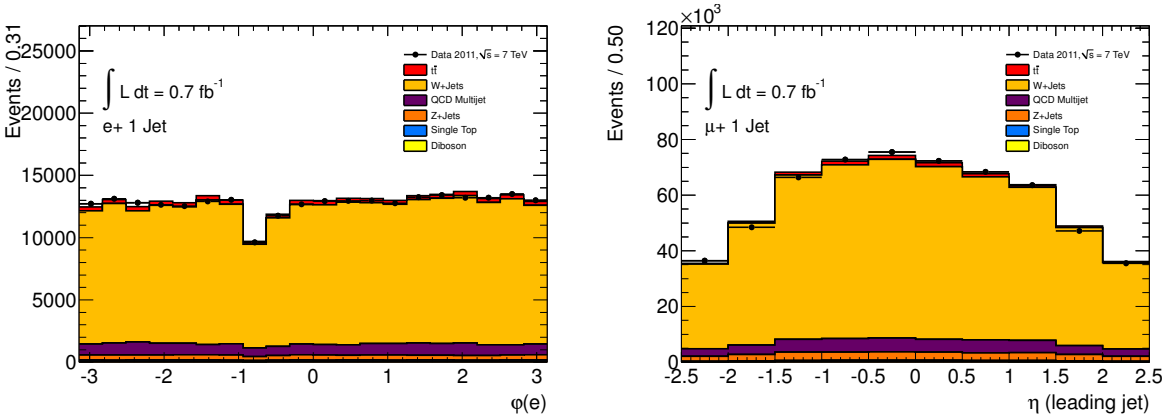

Figure 4.1: The gap caused by the death of 6 adjacent calorimeter front end boards in run 180614, affecting 75% of the $\int \mathcal{L}\,dt = 0.7$ fb^{-1} dataset. The left-hand plot shows the ϕ of electrons in the e+jets channel, showing a clear dip in the region -0.64 $< \phi <$-0.74. The right-hand plot shows the reconstructed jet η in the μ+jets channel, showing a slight asymmetry caused by the jet veto in $0 < \eta < 1.4$. Both plots use the 1-jet inclusive selection which will be described in this chapter.

burst, the event is discarded. This requirement is applied only to data and is considered to not require adjustment in the MC due to the very low rate of these bursts.

A plague of dying FEBs has affected the calorimeter, making the data inaccessible. Two separate mechanisms have been put in place to handle this. In the case of an isolated FEB death, a relatively small amount of the detector is disabled. Jet and $E_{\mathrm{T}}^{\mathrm{miss}}$ reconstruction are only slightly affected and can be corrected for, but the relatively collimated energy deposits from electrons renders it impossible to accurately reconstruct them in such a region. The event will be accepted, but electrons in the region are vetoed. This affects both the $\int \mathcal{L}\,dt = 35$ pb^{-1} and the $\int \mathcal{L}\,dt = 0.7$ fb^{-1} dataset, albeit to different extents, due to a replacement of some of the failed boards during the Christmas 2010 accelerator and detector shutdown.

Additionally, six adjacent FEBs died on 30 April 2011 during run 180614, therefore affecting most of the data analyzed in the $\int \mathcal{L}\,dt = 0.7$ fb^{-1} dataset but none of the $\int \mathcal{L}\,dt = 35$ pb^{-1} dataset. Physically, this corresponds to a region covering (-0.64, -0.74) in ϕ and $(0, 1.4)$ in η. Energy in this region is lost. This has several effects, primarily that the $E_{\mathrm{T}}^{\mathrm{miss}}$ of events where an object crosses this region is mis-reconstructed; accordingly, certain vetoes and corrections are put in place. An event is vetoed if the center of a jet with $p_{\mathrm{T}} > 20$ GeV is within $\Delta R < 0.1$ of the disabled region. Electrons within this region are vetoed, but the event is kept in principle (though in practice, there is always a jet very close to an electron associated with it, so the event will likely be vetoed anyway). For events where a jet is nearby ($0.1 < \Delta R < 0.4$), the core of the jet energy is not lost so the event is kept, but the potential miscalculation in the $E_{\mathrm{T}}^{\mathrm{miss}}$ must nonetheless be corrected for by a smearing procedure. In the MC, the jet and electron vetoes are applied. The secondary correction to smear the missing energy is not applied, giving rise to a small systematic uncertainty. Due to the fact that this affects a portion of the data analyzed (about 3/4), the MC must represent a mixture of the two situations. This is done by choosing a random number for each event in the MC to decide whether or not to apply all of the related cleaning procedures to a given event. The effects of the dead region can be seen in the plots shown in Figure 4.1.

Pileup

The interaction of multiple partons in a single event has been mentioned already in Section 3.1. The average number of interactions per bunch crossing, known as $< \mu >$, is about 2 in the 2010 dataset analyzed in Chapter 7 and about 5 in the portion of the 2011 dataset analyzed in Chapters 8 and 9. This has been shown in Figure 3.5. The modeling of such multiple interactions is extremely difficult, as it resides in the soft regime where QCD becomes divergent. Our understanding of the proton and its interactions are not sufficient to model this well from first principles. Generators are "tuned" to datasets in order to better model these interactions.

The MC has been generated with a best-guess estimate for $< \mu >$ at the time of the most recent processing campaign. A Poisson distribution is used with a most probable value corresponding to that best guess. In both datasets, the data contained less pileup than had been generated in the MC. For the MC needed for comparison to early ATLAS data in 2010, the generators were tuned to Tevatron data. This was found to misestimate effects in much of phase space [100], leading to less pileup in the data than in the MC simulation. The distribution of the number of reconstructed primary vertices is used to approximate the amount of pileup, which is used to reweight the MC to match the data. Weights of about a factor of 2 up or down are derived, depending on the number of vertices (a weight of about 2 for events in MC with 1 reconstructed vertex is used while about 0.5 for events with 5 or more vertices).

The data recorded in 2010 were then used to retune the generators for the MC used in conjunction with the 2011 data [101]. Once again, less pileup was observed in the data than had been expected. The distribution of the average number of interactions per bunch crossing in data and MC can be seen in Figure 4.2. To reweight the MC, a far more precise mechanism was used for this MC than for the previous year's dataset: the exact distribution of $< \mu >$ for the data selected by the GRL is used to reweight the MC. The difference between what is in the simulation and the data is very large in this case, resulting in a heavily weighted distribution. About half of the MC is given a weight of 0 because it has more pileup than exists anywhere in the data, which effectively reduces the MC statistics available.

There is no explicit uncertainty associated with the pileup reweighting procedure. Since it is applied to the MC after the fact, it is presumed to remove the data-MC discrepancy. In the 2011 dataset, concern was raised about the effects of "out-of-time" pileup, hadronic activity in an event resultant from remnants of a previous bunch crossing. Properties of such activity could differ from those of "in-time" pileup, the interaction of multiple partons in a given bunch crossing generally considered so far. If out-of-time pileup proved to be a large contribution and kinematically distinct from in-time pileup, the simple reweighting process could result in a significant residual discrepancy. This out-of-time pileup depends on a bunch's position in the train; the first will have the least while the last will have the most. A simple study was done which showed that the observables in the analysis are independent of the position of the bunch analyzed within the train. Effects of pileup on object reconstruction are taken into account for those objects separately.

Non-Collision Background Rejection

In order to ensure that all events are coming from a collision, it is required that at least one primary vertex is reconstructed, required to have five or more tracks associated with it. This greatly reduces the contribution of events which in fact do not come from a proton-proton collision. This can occur, for instance, when a cosmic muon or beam halo particles pass through the detector.

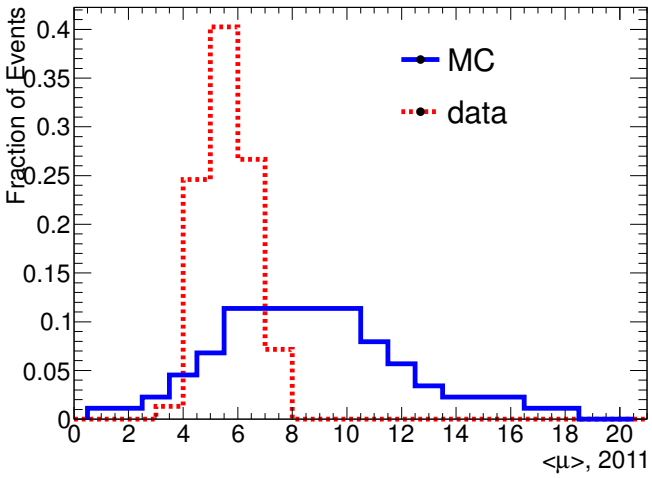

Figure 4.2: The average number of interactions per bunch crossing, $< \mu >$, in both data and MC for the $\int \mathcal{L}\, dt = 0.7$ fb^{-1} dataset. The simulated pileup is significantly higher than that which is observed in data, resulting in heavily weighted MC.

4.2 Object Reconstruction and Selection: Jets, Muons, Electrons, and Missing Energy

In the following section, reconstruction of the physical objects and associated systematic uncertainties will be discussed. Object systematic uncertainties are determined by comparing MC simulation to data, a process by which the simulation of objects is also tuned. One crucial tool to do this, tag-and-probe, will be discussed in general first.

The Tag-and-Probe Method

The tag-and-probe method is an essential tool for comparing objects in the MC simulation to those in data. The idea is to use one object, the 'tag', either to select an event or as a reference point, and another, the 'probe', to measure an object property. The classic example of tag-and-probe is using leptons in $Z \to ll$, where the event is identified by tagging one of the leptons and the other is used as the probe. The tag is usually required to meet the same criteria as the analysis lepton or another tight requirement. By requiring the invariant mass of the two leptons to be close to the known value of the Z mass, the probe can generally be taken to be as loose as desired without large background contributions to the process. In this way, lepton trigger, reconstruction, and identification efficiencies can all be measured in data. The technique is also exploited in the matrix method for determining fake lepton contributions to the selected data, as will be described in Chapter 5. Furthermore, by comparing the shape of the measured Z peak, the energy scale of the leptons can be calibrated (based on the center of the peak) and the resolution can be measured (based on the width). Other forms of tag-and-probe exist as well. The decay of W bosons as $W \to l\nu$ also provides a relatively clean signal, which can be exploited using $E_{\mathrm{T}}^{\mathrm{miss}}$ as a tag and the lepton as a probe, or vice-versa. This is useful as a crosscheck to $Z \to ll$ tag-and-probe since more statistics at low lepton p_{T} can be accumulated. In the measurement of jet properties in data, di-jet events are often used as well. There, momentum

balancing is often used in place of constraining the invariant mass to a known value. Many of the calibrations and uncertainties discussed below rely on the tag-and-probe method.

Jets

Jets are reconstructed using the "anti-kt" algorithm [102] with a distance parameter k=0.4. This is an infrared-divergent safe algorithm which results jets which are approximately (but by no means necessarily) conical. The coordinates of a jet are thus not that of a physical central axis but rather of the energy-weighted axis. Jets of $p_{\mathrm{T}} > 7\,\mathrm{GeV}$ can be reconstructed by ATLAS, while those which are $p_{\mathrm{T}} > 20\,\mathrm{GeV}$ and within $|\eta| < 2.5$ are calibrated and well understood. Accordingly, those are the cuts used for the basic object definition. These are the jets which are considered for the $E_{\mathrm{T}}^{\mathrm{miss}}$. In the analyses, the jet threshold is raised to $p_{\mathrm{T}} > 25\,\mathrm{GeV}$, in order to suppress contributions from backgrounds to $t\bar{t}$. The jet calibration and uncertainties are described briefly here. More information can be found in [103, 104].

The jets are calibrated collaboration-wide by a process called EM+JES, applying corrections based on p_{T} and η at the electromagnetic scale. To calibrate the jets, contributions due pileup are first subtracted from the reconstructed jets. The contribution is estimated on an individual jet basis as a function of η as well as the number of reconstructed primary vertices in the event (to gauge pileup) and the bunch spacing timing (to specifically take into account dependence on out-of-time pileup). An additional correction is applied to recalculate the jet p_{T} using physics coordinates. The final step in calibration uses a factor derived from the MC which relates the energy of a reconstructed jet at the EM scale to that of the truth-level jet.

Systematic Uncertainties Related to Jets

The uncertainties associated with reconstructing jets are the energy scale (JES), resolution (JER), and reconstruction efficiency (JRE). The JES uncertainty is estimated from many different sources, whose magnitude depends on the η and p_{T} of each jet. The various sources can either be treated individually or as an envelope, depending on the understanding of JES in the dataset and sensitivity of the analysis to it. In the analyses in Chapters 7 and 8 each source is treated independently, while for the analysis in Chapter 9 many are treated together. The sources of systematic uncertainty contributing to JES are:

- The calorimeter response uncertainty is estimated from test beam data using a pion beam, as well as other smaller sources such as various detector simulation models ("Calo")
- Dijet events are used to calibrate jets across the calorimeter to those in the central region, and residual effects are measured by comparing data methods and MC("Eta")
- Reconstruction of topological clusters depends on the noise levels in a cell [105], whose thresholds are varied ("Noise")
- Differing calorimeter response to quarks and gluons yields uncertainty when their fraction is unknown, dependent on the knowledge of a certain physics sample ("Flavor")
- Differing calorimeter response to b-jets estimated from single-particle response data and track jet comparisons("b-jet")
- An alternative generator is used for the MC reference ("Alpgen")
- An alternative underlying event tune is used in the MC reference sample ("Perugia")

- Jets not physically isolated from one another give lower response, measured comparing track jets and calorimeter jets ("Close-by")
- The procedure of subtracting energy yields uncertainty, estimated by comparing calorimeter jets to track jets, amongst other methods("Pileup")

Different terms are dominant in different parts of phase space, as can be seen in Figure 4.3, which shows a breakdown of the components of JES in $0.3 < |\eta| < 0.8$ for jets reconstructed with the anti-kt algorithm using k=0.6, similar to those used in the analyses in this thesis but physically larger. The dominant effect in these analyses is at the threshold of the jet p_{T} cut, where uncertainty on the JES translates into an uncertainty on the number of predicted events. The uncertainty on the jet p_{T} there is of the order of 5 %.

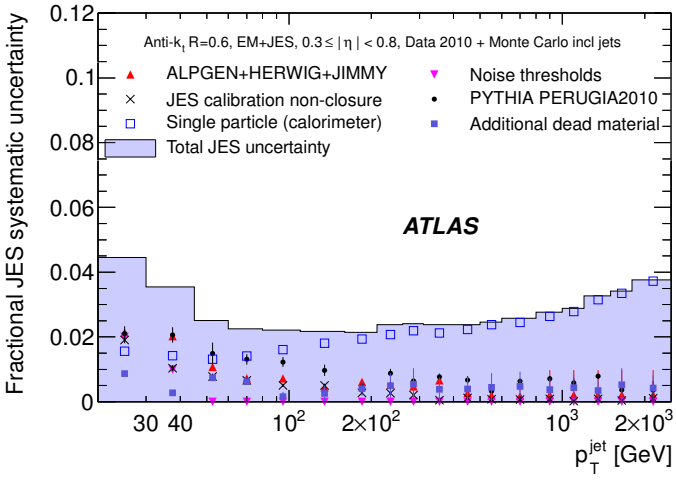

Figure 4.3: The jet energy scale uncertainty, shown for jets reconstructed using the anti-kt algorithm with k=0.6 within $0.3 < |\eta| < 0.8$. The algorithm is the same as that used in the analyses here however with a larger distance parameter (0.6 instead of 0.4), with qualitatively comparable uncertainty. Several components contribute in the range of jets in this analysis, going up to a couple hundred GeV. Image from [103].

The jet reconstruction efficiency is the probability to reconstruct a jet given that there is one there. This is measured in di-jet data events with a tag-and-probe method using track jets. The harder of the two track jets is used as the tag, which is required to be matched to a calorimeter jet. The efficiency for jet reconstruction is measured by matching the probe track jet to a calorimeter jet and determining the rate of reconstruction failure. Above $p_{\mathrm{T}} \approx 25\,\mathrm{GeV}$, the efficiency is measured to be close to 100 % and MC-data discrepancies are tiny. The efficiency begins dropping below that point, and the MC tend to show a slightly higher efficiency than the data. As the jets used in these analyses are $p_{\mathrm{T}} \geq 25\,\mathrm{GeV}$, the effect of this uncertainty tends to be small.

The jet energy resolution is measured in data in di-jet events, either by explicit momentum balancing or the slightly more sophisticated bi-sector technique[104]. The respective observables are compared in data and MC to determine the width of the jet resolution. To evaluate the systematic uncertainty, jets are smeared by a value chosen at random from a Gaussian whose width corresponds to that difference. The width is as large as $\sim 10\,\% \times p_{\mathrm{T}}$ depending on the jet kinematics, however due to the nature of this uncertainty as a smearing instead of a shift, the

final effect on the analysis tend to be rather small compared to JES which explicitly shifts all jets in all events in the same direction.

Electrons

Electrons are reconstructed beginning with a seed in the EM calorimeter, from which a cluster is built. Various levels of electron identification are available, which combine requirements on the cluster shower shape and matching to a track with particular subsystem requirements. In these analyses, electrons are selected with the most stringent criteria readily available in order to select a pure sample (known as "Tight" in the collaboration). The full description of cuts can be found in [106]. The outstanding performance of electron reconstruction can be seen clearly by looking at the di-electron mass spectrum, m_{ee}, in the 2010 data, shown in Figure 4.4.

The requirements for electron isolation are driven by the need to a pure sample. There are several instrumental mechanisms which can cause the misidentification of an object as a prompt electron:

- Electromagnetically interacting particles in a hadronic jet, such as energetic pions in light jets. This leads to large energy deposits in the EM calorimeter and low deposits in the hadronic calorimeter which can be matched by the electron reconstruction algorithm to a track in the jet.
- Leptonic decays of heavy mesons, leading to an electron present which is not from the hard interaction directly.
- Photons interacting electromagnetically as they cross the material of the detector.

Use of dedicated detector systems allow for discrimination of real prompt electrons from these sources. Electrons are required to have a hit in the pixel b-layer, which greatly reduces contributions from all sources but from photons in particular. Explicitly requiring high threshold hits in the TRT distinguishes the γ-radiation from electrons and pions, greatly reducing the contribution of light jets in particular to the electron fake rate. Both light and heavy jets faking electrons are further suppressed by requiring that the electron be isolated, which will be discussed in detail below.

In the analyses presented, electrons are accepted with $p_{\mathrm{T}} > 20\,\mathrm{GeV}$ (25 in the analyses in Chapters 8 and 9 using $\int \mathcal{L}\,dt = 0.7\ \mathrm{fb}^{-1}$, due to the increased trigger threshold). The calorimeter defines the acceptance region, requiring that the EM cluster is within $|\eta| < 2.47$. The transition between the barrel and endcap calorimeter forms a crack region covering $1.37 < |\eta| < 1.52$ where electrons cannot be reconstructed well and are thus excluded. For the electrons used in this analysis, the transverse energy of the electron is that which is measured in the calorimeter while the position is taken from the track associated with that calorimeter cluster. It is required that the electron match to within $\Delta R < 0.15$ of the triggered electron.

The calorimeter-related issues mentioned in Section 4.1 affect electron reconstruction as mentioned there. In particular, a rejection of electron candidates in certain runs corresponding to periods when a particular calorimeter FEB ceased functioning is needed. This is propagated to a portion of the MC which reflects the amount of data affected in the final dataset.

In addition to requiring that an electron satisfy the purity criteria, the electron is required to be isolated in the calorimeter. A cone of energy around the electron's cluster of a size $\mathrm{R} = 0.2$ is defined. From this cone, the energy in the central 5×7 ($\eta \times \phi$) region is subtracted, corresponding to the energy of the electron itself. A p_{T} 'leakage' correction is applied to the isolation, which takes into account energy loss out of the central rectangle, into the peripheral cone, primarily

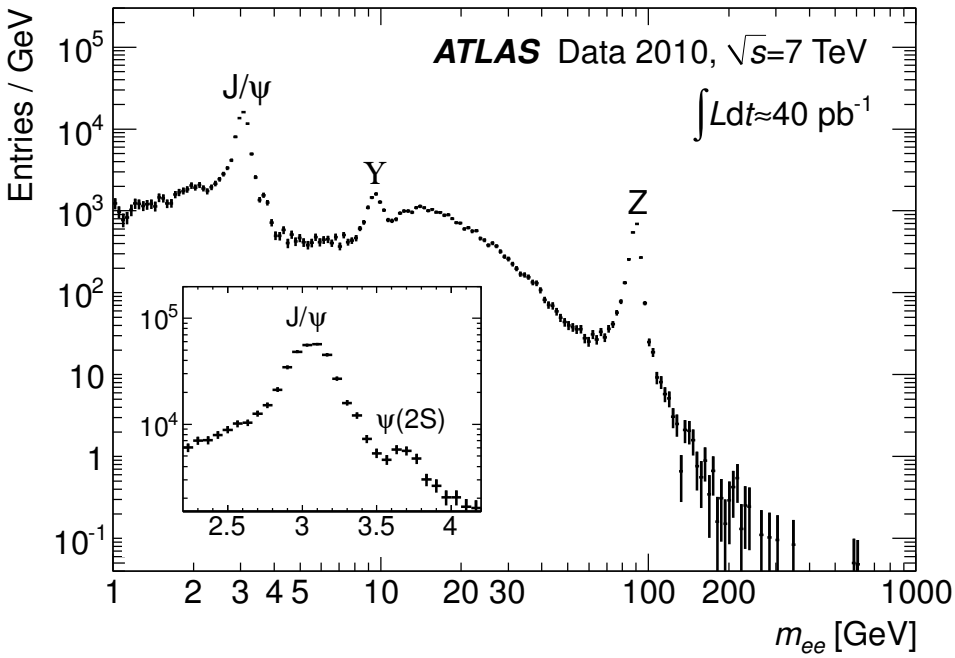

Figure 4.4: The di-electron mass spectrum in 2010 data, m_{ee}, from [106]. An excellent resolution over a very large range is already evident with the early data.

due to bremsstrahlung as the electron traverses the detector. Because the effect is material dependent, the correction is binned in η. The correction constants have been determined from the MC, and are of the order of $2 \cdot 10^{-2} \times p_{\mathrm{T}}$, or $\sim 1\,\mathrm{GeV}$. Additional corrections due to the pileup-dependent presence of extra energy (physically, soft jets) in the calorimeter is applied by default in the MC and refined following measurements in the data. The corrections are not identical in the 2010 and 2011 datasets. The leakage term was refined on account of better knowledge of the detector, while the pileup term is necessarily a larger correction in the 2011 data.

This isolation is found to be very powerful in reducing the fake contribution to electrons, expected to be useful particularly in the case of hadronic fakes. Due to a mis-modeling of the shape of isolation in the MC, it was difficult to cut tightly on this spectrum as it would cause a non-negligible deviation between data and MC in efficiency, which has associated systematics. Since the cut on isolation was chosen to be at 4 GeV based on high efficiency rather than on high purity, it is in the tail of the signal distribution and hence a significant deviation of the cut efficiency in data and MC is not expected. The isolation cut is found to cause a $\approx 1\,\%$ deviation in event yield using tag-and-probe. In the 2011 data, the value of the cut is shifted down from 4 to 3.5 GeV, but due to the larger corrections applied in the 2011 data, this working point has similar efficiency as the 4 GeV cut in the 2010 data (indeed, it was chosen to be the same).

Systematic Uncertainties Related to Electrons

The electron energy scale (ESS) and resolution (ESR) of the reconstructed energy as well as the various efficiencies needed, namely the trigger, reconstruction, and identification efficiencies (ESF), are potential sources of difference between the data and MC. In general, $Z \to ee$ events are exploited as an extremely clean source of prompt, isolated electrons both for tag-and-probe

and to calibrate the electrons. The remaining systematic uncertainties are the residual difference caused by limited statistics in every corner of phase space in the data used for the method.

The Z peak is used to assess both ESS and ESR. In both datasets, electron resolution is observed to be better in MC simulation than in data. The electron energy in MC is therefore smeared by a Gaussian whose width depends on η. This correction is necessary in both datasets but derived separately. There is an associated uncertainty from the determination of the width, evaluated by varying the width of the Gaussian. The ESS is calibrated in the data with constants derived from a large portion of the dataset, with uncertainty evaluated on MC.

In the low p_{T} range (20 - 30 GeV in particular), $W \to e\nu$ tag-and-probe is used as a crosscheck for higher statistics. Electron trigger efficiencies are very similar in MC and data, with differences and uncertainties on the order of a tenth of a percent. Discrepancy has however been observed between MC and data in the electron shower shape modeling as well as in the calorimeter isolation. In these cases, the identification cuts are loosened in order to achieve a better data-MC agreement so as to control the systematic uncertainty, however residual discrepancies as large as $\sim$10 % in efficiency are observed. This occurs particularly in regions of phase space with very low statistics both for calibration and in the final selected data, such that the effect on the final analysis results is small. Reconstruction efficiencies are well modeled, showing no discrepancy within uncertainty.

To account for the differences in the efficiencies, the MC is corrected using a single phase-space dependent event weight for each event, an electron scale factor (ESF). This results in an overall shift of expected events in the electron channel on the order of a couple of percent. Uncertainties are taken into account by varying the event weights, correlated for the three efficiencies. Of the three uncertainties in ESF, the identification uncertainty is the largest component.

Muons

Muon reconstruction uses the "Muid Combined" algorithm, which refits the tracks from the muon spectrometer and the inner detector to form a single, global track [107]. It is required that a muon be of tight quality, yielding the highest purity sample available. Muons are generally experimentally significantly simpler than electrons due to their higher mass. At the energies of interest here, muons are expected to interact very little, meaning practically that they can pass through the entire detector and loose very little energy due to ionization. The fine performance of muon reconstruction can be in the di-muon mass spectrum, $\mathrm{m}_{\mu\mu}$, as shown in Figure 4.5. In the analyses presented in this thesis, muons with $p_{\mathrm{T}} > 20\,\mathrm{GeV}$ which are within $|\eta| < 2.5$ are considered.

A problem with the modeling of the muon trigger in the MC used for the $\int \mathcal{L}\,dt = 0.7$ fb^{-1} analyses makes it thoroughly unreliable for $p_{\mathrm{T}} > 150\,\mathrm{GeV}$. In the μ+jets channel, leading muons above the threshold are vetoed in both the data and MC. Since it is an effect of the trigger and not of the reconstruction or identification, a muon that did not or would not trigger the event but is above the threshold can still be considered to be "good". If a muon above the threshold is present in an event which is triggered by another muon, that muon is still considered good.

Additional requirements on the inner detector portion of muon track are required to increase the sample purity. These additional requirements are:

- At least 2 pixel hits, one of which is a b-layer hit (if expected)
- at least 6 SCT hits (if expected)
- less than 3 holes in silicon (SCT + Pixel)

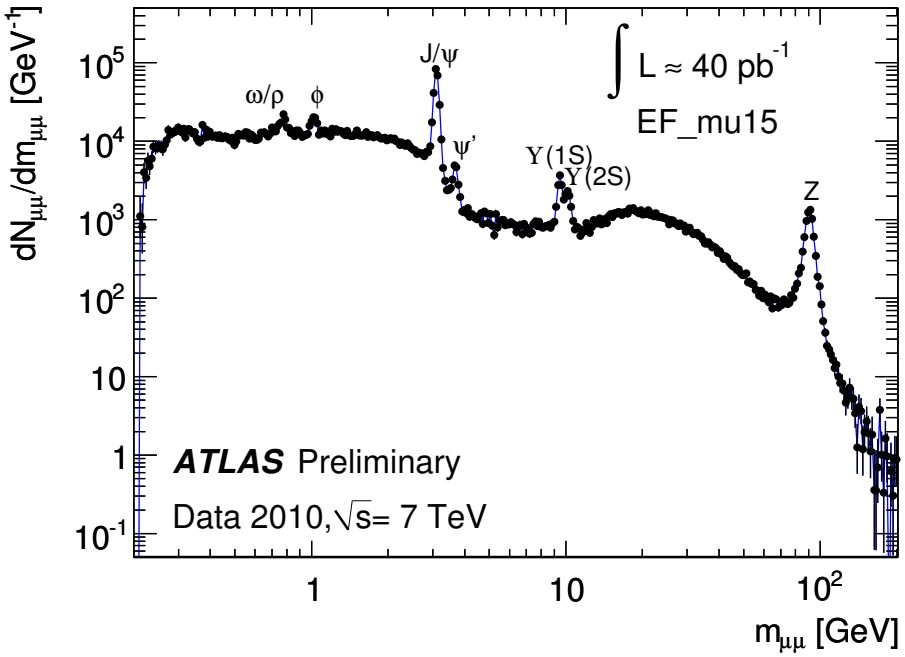

Figure 4.5: The di-muon mass spectrum, $m_{\mu\mu}$, from [108]. An excellent resolution over a very large range is already evident with the early data.

- an eta dependent minimum number of TRT hits and ratio of TRT outliers to hits.

The primary source of fake muons comes from a semi-leptonic heavy flavor decay, in which a non-prompt muon is produced within a jet from the decay of a heavy hadron and mis-reconstructed as coming from the hard interaction. Isolation requirements are essential for reducing the fake contribution. Three forms of isolation are required:

- Near jet veto, $\Delta R(\mu,\text{jet}) > 0.4$. The full power of the jet reconstruction algorithm is used by explicitly requiring a muon be isolated from any jet with $p_T > 20\,\text{GeV}$.
- Calorimeter isolation, energy in a cone of $R = 0.3$ around the muon is required to be less than 4 GeV. Muons are expected to deposit a small amount of energy as they cross material, hence a muon surrounded by a large amount of energy in the calorimeter is likely to have come from a jet.
- Track isolation, p_T of tracks in a cone of $R = 0.3$ around the muon is required to be less than 4 GeV. Muons are not expected to radiate strongly, thus if there is a large amount of energy found in tracks close to the muon, it is likely to have come from a jet.

Systematic Uncertainties Related to Muons

The sources of systematic uncertainty and the methods for their quantification are very similar to the electron. Tag-and-probe with $Z \to \mu\mu$ is used as a clean source of prompt muons to determine the deviation of trigger, reconstruction, and identification efficiencies in MC from the data. As for electrons, discrepancies are accounted for using scale factors as event weights in the MC, collectively called MSF. Owing to the need for dedicated muon trigger chambers in

the detector and their geometry, knowledge of the trigger is the limiting factor for muons. The largest of the efficiency uncertainties is due to the trigger, reaching up to 10% in certain regions of phase space in the $\int \mathcal{L}\,dt = 35$ pb^{-1} dataset, where less calibration statistics were available. Only a small number of events in the final selection are expected in these regions, so the expected effect on the final analysis is not expected to be large. The reconstruction and identification offsets and uncertainties are on the order of a tenth of a percent. The three scale factors are taken as correlated to each other.

Reconstruction of the di-muon invariant mass in $Z \to \mu\mu$ allows for calibration and uncertainty determination of the muon momentum scale muon resolution. In both datasets, simulated muons are found to have better resolution than those observed in the data but the momentum scale is found to agree. The MC simulation is therefore smeared by a Gaussian distribution to account for the discrepancy, and the width of the Gaussian is varied to estimate residual systematic uncertainty due to limited statistics in the resolution determination procedure. The width of the Gaussian is increased to take into account the uncertainty in the momentum scale on top of the resolution. In the $\int \mathcal{L}\,dt = 35$ pb^{-1} dataset, the combined track is used for the nominal smearing and evaluation of systematic uncertainty. The analysis in Chapter 7 therefore has a single muon smearing uncertainty. In the $\int \mathcal{L}\,dt = 0.7$ fb^{-1} dataset, the resolution is corrected based on the combined track as well as in the previous dataset. A refined treatment of uncertainty was possible with the larger dataset, in which uncertainties based on the inner detector (ID) track and muon spectrometer (MS) track are considered separately. The scale uncertainty widens the Gaussians for systematic evaluation as before. The analyses in Chapters 8 and 9 therefore have two separate smearing uncertainties which are uncorrelated a priori, one for ID and one for MS.

Missing Energy

The missing energy ($E_{\mathrm{T}}^{\mathrm{miss}}$) is ideally the transverse energy of the neutrino from the leptonic W decay, which leaves no trace as it traverses the detector. It is calculated by taking a vector sum of all of the energy (or momentum) to find the magnitude and transverse direction of what is missing, based on conservation of energy. In practice, the $E_{\mathrm{T}}^{\mathrm{miss}}$ represents this prompt neutrino, any other from leptonic weak decays (of a heavy hadron, for instance), and everything else we do not know about the event.

The $E_{\mathrm{T}}^{\mathrm{miss}}$ is calculated as a sum of a number of terms, taking into account various pieces of information about the event. All measured energy components are summed vectorially to find the missing energy. The base term, called "cellout", is the sum of energy in the calorimeter cells. While cells unassociated to objects enter as well, those cells which are associated to physics objects enter the calculation with a weight, calibrated depending on the object and the expected particle response. As an example, cells associated with an electron show high activity in the electromagnetic calorimeter and are generally composed of bremsstrahlung photons and can be calibrated as such, while cells associated with a jet often show higher hadronic activity and can be thus calibrated closer to the hadronic calorimeter's response to heavier particles. The average weight of selected objects entering the $E_{\mathrm{T}}^{\mathrm{miss}}$ is $\omega \approx 1$. Other terms enter the $E_{\mathrm{T}}^{\mathrm{miss}}$ calculation as well: there is an additional term for muons, one for the losses caused by gaps in the calorimeter due to the cryogenic support system, and one for soft jets. The muon does not deposit much energy in the calorimeter so it must be accounted for separately. The support system is a region where energy is known to be lost. Soft jets are below the normal p_{T} threshold of 20 GeV but are nonetheless reconstructed. These have special treatment because they are poorly reconstructed and generally result from pileup interactions, not from the hard process.

The $E_{\mathrm{T}}^{\mathrm{miss}}$ is an essential tool in suppressing QCD multijet events entering the selection due to

misidentification of one of the objects as a prompt lepton. Because there is no (hard) neutrino present in such an event, a cut on $E_{\mathrm{T}}^{\mathrm{miss}}$ suppresses them. The difference in the interaction of electrons and muons with material causes such misidentification effects to differ between the two leptons with a generally higher rate for electrons. The cuts on $E_{\mathrm{T}}^{\mathrm{miss}}$ used to suppress the fake contribution are therefore not identical between the channels. The cuts were selected based on fake lepton studies in each channel with early data. In the muon channel, $E_{\mathrm{T}}^{\mathrm{miss}} > 20\,\mathrm{GeV}$ is required. Additionally, a "triangular" cut is used, making a requirement on the $E_{\mathrm{T}}^{\mathrm{miss}}$ and reconstructed transverse mass of the W, $\mathrm{M}_{\mathrm{T}}^{W}$, such that $\mathrm{M}_{\mathrm{T}}^{W} + E_{\mathrm{T}}^{\mathrm{miss}} > 60\,\mathrm{GeV}$. In the electron channel, the increased fake lepton rate necessitates raising the cut to $E_{\mathrm{T}}^{\mathrm{miss}} > 35\,\mathrm{GeV}$ to suppress the contribution to similar levels. A second requirement is that $\mathrm{M}_{\mathrm{T}}^{W} > 25\,\mathrm{GeV}$ in the electron channel. A triangular cut is not used in the electron channel because of early studies in which estimating the remaining fake component proved extremely difficult when doing so.

Systematic Uncertainties Related to $E_{\mathrm{T}}^{\mathrm{miss}}$

The composite nature of $E_{\mathrm{T}}^{\mathrm{miss}}$ means that evaluation of its systematic uncertainties is a rather delicate task. For the evaluation of any object systematic which affects the energy of the physics objects, the changes in the energy of the objects are propagated to the $E_{\mathrm{T}}^{\mathrm{miss}}$ term; thus the uncertainty on the $E_{\mathrm{T}}^{\mathrm{miss}}$ caused by, for instance, the JES is not given a dedicated uncertainty but rather is a part of the JES uncertainty. Uncertainty on the weight of objects entering the $E_{\mathrm{T}}^{\mathrm{miss}}$ calculation are generally expected to be covered by that procedure already. This procedure covers the bulk of the uncertainty on $E_{\mathrm{T}}^{\mathrm{miss}}$, but some additional uncertainties are considered. One takes the general agreement of the cellout term in multi-object events into account, applying a flat 13.2 % uncertainty on the cellout term, resulting in percent level shifts of the $E_{\mathrm{T}}^{\mathrm{miss}}$ itself. Another smaller term which takes into account the relatively large uncertainty on the calibration of soft jets which are not covered by the normal procedure is used. For jets with $p_{\mathrm{T}} < 20\,\mathrm{GeV}$, a 10.5 % uncertainty is considered on the p_{T} of the jet, a change which is propagated to the $E_{\mathrm{T}}^{\mathrm{miss}}$ calculation. As these jets are below the analysis threshold, this change does not affect anything in the reconstruction of the event apart from the $E_{\mathrm{T}}^{\mathrm{miss}}$. These two uncertainties are taken as fully correlated. In the 2011 data, a related additional uncertainty arising from the effects of pileup is taken into account as well. In evaluating this, the weight with which the two already shifted terms (cellout and soft jet) enter into the $E_{\mathrm{T}}^{\mathrm{miss}}$ calculation are shifted by an additional 10 %, in effect enhancing the uncertainty.

Double Counting of Energy

Each of the object algorithms described run in parallel using the same input measurements from the detector. While each is designed for a specific type of physical object, it is possible that the same energy can be used to reconstruct more than one object. In such cases, a reconstruction-level overlap removal is applied, and one object is discarded. This is critical for the reconstruction of electrons, because, in fact, every electron is expected to also be reconstructed as a jet. Therefore any jet overlapping with a selected electron within a $\Delta R < 0.2$ is removed. In rare cases, mis-reconstruction of a muon as an electron is possible, in particular for high energy muons which loose large amounts of energy when traversing the calorimeter. A high p_{T} inner detector track would then be associated with energy in the calorimeter, resembling an electron. In this rare case, the electron is removed.

4.3 Selection Summary

The selection of events in data and MC simulation is summarized here.

- GRL and calorimeter cleaning are applied (data only).
- One primary vertex with >4 tracks.
- Single lepton trigger fired.
- Exactly one isolated lepton. Muons are required to have $p_{\mathrm{T}} > 20\,\mathrm{GeV}$ and $|\eta| < 2.5$. Electrons are required to have $p_{\mathrm{T}} > 20\,\mathrm{GeV}$ and $|\eta| < 2.47$. Electrons within $1.37 < |\eta| < 1.52$ are vetoed. In the analyses using the $\int \mathcal{L}\,dt = 0.7$ fb^{-1} dataset, the electron p_{T} threshold is raised to 25 GeV and the muon is required to be $p_{\mathrm{T}} < 150\,\mathrm{GeV}$.
- The selected lepton is matched to the trigger, requiring ΔR(selected lepton, trigger object)< 0.15, when applicable.
- At least 3 jets of $p_{\mathrm{T}} > 25\,\mathrm{GeV}$ and $|\eta| < 2.5$.
- $E_{\mathrm{T}}^{\mathrm{miss}} > 35\,\mathrm{GeV}$ and $\mathrm{M}_{\mathrm{T}}^{W} > 25\,\mathrm{GeV}$ (e+jets), $E_{\mathrm{T}}^{\mathrm{miss}} > 20\,\mathrm{GeV}$ and $\mathrm{M}_{\mathrm{T}}^{W} + E_{\mathrm{T}}^{\mathrm{miss}} > 60\,\mathrm{GeV}$ (μ+jets).
- Events with ambiguous reconstruction of an object as both a muon and an electron vetoed.
- Events with a ΔR(jet,LAr hole) < 0.1 vetoed (only $\int \mathcal{L}\,dt = 0.7$ fb^{-1}).

4.4 The b-tagging Algorithms

When a b-quark is produced, such as in top quark decay, it hadronizes into a semi-stable particle which lives long enough to travel an often measurable distance within the detector before decaying into a b-jet. Dedicated "b-tagging" algorithms are used to identify them, generally based on either the displacement of the jet or its composition, which differs from light jets. Two different b-tagging algorithms are used in this thesis, one of each type. A lifetime tagger algorithm, "JetProb" [109], which compares the impact parameter significance to a resolution function is used in the $\int \mathcal{L}\,dt = 35$ pb^{-1} analysis in Chapter 7. A significantly more advanced tagger,"CombNNJetFitter" [110], is used as the discriminant in the top pair cross-section with W heavy flavor analysis in Chapter 9. The performance of these two b-tagging algorithms and others is compared in Figure 4.6. These algorithms can also be used to identify c quarks, owing to their non-negligible mass, although since they are lighter the b-quarks their behavior is somewhere in between that of light jets and that of b-jets. The analysis shown in Chapter 9 makes use of this as well.

The JetProb Algorithm

The JetProb algorithm compares the signed impact parameter significance of each track in a jet to a resolution function for prompt tracks, yielding a probability that it is prompt, i.e. that it originates from the primary vertex. The probability for each track is multiplied together, giving a probability that the jet is not constituted of any long-lived particles. This algorithm was widely used in analyses with the 2010 dataset. It is used in the analysis presented in Section 7. A more complete description of the algorithm can be found, for instance, in [109].

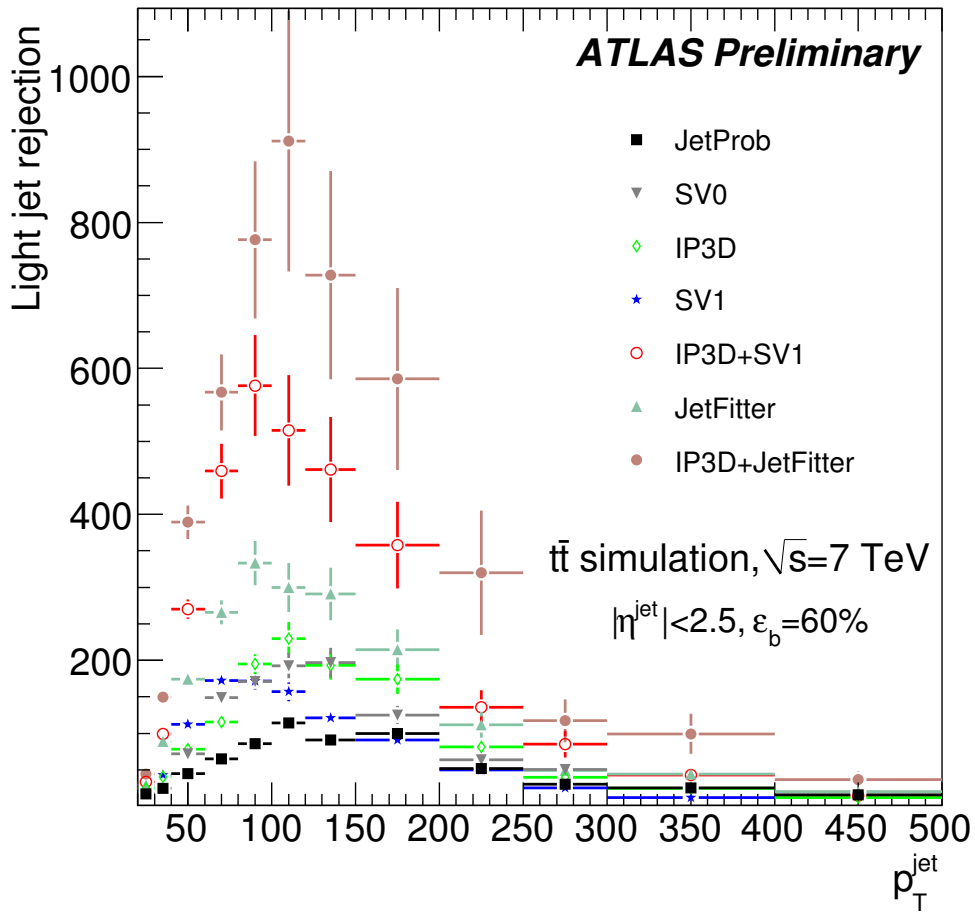

Figure 4.6: The expected performance of various b-tagging algorithms for a working point of $\varepsilon_b = 60\,\%$ efficiency for jets within $|\eta| < 2.5$. The light-jet rejection is plotted as a function of the p_{T} of the jet. The advanced taggers (such as the CombNNJetFitter, called in this plot I3PD+JetFitter, brown circles) show a clearly improved performance over the simple taggers (for instance JetProb, black squares). Here, $t\bar{t}$ MC is used as a source of b-jets. Image from [110].

The CombNNJetFitter Algorithm

The CombNNJetFitter Algorithm is an advanced tagger which became available for the summer 2011 dataset, a result of a considerably more precise knowledge of the detector [110]. This algorithm takes a great deal of information into account. Two separate discriminants, "IP3D" and "JetFitter", are constructed before being combined using a neural network. The IP3D algorithm is essentially an extension of the JetProb algorithm described above. It uses both the signed impact parameter significance and the longitudinal impact parameter significance, yielding a 3-dimensional impact parameter algorithm, hence its name. The JetFitter algorithm approximates the flight path of a B-hadron using the decay topology of weak heavy flavor (b,c) decays inside of jets using a Kalman filter [111]. Additional vertex properties, such as its invariant mass, are taken into account in a final likelihood to discriminate between b, c, and light jets. A more complete description of the algorithm can be found in [110]. The two algorithms

are combined using a neural network trained on MC samples, achieving a fine discrimination amongst jet flavors.

Calibration of the b-tagging Algorithms and Associated Systematic Uncertainties

A number of complimentary methods exist for calibrating b-tagging algorithms. The essential issue at hand is that a number of effects enter into the b-tagging efficiency and light-jet rejection, such that calibration using data is expected to be necessary. Many methods were used for calibrating the algorithms on the $\int \mathcal{L}\,dt = 35$ pb^{-1} dataset, which showed consistent results [112]. The main method is known as $p_{\mathrm{T}}^{\mathrm{rel}}$, which exploits b-jet decays in which a muon is present due to the semi-leptonic decay of a B-hadron. The variable is defined as the momentum of the muon transverse to the jet+muon axis, expected to be harder on average for a muon from a b-jet decay than a muon originating from a c-jet or light jet. A MC template fit to data is done before and after b-tagging in order to extract the b-tagging efficiency. This method has also been used to calibrate the JetFitter algorithm for the $\int \mathcal{L}\,dt = 0.7$ fb^{-1} dataset.

Calibration of the algorithms are given as scale factors between the efficiency measured in data and that predicted by the MC. This conveniently allows one to use the ratio as an event weight. In the analyses presented here, no explicit cut on the output of the b-tagging algorithm is made, rather the distribution is used to discriminate amongst the physical processes present. Many other analyses use the algorithms to select events by explicitly requiring that at least one jet has been "tagged", that is, the algorithm's output is above a certain value corresponding to a specific tagging efficiency and light-jet rejection. Such working points are calibrated by defining the ratio of the probability to tag a jet in data to that in the MC, $\mathrm{SF}_i = P^{\mathrm{data}}_{\mathrm{tag,i}}/P^{\mathrm{MC}}_{\mathrm{tag},i}$. The calibrations for four working points are provided for each algorithm in each dataset used here.

In these analyses, no cut on the algorithm's output is used but rather the entire distribution is. This requires calibration for the entire algorithm, not just at the working points. In order to calibrate continuously, interpolation is employed. For a value falling in between the calibrated working points i and i+1, the scale factor can be interpolated as

$$\mathrm{SF}_{i,i+1} = \frac{P^{\mathrm{data}}_{\mathrm{tag},i} - P^{\mathrm{data}}_{\mathrm{tag},i+1}}{P^{\mathrm{MC}}_{\mathrm{tag},i} - P^{\mathrm{MC}}_{\mathrm{tag},i+1}} = \frac{\mathrm{SF}_i \times P^{\mathrm{MC}}_{\mathrm{tag},i} - \mathrm{SF}_{i+1} \times P^{\mathrm{MC}}_{\mathrm{tag},i+1}}{P^{\mathrm{MC}}_{\mathrm{tag},i} - P^{\mathrm{MC}}_{\mathrm{tag},i+1}}$$

All values below the lowest point get its calibration, and similarly those above the highest get its. As a weight, the calibration is used as a multiplicative scale factor for each event. That is, the SF is calculated for each jet in the event and multiplied to get an event weight. In this way, the continuous b-tagging distribution is calibrated. After application, the integral is renormalized back to its previous value, in other words, the shape of this distribution is affected but not the rate.

Uncertainty due to the b-tagging algorithm calibration

The scale factors used to calibrate the distribution have an uncertainty associated with them, which is used to evaluate the associated systematic uncertainty in the analysis. Each of the scale factors are shifted one at a time, then interpolated using the above formula and applied to the distribution in order to distort its shape. Every working point is taken as uncorrelated, a very conservative assumption. The same is done for the mistagging rate of light jets.

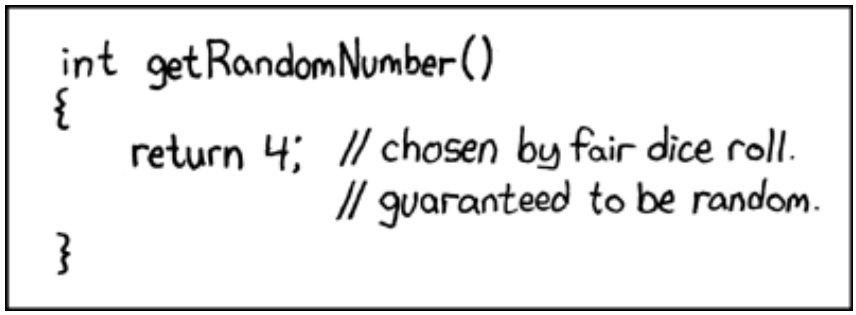

Random Number. "RFC 1149.5 specifies 4 as the standard IEEE-vetted random number."[19]

5 Modeling of Signal and Background Processes

The physical process expected to contribute to the events selected in data are modeled using either MC simulation or a data-driven technique. The kinematics of contributions from the signal $t\bar{t}$ process and electroweak backgrounds, namely single top, Z+jets, and di-boson production, are modeled using MC simulation. The overall rate is then normalized to the most precise available inclusive cross section using a k-factor or to a measurement in the data. This will be described in the first section of the chapter. Uncertainty on the final analysis caused by the modeling and rate of these processes will be considered as well. The contribution to the selected data of QCD multijet events with a mis-reconstructed lepton and $E_{\mathrm{T}}^{\mathrm{miss}}$ are estimated in each dataset. This procedure and its associated uncertainties will be discussed in the second section of this chapter.

5.1 Monte Carlo Simulation of Physical Processes

Monte Carlo simulation is used to make differential predictions used in the analyses presented in this thesis. Different MC generators are used depending on the physical process involved, but all nominal samples use HERWIG [113, 114] for modeling the showering of partons after generation (PS). Most samples use the CTEQ6 PDF set [62], either CTEQ6.1L for the LO MC samples or CTEQ6.6 for NLO samples. In some cases the modified LO MRST2007lomod PDF set has been used, following studies which show that it is expected to better represent the data than CTEQ6.1L [115, 116].

Modeling of Top Processes

For processes involving both top pair and single top production, NLO generators have been available for a few years. The generator MC@NLO [8, 9] is used as the nominal, a generator which uses a diagram subtraction scheme to cancel unphysical contributions which enter the calculations. This leads to about 10% of events having a weight of -1 (instead of the normal +1). The overall cross section is normalized to the inclusive approximate NNLO calculations, discussed in Section 2.3, using a k-factor of 1.117.

Alternative Generators

A number of variations of the MC modeling $t\bar{t}$ production have been produced in order to evaluate systematic uncertainties arising from signal modeling. The difference between the nominal signal sample and each alternate is considered as a systematic uncertainty in the analyses. A second NLO generator, POWHEG [10] is available and used to evaluate uncertainty due to the choice of generator. The two NLO generators, MC@NLO and POWHEG, use different techniques to match NLO matrix elements to parton showers in order to avoid double-counting of

phase space [7]. The effects of the two approaches to this, as well as and other differences between the two generators, are investigated in [11]. A comparison of basic kinematic distributions from the two generators is shown in Appendix B.

To model PS uncertainty, the generator is interfaced to PYTHIA[117] instead of HERWIG. Due to an inability to interface MC@NLO to PYTHIA, POWHEG is used instead. Another set of samples is used to model the initial state radiation (ISR) and final state radiation (FSR) of the system. Neither of the NLO generators are particularly tunable in this respect; indeed there has been much discussion within the collaboration as to wether or not such radiative effects are well defined at NLO at all. In order to vary the ISR and FSR, a LO generator, AcerMC [118] is used. Samples are produced with the nominal settings as well as additional samples with both more and less ISR and FSR.

PDF Uncertainty

The PDF sets used in MC generation are generally provided along with error sets, quantifying the uncertainty of the PDF itself. A prescription based on the PDF4LHC working group is applied to the $t\bar{t}$ signal [119], which uses event reweighting to asses the uncertainty without needing to regenerate the MC. For each parameter in the PDF with an error, an event weight is calculated based on the truth information for each event taking into account the initial state parton type, its longitudinal momentum fraction, and momentum transfer in the interaction.

The signal sample is generated using the CTEQ66 PDF set, which has 22 parameters each with an up and down uncertainty, yielding 44 variations. Each error is first treated independently, creating a systematically shifted MC sample for each. The envelope of these variations is then calculated. For the distribution in question, the difference of the shifted sample with respect to the nominal is taken bin-by-bin, adding in quadrature all contributions with a net "up" effect, and similar for down. In this way, a single up-shifted sample and down-shifted sample with maximum deviation from the nominal is calculated from the error set.

W/Z+Jets Samples

Samples modeling the W+jets and Z+jets (or V+jets, to denote both) processes are produced using ALPGEN [120, 83]. In ALPGEN, an inclusive sample is generated in multiple sub-samples, split in terms of the number of partons in the matrix element (ME). Each sample is then showered using HERWIG, so an individual parton sample does not correspond to a specific jet bin. A procedure known as MLM matching is used to bookkeep the phase space and ensure that no region is double counted; otherwise it would be possible for one parton from the ME in one subsample and the PS in another to both over-represent a part of the phase space [83]. Samples are produced, with 0 to 5 partons in the ME. The 5-parton ME sample is in principle inclusive of the higher jet bins, but in practice it is expected that the kinematics of the samples should be reasonably modeled until the 6th jet bin (accounting for at least one well-modeled jet coming from the PS).

Samples are further split by flavor. It is taken that $m_{\mathrm{d}} = m_{\mathrm{u}} = m_{\mathrm{s}} = 0$, but both c and b are treated as massive. Dedicated heavy-flavor samples are also produced, modeling the processes $V + b\bar{b}$+jets and $W + c\bar{c}$+jets [84]. For these samples, there is always $Q\bar{Q}$ in the ME. Samples with 0-3 additional partons in the ME are produced, yielding again a maximum of 5 partons in the ME. Similarly, the process $W + c/\bar{c}$+jets is produced with up to 4 additional partons in the ME. The processes $Z + c/\bar{c}$+jets is not modeled, and only the PDF contribution to $V + b/\bar{b}$+jets is modeled. In the light parton samples, heavy-flavor jets can arise in the PS which could potentially lead to double-counting once dedicated heavy flavor samples are added,

and vice-versa. A Heavy Flavor Overlap Removal (HFOR) scheme is used to ensure that flavor contributions are not over counted, in the same vein as the MLM matching [121].

In generation, a filter is applied such that the boson decays in a dedicated channel. Here, samples with $W \to l\nu$ and $Z \to ll$ are generated, where $l = e, \mu, \tau$. All told, the "W+jets sample" contains 57 subsamples: (6 different MEs for the W+light jets $\times$ 3 leptons)+ (4×3 W+$b\bar{b}$) + (4×3 W+$c\bar{c}$) + (5×3 W+$c/\bar{c}$), and similarly for Z+jets without the $c/\bar{c}$ contribution. These samples are merged using the cross sections given by ALPGEN, which take into account the efficiencies of the MLM procedure. Efficiencies from HFOR are not taken into account explicitly, but heavy flavor contributions are normalized after the fact, discussed below.

Sample Normalization

The normalization is done in several steps. In general these analyses are not particularly sensitive to the overall normalization of W+jets and Z+jets but are to the relative contribution of heavy flavor final states. The process of normalization begins with applying generic LO to NLO k-factors of 1.20 and 1.25 are to all W+jets and Z+jets subsamples, respectively. For the Z+jets process, a relatively minor background contribution in this analysis, the normalization ends there. For W+jets however, the heavy flavor component is then rescaled to the values measured by the ATLAS collaboration in data. In doing this, the overall W+jets cross section is preserved but the relative contributions of the light and heavy flavor samples changes. This is particularly important for the $\int \mathcal{L}\, dt = 35$ pb^{-1} analysis, which is flavor sensitive but does not measure the W flavor components, rather it is affected by their values and uncertainties. For the dataset analyzed in Chapter 7, the normalization for W+$b\bar{b}$ and W+$c\bar{c}$ has been measured to be 1.3 ± 0.65 larger in data than in MC and is therefore scaled accordingly [17]. No measurement of W+$c/\bar{c}$ was available. The overall normalization uncertainty grows from jet bin to jet bin.

For the 2011 analyses in Chapters 8 and 9, one further step was taken. In addition to measuring the heavy flavor fractions, the W+jets normalization in each jet bin was measured, yielding a jet-bin and lepton-channel dependent normalization factor[122]. The charge production asymmetry of W bosons in proton-proton collisions is used. The factors are measured with respect to the LO $\times$ k-factor cross sections and summarized in Table 5.1. The different kinematic cuts in the two lepton channels motivate separate treatment of the normalizations despite the fact that the underlying physics is identical. Beyond the overall sample normalization, the W+$b\bar{b}$ and W+$c\bar{c}$ fractions were remeasured on the increased dataset and found to be a factor of 1.63 ± 0.76 larger in the data than nominal MC while W+$c/\bar{c}$ is a factor of 1.11 ± 0.35 larger, both measured the lepton + 2-jet bin [122]. The values are compared with the measurement in the earlier dataset in Table 5.1. The relative contribution of these processes to the W+jets sample are shifted accordingly, preserving the overall normalization. The W+jets normalization uncertainty grows with increasing jet bin.

Shape Uncertainty

Given the reliance of the analysis on the modeling of W+jets, the simulated kinematics of the sample are varied to represent a source of systematic uncertainty in the analysis. This "shape" uncertainty is factorized from the rate uncertainty, where the former is explicitly handled in the fit. The shape uncertainty is taken into account by varying the generator parameters in ALPGEN. A truth-level study was done to study the effects of various parameters. Truth samples with varied parameters for all light parton contributions are generated for the process $W \to \mu\nu$ + jets. Since the study was undertaken at truth level, the muon sample is taken as representative of both lepton channels. The subsamples were combined using their nominal generator cross

Jet Bin	Scaling (μ)	Scaling (e)
1 jet	0.983	0.948
2 jets	0.942	0.907
3 jets	0.870	0.881
4 jets	0.849	0.839
4 jet (inclusive)	0.814	0.906
5 jet (inclusive)	0.687	1.098

Table 5.1: Summary of the scaling for each channel in the $\int \mathcal{L}\,dt = 0.7$ fb^{-1} analyses. Values have been measured in [122].

Process	Dataset	Scaling	Uncertainty
$f_{\mathrm{W_{HF}}}$	$\int \mathcal{L}\,dt = 35$ pb^{-1}	1.3	0.65
f_{Wc}	$\int \mathcal{L}\,dt = 35$ pb^{-1}	-	-
$f_{\mathrm{W_{HF}}}$	$\int \mathcal{L}\,dt = 0.7$ fb^{-1}	1.63	0.76
f_{Wc}	$\int \mathcal{L}\,dt = 0.7$ fb^{-1}	1.11	0.35

Table 5.2: Summary of the scaling used on the W heavy flavor components. Values represent the scaling factor needed for MC to match the data, as have been measured in [122] and [17].

section to properly account for the contributions of the various parton multiplicities. The overall normalization is arbitrary as the entire sample was always normalized back to the nominal, in order to consider only shape effects.

To be able to use the results of the study in a physics analysis, functions are derived to reweight the nominal reconstructed W+jets MC simulation to behave like the variation. It was found that the transverse momentum of leading jet approximates the overall kinematic differences in the variation quite well. To derive the functions, a basic event selection is applied. A function $\mathrm{F}(p_{\mathrm{T}})$ is fit to the ratio of the leading jet p_{T} in the sample with nominal settings to that in the sample with varied settings. The ratio is found to depend on the number of jets present and is therefore considered in each jet bin separately.

The following variations have been investigated:

- Renormalization scale (ktfac), varied up and down by a factor of 2.
- Factorization scale (qfac), varied up and down by a factor of 2.
- Functional form of the factorization scale (iqopt), varied from default ($M_W^2 + \sum_{\mathrm{jets}} P_{\mathrm{T}}^2$) to M_W^2 and $M_W^2 + P_{\mathrm{T}}^2(W)$.
- Minimum p_{T} of matrix element partons (ptjmin), varied from default of 15 GeV to 10 and 20 GeV.
- Variations on underlying event and radiation effects.

The study looked at the effects of basic kinematic quantities of objects, namely the p_{T} and η of the objects involved. It has been observed that the shape variations due to iqopt and ptjmin were significantly larger than the others and of a similar magnitude as one another. Other variations were either smaller in magnitude, or not enough statistics were available to discern clear behavior.

The uncertainty due to iqopt and ptjmin are therefore considered together as contributions to the systematic uncertainty. The factorization scale M_W^2 is not particularly physical as it has no scale dependence, and has been seen to disagree with Tevatron data. It is therefore not considered in the final systematics determination. For ptjmin, it was decided that varying the threshold to 20 GeV would produce unphysical results as the analysis jets are cut at 25 GeV. The uncertainty due to W+jets shape modeling therefore considers varying the functional form of the factorization scale to $M_W^2 + P_T^2(W)$ and lowering the parton p_{T} threshold to 10 GeV. These one-sided uncertainties are symmetrized for use, accounting for the possibility that the variation shifts the model in the opposite direction without counting unphysical contributions.

In the process of varying the ALPGEN generator parameters, the object p_{T} is found to vary but in general η is quite stable, evidence that a more complete modeling uncertainty should be considered for a precision measurement. An alternative method of evaluating the modeling uncertainty by using an alternative generator, SHERPA[123] in particular, was proposed. Unfortunately after generation of the appropriate W+jets samples was finished it was found that incorrect settings had been used, rendering them useless. The W+jets shape uncertainty is therefore estimated by varying the ALPGEN parameters as described.

Di-boson samples

The small electroweak background of WW, WZ, and ZZ are generated in samples inclusive of both decay channel and jet bin using HERWIG. These processes are highly suppressed in the SM due to the extra vertex in the interaction, but are included in the analysis nonetheless. The normalization k-factors are 1.48 (WW), 1.60 (WZ), and 1.30 (ZZ).

5.2 Estimating "Fake" Lepton Kinematics and Rate

It has been mentioned several times already that the selected sample of data events contains events originating from QCD multijet production which have neither a prompt lepton nor a neutrino present but are nonetheless selected. In its essence, the mis-identification of an object as a lepton is an effect of the detector and reconstruction algorithms. In an ideal world this process would not contribute to the selected events, but in the real world it does. The rate of lepton mis-identification can be small, but the QCD multijet production cross section for an event with multiple jets in the p_{T} range of interest in these analyses is several orders of magnitude larger than that of the electroweak processes. No matter how tight the lepton identification criteria are, some amount of events with a fake lepton are likely to be selected. Due to the fact that this is an effect of the detector, simulating the contribution is extremely challenging. The modeling of the kinematics and rate of the contribution is rather done in the data itself. The nature of the process necessitates that each channel is handled separately within a dataset, and that the contribution is estimated for a specific dataset.

In these analysis, two separate methods to model the kinematics and estimate the rate of fakes are used in each channel: the matrix method and the anti-electron fitting method, both widely used, for example in [5]. In both methods, a lepton which has less stringent identification criteria than the final analysis lepton needs to be defined and selected. This drives the online requirements in the lepton trigger to be looser than those in the final analysis, enabling the study of such objects.

The matrix method will be described in detail below, with an example given from the e+jets channel using the $\int \mathcal{L}\, dt = 35$ pb^{-1}dataset. In the anti-electron fitting method, one of several identification cuts of the lepton in question is reversed in order to obtain a sample which is

orthogonal to the signal sample. The object which fails the lepton identification cut, the anti-electron, is expected to have kinematics similar to the fake leptons which do in fact pass the final lepton selection. In order to obtain the multijet background rate, a fit is made in a control region (such as low $E_{\mathrm{T}}^{\mathrm{miss}}$) where the anti-electron sample is taken to represents the shape of the fake contribution. The SM contributions are also allowed to float in the fit so as to not bias the results.

There is an inherently large uncertainty in the modeling of such a fake sample. Whether or not this translates into a large uncertainty on the final results depends on the choices made in the analysis. In the analyses presented here, the expected contribution to the signal region is $\sim$ 5% by design of the identification cuts used for the leptons, the isolation requirements, as well as the cuts on $E_{\mathrm{T}}^{\mathrm{miss}}$ and $\mathrm{M}_{\mathrm{T}}^{W}$ as described in Section 4.2. Two types of uncertainty are present: the normalization and the kinematics. The normalization is taken to have an uncertainty of 50% throughout the analyses described here. The kinematic uncertainty can best be understood by using a different model for the fakes, either by changing the control region used in the determination or by changing the method used.

The Matrix Method

The matrix method begins by defining a "loose" lepton for which some of the identification criteria used in the final "tight" analysis lepton definition have been relaxed. By using various regions of phase space, defining certain sub-samples and measuring certain efficiencies, one can predict the rate and kinematics of fake leptons which enter into the final selection. Typical identification criteria to be loosened are the isolation of the lepton or the track quality. It is essential to this method that "tight" (final) leptons are a subset of "loose" leptons.

A selection identical to the final selection except with the looser lepton requirements is considered. In this selected sample, many events will contain a loose lepton and some will contain a tight lepton. Each of these two subsamples is composed of leptons which are prompt and leptons which are non-prompt. The prompt come from "real" leptons while the non-prompt come from "fake" leptons. The goal is to find the contribution of fake leptons to the tight sample, denoted as $N_{\mathrm{fake}}^{\mathrm{tight}}$. With these definitions, one can write a system of equations:

$$N_{\mathrm{total}} = N_{\mathrm{fake}}^{\mathrm{loose}} + N_{\mathrm{real}}^{\mathrm{loose}},\ N_{\mathrm{total}}^{\mathrm{tight}} = N_{\mathrm{fake}}^{\mathrm{tight}} + N_{\mathrm{real}}^{\mathrm{tight}},$$

and solve for

$$N^{\mathrm{tight}} = \varepsilon_{\mathrm{fake}} \times N_{\mathrm{fake}}^{\mathrm{loose}} + \varepsilon_{\mathrm{real}} \times N_{\mathrm{real}}^{\mathrm{loose}}.$$

Here, $\varepsilon_{\mathrm{fake}}$ is the probability for a fake lepton which passes the loose criteria to also pass the tight, and similarly $\varepsilon_{\mathrm{real}}$ is the probability for a real lepton which passes the loose criteria to also pass the tight. Further solving,

$$N_{\mathrm{fake}}^{\mathrm{tight}} = \frac{N^{\mathrm{loose}} \times \varepsilon_{\mathrm{real}} - N^{\mathrm{tight}}}{\varepsilon_{\mathrm{real}} - \varepsilon_{\mathrm{fake}}} \times \varepsilon_{\mathrm{fake}},$$

which gives the overall normalization, once the two efficiencies are measured. One can translate that into event weights and thus predict the kinematics as well:

$$\omega_{\mathrm{tight}} = \frac{\varepsilon_{\mathrm{fake}} \times (\varepsilon_{\mathrm{real}} - 1)}{\varepsilon^{\mathrm{real}} - \varepsilon^{\mathrm{fake}}}$$

$$\omega_{\mathrm{loose}} = \frac{\varepsilon_{\mathrm{fake}} \times \varepsilon_{\mathrm{real}}}{\varepsilon^{\mathrm{real}} - \varepsilon^{\mathrm{fake}}}$$

The event weight ω_{loose} is given to any event where the lepton passes only the loose requirement while ω_{tight} is given to any event where the lepton passes the tight requirement. The main task is using the matrix method is determining the two efficiencies, $\varepsilon_{\text{real}}$ and $\varepsilon_{\text{fake}}$, done by studying control regions which are signal and background dominated, respectively. A general criterion of the efficiencies is if they must be independent of event kinematics; if an ε is found to vary as a function of some particular variable, it must be parameterized as a function of it. There is some art to the determination of the these factors. One example will be shown here.

Example: The Matrix Method in e+jets for the $\int \mathcal{L}\,dt = 35$ pb^{-1} Dataset

The following is an example of the matrix method in the e+jets channel in the $\int \mathcal{L}\,dt = 35$ pb^{-1} dataset. A similar method is used for the final determination of the fakes in the analysis presented in Chapter 7. The "loose" electron used has less stringent cluster-track matching, no requirements from the TRT, and no explicit photon veto (the collaboration wide "Medium" [106], plus the requirement on a hit in the b-layer and isolation).

To measure $\varepsilon_{\text{real}}$, a simple $Z \to ee$ tag-and-probe is applied. The tag is required to be the final analysis electron, isolated and $p_{\text{T}} > 20\,\text{GeV}$, as described in Section 4.2, to increase the sample purity. The probe electron is used to measure $\varepsilon_{\text{real}}$. The two electrons are required to be within a rather broad invariant mass window around the Z mass, $66 < \text{M}_{ee} < 116\,\text{GeV}$, a balance between purity of the region and high statistics. Assuming that the remaining probes passing the final definition are all true, prompt electrons from a Z decay, $\varepsilon_{\text{real}}$ is simply the number of tight probes divided by the number of loose probes. The measured value of $\varepsilon_{\text{real}}$ as a function of the jet bin, η of the electron, and p_{T} of the electron are shown in Figure 5.1. For $\varepsilon_{\text{real}}$, the main kinematic dependence of note is on the electron p_{T}, and to a lesser extent η.

The determination of $\varepsilon_{\text{fake}}$ is done using the fake-dominated control region, requiring that $E_{\text{T}}^{\text{miss}} < 10\,\text{GeV}$ and $\text{M}_{\text{T}}^{W} < 15\,\text{GeV}$. For simplicity, events with more than one loose electron are vetoed. The expected electroweak contributions in this region are at the percent level, but they are nonetheless considered by subtracting the events based on the MC prediction. The remaining electrons are all taken to be fake. Similar to $\varepsilon_{\text{real}}$, $\varepsilon_{\text{fake}}$ is the number of tight probes divided by the number of loose probes, after the removal of the small contribution of prompt electrons. The value of $\varepsilon_{\text{fake}}$ is then

$$\varepsilon_{Fake} = \frac{N_{Fake}^{\text{tight}}}{N_{Fake}^{\text{loose}}} \approx \frac{N_{data}^{\text{tight}} - N_{EW}^{\text{tight}}}{N_{data}^{\text{loose}} - N_{EW}^{\text{loose}}}.$$

The measured value of $\varepsilon_{\text{fake}}$ as a function of the number of jets in the event as well as η and p_{T} of the electron is shown in Figure 5.2. It is found to depend strongly on jet multiplicity, and shows enough dependence on η and p_{T} to warrant parameterization.

At this point, a three-dimensional parameterization was attempted, which made $\varepsilon = \varepsilon(\eta, p_{\text{T}}, N_{\text{jet}})$. The approach was in the end unsuccessful due to a lack of statistics in the data to parameterize them as such. The matrix method was abandoned, and the final analysis with this dataset shown in Chapter 7 used an estimate based on anti-electron fitting.

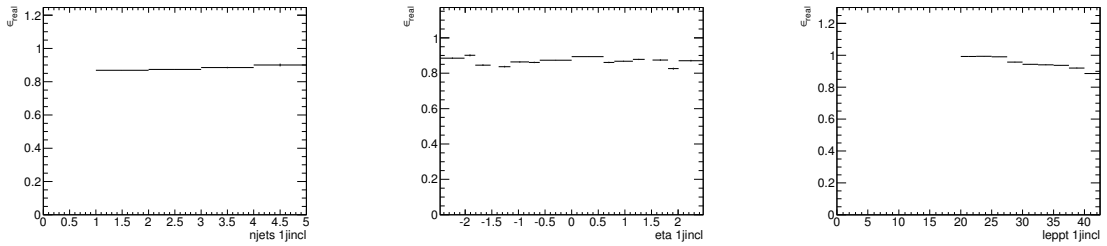

Figure 5.1: Plots of $\varepsilon_{\text{real}}$ in data as a function of the jet multiplicity, η of the electron, and $p_{\text{T}}$of the electron. All plots are shown for the 1-jet inclusive sample. It is stable in the various jet bins, shows some dependence on η and a larger dependence on p_{T}.

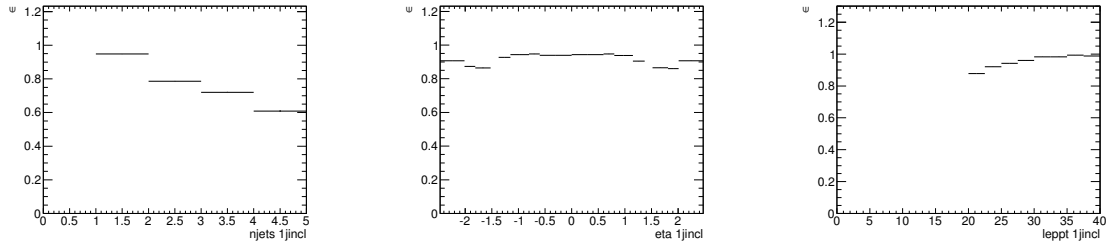

Figure 5.2: Plots of $\varepsilon_{\text{fake}}$ in data as a function of the jet multiplicity, η of the electron, and p_{T} of the electron. All plots are shown for the 1-jet inclusive sample. It is dependent on all three variables shown here, especially jet multiplicity. Statistical error bars are shown but are small.

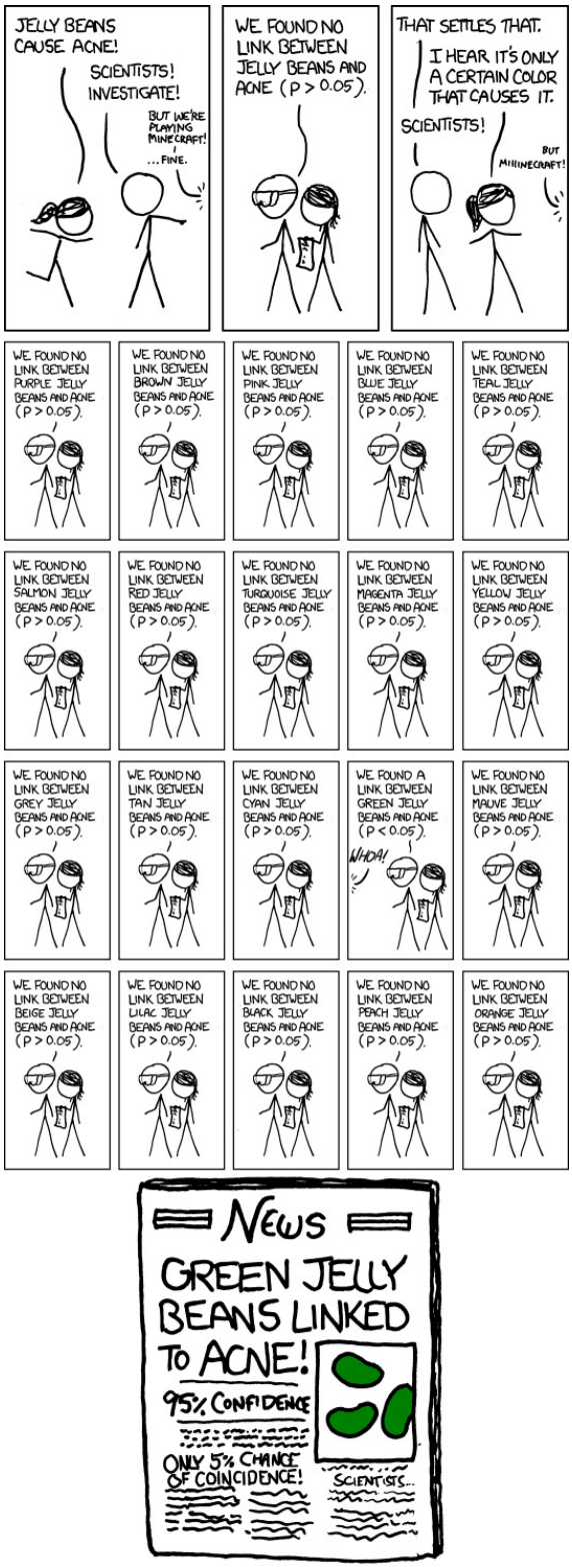

Significant. 'So, uh, we did the green study again and got no link. It was probably a–' 'RESEARCH CONFLICTED ON GREEN JELLY BEAN/ACNE LINK; MORE STUDY RECOMMENDED!'[19]

6 The Profile Likelihood Fit

A binned profile likelihood fit to data is used to measure the parameter(s) of interest in all three of the analyses presented in this thesis. A discriminant is chosen, and a template for the discriminant is derived from simulation for each physical process. It is then normalized to reference values from either theoretical predictions or data, as described in Chapter 5. In the case of the $\sigma_{t\bar{t}}$-only analyses in Chapters 7 and 8, the input template is a discriminant likelihood while in the three-parameter fit in Chapter 9 it is a single variable. The derivation of input templates will be discussed in the appropriate chapter. A binned maximum likelihood estimator is then used to fit the contribution of each process to the distribution observed in data. This serves as a measurement of the parameter(s) of interest. In this method, the expected contribution of physical processes are generalized to be a function of nuisance parameters representing systematic uncertainties. Knowledge of systematic uncertainties is then included as constraints in the fit. In doing this, the likelihood becomes a function of both the normalization of the physical processes and the distortions of the discriminant due to systematic uncertainties. In the fit, systematic uncertainties can be constrained by data to contribute less than their nominal value. This is achieved by using a phase space which is reduced with respect to that which an uncertainty is originally intended to cover, and by using the power of a global fit with prior knowledge regarding the normalization of physical processes and other systematic uncertainties included. The likelihood and its use are described in detail in this chapter.

6.1 The Profile Likelihood

The complete likelihood function, L, is built here. The starting point is a standard Poisson likelihood term for each bin in the template,

$$L_k(\mu_k) = \frac{\mu_k^{n_k} e^{-\mu_k}}{n_k!}$$

where μ_k is the expected number of events in bin k and n_k is the observed number of events.

Each physical process is denoted as β_j, and the full set of physical processes considered will be written as $\vec{\beta}$. The same notation will be used for the set of all μ_k, written as $\vec{\mu}$, and similarly for other parameters. The expected number of events in a given bin is the cross-section weighted sum of all processes considered in the fit in that bin, $\mu_k(\vec{\beta}) = \sum_j \beta_j \nu_{jk}$, where ν_{jk} corresponds to the expected number of events from a physical process j contributing to bin k. These likelihood terms are considered to be statistically independent for each bin and therefore multiplied together to form the basic binned likelihood for the entire template,

$$L_0(\vec{\mu}) = \prod_k L_k(\mu_k) = \prod_k \frac{\mu_k^{n_k} e^{-\mu_k}}{n_k!}.$$

The normalization of each β_j is allowed to float in the fit. Any parameter of interest is unconstrained (i.e. a flat prior is used), while background processes are constrained using a Gaussian

prior corresponding to the uncertainty of the process' rate, denoted Δ_j. Each process is normalized such that $\beta_j = 1$ corresponds to the nominal input cross section. The constraints are included as Gaussian terms in the likelihood as

$$C(\vec{\beta}) = \prod_j \frac{1}{\sqrt{2\pi}\Delta_j} \exp\left[- \frac{(\beta_j - 1)^2}{2\Delta_j^2} \right],$$

where the product is over all physical processes considered. The equation for a binned template likelihood fit to data without the inclusion of nuisance parameters is thus built. This likelihood, $L_{\text{stat}} = L_0(\vec{\beta}) \times C(\vec{\beta})$, is used to determine the statistical uncertainty of the measurement.

In an extremely simple analysis with one background (unconstrained) and the signal, the fit will find the most likely amount of contribution from each of the two processes, based on the predicted shape of each and the data observed. In the analyses presented here, 10-20 processes are included, with background constraints as wide as $\Delta \sim 60\,\%$, depending on the channel and analysis. The way processes are considered and their constraints change amongst the analyses and will be discussed in the appropriate chapter.

Inclusion of Systematic Uncertainties as Nuisance Parameters

The inclusion of systematic uncertainties directly into the likelihood equation gives this method formidable power. The concept is relatively new but becoming more widely used in high energy physics. A recent overview of the methodology is given in [124]. The expected number of events becomes a function of systematic uncertainties, with each modeled as a single parameter δ_i. In this way, $\vec{\mu} = \vec{\mu}(\vec{\beta}, \vec{\delta})$, thus $L(\vec{\mu}) = L(\vec{\mu}(\vec{\beta}, \vec{\delta}))$. In doing this, the contribution of a given systematic uncertainty may also be constrained within this phase space present by data when the global likelihood function is maximized.

Systematic uncertainties are typically given as an up and a down variation, taken to represent one standard deviation ("$1\,\sigma$") such that $\delta_i = 0$ corresponds to the nominal case, while $\delta_i = -1$ is the down variation and $\delta_i = +1$ is the up variation. The uncertainty is made continuous by vertical template morphing, using quadratic interpolation within $\delta_i = \pm 1$ and linear extrapolation beyond, here defined up to $\delta_i = \pm 5$ (i.e $\pm 5\,\sigma$). The morphing function for interpolation and extrapolation, $\epsilon_{jik}(\delta_i)$, for a process j in bin k is thus defined as

$$\epsilon_{jik}(\delta_i) = \begin{cases} \lambda^+_{jik} + (\delta_i - 1)[(\frac{3}{2}\lambda^+_{jik} - 1) + (\frac{1}{2}\lambda^-_{jik} + 1)], & \delta_i > 1 \\ \frac{1}{2}\delta_i[(\delta_i - 1)\lambda^-_{jik} + (\delta_i + 1)\lambda^+_{jik}] - (\delta_i - 1)(\delta_i + 1), & |\delta_i| \leq 1 \\ \lambda^-_{jik} + (\delta_i + 1)[(-\frac{3}{2}\lambda^-_{jik} + 1) + (-\frac{1}{2}\lambda^+_{jik} - 1)], & \delta_i < -1. \end{cases}$$

Here λ^+_{jik} and λ^-_{jik} are the relative shifts in the number of expected events for a given bin and process when taken to the positive or negative extrema of uncertainty i. The sum of expected events in a bin is therefore generalized to be a function of both the physical processes and the nuisance parameters, $\mu_k(\vec{\beta}, \vec{\delta}) = \sum_j \beta_j \nu_{jk} \prod_i \epsilon_{jik}(\delta_i)$. The δ_i terms are Gaussian constrained in the likelihood equation. The δ_i are normal by definition (expectation of 0, uncertainty of 1) and can thus be written as

$$C(\vec{\delta}) = \prod_i \frac{1}{\sqrt{2\pi}} \exp\left[- \frac{\delta_i^2}{2} \right].$$

where the product is over all systematic uncertainties included in the fit.

The Full Likelihood

Multiplying together the basic likelihood term with the Gaussian constraints on background process normalizations and the nuisance parameter constraint, the full likelihood is defined as

$$\begin{aligned} L(\vec{\mu}(\vec{\beta},\vec{\delta})) &= L_0(\vec{\mu}) \times C(\vec{\beta}) \times C(\vec{\delta}) \\ &= \prod_{kji} \frac{\mu_k^{n_k} e^{-\mu_k}}{n_k!} \times \frac{1}{\sqrt{2\pi}\Delta_j} \exp\left[\frac{-(\beta_j-1)^2}{2\Delta_j^2}\right] \times \frac{1}{\sqrt{2\pi}} \exp\left[\frac{-\delta_i^2}{2}\right], \end{aligned}$$

thereby specifying a binned likelihood including nuisance parameters for an arbitrary number of physical processes and systematic uncertainties.

Note on Inclusion of Systematic Uncertainties in the Fit

There has been much discussion and even debate within the collaboration about what properties a certain systematic uncertainty must have in order to qualify for inclusion into a likelihood as a nuisance parameter. The question asked for a given systematic uncertainty can be formulated as, "Can it be described by a single continuous parameter?". One self-evident criteria is therefore that it can be made continuous. The other is more subtle, questioning whether it can be described by a *single* parameter. The variety of conditions and testing required means that the precise configuration of systematic uncertainties in the likelihood changes from analysis to analysis in this thesis.

An example of a situation where a single parameter may not suffice is if a systematic uncertainty is in fact composite and would better be broken into multiple components. It should be noted that experience shows in such cases that splitting a composite uncertainty into multiple components tends to yield consistent fit results with smaller uncertainties. A similar concern is that a given δ_i it may not be fully correlated over the full phase space used. Either case could lead to misestimations if a single parameter is used. Through many discussions some agreements have been reached but no general rules apply. Accordingly, uncertainties are handled on an analysis-by-analysis basis. Much of the decision making is in fact done on the fly. Object scales and resolutions are generally considered in profiling. Some in the collaboration feel uncomfortable profiling modeling uncertainties, resulting in them often being taken out of the likelihood fit for the final versions used in publications. In certain situations an uncertainty should a priori be included and is for the first attempt at the analysis, but pathological behavior is identified resulting in it being removed for the next iteration of fitting. This is often, but not always, caused by a poorly thought through prescription, such as a systematic uncertainty which is binned in phase space and is discontinuous at certain thresholds.

In an extreme case where systematic uncertainties exhibit a degeneracy in their affect on the template shape, the fit looses the power to distinguish amongst the uncertainties and gives nonsensical results. This can happen especially if several uncertainties do not affect the template shape at all. Such "rate-only" uncertainties should be removed.

Obtaining Results from the Likelihood

Once the likelihood is defined, it can be used to estimate a parameter of interest, $\sigma_{t\bar{t}}$, or multiple parameters of interest at once. For the sake of clarity the case of a single parameter of interest will be discussed here, denoted β_0. In the analyses in Chapters 7 and 8 this represents $\sigma_{t\bar{t}}$ and is the sole parameter of interest, while in the analysis in Chapter 9 there are three parameters of interest: $\sigma_{t\bar{t}}$, $f_{\mathrm{W_{HF}}}$, and f_{Wc}.

Maximizing the Likelihood

The fitter maximizes L by minimizing its negative logarithm, $-\ln(L)$, done using the MINUIT package in ROOT [125]. Asymmetric errors are taken at the minimum using MINOS (from MINUIT), which are used for the value quoted as the uncertainty on the parameter from the fit. Additionally, Hessian symmetric uncertainties are extracted from the second derivative at the minimum which are used only to study correlation effects. A full covariance matrix populated with these errors will be shown for the analyses.

Profiling the Likelihood

The profile function $\lambda(\beta_i)$ is obtained, allowing one to check the behavior of the likelihood as a function of the parameter of interest, β_i. In essence this is a projection of the likelihood function onto a certain axis, which can be done for any parameter. To achieve this, the likelihood is first minimized with respect to all parameters ("min"). Then a second fit ("partial") is done where L is minimized as a function of all parameters except for β_i. The first is then subtracted from the second,

$$-\ln(\lambda(\beta_i)) = \ln\left(L(\vec{\beta},\vec{\delta})_{\text{min}}\right) - \ln\left(L(\beta_i,\vec{\beta}',\vec{\delta})_{\text{partial}}\right),$$

where $\vec{\beta}'$ in the partially minimized likelihood includes all physical processes except for β_i. In testing this is done for all parameters to identify pathological behavior in the likelihood, such as a discontinuity or kink in the function. Plots of λ as a function of β_0 will be shown in the analyses

Marginalizing the Likelihood

An alternative method for handling nuisance parameters in a likelihood is marginalization, which integrates over the nuisance parameters. The benefit to this method is that correlations amongst parameters can be taken into account, since the profile technique assumes uncorrelated parameters. The downside is that it requires a numerical integration technique and is therefore computationally intensive and requires careful testing. The marginalized likelihood is obtained by integrating $\int L(\vec{\beta},\vec{\delta})d\vec{\delta}$ using the Metropolis-Hastings algorithm for numerical integration [126, 127].

6.2 Evaluation of Uncertainties

The observed uncertainty at the minimum of the negative log likelihood is used to quantify the effect of all terms minimized in the fit, namely statistical and the included systematic uncertainties. Each component's contribution may be estimated this way. In many cases, ensemble testing is used to evaluate the behavior of the fit and estimate uncertainties. The general methodology is explained here.

Fit Uncertainty

In principle one does not access directly the observed uncertainty due to a given source in the profile likelihood but rather observes the combined uncertainty of statistics and systematics considered in the fit. The various contributions can, however, be estimated by breaking down the observed fit uncertainty into components. The templates can be re-fit to data, removing specific sources of uncertainty from the likelihood fitting one-by-one, such that L is not a function of a

specific δ_i, giving a result excluding that uncertainty. The relative uncertainty (since the central value may shift) is calculated for each of these "N-1" tests, and subtracted in quadrature from the full fit result in order to estimate the contribution of the specific component in question. Doing so assumes no correlations amongst the parameters. All systematic uncertainties may be removed, such that $L = L_{\text{stat}}$, to estimate the purely statistical component. This method only gives approximate contributions of each uncertainty source to the fit.

Ensemble Testing

No observed data are used in ensemble testing, rather pseudo-experiments (PEs) are created from the simulation. Each is intended to represent a possible outcome of the measurement. The number of events predicted in bin k as a function of the physical processes is given by $\mu_k(\vec{\beta}) = \sum_j \beta_j \nu_{jk}$, as defined in the previous section. The actual number of events predicted for a process and bin, ν_{jk}, is calculated by using simulation for the process. To assemble a PE, ν_{jk} is fluctuated following a certain distribution to test a specific uncertainty. Each physical source in a bin is fluctuated independently. The analysis is then performed, fitting the usual templates to the PE as if it were the observed data. This process is repeated, typically thousands of times, creating an ensemble of PEs. Since the fluctuation of each PE is independent, the ensemble fit results are expected to be Gaussian distributed around the expectation value of the fit with a width corresponding to the magnitude of this uncertainty source in the analysis.

Statistical Uncertainty

To evaluate the expected statistical uncertainty, PEs are drawn with a Poisson fluctuation for the expected number of events in a given bin (i.e. $\sqrt{\nu_{jk}}$). As the prediction in each bin is essentially a multi-source counting experiment, the Poisson distribution is appropriate to use. The expected statistical uncertainty can be compared with the results of the final fit to data. The observed statistical uncertainty is a part of the fit uncertainty, and the expected statistical uncertainty will not be used in the final results. The likelihood function L_{stat} is used, i.e. with no nuisance parameters.

Template Statistics Uncertainty

This method presumes that sufficient simulation statistics are available for the physical distribution in question to be smooth. In practice, the effect of limited simulation statistics in the templates can be quantified as a systematic uncertainty in the analysis. To evaluate this, PEs are constructed by first drawing from a Gaussian whose width corresponds to the simulation statistics available, which is in turn used to draw a Poisson as described above. A Gaussian is used to reflect the assumption of large statistics. The resulting distribution is thus a convolution of a Poisson distribution and a Gaussian distribution. In order to isolate the "template statistics" portion, the difference is taken in quadrature of the Poisson only test from the Gaussian and Poisson test. One can see that in the limit of infinite simulation statistics the width of the Gaussian becomes negligible and the two tests return the same result, yielding no additional uncertainty due to this limitation.

This method yields a rough estimate of the uncertainty, but in practice its magnitude gives an idea of whether or not the limited statistics are problematic in general. A large uncertainty from the template statistics means that the general method begins to break down. The templates used for fitting may not be smooth enough to be reliably used. Furthermore, the PEs used for testing can be biased if the underlying distribution does not have enough statistics.

Systematic Uncertainty

The systematic uncertainties which are not fitted are still technically included in the definition of the likelihood via nuisance parameters. In the fit, they are fixed to their nominal values ($\delta_i = 0$). In order to evaluate the magnitude of one such "external" uncertainty in the analysis, the nuisance parameter is fixed to its extremum and PEs are drawn, fitting a Gaussian to the results of the fit to the PEs. This fixing distorts the nominal template to be its $\pm 1\,\sigma$ deviation in terms of that uncertainty. The mean of the Gaussian of fit results is taken to be the expected fitted value, thus the uncertainty due to a given source is taken to be

$$\frac{< \beta_{\text{nominal}} > - < \beta_{\text{fixed delta}} >}{< \beta_{\text{nominal}} >}.$$

To first order, the difference in the result of the fit to data with and without the parameter fixing is the magnitude of the uncertainty, but testing with PEs creates a smooth distribution insensitive to a probable or improbable fit. The expected behavior can be evaluated using the nominal values for all parameters other than the systematic uncertainty being tested, or it can be done using the fitted values of the likelihood to be more precise. In the results presented here, the fitted values are used, so the external systematic uncertainties are evaluated at the observed minimum, not the expected. Each contribution of an external systematic is added in quadrature to the results from the fit.

Final Uncertainty

The full expected fit uncertainty, which is the observed statistical uncertainty as well as the constrained systematic uncertainties included in the fit, can be estimated with PEs before fitting. This can be done by fluctuating $\vec{\delta}$ and $\vec{\beta}$ within their uncertainty as well as allowing the Poisson fluctuation on statistical uncertainty. As for the pure statistical test, this checks the fit behavior but will not be used in final results.

The final quoted uncertainty on a measurement is the sum in quadrature of the fit uncertainty (which includes observed statistical uncertainty) and all externally evaluated systematic uncertainties (including template statistics). Following convention, the uncertainty will be quoted both in total and broken down into components as statistical, systematic, and luminosity. The fit uncertainty is broken down into its components as statistical and systematic uncertainties using the statistics-only fit and N-1 testing.

Linearity Tests

The linearity of the fit is checked using ensemble testing in order to further ensure a non-biased result. The parameter of interest is set to a given value other than 1 before a PE is drawn. PEs are then drawn at each of many points across a large range, and the central values with their RMS are then plotted. A line is fit through the points. A perfectly unbiased fit should return a slope of 1 with a y-intercept of 0. For testing $\sigma_{t\bar{t}}$, input values are injected for over the range $[120, 200]$ pb in steps of 20 pb in all three analyses. For the 3-parameter analysis in Chapter 9, linearity each of the flavor ratios is checked for over a range of $[0.4, 2.0]$ in steps of 0.2. If a significant bias is found, the results of the fit can be corrected for a posteriori.

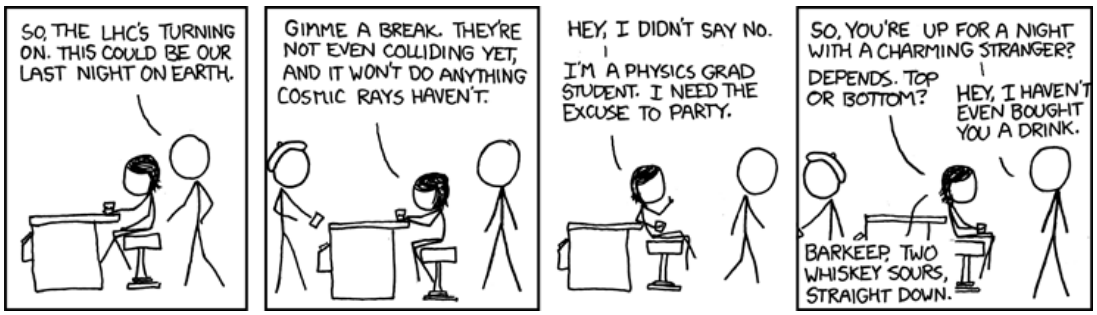

Turn-On. "Supercollider? I 'ardly know 'er!"[19]

7 Measurement of $\sigma_{t\bar{t}}$ in $\int \mathcal{L}\,dt = 35$ pb^{-1} Using b-tagging

The single most precise measurement of $\sigma_{t\bar{t}}$ at ATLAS using the $\int \mathcal{L}\,dt = 35$ pb^{-1} dataset collected during 2010 has been submitted for publication to Physics Letters B [17] and is shown here. The measurement uses the semileptonic decay channel of $t\bar{t}$ in both the e+jets and μ+jets channels. A binned profile likelihood template fit to data is used to extract the signal, with many systematic uncertainties included in the fit as nuisance parameters. The templates used in the fit are a discriminant likelihood constructed from kinematic variables and a flavor sensitive b-tagging weight variable, which is optimized to discriminate the $t\bar{t}$ process from W+jets.

7.1 Selection

The events selected in this analysis have a high p_{T}, prompt lepton (e,μ), multiple jets, and large missing energy, summarized in Section 4.3. The event yields are shown in Table 7.1 for μ+jets (upper) and e+jets (lower) channels in each jet bin. In the fit, events with three or more jets are used with each lepton for a total of 6 channels. The 1-2 jet bins are shown as a control region. The fake lepton contribution is taken from the anti-electron fitting method for e+jets and the matrix method for μ+jets, as discussed in Section 5.2. Basic kinematic plots in both the low jet multiplicity control region and high jet multiplicity signal region are shown for e+jets in Appendix C.

7.2 The Input Distribution

The discriminant is a likelihood which takes four variables as input, and is trained to discriminate $t\bar{t}$ from W+jets based on MC simulation. The training of the likelihood discriminant and its evaluation is done using TMVA [128], which trains for signal divided by signal over background, S/S+B. The shape of W+jets is taken as representative of all of the background processes for the training process. It is expected to be the dominant source of background events, as can be seen in Table 7.1. For $t\bar{t}$ and W+jets the MC is split in half, where one half is used as a reference sample to train the likelihood and the other half is used in evaluation, that is, to create the template for the process to be used in the fit. The discriminant is evaluated for all other background processes and data as well.

The W+jets sample includes all of the various flavor contributions, scaled as discussed in Section 5.1. The analysis is flavor-sensitive due to the inclusion of continuous b-tagging as an input to the discriminant likelihood. The variables which are used as input are described here, and the discriminant is shown before the fit.

Lepton Pseudorapidity

Lepton pseudorapidity (η) is a simple physical quantity which is quite useful in discriminating $t\bar{t}$ from W+jets, due to the differing production mechanisms of the leptonically decaying W. In

μ+**jets Channel**	1 Jet	2 Jet	3 Jet	4 Jet	$\geq$ 5 jet
$t\bar{t}$	20 ± 9	85 ± 22	165 ± 23	156 ± 18	109 ± 27
W+jets	18000 ± 2100	4300 ± 1000	980 ± 410	220 ± 140	59 ± 38
Fakes (QCD multijet)	316 ± 95	180 ± 54	79 ± 24	19 ± 6	11 ± 3
Single Top	58 ± 10	64 ± 11	31 ± 7	11 ± 4	4 ± 2
Z+jets	700 ± 140	210 ± 50	58 ± 26	14 ± 10	5 ± 4
Diboson (WW,WZ,ZZ)	67 ± 10	56 ± 9	16 ± 4	3 ± 2	0.6 ± 0.8
Total Predicted	19200 ± 2380	4900 ± 1140	1320 ± 500	420 ± 180	187 ± 74
Data Observed	20076	5039	1289	436	190

e+**jets Channel**	1 Jet	2 Jet	3 Jet	4 Jet	$\geq$ 5 jet
$t\bar{t}$	15 ± 5	63 ± 12	117 ± 17	109 ± 15	76 ± 19
W+jets	8500 ± 1100	2160 ± 500	520 ± 220	124 ± 77	35 ± 23
Fakes (QCD,$\gamma + jets$)	410 ± 200	160 ± 81	64 ± 32	12 ± 6	8 ± 4
Single Top	36 ± 7	42 ± 8	21 ± 5	7 ± 3	3 ± 2
Z+jets	166 ± 38	147 ± 43	60 ± 28	21 ± 15	8 ± 6.0
Diboson (WW,WZ,ZZ)	36 ± 6	29 ± 6	9 ± 3	2 ± 1.5	0.4 ± 0.6
Total Predicted	9140 ± 1350	2600 ± 650	800 ± 300	275 ± 117	129 ± 55
Data Observed	9849	2568	755	261	123

Table 7.1: Selected events in both data and from expectations in the μ+jets (top) and e+jets (bottom) channels. The uncertainties shown are those which affect rate the most, namely limited MC statistics, theoretical cross sections, JES, luminosity. For $t\bar{t}$, ISR/FSR are included as well. Observed event counts agree with predictions within uncertainty.

a W+jets event the lepton is produced rather homogeneously in η in the detector frame, while it tends to be central in a $t\bar{t}$ event.

For a muon, η of the object is taken: $\eta^{\ell} = \eta$. For electrons it is not quite so simple due to the discontinuity of acceptance caused by the calorimeter crack region. In the electron case, the η of the calorimeter cluster associated to the electron is used, yielding a clean distribution with precisely no events in the gap region (using the reconstructed electron's η, which is actually the η of the track associated with the electron, would give a small tail into the vetoed region caused by events whose track are within the η range of the calorimeter crack but whose cluster is actually outside of the gap). In order to make this distribution continuous, η is transformed in the electron channel as:

$$\eta^{\ell} = \begin{cases} \eta & \text{for} \quad |\eta| < 1.37 \\ \eta - 0.15 & \text{for} \quad 1.52 < \eta < 2.47 \\ \eta + 0.15 & \text{for} \quad -2.47 < \eta < -1.52. \end{cases}$$

Normalized Transverse Energy, $H_{\mathrm{T,3p}}$

It is a rough but true statement that $t\bar{t}$ events are on average more energetic than W+jets events, due to the fact that the threshold for production of $t\bar{t}$ is higher than that of W+jets ($2m_{\mathrm{top}} \gg M_{\mathrm{W}}$), giving the Ws (and their decay constituents) less transverse momentum on average in a W+jets event than in a $t\bar{t}$ event. This combined with the rapidly increasing strong

coupling strength at low energies means that the additional jets due to QCD jet production in association with the W will tend to be soft, indeed far softer on average than the jets in a $t\bar{t}$ event.

One can construct a class of variables known as H_{T} which are a measure the transverse momentum of the event as a whole. It has been found by testing that the transverse momentum of third and fourth jets yield a particularly high separation power; their sum therefore forms the numerator of the variable used. In the 3-jet bin it is only the third jet, and in the lower jet bins the variable is not defined. Higher jets were left out in order to control pileup and large radiation effects, because the 5-jet bin is inclusive and could have many more jets present. The denominator is the sum of the absolute value of the longitudinal momentum, p_{z}, of all objects in the event, including the neutrino, which is calculated using the event kinematics and solved for by taking the smaller neutrino solution. This variable, called $H_{\mathrm{T,3p}}$, is defined as:

$$H_{\mathrm{T,3p}} = \frac{\sum_{i=3}^{\mathrm{N_{jets}}\leq 4} |p^2_{\mathrm{T,i}}|}{\sum_{j=1}^{\mathrm{N_{objects}}} |p_{\mathrm{z,j}}|}.$$

This definition as such yields a particularly clumped distribution, so it is transformed as $H_{\mathrm{T,3p}} \rightarrow \exp(-4 \times H_{\mathrm{T,3p}})$ to obtain a smoother input distribution for the likelihood discriminant.

Aplanarity

The aplanarity A is a measure of the topography of the event. A is defined as 1.5 times the smallest eigenvalue of the momentum tensor, which is defined as:

$$M_{ij} = \frac{\sum_{k=1}^{\mathrm{N_{objects}}} p_{ik} p_{jk}}{\sum_{k=1}^{\mathrm{N_{objects}}} p_k^2},$$

where p_{ik} is the i-th momentum component of object k and p_k is the absolute value of its momentum. All jets in the event and the charged lepton are considered in the definition. The result is a clumped distribution which is smoothed by transforming $A \rightarrow \exp(-8 \times A)$.

Mean of Two Highest JetProb Weights

The output of the JetProb algorithm, discussed in Section 4.4, is used as an input to the likelihood. Based on the knowledge that a $t\bar{t}$ event should contain two b-jets, a variable is constructed which is the mean of the b-tagging algorithm's value for two most b-like jets. This variable, $\overline{w}_{\mathrm{JP}}$, shows a strong discriminating power due to the fact that W+jets events are dominated by light jet production. Nonetheless, the uncertainty on $f_{\mathrm{W_{HF}}}$ is large enough that this becomes a sizable uncertainty in the analysis. Furthermore the uncertainty in the calibration of the algorithm, a process described in Section 4.4, becomes a large systematic uncertainty.

After the calibration procedure described in Section 4.4 was applied, a remnant discrepancy in the background dominated events in the light part of the spectrum – below the lowest calibrated working point – was observed. While unfortunate this is not particularly surprising, as the algorithm is only very roughly calibrated in this regime. This is handled in two ways in the analysis. In the distribution, all points below the lowest working point are lumped together into a single bin, averaging out the coarse calibration. The problem is solved in the bins which have a high signal to background ratio (4 and 5 jets). In the background dominated 3-jet bin it is thought that the mismodeling is too dramatic to be trustworthy. Accordingly the variable $\overline{w}_{\mathrm{JP}}$ is not used in the 3-jet bin but is still used in the others.

The Input Likelihood

The four variables (three in the 3-jet bin, without $\overline{w}_{\mathrm{JP}}$) are combined into a likelihood discriminant for each of the six physics channels: e+jets and μ+jets, which are further split into 3-jet exclusive, 4-jet exclusive, and 5-jet inclusive events. These six physics channels are treated on equal footing in the fit, with 20 bins in each histogram, yielding a total 120-bin fit. In addition to being necessary following the theoretical considerations in the introduction, for similar reasons this serves to mitigate systematic uncertainties by absorbing signal events which migrate away from the 4-jet bin. Furthermore, the 3-jet bins serve to constrain the background contribution.

The expected separation between W+jets and $t\bar{t}$ can be seen in each channel in Figure 7.1. One can see that the 3-jet bin in both channels suffers from a significantly lower discriminating power due to omitting $\overline{w}_{\mathrm{JP}}$ in the likelihood discriminant. A clean separation between signal and background is achieved in particular in the 4-jet bins and the μ+5 jet bin. This is not the case in e+5 jets due to the significantly reduced background fraction in the channel, which comes from the harsher cuts to control the fake rate, reducing an already small background in the 5-jet bin to be even smaller in the electron channel. The sum of all prediction contributions is compared to the data before the fit in Figure 7.2.

Validation

The variables have been chosen based on expected discriminant power, with potential sensitivity to systematic uncertainties taken into account in the decision as well. It is essential to validate the choices to ensure that the variables are well-modeled, in particular in the background dominated regions. The set of variables used in the analysis is shown both in the two-jet control region and in the signal region for both channels. There is generally a good agreement between MC predictions and measured data. The data-MC agreement is shown for the variables of interest in Figures 7.7-7.14 at the end of this chapter. No discrepancies beyond uncertainties are observed.

7.3 The Fit Likelihood

The profile likelihood formalism developed in Chapter 6 is used to fit the discriminant templates for the signal and various backgrounds to data. The choices made are described here, and the expected behavior of the fit is evaluated as necessary.

The Fit Parameters

The sole parameter of interest in this six-channel, 120 bin fit is $\sigma_{t\bar{t}}$. Prior knowledge of the various backgrounds are included in the fit as constraints, and nuisance parameters describing systematic uncertainties are included and potentially constrained. The main background, W+jets, is taken as uncorrelated a priori amongst the six channels, with the uncertainty on the normalization in each jet bin increasing from bin to bin. The uncertainty on $f_{\mathrm{W_{HF}}}$ and f_{Wc} are handled in terms of nuisance parameters, with one for $f_{\mathrm{W_{HF}}}$ and another for f_{Wc} in each of the jet bins, taken as correlated between the two lepton channels, for a total of 6 δs. The QCD multijet production is treated a priori uncorrelated in each jet bin and channel as well, with a flat 50 % normalization uncertainty for each. The uncertainty due to the shape of QCD multijet production is not treated as a nuisance parameter due to its discrete nature. The normalization of smaller electroweak background (Z+jets, single top, and di-boson production) are each treated as a single β parameter in the fit, each constrained within their theoretical uncertainty. No modeling uncertainty is considered for these processes. The small magnitude of

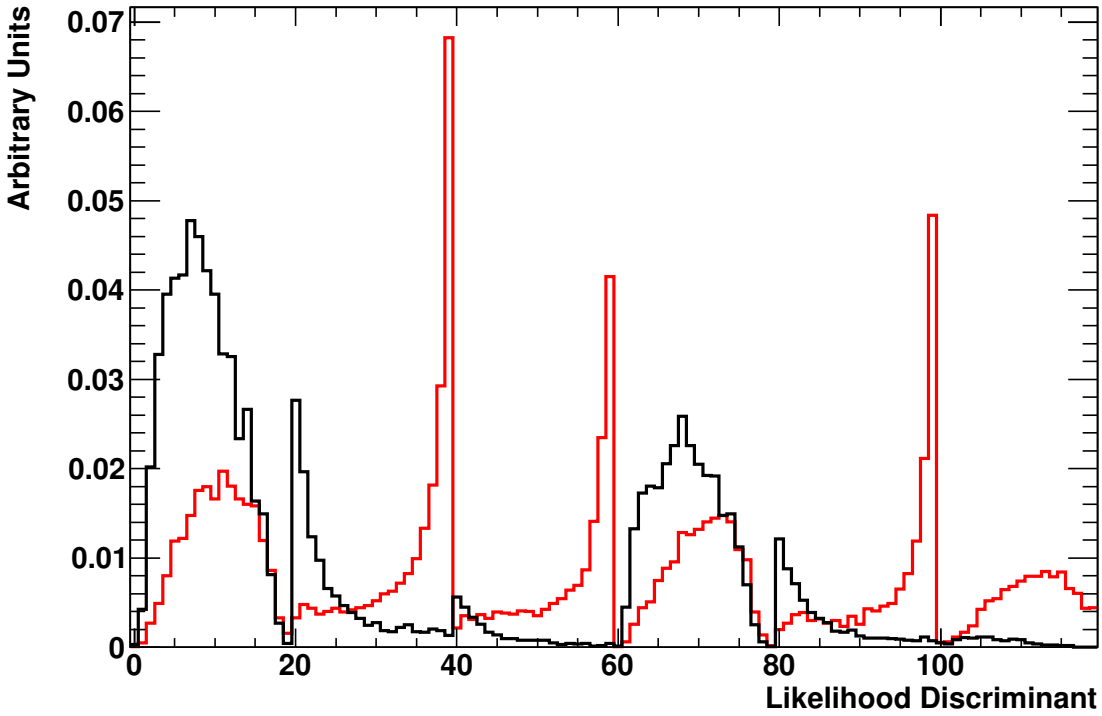

Figure 7.1: The separation power of the likelihood discriminant in all six analysis bins, comparing $t\bar{t}$ (red) and W+jets (black). The left three plots are μ+jets, the right three are e+jets. In each channel, from left to right each group of twenty bins are 3-jet exclusive, 4-jet exclusive, and 5-jet inclusive.

these backgrounds in the signal region and the relative insensitivity of the fit to them warrants such treatment. The βs and their constraints are summarized in Table 7.2.

The dominant object-related uncertainties are the b-tag and mistag scale factors at each of the four calibrated operating points, which are each profiled as independent nuisance parameters, totaling 8 in all. All object related uncertainties (energy scales, efficiencies, and resolutions) are profiled in the likelihood as well. The uncertainty due to PDFs are not included in the fit because there are too many uncorrelated parameters; including them would have effectively doubled the number of degrees of freedom in the fit, which is simply impractical. After much discussion, uncertainties which are not clearly continuous – the signal generator, the parton shower, W+jets shape, and the QCD model – are not included in the fit. In such cases the interpretation of the result of the nuisance parameter in the fit are too unclear for the taste of some. In a similar fashion, much work was done by others to show that initial and final state radiation (ISR/FSR) could be considered as a continuous uncertainty and thus cleanly included in the fit. This came under heavy fire during collaboration review and they have thus been removed from the fit, meanwhile scientific publications have ascended to the status of laws and sausages, being things which one is better off not seeing being made.

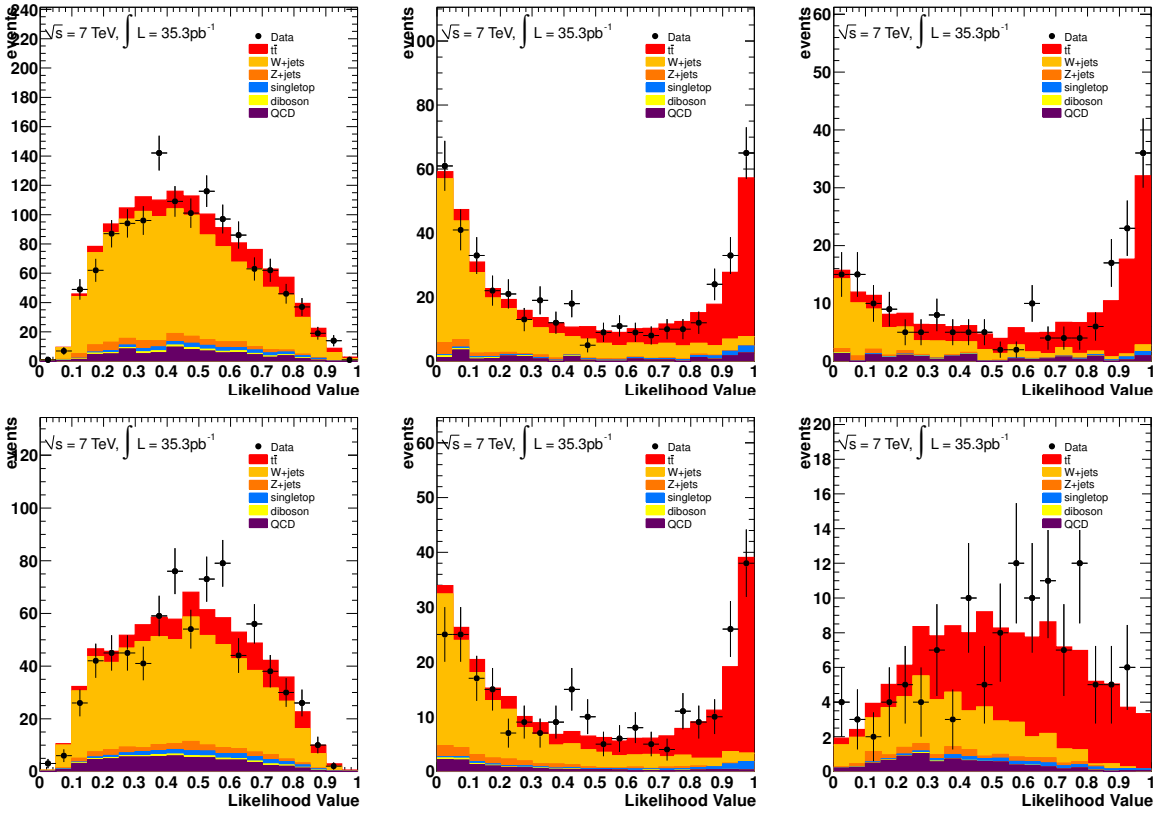

Figure 7.2: The likelihood discriminant for the sum of the signal and all background components compared to data before the fit in each of the six channels. The top three plots are μ+jets, the bottom three are e+jets. The left column is 3-jet exclusive, middle column is 4-jet exclusive, and right column is 5-jet inclusive. Errors on the measured data points are purely statistical. One can see a generally reasonable agreement within the available data statistics.

Parameter	**Constraint**
$\beta(t\bar{t})$	none
$\beta(\mathrm{W}\rightarrow l$ + 3 jets)	0.42
$\beta(\mathrm{W}\rightarrow l$ + 4 jets)	0.48
$\beta(\mathrm{W}\rightarrow l$ + 5 or more jets)	0.54
$\beta(Z$+jets)	0.30
β(Single top)	0.106
β(Diboson)	0.06
β(QCD in l + N jets)	0.5

Table 7.2: The input constraints on the various samples. Here, l is either e or μ, and "N jets" is all three jet bins, i.e. 3 exclusive, 4 exclusive, and 5 inclusive.

Behavior of the Fit

The linearity of the fit is checked in steps of 10 pb over the range [120,200] pb, with results shown in Figure 7.3. A small offset of -1.6 pb is identified and corrected for in the final fit.

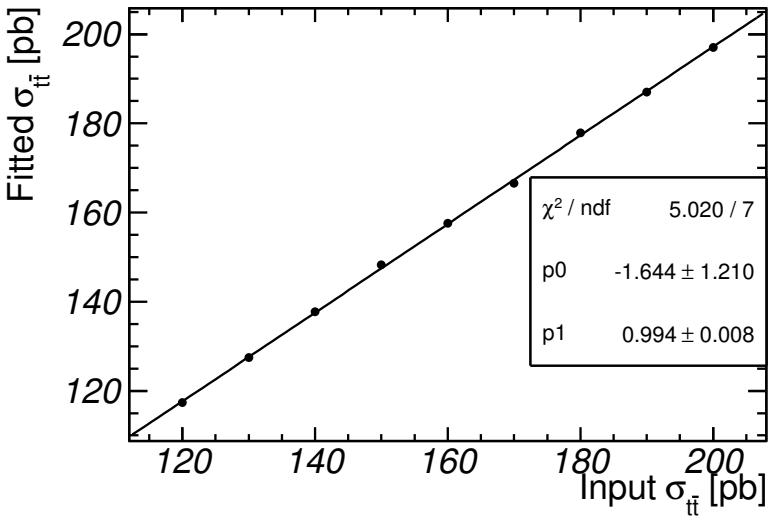

Figure 7.3: The linearity of the fit over the range $\sigma_{t\bar{t}} = [120,200]$ pb. A small offset of about 1.6 pb is observed (the y-intercept, p0, of the fit), for which the final results are corrected.

7.4 Results of the Fit and Systematic Uncertainties

After correcting for the small offset observed in the linearity test, the result of the fit is

$$\sigma_{t\bar{t}} = 187^{+16}_{-15} \text{ (fit) pb.}$$

The externally evaluated systematic uncertainties are not yet added to the uncertainty. The fitted result is shown in Figure 7.4, where excellent data-MC agreement can be seen. The full correlation matrix of all $\vec{\beta}$ and $\vec{\delta}$ are shown in Figure 7.5. All observed correlations are as expected and not particularly strong. The profiled likelihood as a function of $\sigma_{t\bar{t}}$ is shown near the minimum in Figure 7.6. A smooth curve is observed. The results of the fit for every β and δ parameter can be seen in Table 7.3, all of which are consistent with expectations within uncertainty.

The systematic uncertainties considered in this analysis are summarized and discussed throughout Chapters 3–5 and listed in Appendix A. The magnitude of the uncertainties in this analysis are summarized in Table 7.4, evaluated following the procedure developed in Chapter 6. One can see that the analysis is clearly dominated by systematic uncertainty, although statistical uncertainty is the single largest contribution, at about 6 % relative uncertainty on $\sigma_{t\bar{t}}$. The dominant systematic uncertainties are the b-tagging algorithm calibration and ISR/FSR modeling for $t\bar{t}$, each contributing about 5 %. The sub-leading uncertainties at 3-4 % are MC generator choice, jet energy scale, and the uncertainty on $f_{\mathrm{W_{HF}}}$.

Once including all external systematic uncertainties, the final result of this analysis is

$$\sigma_{t\bar{t}} = 187 \pm 11(\text{stat.})\ ^{+18}_{-17}(\text{syst.}) \pm 6(\text{lumi.})\ \text{pb} = 187^{+22}_{-21}\ \text{pb}.$$

This represents the single most precise measurement of $\sigma_{t\bar{t}}$ with the 2010 $\int \mathcal{L}\,dt = 35\ \text{pb}^{-1}$ dataset at ATLAS. Interpretation of this result will be discussed in Chapter 10.

Cross Checks

A number of checks of the fit have been done, in particular testing stability of the central value and assumptions made in the nuisance parameters. Concern was raised during collaboration review of this work surrounding the legitimacy of including each JES term as a single nuisance parameter, since this presumes a correlation across phase space. Studies indicated that correlations were at the 90% level, implying a negligible effect of the assumption of full correlation. Extensive testing was nonetheless undertaken.

An example of a test performed was to first re-fit after removing a nuisance parameter from the likelihood (the calorimeter JES component) and comparing results with the nominal, as a check of stability and uncertainty estimation. Results were found to be stable within the uncertainty caused by that additional term. A further test was to assume different correlations in p_{T} and η, to check if uncertainty was being underestimated by using one part of phase space to constrain another where no such correlation should be assumed. To do this, the uncertainty was split into three components: 50 % of the uncertainty was treated normally, while 25 % increased with jet p_{T} and 25 % decreased. The test was constructed such that for any jet p_{T}, the sum of the three terms would yield the default uncertainty. The overall fit uncertainty was found to be lower than in the nominal case. In another case, the component's magnitude was varied up and down additionally as a function of jet $|\eta|$, and the resulting uncertainty was found to be compatible. These tests, and several others documented fully in Appendix C of [14], showed stable, consistent results with well estimated uncertainties.

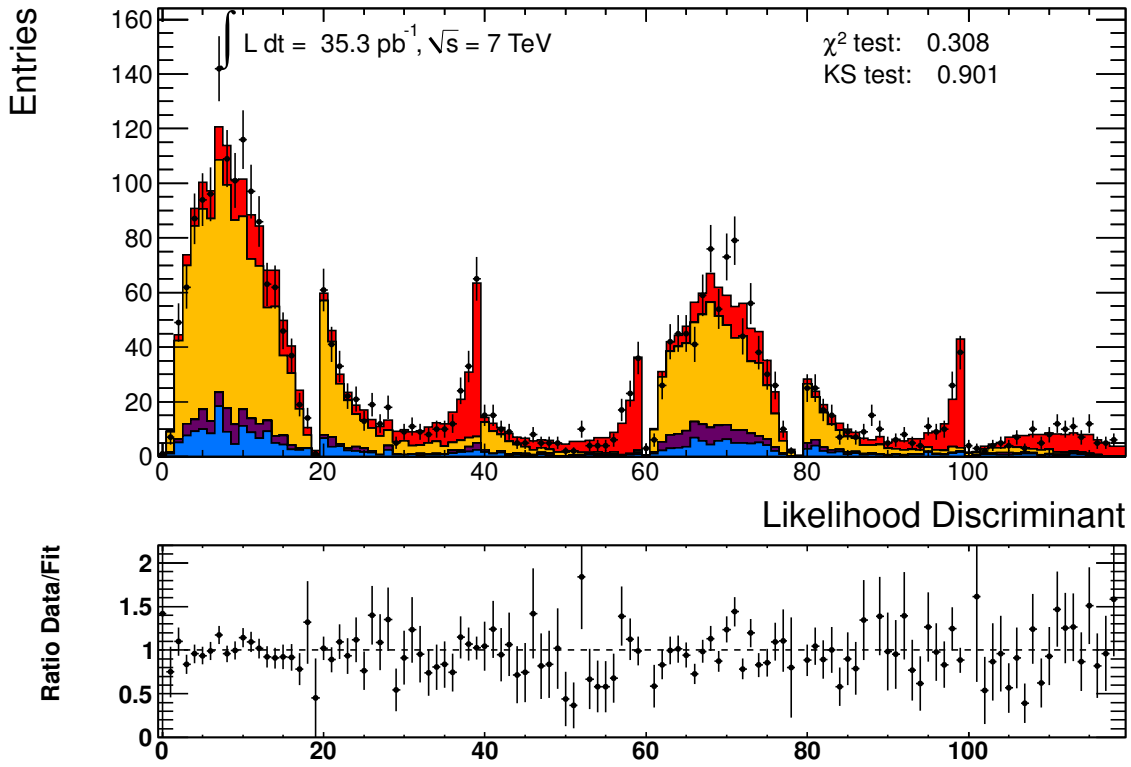

Figure 7.4: The fitted result compared with the data, showing excellent agreement overall. The left three channels are μ+jets, the right three are e+jets. Both count 3-jet exclusive, 4-jet exclusive, and 5-jet inclusive. Each of the six channels has 20 bins in the fit.

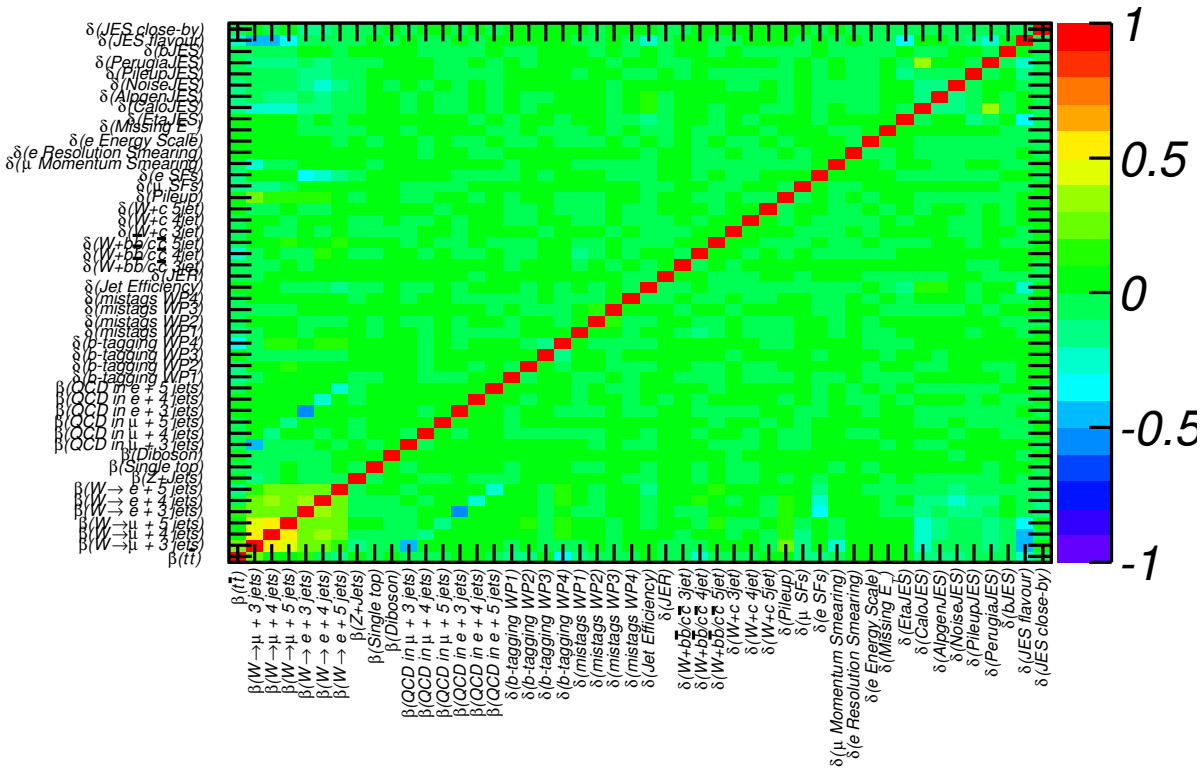

Figure 7.5: The correlation amongst all parameters in the fit, obtained from the fit to data. Correlations are as expected.

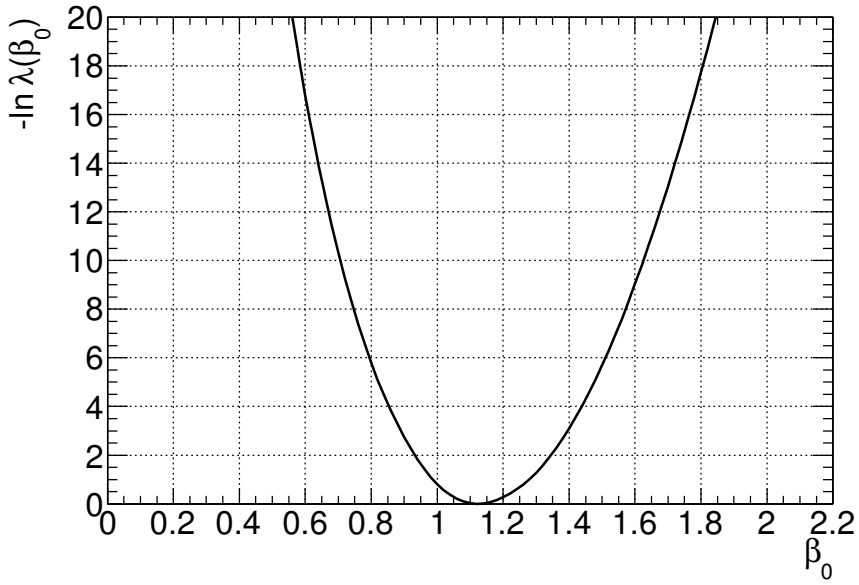

Figure 7.6: The profile likelihood as a function of $\sigma_{t\bar{t}}$ is shown near its minimum. Smooth profiling is observed.

Parameter	Value	Error	Error Up	Error Down
$\beta(t\bar{t})$	1.1236	0.0944	0.1011	-0.0906
$\beta(W$ in μ + 3 jets)	0.8771	0.0873	0.1061	-0.0809
$\beta(W$ in μ + 4 jets)	0.8575	0.1279	0.1527	-0.1178
$\beta(W$ in μ + 5 jets)	0.7588	0.2163	0.2578	-0.1957
$\beta(W$ in e + 3 jets)	0.9124	0.1025	0.1060	-0.0994
$\beta(W$ in e + 4 jets)	0.8479	0.1547	0.1607	-0.1490
$\beta(W$ in e + 5 jets)	0.5844	0.2592	0.2741	-0.2455
β(Z+Jets)	1.1180	0.2796	0.2791	-0.2828
β(Single top)	1.0056	0.1059	0.1059	-0.1059
β(Diboson)	1.0007	0.0600	0.0600	-0.0600
β(QCD in μ + 3 jets)	0.9094	0.4785	0.4803	-0.4801
β(QCD in μ + 4 jets)	1.0096	0.4729	0.4732	-0.4733
β(QCD in μ + 5 jets)	0.6455	0.4722	0.4729	-0.4723
β(QCD in e + 3 jets)	1.0655	0.4881	0.4906	-0.4910
β(QCD in e + 4 jets)	1.0080	0.4966	0.4971	-0.4972
β(QCD in e + 5 jets)	0.8557	0.4909	0.4916	-0.4915
δ(b-tag WP1)	-0.7265	1.0978	1.1107	-0.9672
δ(b-tag WP2)	0.6253	0.9646	0.9566	-0.9658
δ(b-tag WP3)	-0.0318	0.9121	0.9080	-0.9163
δ(b-tag WP4)	0.2144	0.8694	0.8813	-0.8627
δ(mistag WP1)	0.3433	1.0025	0.9824	-1.0130
δ(mistag WP2)	-0.3573	0.9745	0.9741	-0.9727
δ(mistag WP3)	0.3048	0.9900	0.9863	-0.9889
δ(mistag WP4)	0.0155	0.9951	0.9952	-0.9950
δ(JES)	0.9877	0.5286	0.5418	-0.5090
δ(JER)	0.5819	0.9077	0.9060	-0.9213
δ(W+bb/cc Fraction 3 jets)	-0.5879	0.9566	0.9557	-0.9602
δ(W+bb/cc Fraction 4 jets)	0.1945	0.8674	0.8772	-0.8620
δ(W+bb/cc Fraction 5 jets)	-0.3314	0.9168	0.9423	-0.8981
δ(W+c Fraction 3 jets)	0.4251	0.9473	0.9467	-0.9480
δ(W+c Fraction 4 jets)	0.0570	0.9766	0.9764	-0.9768
δ(W+c Fraction 5 jets)	-0.1269	0.9974	0.9974	-0.9974
δ(Pileup)	0.2372	0.7695	0.7623	-0.7758
$\delta(\mu$ SFs)	-0.0480	0.9875	0.9875	-0.9870
δ(e SFs)	0.0570	0.9400	0.9413	-0.9371
$\delta(\mu$ Momentum Smearing)	-0.1645	1.3664	1.1531	-1.3183
δ(e Energy Resolution)	0.1638	0.7652	0.7534	-0.7627
δ(e Energy Smearing)	0.2623	0.7817	0.7526	-0.7935
δ(Missing Et)	-0.3195	0.6002	0.6361	-0.5551
δ(JES Eta)	1.0882	0.4783	0.4909	-0.5229
δ(JES Calo)	-0.6341	0.4880	0.5793	-0.4338
δ(JES Alpgen)	-0.6025	0.5713	0.7319	-0.4873
δ(JES Noise)	-0.2967	0.7438	0.8626	-0.6115
δ(JES Pileup)	0.0959	0.6814	0.6229	-0.6804
δ(JES Perugia)	-0.0567	0.3534	0.2697	-0.9915
δ(JES b-Jet)	-0.3575	0.7138	0.7607	-0.6514

Table 7.3: The full results of the fit for $\vec{\beta}$ and $\vec{\delta}$ including their uncertainties. The asymmetric error is observed at the fit minimum and the symmetric errors are from the hessian error matrix.

Statistical Uncertainty (%)	**+5.8**	**-5.7**
Simulation (%)		
b-tagging calibration	+4.1	-3.8
Jet energy scale	+3.9	-2.9
Jet reconstruction efficiency	+0.01	-0.3
Jet energy resolution	+0.3	-0.01
Electron scale factor	+1.6	-1.4
Muon scale factor	+1.2	-1.1
Electron smearing	+0.0	-0.0
Muon smearing	+0.4	-0.4
Electron energy scale	+0.5	-0.3
$E_{\mathrm{T}}^{\mathrm{miss}}$(softjet + cellout)	+0.01	-0.01
$E_{\mathrm{T}}^{\mathrm{miss}}$(pileup)	+0.01	-0.01
Background Modeling (%)		
W+jets HF content	+2.7	-2.4
W+jets shape	+1.0	-1.0
QCD shape	+0.8	-0.8
$t\bar{t}$ Signal Modeling (%)		
ISR/FSR	+5.2	-5.2
MC Generator	+4.2	-4.2
Hadronization	+0.4	-0.4
PDF	+1.5	-1.5
Method (%)		
Templates statistics	+1.1	-1.1
Total Systematic (%)	**+9.7**	**-9.0**

Table 7.4: Table of estimated systematic uncertainties. Systematic uncertainties included in the fit are estimated by N-1 testing. The remaining systematic uncertainties are added in quadrature afterwards. Statistical uncertainty is the single largest component but systematic uncertainty dominates overall.

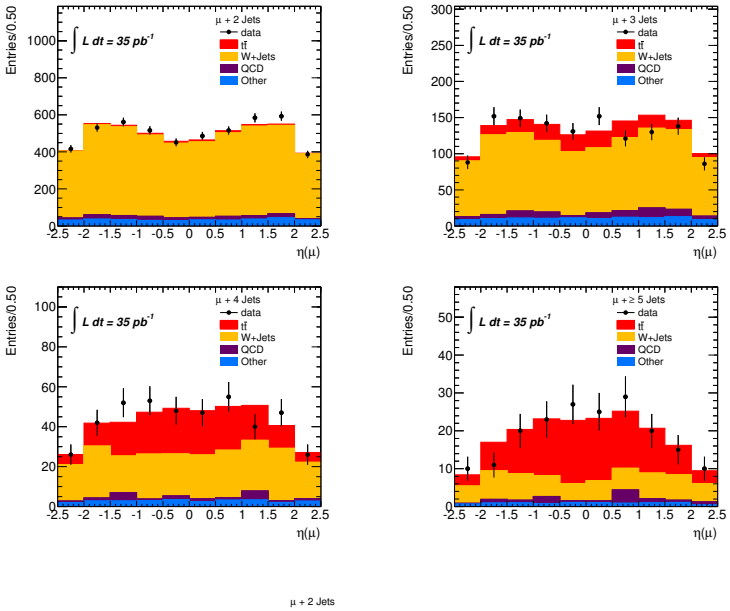

Figure 7.7: The input variable η^{ℓ} for the likelihood discriminant in the μ+jets channel. The 2-jet bin is shown as a control region (top left), and the signal region is shown in the 3-jet bin (top center), 4-jet bin (top right) and 5-jet inclusive bin (lower left).

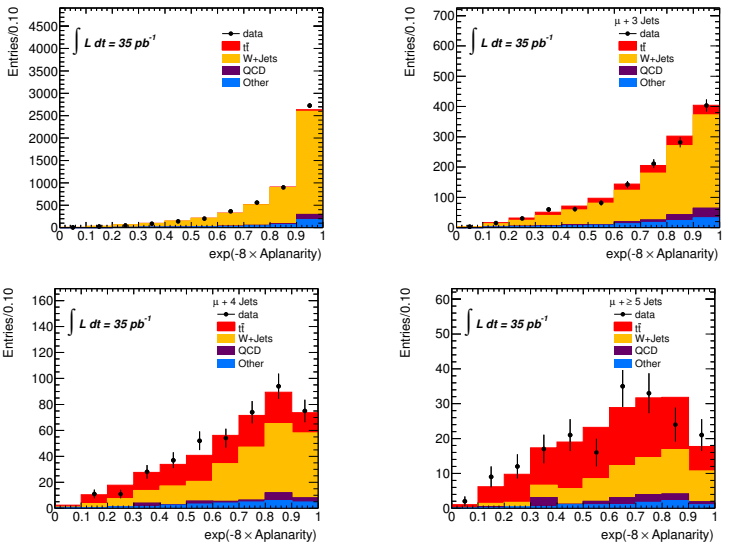

Figure 7.8: The input variable $\exp(-8 \times A)$ for the likelihood discriminant in the μ+jets channel. The 2-jet bin is shown as a control region (top left), and the signal region is shown in the 3-jet bin (top center), 4-jet bin (top right) and 5-jet inclusive bin (lower left).

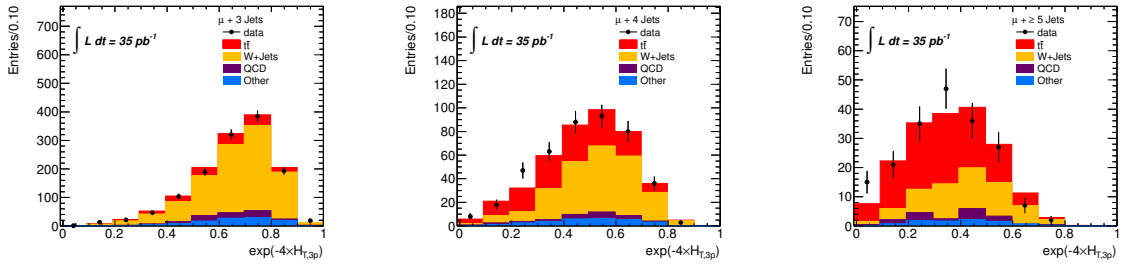

Figure 7.9: The input variable $\exp(-4 \times H_{\mathrm{T,3p}})$ for the likelihood discriminant in the μ+jets channel. By definition the variable can only be constructed in events with 3 or more jets. The signal region is shown in the 3-jet bin (left), 4-jet bin (center) and 5-jet inclusive bin (right).

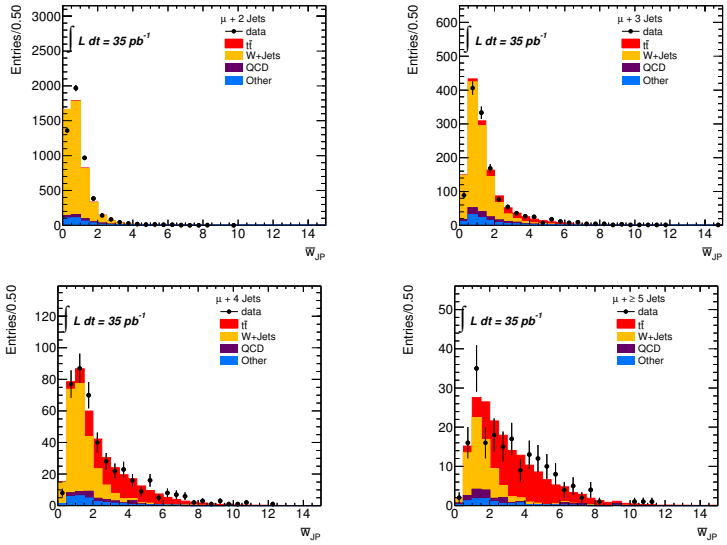

Figure 7.10: The input variable $\overline{w}_{\mathrm{JP}}$ for the likelihood discriminant in the e+jets channel. The 2-jet bin is shown as a control region (top left), and the signal region is shown in the 3-jet bin (top center), 4-jet bin (top right) and 5-jet inclusive bin (lower left).

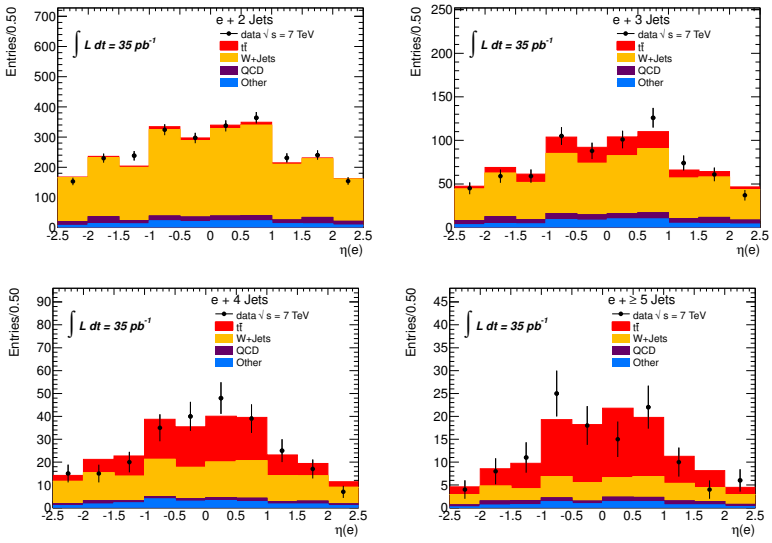

Figure 7.11: The input variable η^{ℓ} for the likelihood discriminant in the e+jets channel. The 2-jet bin is shown as a control region (top left), and the signal region is shown in the 3-jet bin (top center), 4-jet bin (top right) and 5-jet inclusive bin (lower left).

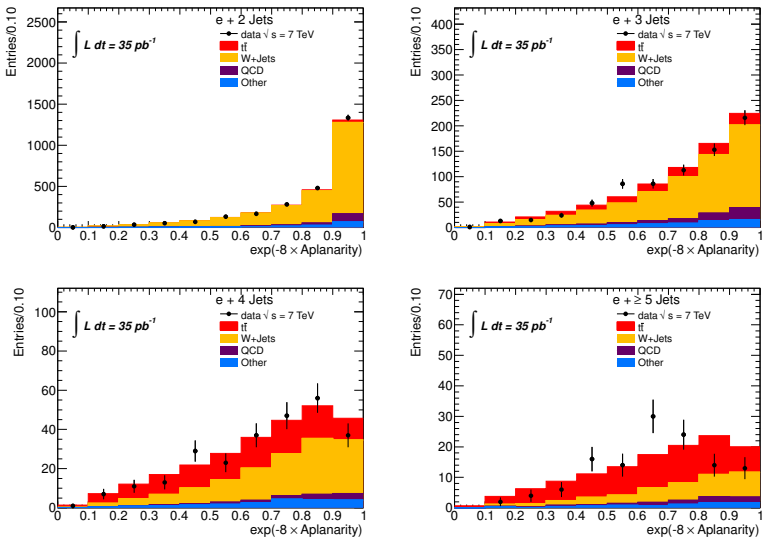

Figure 7.12: The input variable $\exp(-8 \times A)$ for the likelihood discriminant in the e+jets channel. The 2-jet bin is shown as a control region (top left), and the signal region is shown in the 3-jet bin (top center), 4-jet bin (top right) and 5-jet inclusive bin (lower left).

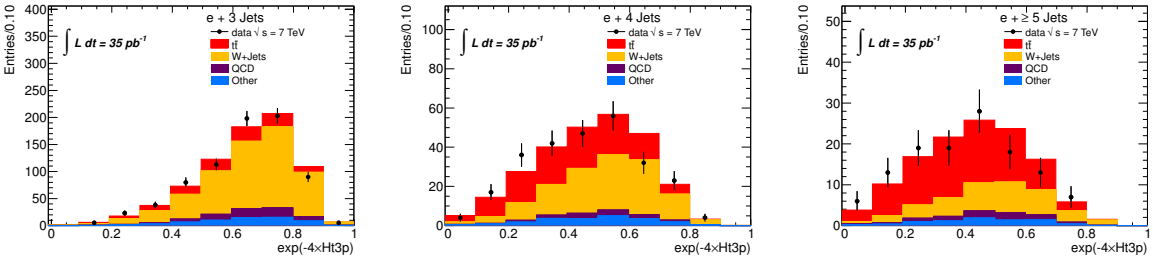

Figure 7.13: The input variable $\exp(-4 \times H_{\mathrm{T,3p}})$ for the likelihood discriminant in the e+jets channel. By definition the variable can only be constructed in events with 3 or more jets. The signal region is shown in the 3-jet bin (left), 4-jet bin (center) and 5-jet inclusive bin (right).

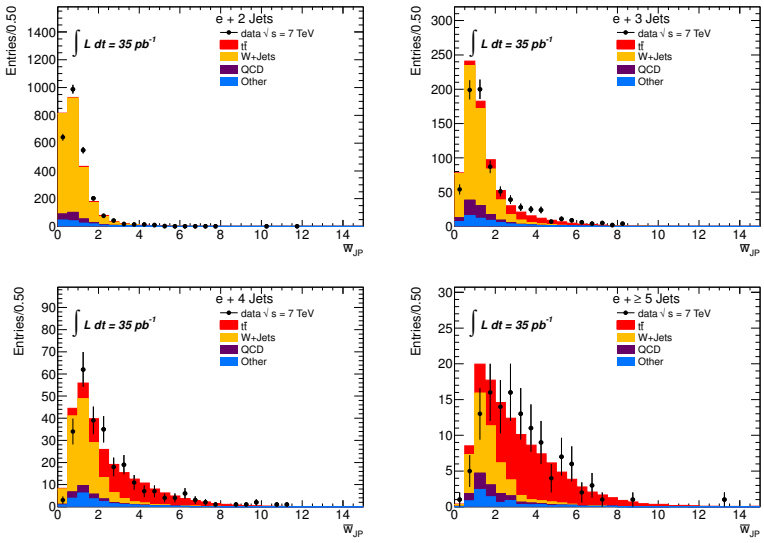

Figure 7.14: The input variable $\overline{w}_{\mathrm{JP}}$ for the likelihood discriminant in the e+jets channel. The 2-jet bin is shown as a control region (top left), and the signal region is shown in the 3-jet bin (top center), 4-jet bin (top right) and 5-jet inclusive bin (lower left).

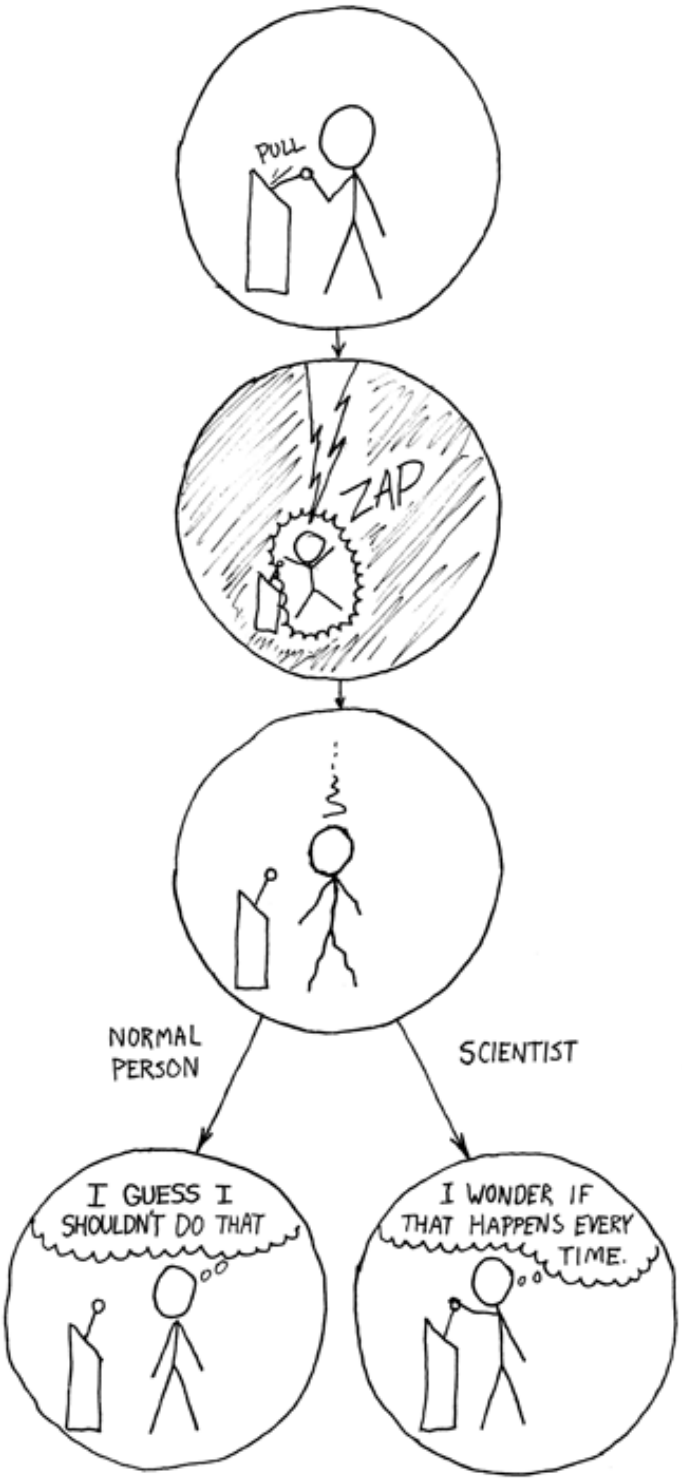

The Difference. "How could you choose avoiding a little pain over understanding a magic lightning machine?"[19]

8 Measurement of $\sigma_{t\bar{t}}$ in $\int \mathcal{L}\,dt = 0.7$ fb^{-1} Without b-tagging

In the first half of 2011 the LHC continued to deliver proton-proton collisions at an ever increasing rate. When the time came to define the datasets to be used for the summer conferences, $\int \mathcal{L}\,dt = 0.7$ fb^{-1} of analyzable data had been recorded, a 20× increase in data compared to the 2010 dataset analyzed in the previous chapter. The analysis described in Chapter 7 served as the basis for a similar analysis with this increased dataset. In principle the number of events scales directly with luminosity, but changing cuts and conditions can reduce the yield in the final selected sample. In the e+jets channel the electron trigger threshold was raised as discussed in Section 4.2, necessitating raising the cut on electron p_{T} from 20 to 25 GeV. Furthermore, a large dead region in the calorimeter caused by a hardware malfunction necessitated certain additional cuts, leading to undesirable asymmetries in the detector and selection. This also led to increased systematic uncertainties, as have been discussed in Section 4.1. On the accelerator side, the higher pileup environment increases certain object systematic uncertainties, JES in particular, as well as increasing the uncertainty on the luminosity determination. The main difference in this analysis, apart from the hugely increased dataset, is that the b-tagging distribution is not used in the discriminant likelihood, but rather the transverse momentum of the leading jet is used instead. This choice makes the analysis highly insensitive to flavor effects, including the assumption that a top quark always decays as $t \to Wb$. The treatment is otherwise very similar but sensitivity to certain uncertainties naturally changes due to the changing of this input variable.

8.1 Selection

In order to be consistent with a $t\bar{t}$ final state, events are selected which have a lepton, multiple jets and large missing energy, summarized in Section 4.3. The modeling of processes expected to contribute to the data selected was discussed in Chapter 5. In this analysis, the W+jets contribution in each jet bin is normalized to a result from the collaboration which exploits the charge asymmetry in W production at the LHC, and the heavy flavor content is normalized to measurements with the same dataset, although this analysis is relatively insensitive to flavor. The QCD multijet contribution is estimated using the matrix method. The predictions and yields are shown in Table 8.1. The uncertainty for QCD is taken from the matrix method, while in other cases the uncertainty shown is purely statistical. The predictions for basic kinematic distributions are compared with this dataset in Appendix D.

8.2 The Input Distribution

The analysis uses TMVA to form a likelihood discriminant optimized to separate signal, $t\bar{t}$ in the lepton+jets channel, from its main background, W+jets. This is the same procedure as is described in Section 7.2. While this analysis is designed to be flavor insensitive, W+jets includes

μ+jets Channel	1 Jet	2 Jet	3 Jet	4 Jet	$\geq$ 5 jet
$t\bar{t}$	319 ± 18	1342 ± 37	2734 ± 52	2714 ± 52	2030 ± 45
W+jets (DD)	383200 ± 600	93440 ± 310	20140 ± 140	4644 ± 68	1082 ± 33
QCD multijet (DD)	25000 ± 12000	11000 ± 6000	3200 ± 1600	900 ± 400	290 ± 150
Single Top	996 ± 32	1148 ± 34	594 ± 24	210 ± 15	84 ± 9
Z+jets	17270 ± 130	5492 ± 74	1510 ± 39	436 ± 21	149 ± 12
Diboson (WW,WZ,ZZ)	1093 ± 33	1009 ± 32	308 ± 18	69 ± 8	18 ± 4
Total Predicted	428000 ± 12000	113000 ± 6000	28400 ± 1600	8900 ± 400	3660 ± 160
Data Observed	433931	111741	28643	8680	3814

e+jets Channel	1 Jet	2 Jet	3 Jet	4 Jet	$\geq$ 5 jet
$t\bar{t}$	225 ± 15	1005 ± 32	1934 ± 44	1835 ± 43	1463 ± 38
W+jets(DD)	161600 ± 400	43170 ± 210	10840 ± 100	2486 ± 50	1032 ± 32
QCD multijet (DD)	11000 ± 5000	4800 ± 2400	1600 ± 800	510 ± 250	177 ± 89
Single Top	571 ± 24	711 ± 27	391 ± 20	156 ± 13	65 ± 8
Z+jets	3732 ± 61	2444 ± 49	996 ± 32	333 ± 18	146 ± 12
Diboson (WW,WZ,ZZ)	599 ± 25	538 ± 23	178 ± 13	45 ± 7	10 ± 3
Total Predicted	177000 ± 5000	52600 ± 2400	15900 ± 800	5360 ± 260	2892 ± 100
Data Observed	179469	51820	15614	5398	2812

Table 8.1: The yields in both lepton channels for MC predictions and observed data for the $\int \mathcal{L}\,dt$ = 0.7 fb^{-1} analysis. Uncertainties are purely statistical except for the QCD multijet prediction, whose uncertainty is taken from the matrix method.

all contributions from the various flavor components available in order to better estimate smaller kinematic differences which can arise when a W is produced along with different flavors of quarks.

The Input Variables

The likelihood discriminator takes four variables as input. Three of the variables are exactly as they have been described in Section 7.2: the transformed Aplanarity A, the transformed normalized transverse momentum of the event $H_{\mathrm{T,3p}}$, and the lepton pseudorapidity η. The fourth variable used in this analysis is the transverse momentum of the leading jet, $P_{\mathrm{T}}^{\mathrm{J1}}$. The variables $H_{\mathrm{T,3p}}$ and $P_{\mathrm{T}}^{\mathrm{J1}}$ are not redundant: the numerator of $H_{\mathrm{T,3p}}$ is a sum over the p_{T} of the third and fourth jets only, i.e. the leading jet in the event does not enter by construction. The leading jet in $t\bar{t}$ is expected to be harder than the leading jet in W+jets on average. This arises due to the distinct production mechanism. The leading jet in $t\bar{t}$ is generally a b-jet from the top decaying as $t \to Wb$. The $P_{\mathrm{T}}^{\mathrm{J1}}$ spectrum in $t\bar{t}$ events peaks at a $\sim 1/2\times m_{\mathrm{top}}$, as can be see in Figures 8.8 and 8.12.

The four variables can be seen in both signal and control regions for μ+jets in Figures 8.7-8.10 and similarly for e+jets in Figures 8.11-8.14, found at the end of this chapter. One can see in these plots a general data-MC agreement. The separation of the discriminant in each of the six physics channels can be seen in Figure 8.1, where the signal and background are each normalized to unity. The shape of the $t\bar{t}$ signal can be seen to be similar in the six channels, due to the relatively constant amount of signal present and similar separation power. The likelihood before fitting can be seen as well in Figure 8.2 with both predictions and data shown. Here, too, one

can see a generally good agreement.

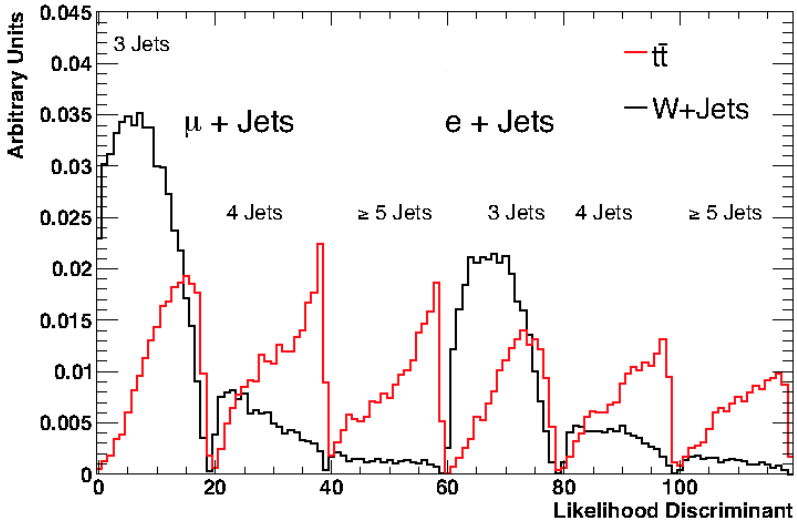

Figure 8.1: The expected separation power of the input likelihood discriminant between the signal, $t\bar{t}$, and background, W+jets. Each of the six physics channels has twenty bins, and for each channel the signal and background are each normalized to the expected yield.

8.3 The Fit Likelihood

The binned profile likelihood template fit to data developed in Chapter 6 and used already in Chapter 7 is employed in this analysis to measure $\sigma_{t\bar{t}}$. The physical processes considered are the same as in the previous chapter. The constraints on the normalization of the various background contributions are summarized in Table 8.2.

All object-related systematic uncertainties – scales, resolutions, and efficiencies – are included in the fit. Many of the modeling systematic uncertainties are excluded from the fit and evaluated externally, in particular the signal generator and parton showering uncertainties, the uncertainty due to PDFs, the modeling uncertainty of the W+jets background, and the QCD shape uncertainty. The initial and final state radiation modeling are included in the fit. This was done after a study showed that the shape changes could be considered continuous, as expected. The linearity of the fit is tested over a wide range of potential $\sigma_{t\bar{t}}$ values, from 120 to 200 pb, and reveals no bias, as shown in Figure 8.3.

8.4 Results of the Fit and Systematic Uncertainties

The likelihood fit to data yields

$$\sigma_{t\bar{t}} = 178.97^{+7.02}_{-6.92}\,\text{pb}, \text{ (fit)}.$$

This is not yet a complete determination of the uncertainty, since external systematics are not yet included. The distributions after fitting are shown in Figure 8.4, showing excellent data-MC agreement. The fit results for parameters other than $\sigma_{t\bar{t}}$ are also of some interest here; the

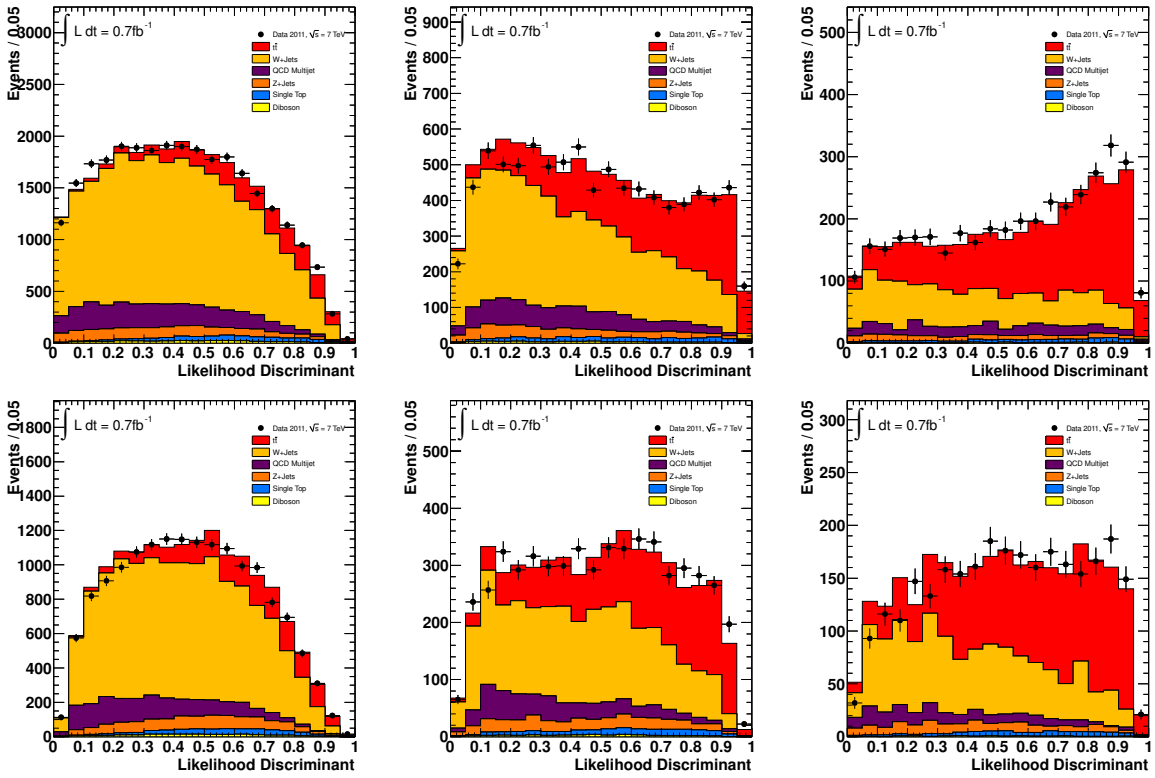

Figure 8.2: The likelihood discriminant for MC and data before the fit. The top row is μ+jets, the bottom row is e+jets. The left hand column is 3-jet exclusive, middle is 4-jet exclusive, and right-most in 5-jet inclusive.

Parameter	**Constraint**
$\beta(t\bar{t})$	none
$\beta(\mathrm{W}\rightarrow l + 3$ jets)	0.42
$\beta(\mathrm{W}\rightarrow l + 4$ jets)	0.48
$\beta(\mathrm{W}\rightarrow l + 5$ or more jets)	0.54
$\beta(Z$+jets)	0.01
β(Single top)	0.107
β(Diboson)	0.06
β(QCD in l + N jets)	0.5

Table 8.2: The input constraints on the various samples. Here, l is either e or μ, and "N jets" is all three jet bins, i.e. 3 exclusive, 4 exclusive, and 5 inclusive.

complete fit results are shown in Table 8.3. The β values returned by the fit for the various W+jets processes are entirely consistent with the values used to normalize the samples. The normalization of the QCD processes returned by the fit vary widely, which is not surprising given the difficulty of determining the normalization. The results are consistent with the input uncertainty. The profile likelihood is perfectly smooth near its minimum for the parameter of interest, shown in Figure 8.5.

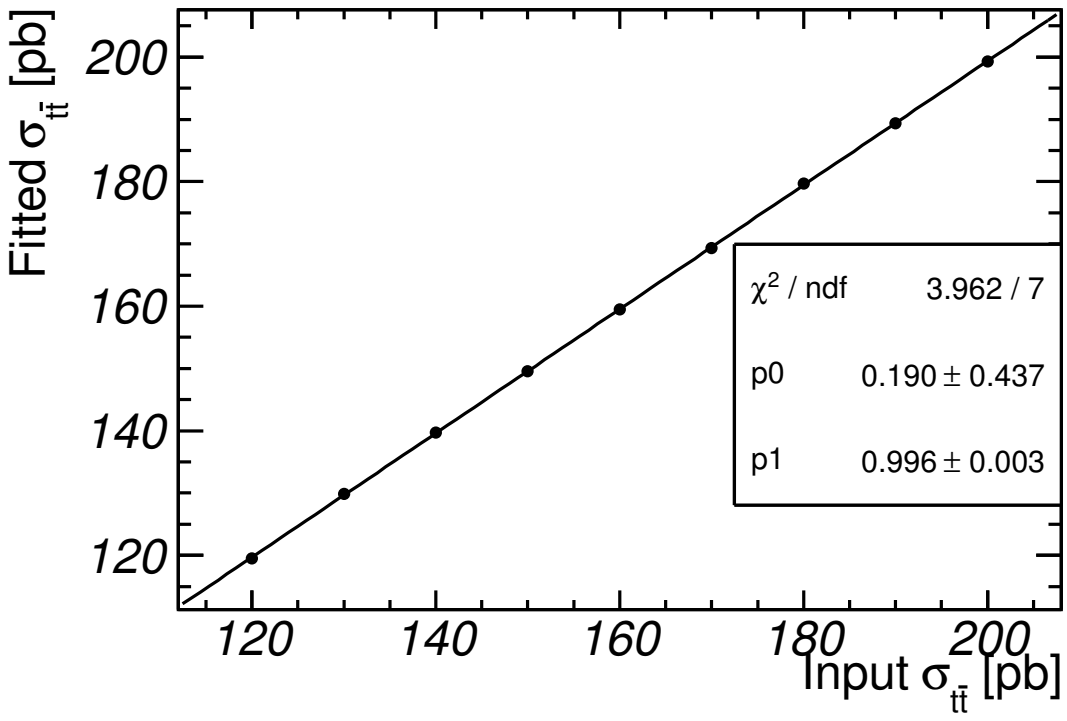

Figure 8.3: The linearity of the fit is tested over the range of input $\sigma_{t\bar{t}}$ values [120,200] pb in steps of 10 pb. No significant bias is observed.

In many cases the fit is able to constrain the uncertainty from a given systematic source, for instance ISR/FSR are constrained to $\sim 20\,\%$ of their original size. Every value returned is consistent with the envelope given by the combined performance groups, $\delta = 0 \pm 1$. In some cases, the result is not consistent with the nominal value in the MC. As an example, the value for Perugia JES at the likelihood's minimum is -0.86 ± 0.17: the fit prefers something much closer to the down-shifted systematic uncertainty than the nominal. This does not constitute a measurement of the uncertainty but rather a constraint from a global fit in a portion of phase space. Nonetheless, experience has shown that the fit points us in the right direction when the value for a δ at the likelihood's minimum is far from its nominal[1].

The correlation of all of the parameters of interest in the fit can be seen in Figure 8.6. The observed correlations are generally as expected. The W+jets parameters are correlated to one another within a given lepton channel, and the QCD parameter for a given physics channel is anti-correlated to the W+jets component in that same channel. Various correlations exist amongst the various JES parameters, which is not surprising given that the same objects are

[1] The best example comes from a moment when we were testing the fitter for the analysis in the previous chapter. The fit preferred a value for JER of almost exactly $\delta = -1$, thought by us to be interesting but of no particular importance at the time. Within a few days, it was shown that the resolution of jets in MC does not agree with that in data, and it was officially recommended that the jet p_{T} should be smeared in the MC, and new smaller uncertainties were provided.

affected in similar ways. Furthermore, it was recently found that the flavor and close-by jet components of JES were over counted, effectively being a part of many of the JES terms, causing each of the terms to be artificially correlated. The lepton scale factors are anti-correlated to many of the βs because they directly affect the event count rates, very similarly across all samples.

The results of the breakdown and the external systematic uncertainties can be seen in Table 8.4. The statistical uncertainty is about 2.2 %, and the uncertainty due to limited template statistics is smaller but a similar value, 1.8 %. The analysis is clearly dominated by systematic uncertainty, and of those, luminosity is the largest component (3.7 %) followed by the generator uncertainty(3 %). Several object uncertainties contribute at about a 2 % level, namely JES and MSF uncertainties.

The final result with its total uncertainty is

$$\sigma_{t\bar{t}} = 179 \pm 3.9\,(\mathrm{stat.}) \pm 9.0\,(\mathrm{syst.}) \pm 6.6\,(\mathrm{lumi.})\,\mathrm{pb} = 179 \pm 11.8\,\mathrm{pb}.$$

This result corresponds to a precision of 6.6 %, making it more precise than the best available theoretical predictions and comparable to the most precise results from the Tevatron [13, 71, 72]. This result marks a milestone, ushering in an era of precision in top physics and the LHC.

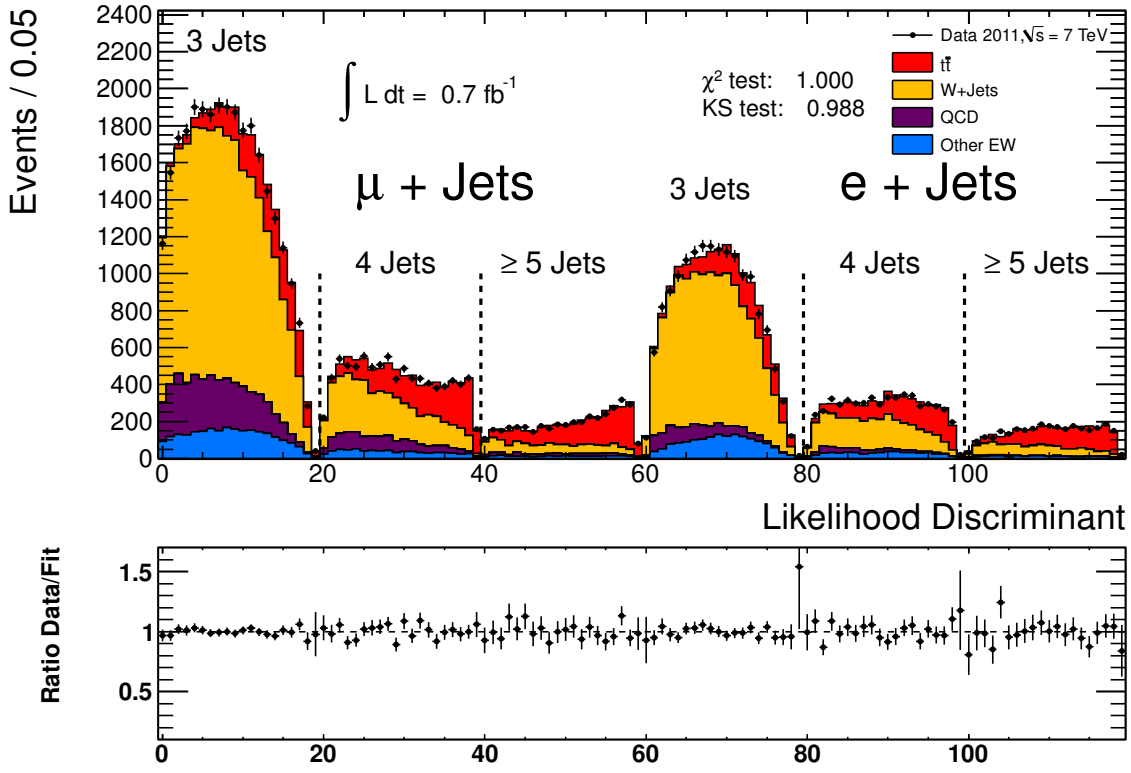

Figure 8.4: The output of the profile likelihood fit, showing excellent data-MC agreement. Each of the six physics channels has 20 bins. The left three channels are μ+jets and the right three are e+jets, in both cases the plots are first 3-jet exclusive, then 4-jet exclusive, and finally 5-jet inclusive. Error bars are statistical only.

Parameter	Value	Error	Error Up	Error Down
$\beta(t\bar{t})$	1.0875	0.0432	0.0427	−0.0421
$\beta(W$ in $\mu + 3$ jets)	0.9738	0.0687	0.0710	−0.0684
$\beta(W$ in $\mu + 4$ jets)	0.8649	0.1026	0.1083	−0.1061
$\beta(W$ in $\mu + 5$ jets)	0.9114	0.1557	0.1589	−0.1510
$\beta(W$ in $e + 3$ jets)	1.0510	0.0555	0.0597	−0.0588
$\beta(W$ in $e + 4$ jets)	1.0376	0.0987	0.1057	−0.1025
$\beta(W$ in $e + 5$ jets)	0.8296	0.1206	0.1267	−0.1257
$\beta(Z$+jets)	0.9572	0.2604	0.2745	−0.2728
β(Single top)	1.0052	0.1066	0.1069	−0.1065
β(Diboson)	1.0037	0.0620	0.0620	−0.0620
β(QCD in $\mu + 3$ jets)	1.2376	0.2928	0.3307	−0.3426
β(QCD in $\mu + 4$ jets)	1.2720	0.3730	0.4234	−0.4152
β(QCD in $\mu + 5$ jets)	0.8291	0.3861	0.4044	−0.4095
β(QCD in $e + 3$ jets)	0.6113	0.2157	0.2286	−0.2339
β(QCD in $e + 4$ jets)	0.6152	0.3195	0.3406	−0.3462
β(QCD in $e + 5$ jets)	0.4164	0.3984	0.4221	−0.4170
δ(AlpgenJES)	0.4155	0.4143	0.2725	−0.4030
δ(bJES)	0.0964	0.6818	0.5956	−0.6241
δ(CaloJES)	0.0051	0.4264	0.3410	−0.3654
δ(NoiseJES)	−0.3515	0.3979	0.5469	−0.3047
δ(PerugiaJES)	−0.8653	0.1734	0.1824	−0.1397
δ(EtaJES)	−0.1943	0.2129	0.2166	−0.1978
δ(PileupJES low p_{T}/central)	0.5219	0.1669	0.1539	−0.1633
δ(PileupJES low p_{T}/forward)	0.4685	0.2566	0.2361	−0.2791
δ(PileupJES high p_{T}/central)	0.6366	0.4684	0.3133	−0.4291
δ(PileupJES high p_{T}/forward)	0.0430	0.9105	0.6602	−0.6345
δ(Jet Efficiency)	0.1998	0.1357	0.1345	−0.1344
δ(JER)	0.1752	0.9544	0.9510	−0.9565
δ(FSR)	0.0661	0.2086	0.1897	−0.2239
δ(ISR)	0.3392	0.1978	0.1801	−0.2263
$\delta(\mu$ SFs)	0.0923	0.8187	0.7793	−0.7362
$\delta(\mu$ Momentum Smearing at MS)	−0.1197	0.8364	0.7873	−0.8234
$\delta(\mu$ Momentum Smearing at ID)	−0.2356	0.9337	0.9757	−0.8533
$\delta(\mu$ Energy Scale)	0.0437	1.0838	1.0485	−0.9946
δ(e SFs)	−0.2300	0.9290	0.9152	−0.8999
δ(e Resolution Smearing)	0.3176	0.7668	0.6538	−0.7566
δ(e Energy Scale)	−0.7455	0.5967	0.7997	−0.5331
$\delta(E_{\mathrm{T}}^{\mathrm{miss}}$LAr)	0.0605	0.5062	0.5167	−0.5230
$\delta(E_{\mathrm{T}}^{\mathrm{miss}}$cellout+softjet)	0.4466	0.4641	0.3333	−0.6785

Table 8.3: The full results of the fit for $\vec{\beta}$ and $\vec{\delta}$ including their uncertainties. The asymmetric errors are from the minimum of the fit, while the symmetric errors are from the hessian error matrix.

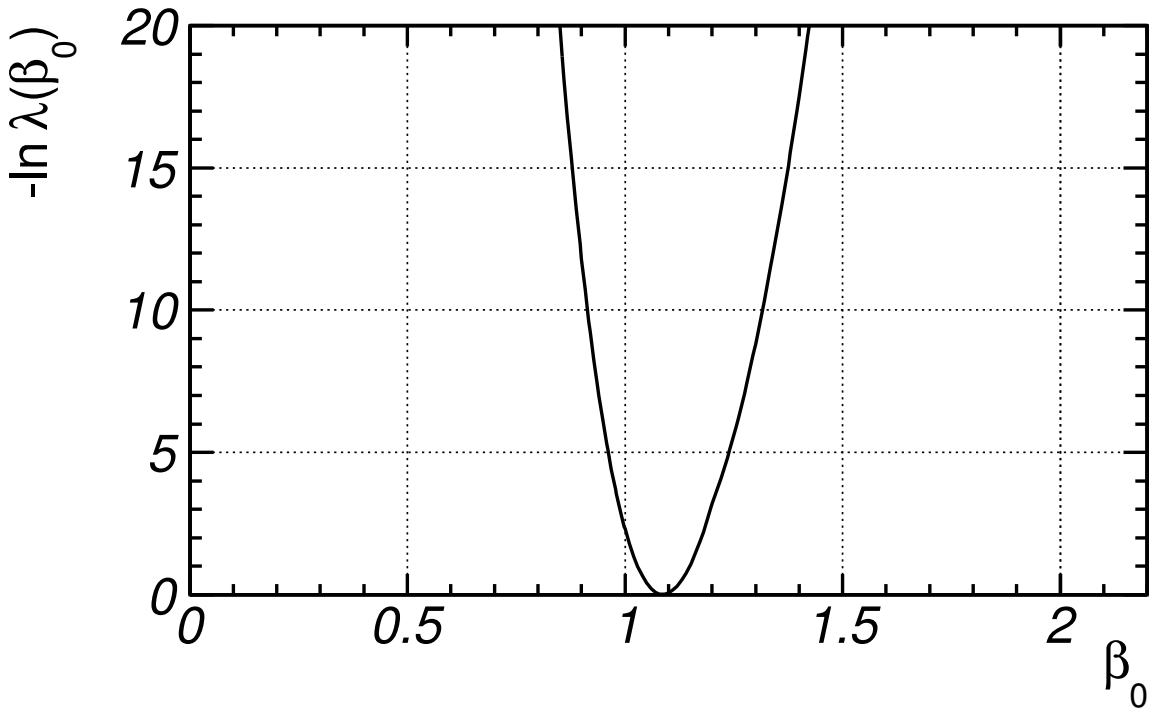

Figure 8.5: The negative log likelihood of λ as a function of β_0, that is, $\sigma_{t\bar{t}}$ is shown near its minimum. The profiling is shown to be smooth, the sign of a healthy likelihood.

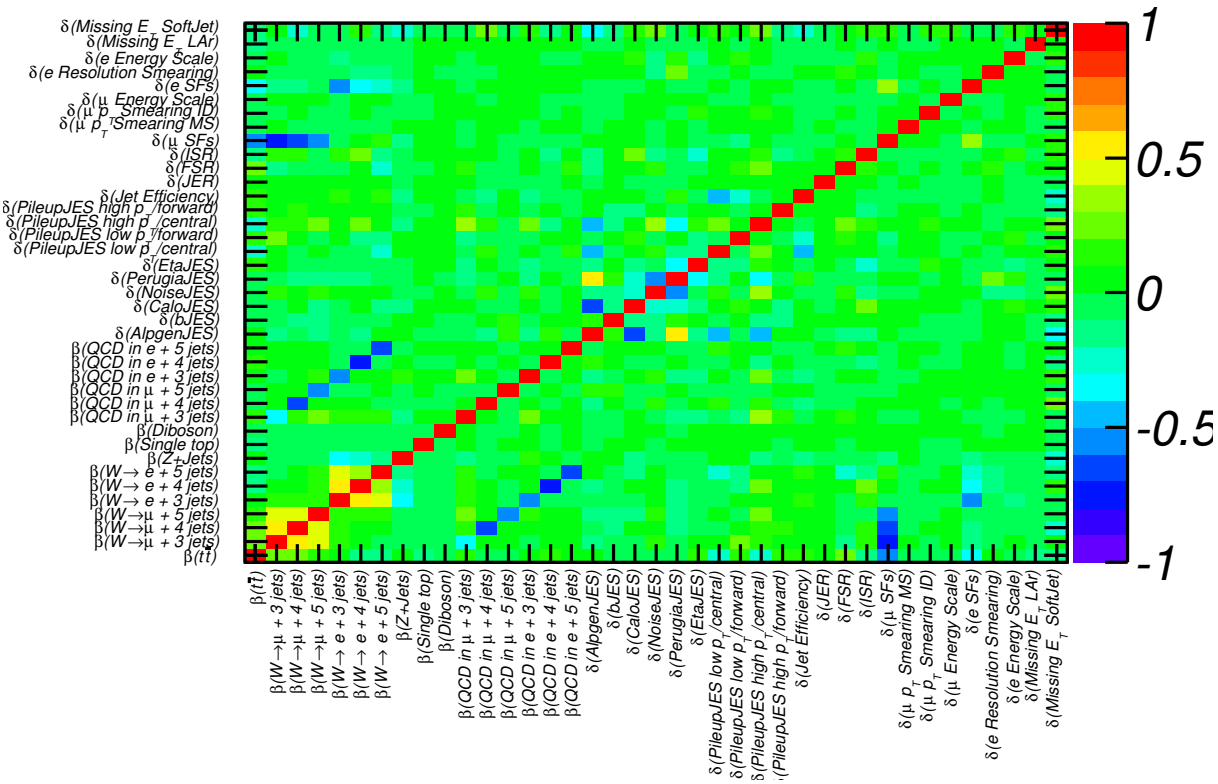

Figure 8.6: The observed correlation of parameters in the fit. Correlations are generally as expected.

Uncertainty	up (pb)	down (pb)	up (%)	down (%)
Fit	7.0	6.9	3.9	3.8
Breakdown				
Statistical	3.9	−3.9	2.2	−2.2
Jets	3.2	−4.3	1.8	−2.4
Muon	4.1	−4.1	2.3	−2.3
Electron	2.7	−3.0	1.5	−1.7
$E_{\mathrm{T}}^{\mathrm{miss}}$	2.0	−1.6	1.1	−0.9
ISR/FSR	3.0	−2.3	1.7	−1.3
External				
Generator	5.4	−5.4	3.0	−3.0
Hadronization	0.9	−0.9	0.5	−0.5
PDF	1.8	−1.8	1.0	−1.0
QCD shape	0.7	−0.7	0.4	−0.4
W shape	0.9	−0.9	0.5	−0.5
Template statistics	3.2	−3.2	1.8	−1.8
Systematic	9.0	−9.0	5.0	−5.0
Stat. + syst.	9.8	−9.8	5.4	−5.4
Luminosity	6.6	−6.6	3.7	−3.7
Total	11.8	−11.8	6.6	−6.6

Table 8.4: Estimated uncertainties affecting the $\sigma_{t\bar{t}}$ measurement. A complete list of sytematic uncertainties considered can be found in Appendix A

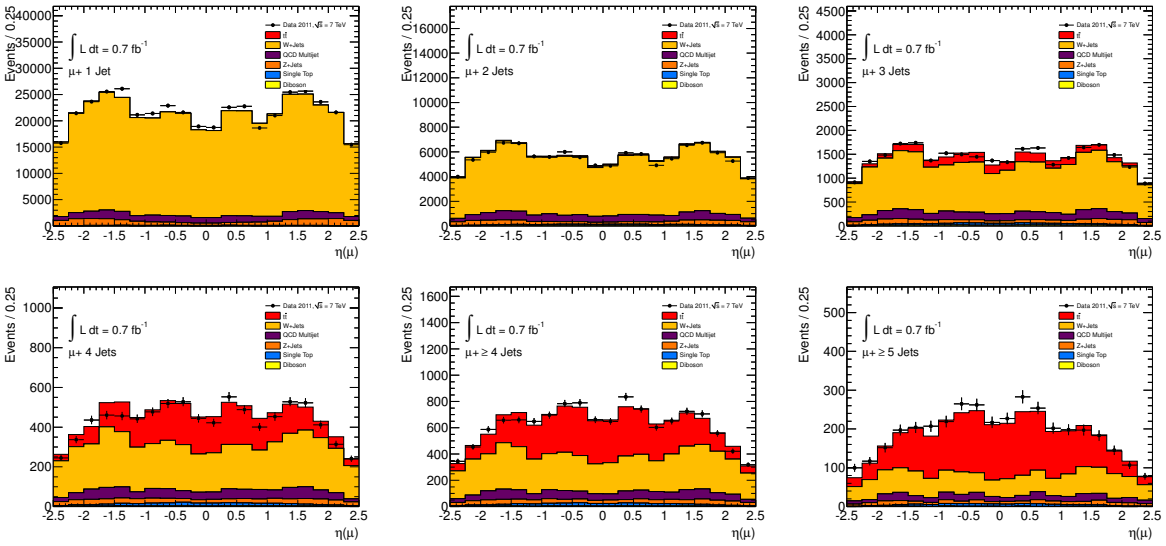

Figure 8.7: The input variable η^{ℓ} for the likelihood discriminant in the μ+jets channel. The 1 and 2-jet bins are shown as a control region (top left, top center), and the signal region is shown in the 3-jet bin (top right), 4-jet bin (bottom left), and 5-jet inclusive bin (bottom right). The 4-jet inclusive bin is shown as well (bottom center).

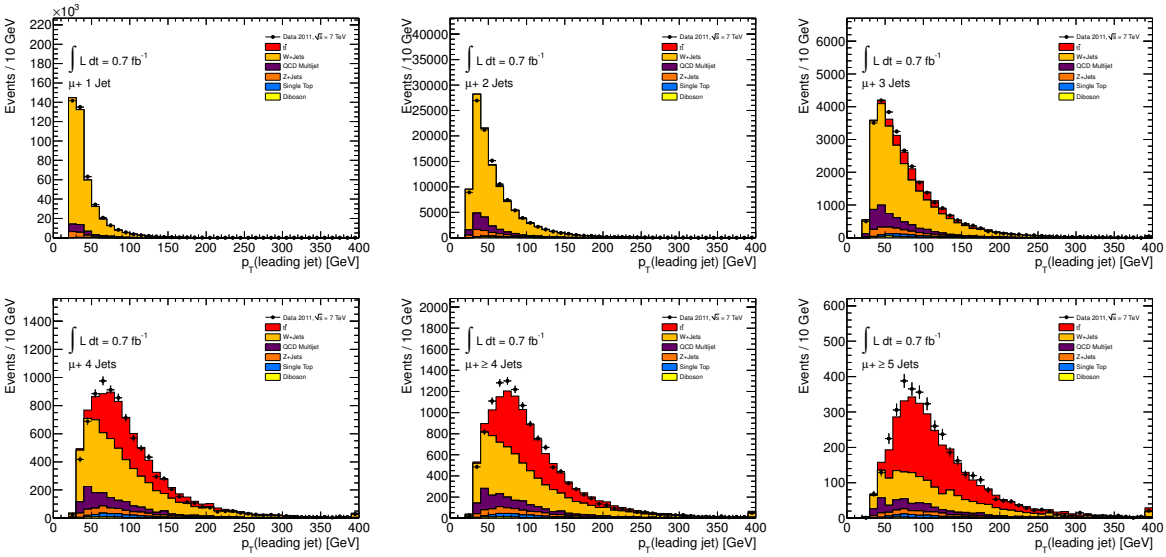

Figure 8.8: The transverse momentum of the leading jet, $P_{\mathrm{T}}^{\mathrm{J1}}$, in the μ+jets channel. The 1 and 2-jet bins are shown as a control region (top left, top center), and the signal region is shown in the 3-jet bin (top right), 4-jet bin (bottom left), and 5-jet inclusive bin (bottom right). The 4-jet inclusive bin is shown as well (bottom center).

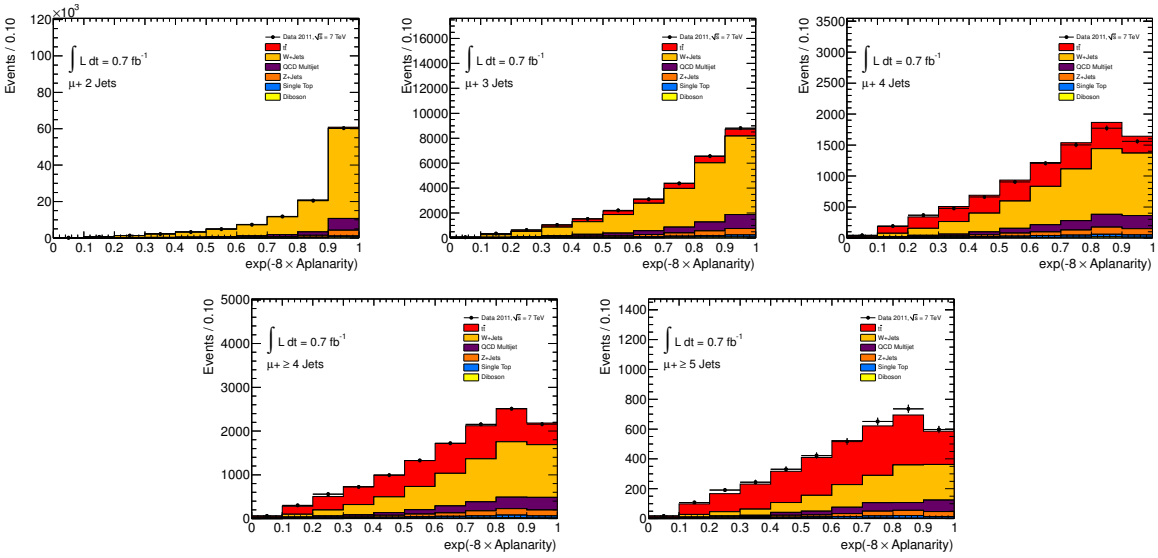

Figure 8.9: The transformed Aplanarity of the event, A, in the μ+jets channel. The 2-jet bin is shown as a control region (top left), and the signal region is shown in the 3-jet bin (top center), 4-jet bin (top right), and 5-jet inclusive bin (bottom right). The 4-jet inclusive bin is shown as well (bottom left).

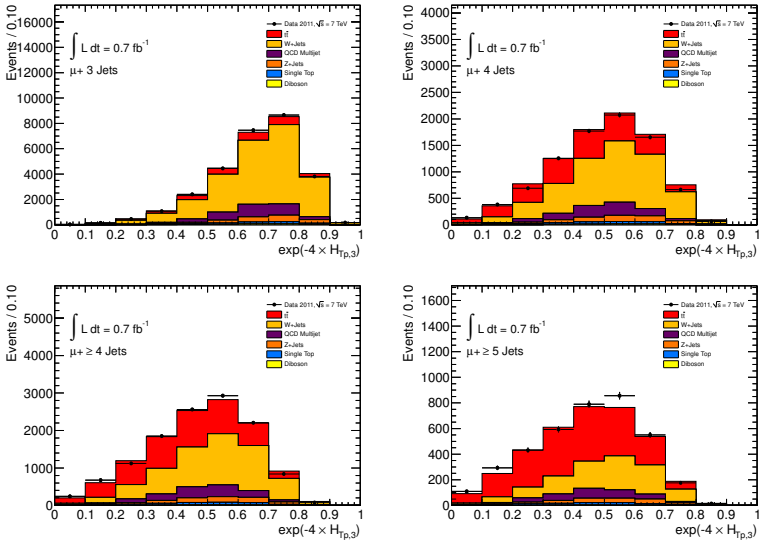

Figure 8.10: The transformed normalized momentum of the event, $H_{\mathrm{T,3p}}$, in the μ+jets channel. The signal region is shown in the 3-jet bin (top left), 4-jet bin (top right), and 5-jet inclusive bin (bottom right). The 4-jet inclusive bin is shown as well (bottom left). The variable is not defined for lower jet multiplicity bins.

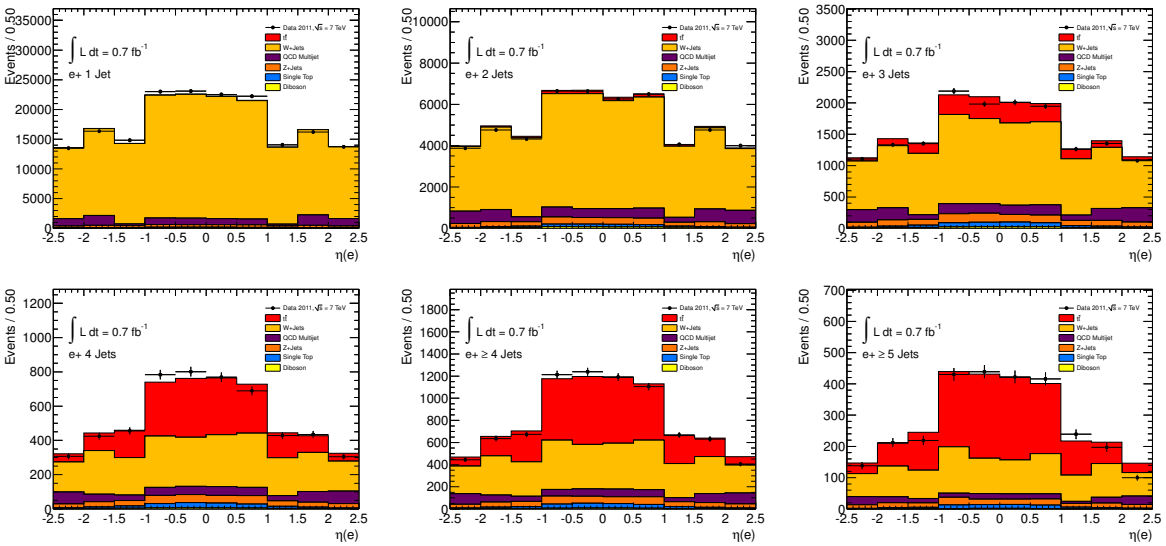

Figure 8.11: The input variable η^{ℓ} for the likelihood discriminant in the e+jets channel. The 1 and 2-jet bins are shown as a control region (top left, top center), and the signal region is shown in the 3-jet bin (top right), 4-jet bin (bottom left), and 5-jet inclusive bin (bottom right). The 4-jet inclusive bin is shown as well (bottom center).

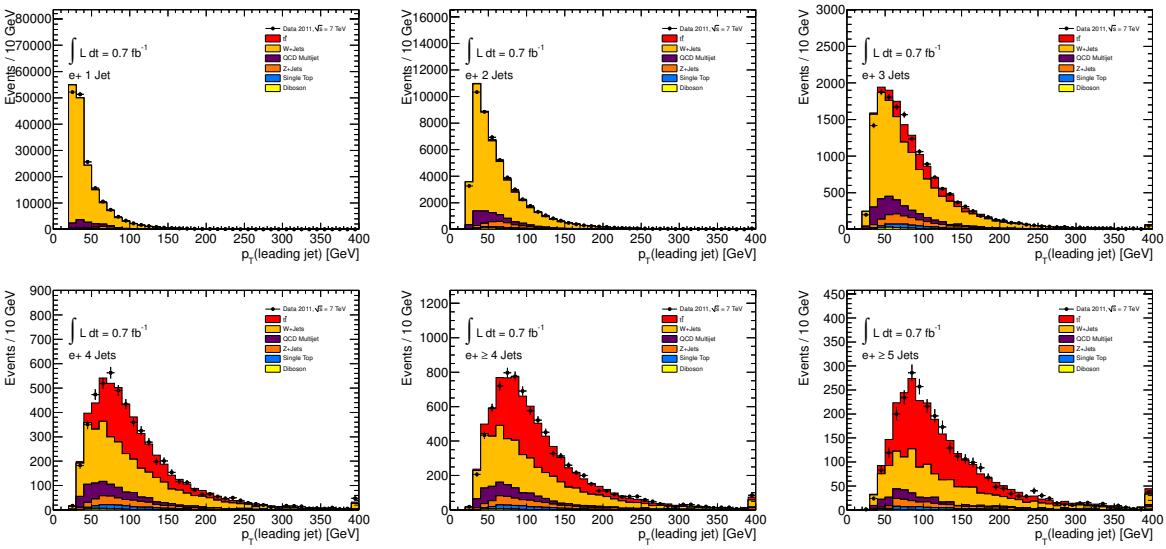

Figure 8.12: The transverse momentum of the leading jet, $P_{\mathrm{T}}^{\mathrm{J1}}$, in the e+jets channel. The 1 and 2-jet bins are shown as a control region (top left, top center), and the signal region is shown in the 3-jet bin (top right), 4-jet bin (bottom left), and 5-jet inclusive bin (bottom right). The 4-jet inclusive bin is shown as well (bottom center).

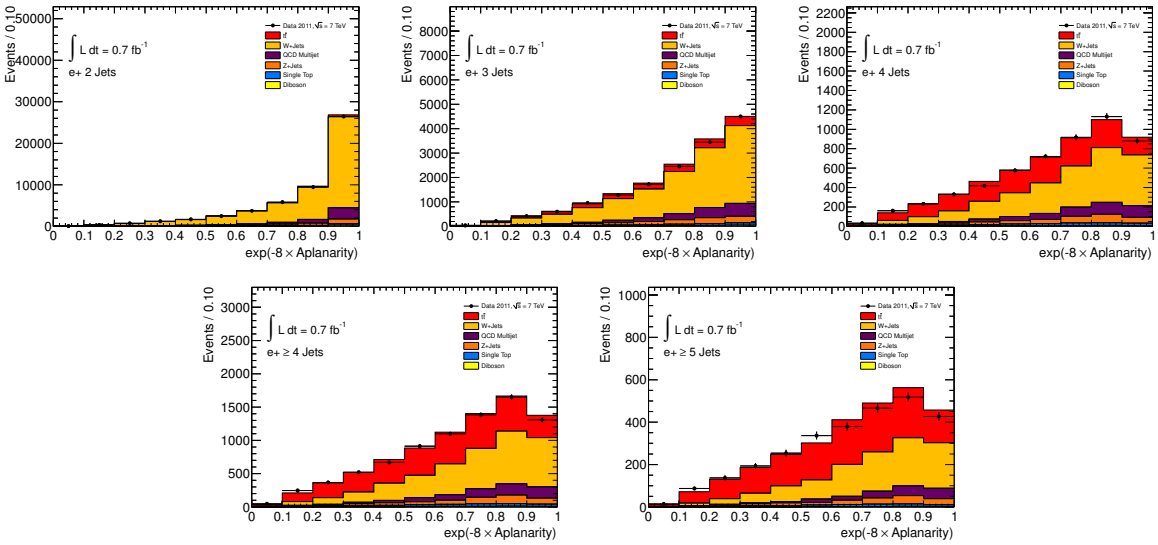

Figure 8.13: The transformed Aplanarity of the event, A, in the e+jets channel. The 2-jet bin is shown as a control region (top left), and the signal region is shown in the 3-jet bin (top center), 4-jet bin (top right), and 5-jet inclusive bin (bottom right). The 4-jet inclusive bin is shown as well (bottom left).

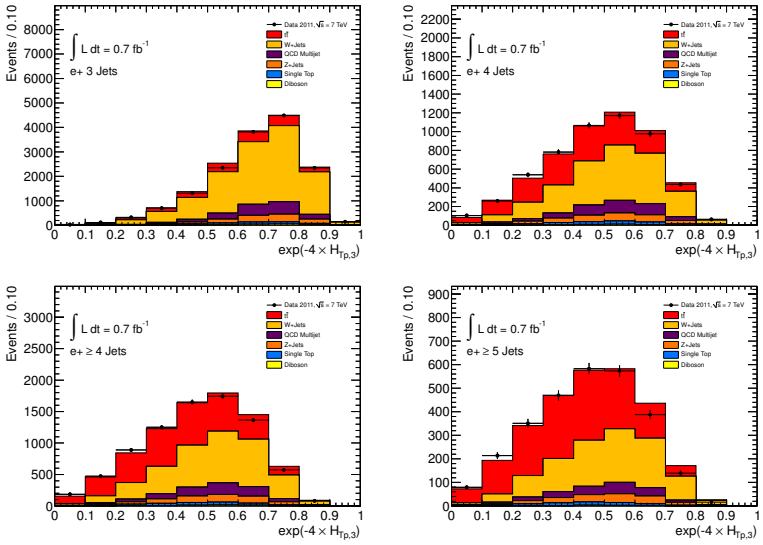

Figure 8.14: The transformed normalized momentum of the event, $H_{\mathrm{T,3p}}$, in the e+jets channel. The signal region is shown in the 3-jet bin (top left), 4-jet bin (top right), and 5-jet inclusive bin (bottom right). The 4-jet inclusive bin is shown as well (bottom left). The variable is not defined for lower jet multiplicity bins.

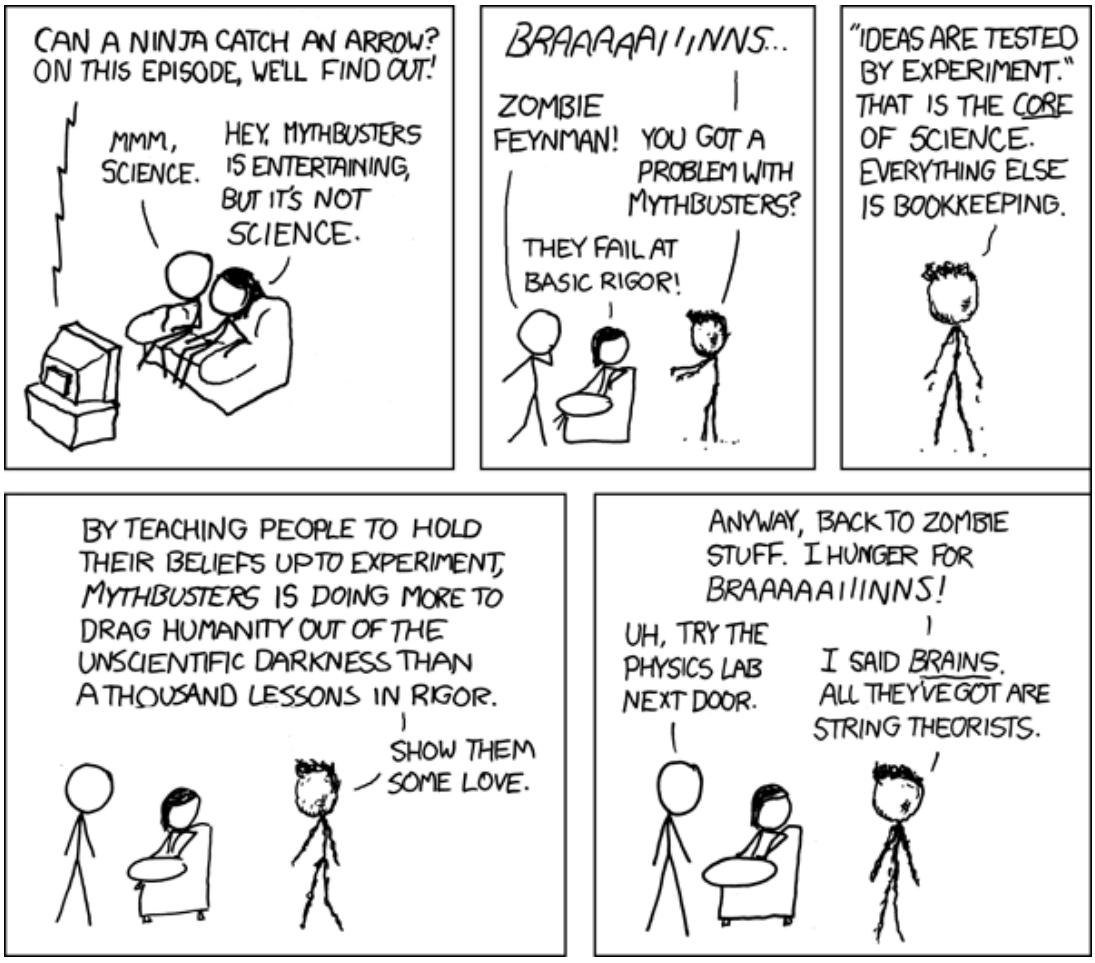

Unscientific. "Last week, we busted the myth that electroweak gauge symmetry is broken by the Higgs mechanism. We'll also examine the existence of God and whether true love exists."[19]

9 Simultaneous Measurement of $\sigma_{t\bar{t}}$, $f_{\mathrm{W_{HF}}}$, and f_{Wc} in $\int \mathcal{L}\,dt = 0.7$ fb^{-1}

With the formalism developed in Chapter 6 and experience gained throughout the course of the analyses presented in Chapters 7 and 8, it is possible to turn to a related analysis in which otherwise irreducible background contributions to the data are themselves turned into parameters of interest in the fit, allowing for a measurement of multiple parameters simultaneously. In particular, a single flavor-sensitive distribution is used to measure the top pair production cross section as well as the ratio of events in which a W boson is produced in association with a pair of heavy quarks ($b\bar{b}$ or $c\bar{c}$) to the events in which a W boson is produced with other jets, $f_{\mathrm{W_{HF}}}$, and similarly the ratio f_{Wc} for a W boson in association with a c or $\bar{c}$. These ratios have been defined in Section 2.3 such that

$$f_{\mathrm{W_{HF}}} \cdot \left(\frac{\sigma(W{+}Q\bar{Q})_{\mathrm{incl.}}}{\sigma(W{+}2\ \mathrm{jets})_{\mathrm{incl.}} - \sigma(W{+}Q\bar{Q})_{\mathrm{incl.}}} \right)_{\mathrm{MC}} = \left(\frac{\sigma(W{+}Q\bar{Q})_{\mathrm{incl.}}}{\sigma(W{+}2\ \mathrm{jets})_{\mathrm{incl.}} - \sigma(W{+}Q\bar{Q})_{\mathrm{incl.}}} \right)_{\mathrm{Measured}},$$

$$f_{\mathrm{Wc}} \cdot \left(\frac{\sigma(W{+}c/\bar{c}{+}\mathrm{jet})_{\mathrm{incl.}}}{\sigma(W{+}2\ \mathrm{jets})_{\mathrm{incl.}} - \sigma(W{+}c/\bar{c}{+}\mathrm{jet})_{\mathrm{incl.}}} \right)_{\mathrm{MC}} = \left(\frac{\sigma(W{+}c/\bar{c}{+}\mathrm{jet})_{\mathrm{incl.}}}{\sigma(W{+}2\ \mathrm{jets})_{\mathrm{incl.}} - \sigma(W{+}c/\bar{c}{+}\mathrm{jet})_{\mathrm{incl.}}} \right)_{\mathrm{Measured}}.$$

They were measured with respect to the MC scaled to the ATLAS data, the default taken in the analysis in the preceding chapter. Those measurements by the collaboration were $f_{\mathrm{W_{HF}}} = 1.63$ and $f_{\mathrm{Wc}} = 1.11$ with respect to the ALPGEN MC cross sections. A result from this analysis of $f_{\mathrm{W_{HF}}} = f_{\mathrm{Wc}} = 1.0$ would therefore be identical to the ATLAS measurements but not the default in the MC.

The discriminant distribution used is based on the output of a b-tagging algorithm which utilizes a neural network (amongst other techniques) to discriminate amongst b, c, and light jets. The output is used as a continuous distribution, in a similar fashion to the continuous b-tagging variable used in the $\int \mathcal{L}\,dt = 35$ pb^{-1} analysis described in Chapter 7. The dataset and selection used here are identical to those used in Chapter 8, namely the analysis uses $\int \mathcal{L}\,dt = 0.7$ fb^{-1}of data collected in 2011 with the selection of both semi-leptonic decay channels, summarized in Section 4.3.

In this analysis the 2-jet bin is used as well. Although the $t\bar{t}$ contribution is expected to be small compared to the higher jet multiplicity bins, the $W{+}Q\bar{Q}$ cross section is expected to peak there. Similarly, $W + c/\bar{c}$ is expected to be larger there than in higher bins. Including the 2-jet bin therefore increases the precision of the $f_{\mathrm{W_{HF}}}$ and f_{Wc} determinations. The 4 and 5-jet bins are now grouped together as 4-jet inclusive, due to low MC statistics available in the W+jets samples, especially those containing heavy flavor jets.

Comparison of simulation with observation for basic kinematic distributions in the dataset are shown in Appendix D. Additionaly, for the sake of comparison, the discriminant variables used in the previous analysis are also shown in the 2-jet exclusive and 4-jet inclusive jet bins, in Figures 8.7-8.14.

9.1 The Input Distribution

The Combined JetFitter Neural Network [110](“CombNNJetFitter”) b-tagging algorithm output is used as the kinematic distribution for the binned profile likelihood template fit to data. The construction, calibration, and performance of the algorithm has been discussed in Section 4.4.

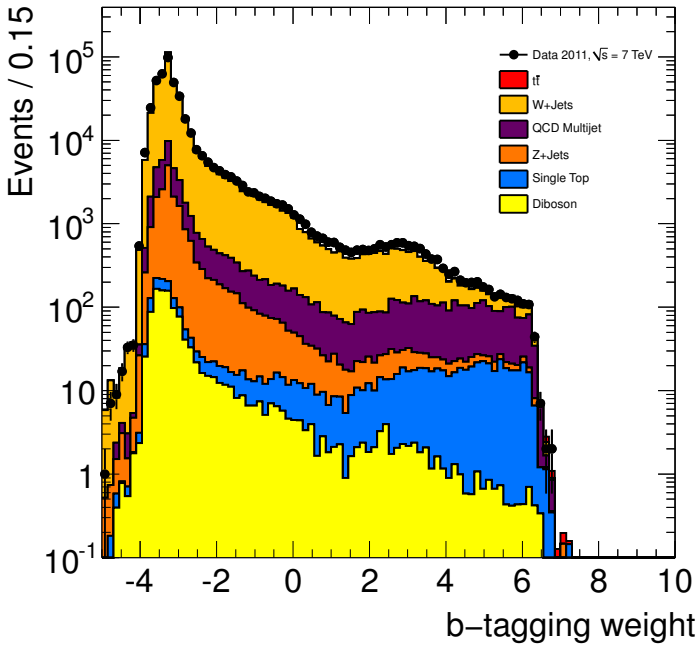

Figure 9.1: The output of the b-tagging algorithm in the μ+1 jet control region. An overly fine binning is used here in order to highlight the features of this distribution, including the non-continuities at high negative values, the bump around a value of 3 corresponding to c-jets, and the steeply falling spectrum above ≈ 6.

The Variable in This Analysis

Based on the assumption that a $t\bar{t}$ event will have 2 b-jets, the discriminant variable is defined as the average b-tagging weight of the two most b-like jets in the event, $\bar{\omega}_{12}$. A b-jet is expected to have a high value from the algorithm; for comparison, 60% of b-jets are expected to have $\omega > 2.0$. By construction, this distribution will be similar for $W + b\bar{b}$ events, differing due to the kinematics of the b-jets. The distribution of $W + c\bar{c}$ events will be shifted since the c-jets are experimentally in between light and b-jets, a consequence of m_{charm} being non-negligible but smaller than a m_{bottom}. Events which are W+ light jets will peak very low, while those containing one c-jet and one light will average the two weights, landing in between the W+light jets peak and the $W + c\bar{c}$ peak.

In addition to the calibration procedure described in Section 4.4, two thresholds are imposed, one in the high and one in the low end of the distribution. Nothing is cut away, but rather values beyond the cutoff are lumped together. In this way, the first and last bin of the distribution represent a wide range of output values. The lower part of the spectrum is grouped together for three reasons. First, the distribution itself becomes discontinuous at very low values, as can

be seen at a value of $\omega \approx -4.5$ in Figure 9.1. This is problematic for fitting. Additionally, the steeply falling spectrum can contribute to uncertainty due to arbitrary bin thresholds. Lastly, it is clear from the calibration procedure that the very light part ($\omega \approx -3$) of the spectrum is not calibrated, and thus is not expected to agree perfectly with predictions. All jets below the lowest working point, ω = -1.25, which corresponds to a b-tagging efficiency of 80 %, have the same calibration. This rough calibration yields poor MC-data agreement in the low part of the spectrum when viewed in fine bins, but differences average out over the whole low ω range. One could consider cutting away the region, however much sensitivity would be lost in the analysis: in addition to the general loss of statistics, most W plus light jet events would be cut away and many W+c events as well. Thus the lower part of the spectrum is retained in a single bin.

At the high end of the spectrum, above $\omega = 2.40$, which corresponds to a b-tagging efficiency of 57 %, the events are lumped together for the far simpler reason that statistics begin to run out, in particular in the simulation. The fit needs a modicum of statistics, in particular in each bin of the templates to perform well. One can compare the distributions before this clumping in Figure 9.1 with those after in Figure 9.2, where the former uses fine binning to show structure and the latter uses the coarse binning used in the fit.

The analysis discriminant is shown in both lepton channels in all three jet bins in Figures 9.2 and 9.3. One can see the same distribution in several different forms, namely in logarithmic scale with data overlaid, and the separation power of the three parameters of interest on linear scale, both shown as a complete distribution and zoomed in to show the wide distribution meaningfully. The W+light jet component, as well the next numerically largest background, Z+jets, are shown as well for comparison.

9.2 The Fit Likelihood

A binned profile likelihood template fit to data is performed, following the method developed in Chapter 6. The specifics of its configuration are described here. The parameters of interest in the likelihood are $\sigma_{t\bar{t}}$, $f_{\mathrm{W_{HF}}}$, and f_{Wc}, each of which are unconstrained and fitted as a single parameter, that is, taken to be the same across all jet bins. While this is self explanatory for top pair production, it requires some justification in the case of heavy flavor associated production. From the arguments developed in Section 2.3, it can be seen that the underlying physics in each of the jet bins is identical, with an "extra" radiated light jet in the higher bins. The production mechanism for the heavy flavor contribution overwhelmingly remains the same, regardless of how many light jets are produced in the event.

The main background to all of the processes of interest is W+light jet production, which is normalized in the same way as described in Chapter 8, and taken as a separate parameter in each jet bin and each channel, with an uncertainty increasing from each jet bin to the next within a given channel. Constraints are the same as in the previous chapter, shown in Table 8.2.

The starting point of this analysis was the inclusion of nearly all systematic uncertainties as nuisance parameters in the likelihood. However, the inclusion of nuisance parameters into the fit for many systematic uncertainties has proved problematic due to the insensitivity of the fit variable to them. One can understand clearly that, for example, changing the electron scale factor has no effect on the shape of the b-tagging distribution. Indeed, many systematic uncertainties show a negligible effect on the shape and thus only affect the rate of the processes involved. The inclusion of rate-only uncertainties led to non-sensical results in testing. Thus all rate-only uncertainties are removed from the likelihood.

The main object uncertainties affecting the discriminant, the uncertainty on the b-tagging calibration, are included in the fit as eight separate parameters, as previously. Apart from

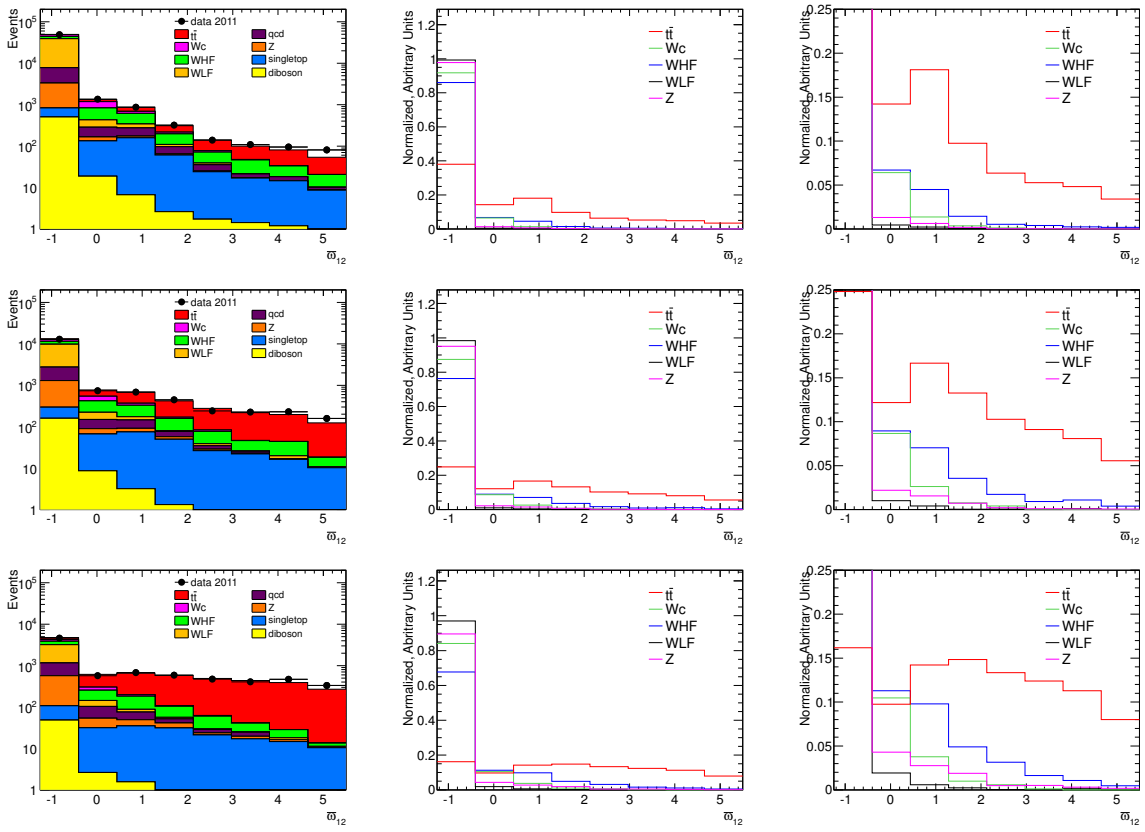

Figure 9.2: The input distribution in e+jets. The rows descend in increasing jet bin, beginning with e+2 jets and ending with e+4 jets (inclusive). The left most column is the input distribution with eight bins after both high and low cutoffs are applied, as it is used in the fit. The next two columns of plots show the expected discriminating power, where each contribution is normalized to unity so that the shapes can be seen. The central column is the full distribution, while the right most column cuts off the y-axis in order to be able to see more clearly the discriminating power in the region which is not dominated by light jets.

these, JES – taken as an envelope – has enough of a shape affect to allow for inclusion. The other uncertainties which remain as nuisance parameters in the fit are those affecting $t\bar{t}$ shape, namely the initial and final state radiation (ISR/FSR), the generator, and showering modeling, as described in Section 5. Other uncertainties affecting jets (JER, pileup contribution to JES, and b-JES) yield extremely unsmooth profiling and are thus not included either. Given the general power of the profile likelihood method to constrain uncertainties, the exclusion of many object uncertainties is expected to enlarge the overall uncertainty in the analysis with respect to the analysis in the previous chapter, even though the same dataset and prescriptions for systematic uncertainties are used.

Expected Behavior

The expected behavior of the likelihood is evaluated. Checks include linearity of the fit, correlation amongst the parameters of interest, and expected uncertainty from the fit. To check linearity, varied fractions of each of the three parameters of interest are injected (separately) and

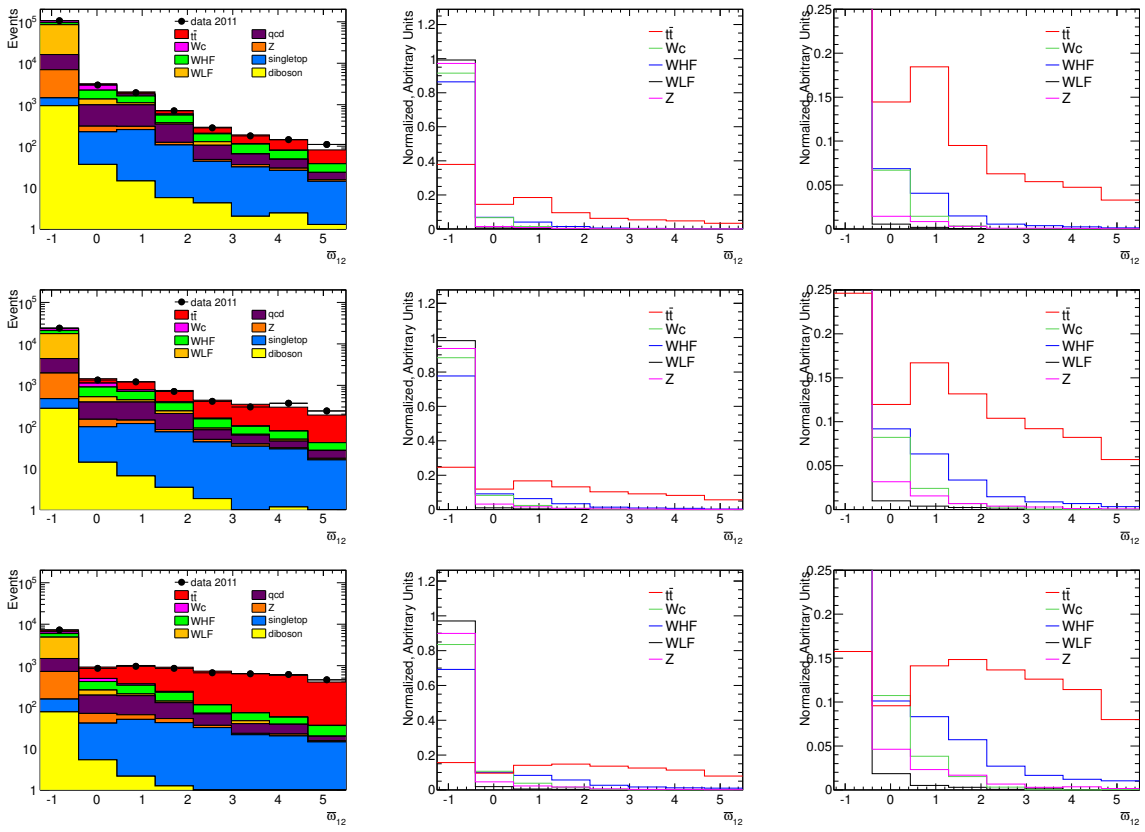

Figure 9.3: The input distribution in μ+jets. The rows descend in increasing jet bin, beginning with μ+2 jets and ending with μ+4 jet (inclusive). The left most column is the input distribution with eight bins after both high and low cutoffs are applied, as it is used in the fit. The next two columns of plots show the expected discriminating power, where each contribution is normalized to 1 so that the shapes can be seen. The central column is the full distribution, while the right most column cuts off the y-axis in order to be able to see more clearly the discriminating power in the region which is not dominated by light jets.

then fit to check for any possible bias. For $\sigma_{t\bar{t}}$ the range [120-200] pb is used in steps of 10 pb. For $f_{\mathrm{W_{HF}}}$ and f_{Wc} the range [0.4-2.0] is used with steps of 0.2. At each point, 1,000 pseudo-experiments are drawn and the full fit including nuisance parameters is made. The results are shown in Figure 9.5. The test for $\sigma_{t\bar{t}}$ shows a $\sim$1 % offset, treatment of which will be discussed in the results section. The results for the linearity of $f_{\mathrm{W_{HF}}}$ and f_{Wc} are extremely good.

Correlation amongst the various parameters of interest is also expected: one can see from the input distributions in Figures 9.2 and 9.3 that $\sigma_{t\bar{t}}$ and $f_{\mathrm{W_{HF}}}$ should be anti-correlated, and similarly $f_{\mathrm{W_{HF}}}$ and f_{Wc}. Using a statistics only fit (i.e. without any nuisance parameters), thousands of PEs are drawn, and the result of the fits for each pair of two parameters of interest are plotted against one another, from which the correlation is estimated. This is shown in Figure 9.4. There, an anti-correlation between $\sigma_{t\bar{t}}$ and $f_{\mathrm{W_{HF}}}$ as well as an anti-correlation between $f_{\mathrm{W_{HF}}}$ and f_{Wc} are observed using ensemble testing, as naively expected. By transience, there is then an expected correlation between $\sigma_{t\bar{t}}$ and f_{Wc} observed in pseudo-experiment testing. Expected correlations are in the range of 40-75 %. The measured correlation and effects of this

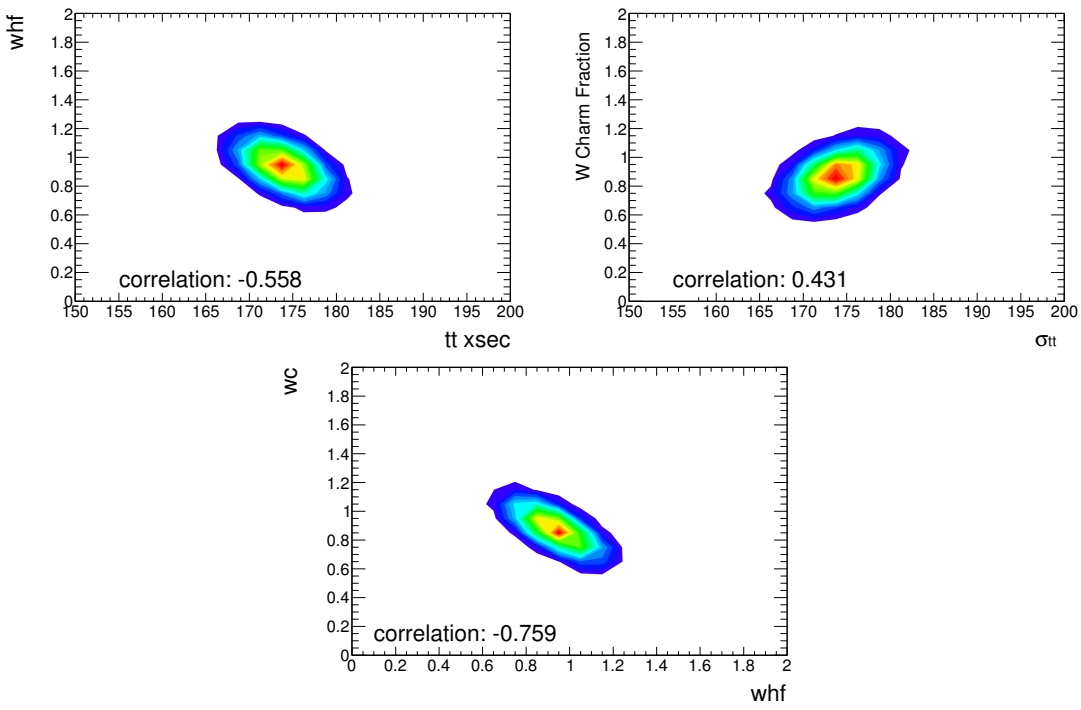

Figure 9.4: The correlation amongst the three input parameters of interest, estimated by drawing PEs from a statistics-only fit. Correlations in the 40-75% range are expected.

will be discussed in the results section at the end of this chapter.

9.3 Results of the Fit and Systematic Uncertainties

The main results of the fit are

$$\begin{aligned} \sigma_{t\bar{t}} &= 172.8^{+16.9}_{-16.7}\,\mathrm{pb},\ \text{(fit)}, \\ f_{\mathrm{W_{HF}}} &= 0.97^{+0.18}_{-0.18}\ \text{(fit)}, \\ f_{\mathrm{Wc}} &= 0.74^{+0.19}_{-0.18}\ \text{(fit)}. \end{aligned}$$

The fitted distribution is shown in Figure 9.6, showing excellent agreement. The results of the fit for $\vec{\beta}$ and $\vec{\delta}$ are shown in Table 9.1. From the main results of the fit, one can see that the background processes, in general, agree quite well with their input values, which provides a sanity check for the fit behavior. The fitted δ parameters and their uncertainties are clearly consistent with the $\pm 1\,\sigma$ envelope but not always with the nominal value, in particular for the b-tagging scale factors. The JES uncertainty is taken as an envelope and found to be quite close to the central value in the MC but with a significantly reduced uncertainty. Given that the $t\bar{t}$ modeling uncertainties are profiled here, they deserve special attention. The FSR is found to be close to the nominal with uncertainty constrained to about half of its input magnitude, while ISR is found to slightly favor the lower variation with an uncertainty strongly reduced. The generator uncertainty moves in the direction of the alternate, POWHEG, but one cannot say definitely that the data favor one or the other given the uncertainty. The case of hadronization favors the nominal (HERWIG) of its alternative (PYTHIA) rather closely.

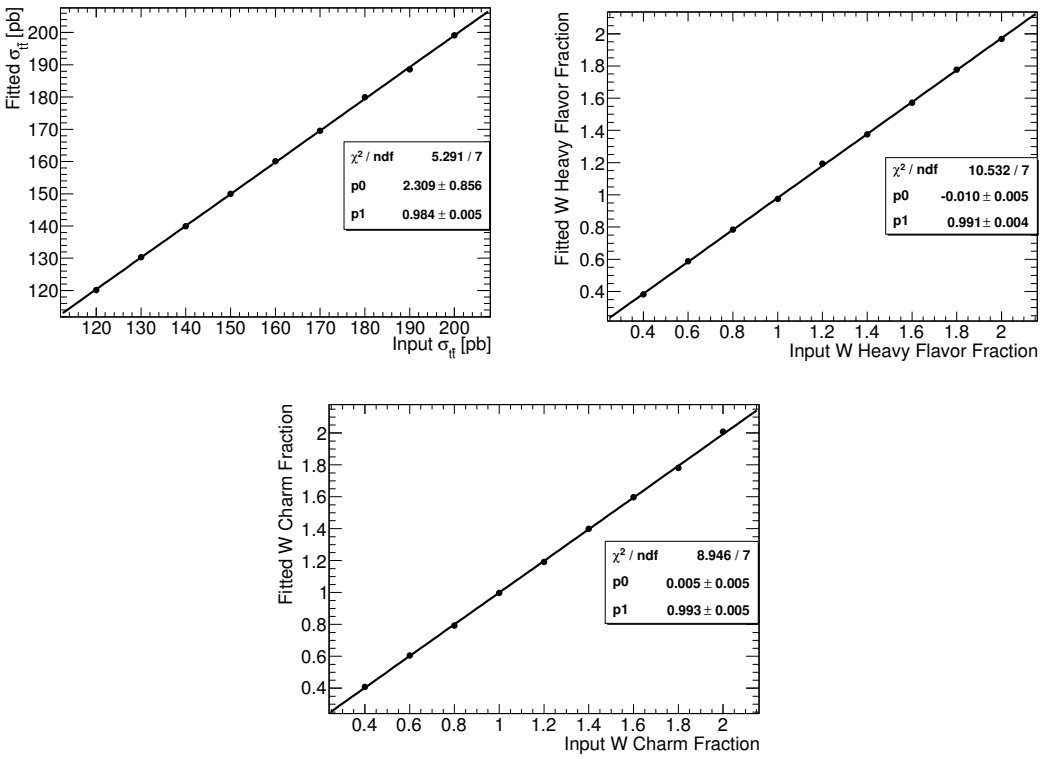

Figure 9.5: The linearity tests with fit results for the $\sigma_{t\bar{t}}$, $f_{\mathrm{W_{HF}}}$ and f_{Wc} analysis. Offsets in both the linearity and slope of $t\bar{t}$ are observed and corrected for. The linearity tests for $f_{\mathrm{W_{HF}}}$ and f_{Wc} reveal no bias.

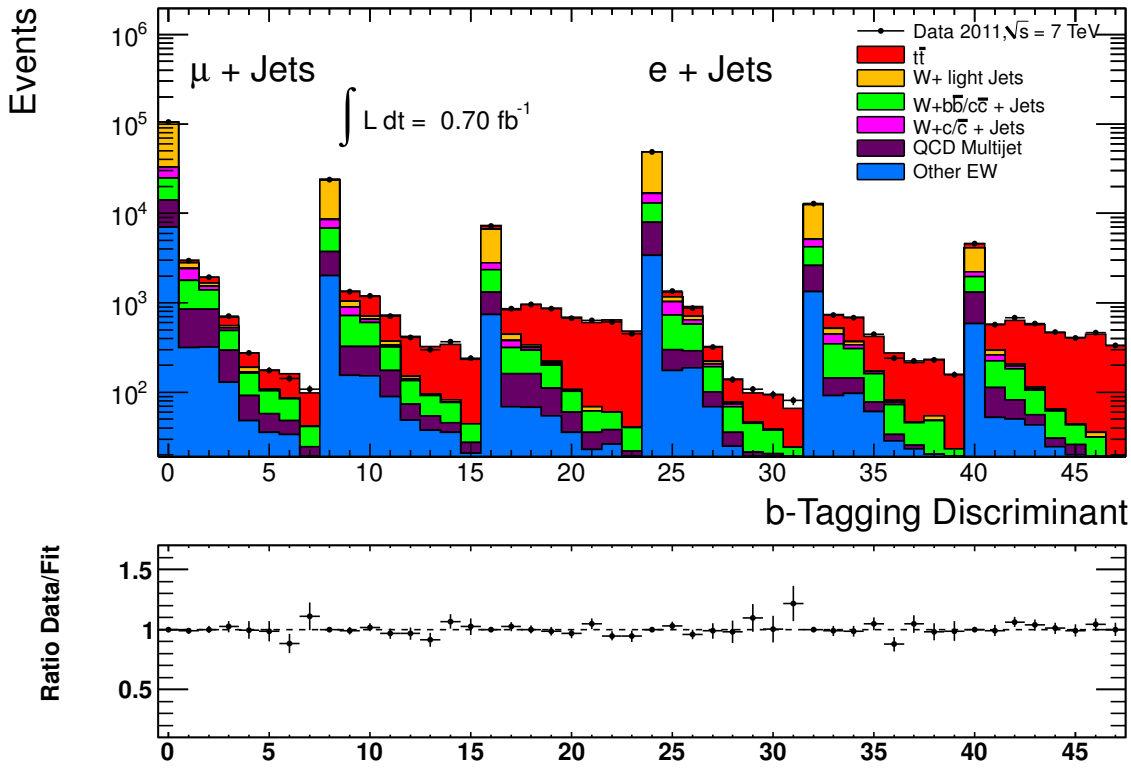

Figure 9.6: The six-channel distribution after the fit, showing excellent data-MC agreement. Each of the six channels has eight bins. Left most are e+2 jets, followed by e+3 jets and e+4 jets (inclusive). The μ+jets channels follow. Errors on data points are statistical only.

Parameter	Value	Error	Error Up	Error Down
$\beta(t\bar{t})$	1.0499	0.0544	0.1027	-0.1015
$\beta(f_{\mathrm{W_{HF}}})$	0.9709	0.0894	0.1761	-0.1769
$\beta(f_{\mathrm{Wc}})$	0.7377	0.1031	0.1880	-0.1749
β(W in μ + 2 jets)	1.0412	0.0233	0.0595	-0.0748
β(W in μ + 3 jets)	1.1024	0.0401	0.0940	-0.1194
β(W in μ + 4 jets)	1.0952	0.0687	0.1522	-0.1756
β(W in e + 2 jets)	1.0025	0.0318	0.0732	-0.0870
β(W in e + 3 jets)	1.0076	0.0568	0.1134	-0.1311
β(W in e + 4 jets)	0.8930	0.0935	0.1600	-0.1869
$\beta(Z$+jets)	1.0145	0.2063	0.2962	-0.2994
β(Single top)	1.0017	0.0966	0.1060	-0.1061
β(Diboson)	1.0010	0.0616	0.0623	-0.0616
β(QCD in μ + 2 jets)	0.7726	0.0725	0.1123	-0.1133
β(QCD in μ + 3 jets)	0.6953	0.1177	0.1473	-0.1575
β(QCD in μ + 4 jets)	0.7521	0.1914	0.2209	-0.2281
β(QCD in e + 2 jets)	1.0293	0.1941	0.3483	-0.3566
β(QCD in e + 3 jets)	0.8780	0.2449	0.3637	-0.3783
β(QCD in e + 4 jets)	1.2189	0.2909	0.4082	-0.4288
δ(b-tagging WP1)	-0.1648	0.2367	0.2580	-0.2188
δ(b-tagging WP2)	0.5092	0.2564	0.2676	-0.2657
δ(b-tagging WP3)	0.6220	0.2764	0.2856	-0.2704
δ(b-tagging WP4)	1.0826	0.3988	0.4921	-0.5199
δ(mistags WP1)	-0.8807	0.9381	0.9477	-0.9613
δ(mistags WP2)	-0.0066	0.9452	0.9507	-0.9573
δ(mistags WP3)	0.1370	0.9544	0.9882	-0.9510
δ(mistags WP4)	-0.1926	0.8614	0.9600	-0.9740
δ(FSR)	0.1215	0.4459	0.5008	-0.4364
δ(ISR)	-0.3583	0.2016	0.2571	-0.2695
δ(MC Generator)	0.3863	0.3680	0.5539	-0.6430
δ(Hadronization)	0.1581	0.3634	0.4592	-0.4265
δ(JES)	0.1064	0.2030	0.5735	-0.4414

Table 9.1: The main fit results of the simultaneous $\sigma_{t\bar{t}}$, $f_{\mathrm{W_{HF}}}$ and f_{Wc} fit. All $\vec{\beta}$ and $\vec{\delta}$ beyond the three parameters of interest are consistent within the uncertainties, although some δ clearly favor a value different from the nominal. The asymmetric error is observed at the fit minimum and the symmetric errors are from the hessian error matrix.

Profiling the Fit

In order to check the behavior of profiling in the fit, the parameters of interest are profiled over a wide range. The profiled likelihood as a function of each of the three parameters of interest are shown near the minimum of the fit for each in Figure 9.7. Smooth curves are in general observed, though some benign features are found. An example is the bump in profiling f_{Wc} at $\beta_{17} \approx 1.4$, i.e. at $10\,\sigma$, sufficiently far away from the minimum that it is not of concern.

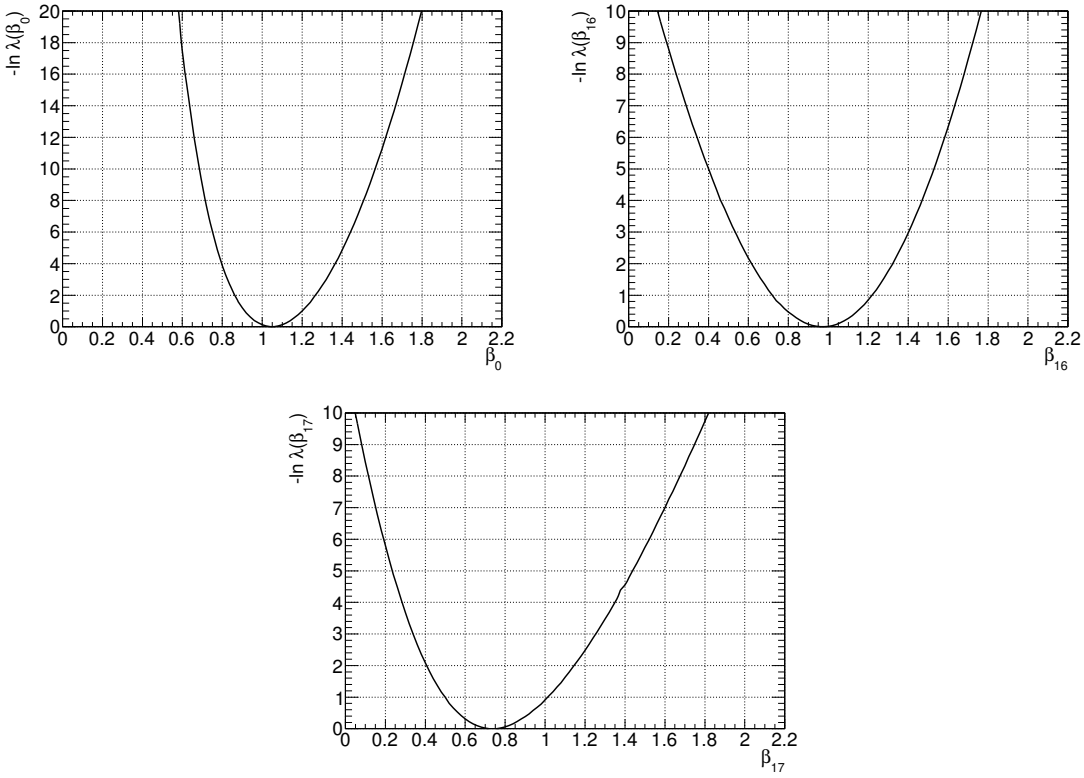

Figure 9.7: Profiling the three parameters of interest. The top left (β_0) is the profile likelihood as a function of $\sigma_{t\bar{t}}$, top right (β_{16}) $f_{\mathrm{W_{HF}}}$, and bottom (β_{17}) is f_{Wc}. An insignificant bump for f_{Wc} at $\beta_{17} \approx 1.4$, far away from the minimum. The profiling is otherwise smooth.

Correlations of Parameters

The observed correlation amongst the various parameters in the fit is shown in matrix form in Figure 9.8. One can see from the rather colorful plot that there are non-negligible correlations, which can be viewed in a few categories. Reading the plot roughly from left to right and top to bottom, $\sigma_{t\bar{t}}$ has strong (anti-)correlations with the generator and JES systematics. Of considerable noteworthiness is the near-full correlation of $\sigma_{t\bar{t}}$ to the generator uncertainty. The W+jets parameters have correlations which are expected. They are anti-correlated to JES due to the strong affect of JES on the W+jets rate. They are also anti-correlated to fakes because the discriminant shape is quite similar. The various W+jets parameters are correlated to one another. The three parameters of interest have measured correlations amongst one another similar to those expected, but less strong. In general, the $f_{\mathrm{W_{HF}}}$ and f_{Wc} parameters show less

correlation to the uncertainties than $\sigma_{t\bar{t}}$ does. One concern here is that the uncertainty on a parameter of interest can be incorrectly estimated by the profile likelihood technique if it is correlated to an uncertainty, which has been tested and will be discussed below. The method of N-1 testing to breakdown the fit uncertainty into contributions becomes a poor estimator because it requires the terms to be uncorrelated.

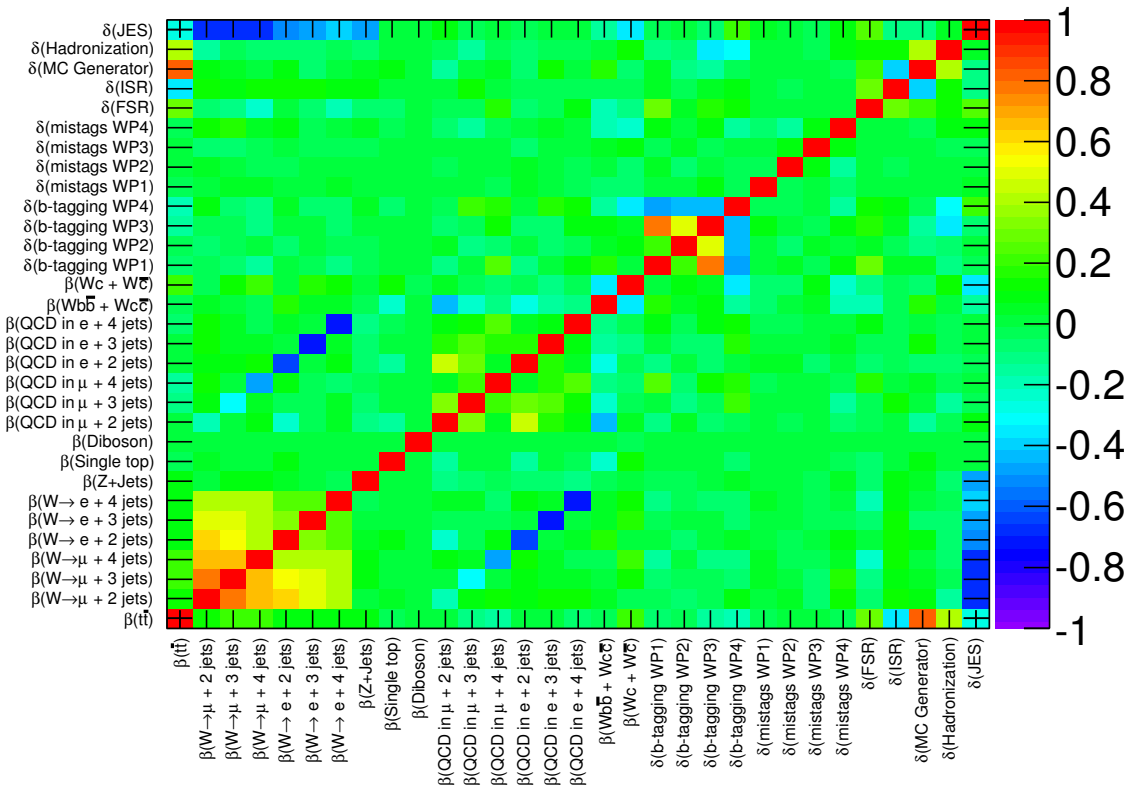

Figure 9.8: The correlation of the parameters in the fit are shown as measured. In some cases the correlation is different than anticipated.

Cross Check: Marginalization of The Likelihood

Given that correlations are observed, in particular between $\sigma_{t\bar{t}}$ and some of the nuisance parameters, the likelihood will be marginalized as a cross check of the results. The process of marginalization has been sketched in Chapter 6. To integrate, the Metropolis-Hastings algorithm is used with 10^4 burn-in (pre-integration) steps and 10^6 integration steps [126, 127]. The number of steps is chosen by marginalizing the same likelihood multiple times with various step configurations and running each configuration multiple times. Since the technique uses numerical integration, results will not be identical unless the same seed is specified, which could bias the results. The chosen steps were found to give results precise enough for this test. It should be noted that using an integration technique such as this should be treated with care and requires many checks for biases (for instance correlation of one integration point to the next) which have not been performed. These results are therefore taken as guidance for a crosscheck but are

themselves not thoroughly vetted.

Using marginalization, the result for $\sigma_{t\bar{t}}$ reveals a 2.9 % shift in the central value, with similar but slightly smaller uncertainty (9.7 % vs. 9.3 %). It is no surprise that the central value shifts given the relatively large correlations measured in data, and it is encouraging that the relative uncertainty is similar. It would seem reasonable to quote an additional 2.9 % methodological uncertainty on the measurement of $\sigma_{t\bar{t}}$ using the current configuration. Doing so would raise the "fit" uncertainty from 9.7 % to 10.1 %.

Turning to the heavy flavor cross section, $f_{\mathrm{W_{HF}}}$ has a near identical central value ($\Delta f_{\mathrm{W_{HF}}}$ =+0.005 %) from profiling and marginalization, while the uncertainty goes up by a relative 1.1 % (from 18.2 % to 18.4 %). This is considered to be consistent. The case of f_{Wc} is harder to evaluate given both the limited sensitivity of the fit to its contribution and the previously discussed issue of low MC statistics. The central value shifts up by 9.2 % while the uncertainty stays nearly the same, going down from 24.6 % to 24.2 %. For a method as sensitive as marginalization, results for such a problematic parameter should be taken lightly before extensive testing is undertaken.

The results of the check with marginalization is shown in Table 9.2, compared with results from profiling and, in the $\sigma_{t\bar{t}}$ case, those corrected for the linearity offset. The results of this check yield clear evidence that results in a highly-correlated environment with a profile likelihood fit need to be carefully evaluated. In the case at hand, the difference in the central value for the results between the marginalized and profiled likelihood could be taken as an additional methodological uncertainty. The large uncertainties coming from the rest of the analysis render the results practically the same. Accordingly, it would prove more fruitful to study the likelihood behavior in such an environment than to simply assign a larger systematic uncertainty.

Method	**Mean**	**Uncertainty (rel)**	**Median**
	$\sigma_{t\bar{t}}$		
Profiling	1.0499	9.7 %	-
Marginalization	1.0803	9.3 %	1.0766
Change (rel)	+2.9 %	-4.3 %	-
Profiling (Uncorrected)	1.0499	9.7 %	-
Profiling (Linearity Offset)	1.0589	9.7 %	-
Change (rel)	+0.9 %	-	-
	$f_{\mathrm{W_{HF}}}$		
Profiling	0.9709	18.2 %	-
Marginalization	0.9754	18.4 %	0.9756
Change (rel)	+0.005 %	+1.1 %	-
	f_{Wc}		
Profiling	0.7377	24.6 %	-
Marginalization	0.8015	24.2 %	0.7915
Change (rel)	+9.2 %	-1.6 %	-

Table 9.2: The results of the marginalized likelihood compared to the profiled likelihood. For each parameter of interest, the results of both are shown. The corrected value for $\sigma_{t\bar{t}}$ with profiling is the result after calibrating for the offset observed in the linearity test. The marginalized uncertainty is the RMS of the mean of the fit, while for profiling it is an average of the two asymmetric uncertainties (the last two columns in Table 9.1).

Systematic Uncertainties

The fit uncertainty is broken into components, but for $\sigma_{t\bar{t}}$, this breakdown is not reliable due to large correlations observed. It is nonetheless relatively clear that the generator uncertainty is dominant, having an uncertainty on its own similar to the rest of the fit combined. Amongst the externally evaluated systematic uncertainties, electron scale factors, the pileup component of JES, and the b-JES are dominant, where the lattermost is highly asymmetric. The results are summarized in Table 9.3. A complete list of sytematic uncertainties considered can be found in Appendix A.

The $f_{\mathrm{W_{HF}}}$ fit uncertainty is dominated by the statistical component (13 %), while the dominant object uncertainty in the fit is the b-tagging algorithm calibration. Amongst the external systematics, the pileup component of JES dominates along with electron scale factors, where the latter yields a large asymmetry. It is of note that the MC statistical uncertainty is at the level of about 6 %. This alone is not a limiting factor but it is likely that not having enough simulation MC statistics artificially enlarges the effects of systematic uncertainties, which thereby obtain a statistical component. The results are summarized in Table 9.3.

The fit uncertainty for f_{Wc} is split in almost equal parts between statistical uncertainty and the b-tagging algorithm calibration, each at the level of about 15 %. Other in-fit uncertainties are much smaller. The out of fit uncertainties blow up to large values, often asymmetric. The worst offender is the pileup JES term, which has a relative uncertainty of +12 - 38 %. This can be due in part to the insensitivity of the fit to f_{Wc} but certainly a large part is due to the low MC statistics, which alone contributes a 10 % uncertainty. With such an unsmooth and statistically limited distribution, evaluation of systematic uncertainties is of limited reliability. The results are summarized in Table 9.3.

It should be noted that several commonly considered systematic uncertainties are not taken into account here. The uncertainty due to PDF is not considered due to purely technical reasons, but it can be estimated to be of the same order as in the analyses in the previous chapters, about 1 %, although it may be large effect on $f_{\mathrm{W_{HF}}}$. The uncertainty due to modeling of fake leptons is not taken into account. Doing so properly would require a detailed study of the flavor composition of such events, which is beyond the scope of this work. The effect should be very small nonetheless: the shape is expected to be similar to the full W+jets shape itself, and therefore most of the events will be in the background dominated first bin. If the analysis in Chapter 7 which used a flavor-sensitive variable as a discriminating variable is any guide, uncertainties should be on the order of 1 % due to modeling. Most importantly, the modeling uncertainty of W+jets has not been properly taken into account here. Naively evaluating the systematic uncertainty using the method described in Chapter 5 yields uncertainties of < 1 % on all three parameters. Given that the derivation of the rescaling functions did not take flavor into account it is not obvious that they are readily applicable. Furthermore, the clear dependence of $\sigma_{t\bar{t}}$ on the modeling of $t\bar{t}$ implies that there should be a larger dependence of $f_{\mathrm{W_{HF}}}$ and f_{Wc} on their MC modeling as well. A more thorough evaluation would use an alternative MC generator for W+jets as is done for $t\bar{t}$, but no second sample of generated events was available at the time. Additional uncertainties regarding the flavor composition of the backgrounds, in particular of the Z+jets sample would be sensible, though the rate is so low it is not likely to be a large uncertainty.

Final Results

The final results of the fit, with all uncertainties taken into account, are

$$\begin{aligned}
\sigma_{t\bar{t}} &= 172.8 \pm 2.8\ (\text{stat.})^{+21}_{-27}\ \ (\text{syst.}) \pm\ 6.4\ (\text{lumi.})\text{pb} = 172.8^{+22}_{-28}\ \text{pb},\\
f_{\mathrm{W_{HF}}} &= 0.97 \pm 0.14\ (\text{stat.})^{+0.21}_{-0.22}\,(\text{syst.}) \pm 0.04\,(\text{lumi.}) = 0.97^{+0.25}_{-0.27},\\
f_{\mathrm{Wc}} &= 0.74 \pm 0.16\ (\text{stat.})^{+0.40}_{-0.67}\,(\text{syst.}) \pm 0.04\,(\text{lumi.}) = 0.74^{+0.45}_{-0.71}.
\end{aligned}$$

The results for $f_{\mathrm{W_{HF}}}$ and f_{Wc} are in clear agreement with the previous measurements from ATLAS, $f_{\mathrm{W_{HF}}} = f_{\mathrm{Wc}} = 1.0$. The central value for $f_{\mathrm{W_{HF}}}$ is very close, with comparable uncertainty. The f_{Wc} measurement is clearly lower, however the uncertainties here are large and within those, consistent. The result for $\sigma_{t\bar{t}}$ will be discussed in the next chapter along with the results from the other analyses presented in this thesis.

Uncertainty	up (pb)	down (pb)	up (%)	down (%)
Fit	16.92	−16.80	9.82	−9.76
Breakdown				
Statistical	2.76	−2.76	1.77	−1.77
Tag	9.60	−9.46	5.83	−5.75
ISR/FSR	8.54	−5.29	5.19	−3.21
JES	7.52	−10.42	4.57	−6.33
Hadronization	9.09	−8.35	5.52	−5.07
Generator	14.21	−13.73	8.63	−8.34
External				
JET/$E_{\mathrm{T}}^{\mathrm{miss}}$	10.92	−19.02	6.64	−11.55
Lepton	8.63	−11.79	5.24	−7.16
Template statistics	1.05	−1.05	0.64	−0.64
Syst	21.16	−27.40	12.86	−16.65
Stat. + Syst	21.39	−27.56	13.00	−16.74
Lumi	6.37	−6.37	3.70	−3.70
all	22.24	−27.56	13.51	−16.75

Table 9.3: Table of estimated systematic uncertainties for $\sigma_{t\bar{t}}$. The breakdown is not reliable because of large correlations amongst the parameters. Uncertainty is dominated by the choice of generator, but the magnitude of its dominance is unclear.

Uncertainty	up (frac)	down (frac)	up (%)	down (%)
Fit	0.18	−0.18	18.32	−18.15
Breakdown				
Statistical	0.14	−0.14	13.23	−13.23
Tag	0.06	−0.06	5.85	−6.45
ISR/FSR	0.04	−0.05	4.23	−5.17
JES	0.00	−0.04	0.00	−4.08
Hadronization	0.00	−0.04	0.00	−3.70
Generator	0.03	−0.04	2.94	−4.50
External				
JET/$E_{\mathrm{T}}^{\mathrm{miss}}$	0.15	−0.13	14.87	−13.42
Lepton	0.05	−0.14	4.72	−13.69
Template statistics	0.06	−0.06	6.15	−6.15
Syst	0.21	−0.22	20.51	−21.70
Stat. + Syst	0.25	−0.26	24.90	−26.41
Lumi	0.04	−0.04	3.70	−3.70
all	0.25	−0.27	25.17	−26.67

Table 9.4: Table of estimated systematic uncertainties for $f_{\mathrm{W_{HF}}}$. The fit is dominated by statistical error while the overall uncertainty also has major contributions from the pileup component of JES and the electron scale factor.

Uncertainty	up (frac)	down (frac)	up (%)	down (%)
Fit	0.19	−0.18	25.2	−23.9
Breakdown				
Statistical	0.16	−0.16	21.6	−21.6
Tag	0.13	−0.11	17.6	−14.8
ISR/FSR	0.02	−0.02	2.7	−2.7
JES	0.06	−0.07	8.1	−9.5
Hadronization	0.06	−0.04	8.1	−5.4
Generator	0.03	−0.03	4.1	−4.1
External				
JET/$E_{\mathrm{T}}^{\mathrm{miss}}$	0.19	−0.53	25.7	−71.6
Lepton	0.29	−0.41	39.2	−55.4
Template statistics	0.10	−0.10	13.5	−13.5
Syst	0.40	−0.67	54.1	−90.5
Stat. + Syst	0.45	−0.71	60.8	−95.9
Lumi	0.04	−0.04	5.4	−5.4
all	0.45	−0.71	61.1	−96.1

Table 9.5: Table of estimated systematic uncertainties for f_{Wc}. The fit is dominated by the statistical component with a major contribution from the calibration of the b-tagging algorithm. The pileup JES term and electron scale factor are large and asymmetric. The contribution from template statistics uncertainty becomes large. This has the effect that externally evaluated uncertainties will be artificially enlarged.

10 Interpretations of Results and a Glance Towards the Future

Three separate measurements of the top quark pair production cross section have been presented in this thesis, each using a binned profile likelihood template fit to data. The first measurement used a likelihood discriminant as input, formed of 3 kinematic variables and the output of a b-tagging algorithm, in $\int \mathcal{L}\,dt = 35$ pb^{-1} of data recorded during 2010. This result is now submitted for publication, greatly improving the sensitivity of $\sigma_{t\bar{t}}$ with respect to the previous ATLAS publication. The second analysis used a similar technique but without explicit flavor sensitivity using $\int \mathcal{L}\,dt = 0.7$ fb^{-1} of data collected during the first half of 2011. The third analysis used a single-variable input to simultaneously measure $\sigma_{t\bar{t}}$, $f_{\mathrm{W_{HF}}}$, and f_{Wc} in the $\int \mathcal{L}\,dt = 0.7$ fb^{-1} dataset.

The measurements of $\sigma_{t\bar{t}}$ from the three analyses presented are

$$\sigma_{t\bar{t}} = 187 \pm 11 \text{ (stat.) } {}^{+18}_{-17} \text{ (syst.) } \pm 6 \text{ (lumi.) pb} = 187 \,{}^{+22}_{-21} \text{ pb}, \int \mathcal{L}\,dt = 35 \text{ pb}^{-1},$$
$$\sigma_{t\bar{t}} = 179 \pm 3.9 \text{ (stat.) } \pm 9.0 \text{ (syst.) } \pm 6.6 \text{ (lumi.) pb} = 179 \pm 11.8 \text{ pb}, \int \mathcal{L}\,dt = 0.7 \text{ fb}^{-1}, \text{Ch. 8},$$
$$\sigma_{t\bar{t}} = 173 \pm 2.8 \text{ (stat.) } {}^{+21}_{-27} \text{ (syst.) } \pm 6.4 \text{ (lumi.) pb} = 173 \,{}^{+22}_{-28} \text{ pb}, \int \mathcal{L}\,dt = 0.7 \text{ fb}^{-1} \text{Ch. 9}.$$

The theoretical prediction used for comparison throughout is

$$\sigma_{t\bar{t}} = 164.6^{+11.5}_{-15.8} \text{ pb}.$$

All three measurements of $\sigma_{t\bar{t}}$ are in agreement with the prediction within uncertainty but are systematically above the predicted central value by 5-10 %. This can be clearly seen in Figure 10.1, which shows the measurements presented here together with the earlier measurement from the collaboration, compared with the prediction. The two most precise measurements use a similar method to each other on different data sets with different observables. The two are statistically independent and dominated by different systematic uncertainties.

In addition to the top pair production cross section, the analysis in Chapter 9 measured simultaneously $f_{\mathrm{W_{HF}}}$ and f_{Wc}. These are measured to be

$$f_{\mathrm{W_{HF}}} = 0.97 \pm 0.14 \text{ (stat.)} \,{}^{+0.21}_{-0.22} \text{ (syst.)} \pm 0.04 \text{ (lumi.) pb} = 0.97^{+0.25}_{-0.27},$$
$$f_{\mathrm{Wc}} = 0.74 \pm 0.16 \text{ (stat.)} \,{}^{+0.40}_{-0.67} \text{ (syst.)} \pm 0.04 \text{ (lumi.) pb} = 0.74^{+0.45}_{-0.71}.$$

with respect to the fractions present in the MC simulation scaled to the previous ATLAS measurement in the same dataset. The measurement of $f_{\mathrm{W_{HF}}}$ is consistent with the earlier ATLAS measurement ($f_{\mathrm{W_{HF}}}$ =1), which has different main systematic uncertainties. The uncertainty on f_{Wc} in this method is too large to make a meaningful qualitative statement.

The measurement of $f_{\mathrm{W_{HF}}}$ is of particular interest here as it measures an important physical quantity with increased sensitivity with respect to the previous measurement. The ATLAS measurement which is taken as a starting point was $f_{\mathrm{W_{HF}}} = 1.63 \pm 0.76$ (47 % relative) with respect to the MC. That measurement was consistent with leading order predictions in the MC

(for which $f_{\mathrm{W_{HF}}} = 1.0$ there). Scaling the result of the analysis in Chapter 9 with respect to the MC yields $f_{\mathrm{W_{HF}}} = 1.58^{+41}_{-44}$, more clearly above the LO MC than previous measurements. Given that there are relatively large uncertainties for both W+jets in general and heavy-flavor related processes in particular, this is not surprising. The results are certainly consistent within theoretical errors, estimated to be 50-100 %. The same game can be played with f_{Wc}. The ATLAS measurement is $f_{\mathrm{Wc}} = 1.11 \pm 0.35$ (32 % relative), though here the dedicated ATLAS measurement is naturally more sensitive, as the analysis variable at hand is not optimized for c-jet separation. The measurement of $f_{\mathrm{W_{HF}}}$ supports the earlier findings of ATLAS. This establishes treating the heavy flavor component of W+jets, an irreducible background to $t\bar{t}$, as a signal itself in the same measurement using the ATLAS detector.

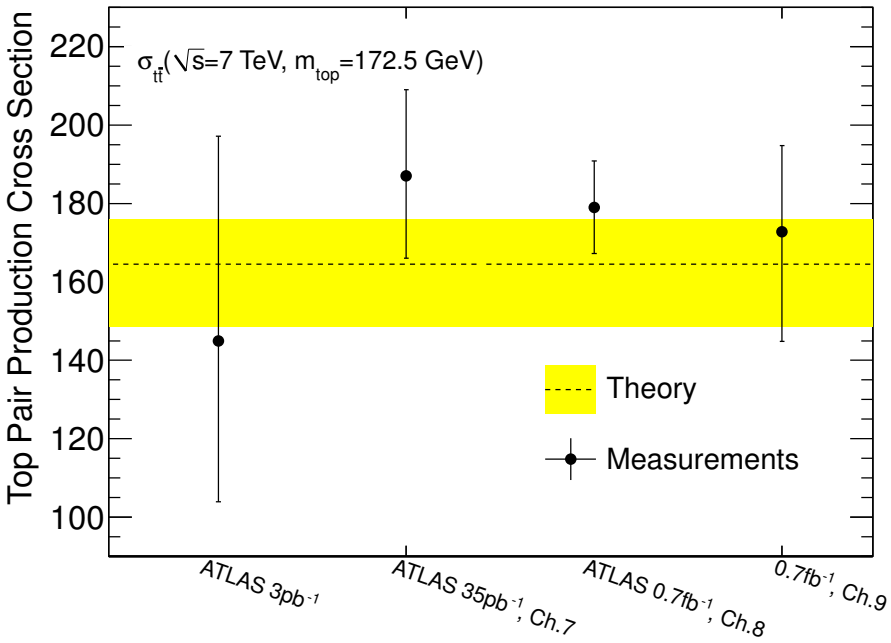

Figure 10.1: The three measurements presented in this thesis using $\int \mathcal{L}\,dt = 35\,\mathrm{pb}^{-1}$–$0.7\,\mathrm{fb}^{-1}$of data, along with the earlier ATLAS measurement using $\int \mathcal{L}\,dt = 3\ \mathrm{pb}^{-1}$(left most point)[5], and a theoretical prediction (horizontal line, uncertainty band) [13]. Experimental error on the most precise $\sigma_{t\bar{t}}$ determination is smaller than uncertainty of the prediction. Error bars on measurements include all uncertainties. Both the predictions and measurements assume $m_{\mathrm{top}} = 172.5\,\mathrm{GeV}$.

10.1 The Meaning of These Results

The results in this thesis represent the path towards a precision measurement of $\sigma_{t\bar{t}}$ at ATLAS. The analysis in Chapter 8 using $\int \mathcal{L}\,dt = 0.7\ \mathrm{fb}^{-1}$ achieves a relative precision of about 7 %, similar to that achieved recently at the Tevatron [71, 72]. It is possible after one year of colliding beams operation to reach a precision which required a decade at the Tevatron. This is only natural given higher statistics, more advanced detector technology, and experience gained in earlier experiments applicable here. Unlike those analyses performed at the Tevatron, which are

either in their final form or nearing it, those at the LHC are just beginning. Already a dataset of more than five times larger than the data analyzed here is available. For an analysis such as this, which is overwhelmingly dominated by systematic uncertainties, just adding data does not help; it must be better understood. This comes naturally from a larger available calibration dataset. This particular analysis can nonetheless benefit from simple addition of statistics because of profiling the likelihood, by which higher statistics can further limit the systematic uncertainties in-situ. In the current form however, the dominant uncertainties are those which are excluded from the fit, overwhelmingly the signal modeling uncertainties.

In the analysis in Chapter 7, the ISR and FSR modeling was removed from the fit due to objections from the collaboration during the process of publishing, but it was included in the result in Chapter 8 which was only preliminarily approved to be shown at a conference. With external evaluation, as is done in Chapter 7, the uncertainty due to ISR/FSR modeling is actually larger than that of the generator (Table 7.4). Similarly in the analysis in Chapter 7 where the ISR/FSR modeling uncertainties are included in the fit, they are constrained to about 20 % of their original size. Their combined uncertainty contributes about 1.5 % (Tables 8.4 and 8.3). The unconstrained uncertainty from each source is about 5 %. Given that the signal generator modeling uncertainties are in general not to be included in profile fitting in collaboration publications in the near future, it is clear that reducing these uncertainties by better understanding is necessary to improve the precision of the result. Indeed, if the analysis would be redone now with the full dataset currently available at $\sqrt{s} = 7$ TeV these modeling uncertainties would be even more clearly dominant. This brings us back to the questions posed in the introduction.

The hypothesis being tested was phrased as "QCD NLO kinematics and NNLO rate predict the behavior of top quark pairs produced in proton-proton collisions at the LHC". What is clear from the discussion above is that one of the conditions necessary to test this hypothesis, NLO kinematics being well described, must be called into question. The result is: the measurements using NLO kinematics to model the signal agree with NNLO rate within uncertainty, but the central value of the measurements are higher. The uncertainty in signal modeling is one of the dominant uncertainties. There are at least two implications of this. Experimentally, one cannot answer this question much better than has been done already without improving the modeling of NLO kinematics. Taken to the extreme where no other uncertainties contribute, the generator uncertainty and ISR/FSR will each give $\sim$5 % uncertainty if they are not profiled or otherwise improved upon. This yields the same uncertainty as is present in the analysis in Chapter 9, which actually achieves a better precision than $5 \otimes 5 \approx 7$ % by profiling ISR/FSR, even with all other uncertainties included. The conclusion is clear: to improve this result, the uncertainty due to these sources must be brought down, whether it be by better theoretical understanding, experimentally differentiating the two either by an in-situ technique such as profiling or in an independent analysis, or by changing the acceptance and kinematic sensitivities to the differences in the analysis itself.

There is a further implication of these results. Neither of the two generators used in the measurements produce results agreeing with the central value of the NNLO $\sigma_{t\bar{t}}$ calculation used for comparison. The identical measurement with reduced uncertainties from modeling sources would only be more evident. The truly experimental uncertainty in the analysis is already negligible compared to the theoretical uncertainty which enters the analysis. These results motivate more precise predictions. Tuning the generator to agree with measurements is certainly possible, but it will not *measure* anything further. It would be acknowledging that predictions cannot be that precise and imply that the underlying theory cannot be tested more precisely.

There are a few possibilities in order to better understand the difference between expectation and measurement. It could very well be that the NLO kinematics are not good enough, that higher-order effects affect the kinematics. One could think of either a full-blown higher order generator or a kinematically dependent k-factor to make the NLO MC behave like a higher order prediction. On the experimental side, one could think to reduce sensitivity to theoretical uncertainty, in particular those due to acceptance. Broadening kinematic cuts would reduce sensitivity to kinematic differences between generators, however this would greatly increase experimental uncertainties, those affecting jets in particular. Another possibility would be unfolding the measurement to quote a fiducial cross section. Such projects may be undertaken in the future, and indeed many discussions have begun amongst various physicists along these lines. It is clear that simply rerunning these analyses without first making progress on these issues will not lead to a deeper knowledge of nature.

10.2 An Outlook: The Coming Precision

The measurements presented here, in particular those using the $\int \mathcal{L}\, dt = 0.7$ fb^{-1} dataset, hail the arrival of the era of precision physics above the scale of the W and Z bosons. The top quark is now being studied to extreme precision, not only in the inclusive production cross section measurement described here. In recent months, results have become available such as the production cross section of top quark pairs with an additional photon and with additional jets [129, 130], as well as inclusive production in the difficult all-hadronic decay channel [131]. Differential cross section measurements have been made, analyzing effects such as the charge asymmetry in top quark pair production at the LHC [132]. Measurements of single-top quark production cross section have been made as well [133]. Properties of the top quark are being measured, in particular the mass and charge [134, 135]. Most of these measurements are approaching the precision of similar measurements at the Tevatron and will soon surpass them, if they have not already. These measurements test and verify properties and behavior of the top quark.

Such knowledge allows for searches for particles and interactions which are not a part of the Standard Model, and for setting limits on many theories which could exist over a very broad energy range. Knowledge of the top quark was used, for instance, in a search for particles which decay into a $t\bar{t}$ pair, attempting to measuring an excess of $t\bar{t}$ events [136]. Indeed analyses throughout the collaboration are setting limits on such theories not only using top quarks. This is done in particular setting lower limits for the masses of particles based on the non-observation of them. Many theories, some popular, are becoming disfavored as a result. To date there is no direct evidence for particles or interactions which are not already understood within the Standard Model.

The Standard Model is being tested to high precision in many ways. The inclusive cross section of rare processes such as di-boson production have been recently measured and found to be in agreement with NLO QCD predictions [137, 138, 139]. Here, as in the case of the top quark pair production cross section, it may soon become necessary to obtain more precise predictions in order to test QCD at a higher order. Those analyses are statistically limited as of yet, with systematic uncertainties of a similar magnitude as the predictions. One of the last predictions of the SM which is not verified is the production of a Higgs boson, being searched for vigorously by all collaborations in the field. Stringent limits have recently been set by both the ATLAS and CMS collaborations, effectively ruling out the possibility of a SM Higgs over a huge mass range [37, 38]. Only a small range remains, in which there is some insignificant but

nonetheless exciting signal-like excess.

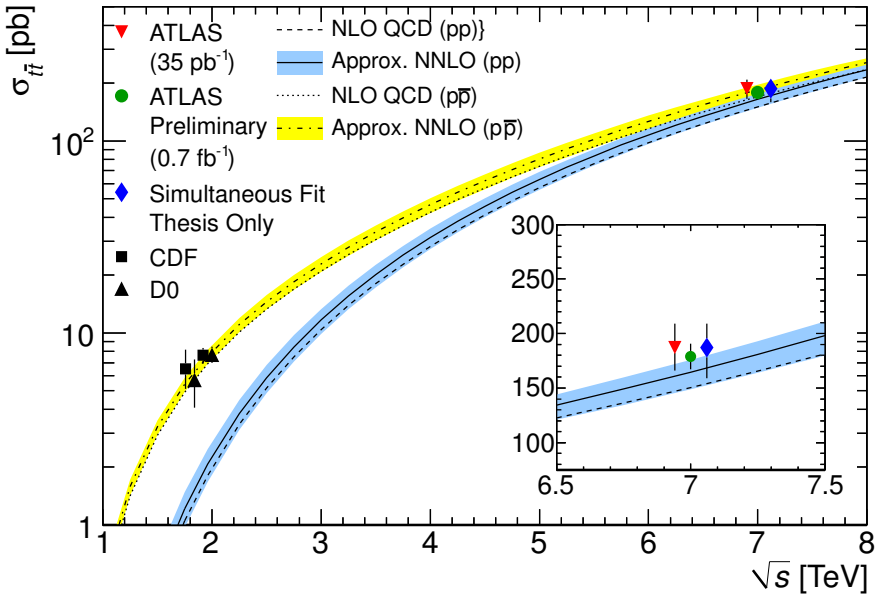

Figure 10.2: The top pair production cross section as a function of center-of-mass collision energy, comparing the three results presented in this thesis with theoretical predictions for pp collisions from Hathor[13]. The latest results from the Tevatron are shown as well, with the prediction for $p\bar{p}$ collisions. Theoretical predictions are shown with the uncertainty band corresponding to scale and PDF uncertainties. The general success of the predictions for $\sigma_{t\bar{t}}$ using QCD can be seen.

Our understanding of fundamental particles and their interactions is being reckoned with measurements of an unprecedented precision reaching energies well above those previously measured. Many assumptions of the Standard Model are being tested, from the charge to the top quark to the existence of the Higgs boson. The work presented in this thesis tests our understanding of the strong force more than anything else. Viewed in the grand scheme, agreement between the measurements and the predictions are found, a great achievement for QCD which provides further support for the theory. The measurements of $\sigma_{t\bar{t}}$ presented in this thesis are compared to the best available theoretical predictions in Figure 10.2, where a beautiful agreement between prediction and measurement can be seen. Looking more closely however, this work shows that to use the top quark pair production cross section to test our understanding of nature more finely, the predictions themselves must becomes more precise.

A Summary of Systematic Uncertainties

The detector related systematic uncertainties considered in the analyses are summarized here.

- **JES** Jet Energy Scale, nine components in total: Calo, Eta, Noise, Flavor, b-JES, Alpgen, Perugia, Close-by, Pileup.
- **JER** Jet Energy Resolution.
- **JRE** Jet Reconstruction Efficiency.
- **JRE** Jet Reconstruction Efficiency.
- **ESS** Electron Energy Scale
- **ESR** Electron Energy Resolution
- **ESF** Electron Scale Factors, 3 components: trigger, reconstruction, identification.
- **MMS** Muon Momentum Scale.
- **MSS** Muon Momentum Resolution, considered separately for ID and MS for $\int \mathcal{L}\, dt = 0.7$ fb^{-1}.
- **MSF** Muon Scale Factors, 3 components: trigger, reconstruction, identification.
- **MET** Missing Energy Resolution, soft jet and cell out terms.
- **LAr** LAr calorimeter gap, only $\int \mathcal{L}\, dt = 0.7$ fb^{-1}.
- **b-Tag** Calibration of the b-tagging algorithm efficiency.
- **mistag** Calibration of the b-tagging algorithm mistagging rate.

In addition, contributions due to modeling of the signal are considered:

- **Generator** Considering POWHEG as signal in place of MC@NLO.
- **Hadronization** Considering PYTHIA for the parton shower of the signal simulation in place of HERWIG.
- **ISR** Initial State Radiation, increased and decreased from nominal.
- **FSR** Final State Radiation, increased and decreased from nominal.
- **PDF** Vary within envelope of PDF set uncertainty.

Modeling variations of the dominant sources of background to the signal are considered as well. Uncertainty on the rate of background processes are used directly as input to the measurement. Alternate models considered are:

- **W Shape** Generation parameters in ALPGEN varied.

- **QCD Shape** Alternate estimation from data using different method or control region.

In addition, two methodological uncertainties are considered:

- **Lumi** Luminosity normalization.
- **Template Statistics** Statistical uncertainty of MC Simulation.

B Kinematic Comparison of $t\bar{t}$ in MC@NLO and POWHEG

The basic kinematic expectations of the $t\bar{t}$ signal process generated by MC@NLO are compared to the identical distributions in POWHEG. In the analyses here, MC@NLO is used for the signal model and POWHEG is used as an alternative to assess systematic uncertainties. The samples are generated, simulated, and reconstructed as described in Chapter 4 of this thesis. All distributions are shown in the e+jets channel after object selection at the reconstruction level with no truth-matching applied. The simulation shown corresponds to the $\int \mathcal{L}\, dt = 0.7$ fb^{-1} dataset, for which a total of 15 million events were generated using MC@NLO and 3 million using POWHEG. The only error shown is statistical. The fact that limited statistics are available probably causes the estimated size of the systematic uncertainty due to this in the analyses in this thesis to be overestimated.

The p_{T} and η of both jets and the electrons are compared. The missing energy and transverse mass of the W boson are shown as well. The distribution of the CombNNJetFitter b-tagging algorithm for the most b-like jet is also shown. All comparisons use the 3-jet bin, the 4-jet bin, and the 5-jet inclusive bin, organized in jet multiplicities. All distributions are normalized to unity, shown for each distribution both overlayed and divided (MC@NLO/POWHEG).

The most interesting feature of these comparisons is seen in the leading jet p_{T} when looking at the three jet bins, shown side by side in Figure B.1. In the 3-jet bin the POWHEG simulation shows a softer spectrum than that of MC@NLO while in the 5-jet bin the trend is evidently reversed and POWHEG is harder. In the 4-jet bin the distributions are quite similar for the leading jet p_{T}. The effect is clearest in the 5-jet bin, where the trend can be seen for each jet in the event.

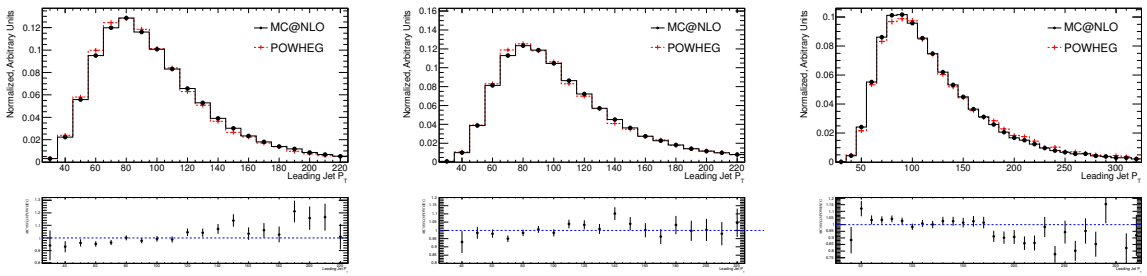

Figure B.1: Kinematic comparison of the leading jet p_{T} in MC@NLO and POWHEG in the e+jets channel. The left most plot is the 3-jet bin, followed by the 4-jet bin and the 5-jet inclsuive bin.

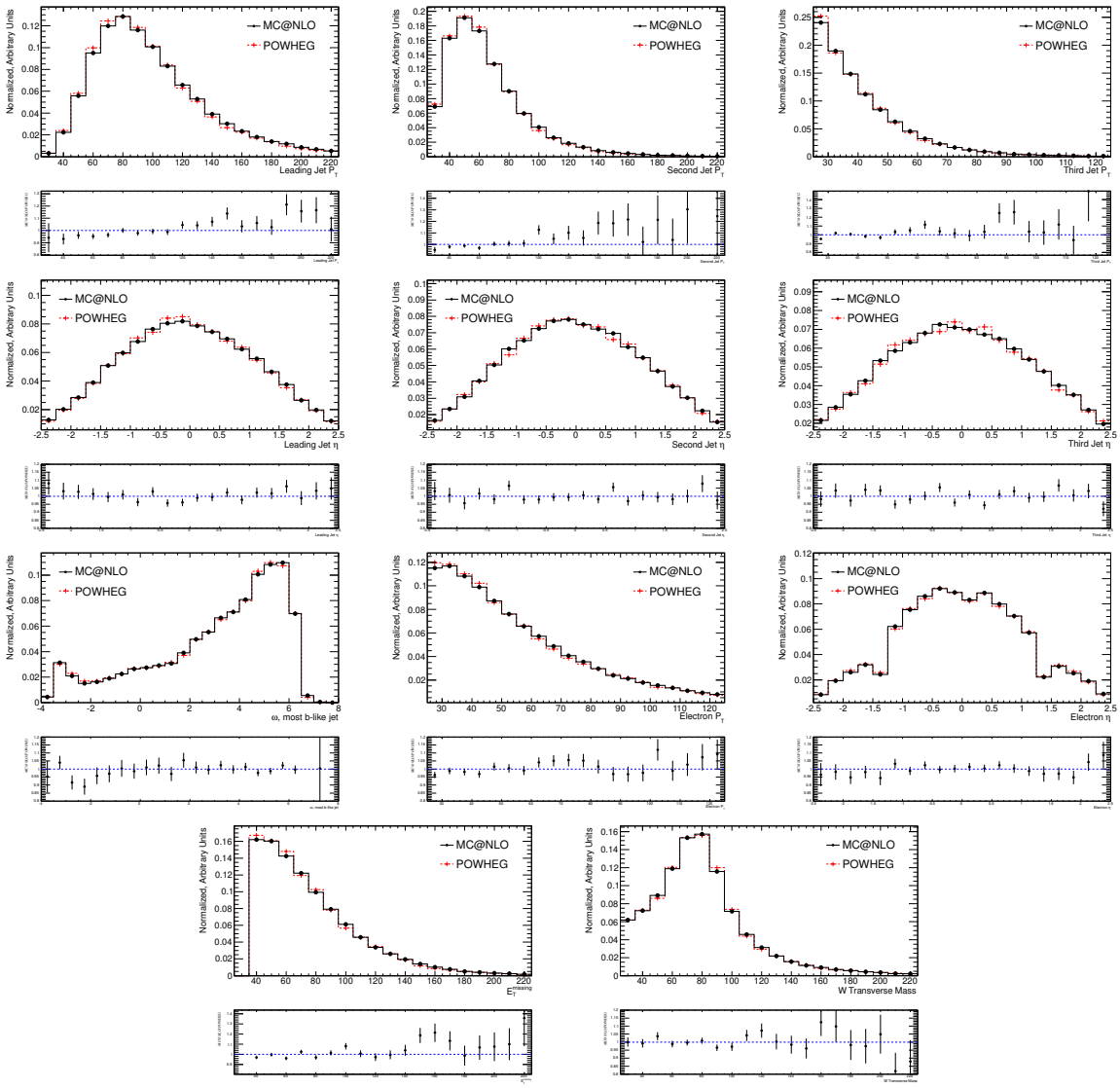

Figure B.2: Kinematic comparison of MC@NLO and POWHEG in the e+3 jets bin.

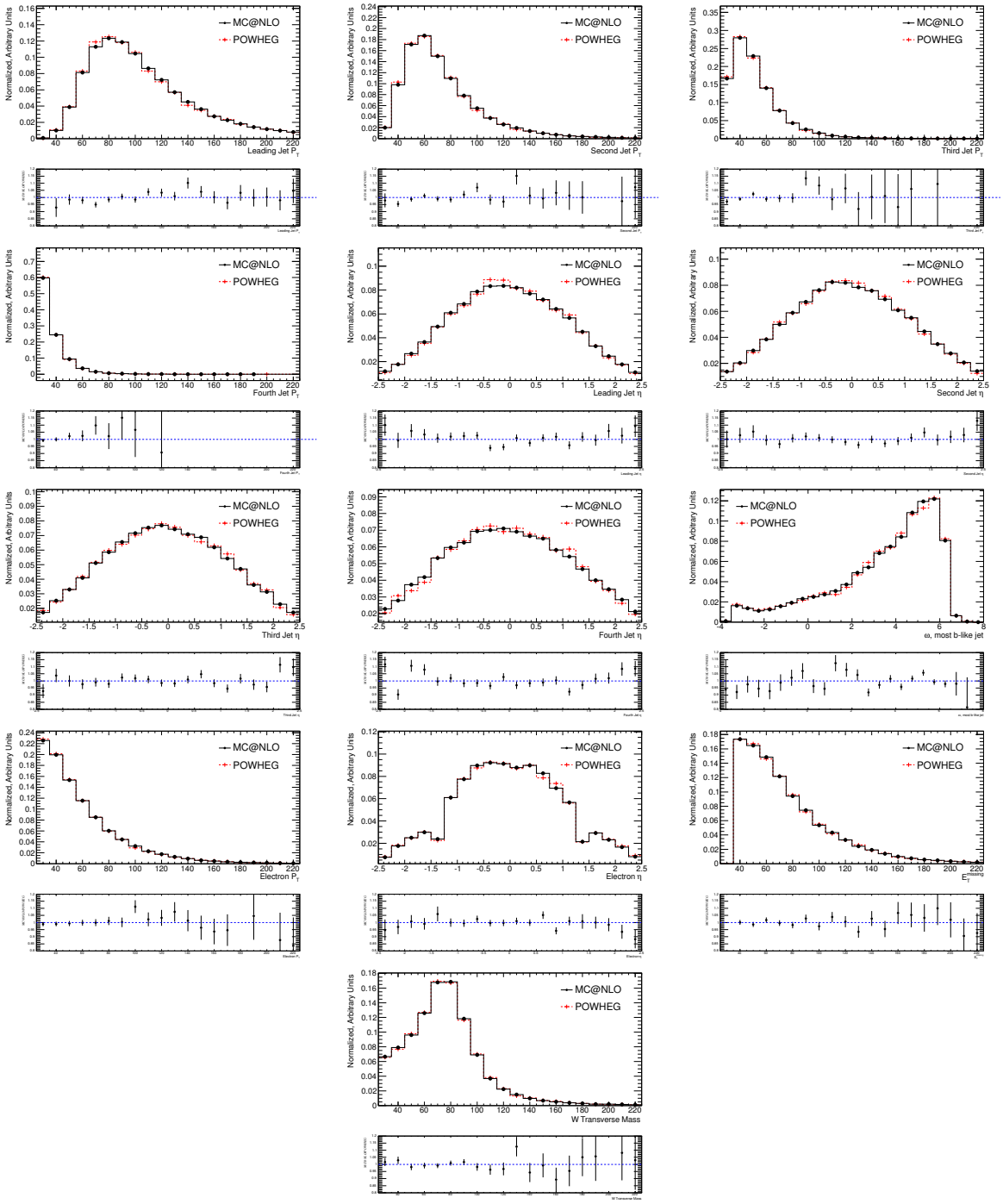

Figure B.3: Kinematic comparison of MC@NLO and POWHEG in the e+4 jets bin.

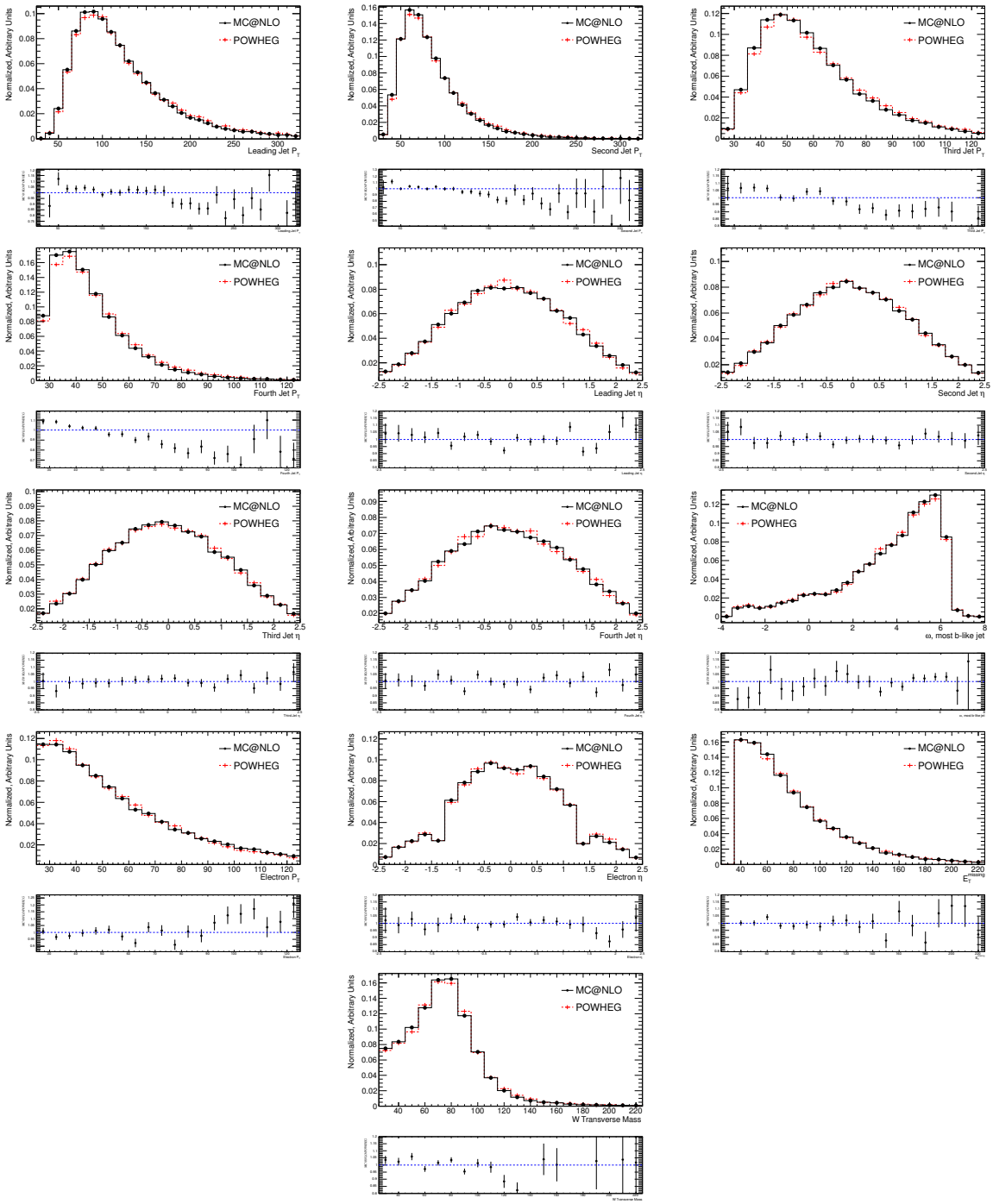

Figure B.4: Kinematic comparison of MC@NLO and POWHEG in the e+5 jets (inclusive) bin.

C Control Plots for the $\int \mathcal{L}\,dt = 35$ pb^{-1} Dataset

The expectations from MC simulation compared with observed data for the $\int \mathcal{L}\,dt = 35$ pb^{-1} dataset. All plots are shown for each jet multiplicity available, including the 4-jet bin, both inclusive and exclusive. The 5-jet bin is always inclusive. The e+jets channel is shown.

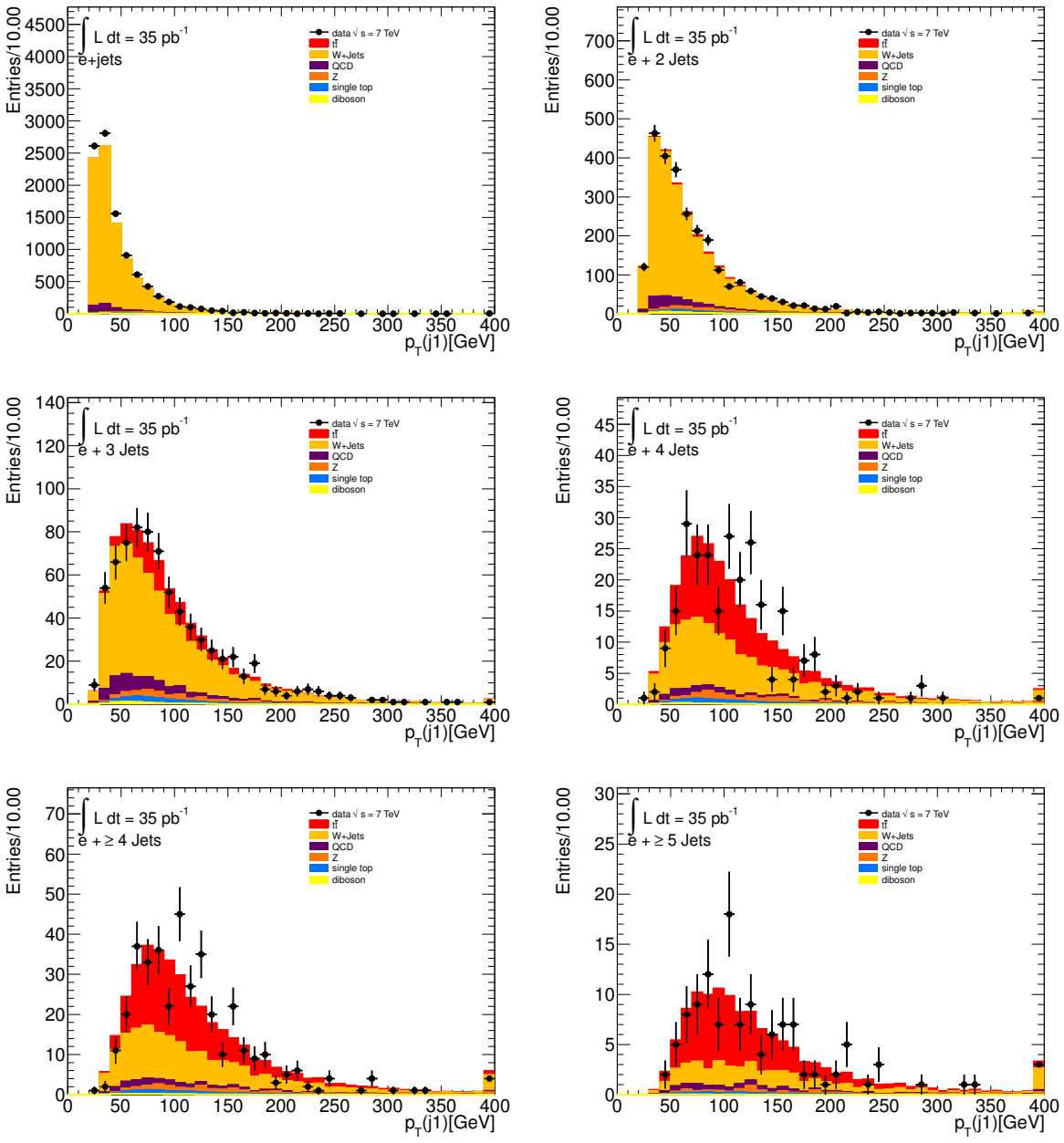

Figure C.1: Leading jet p_{T} in the e+jets channel.

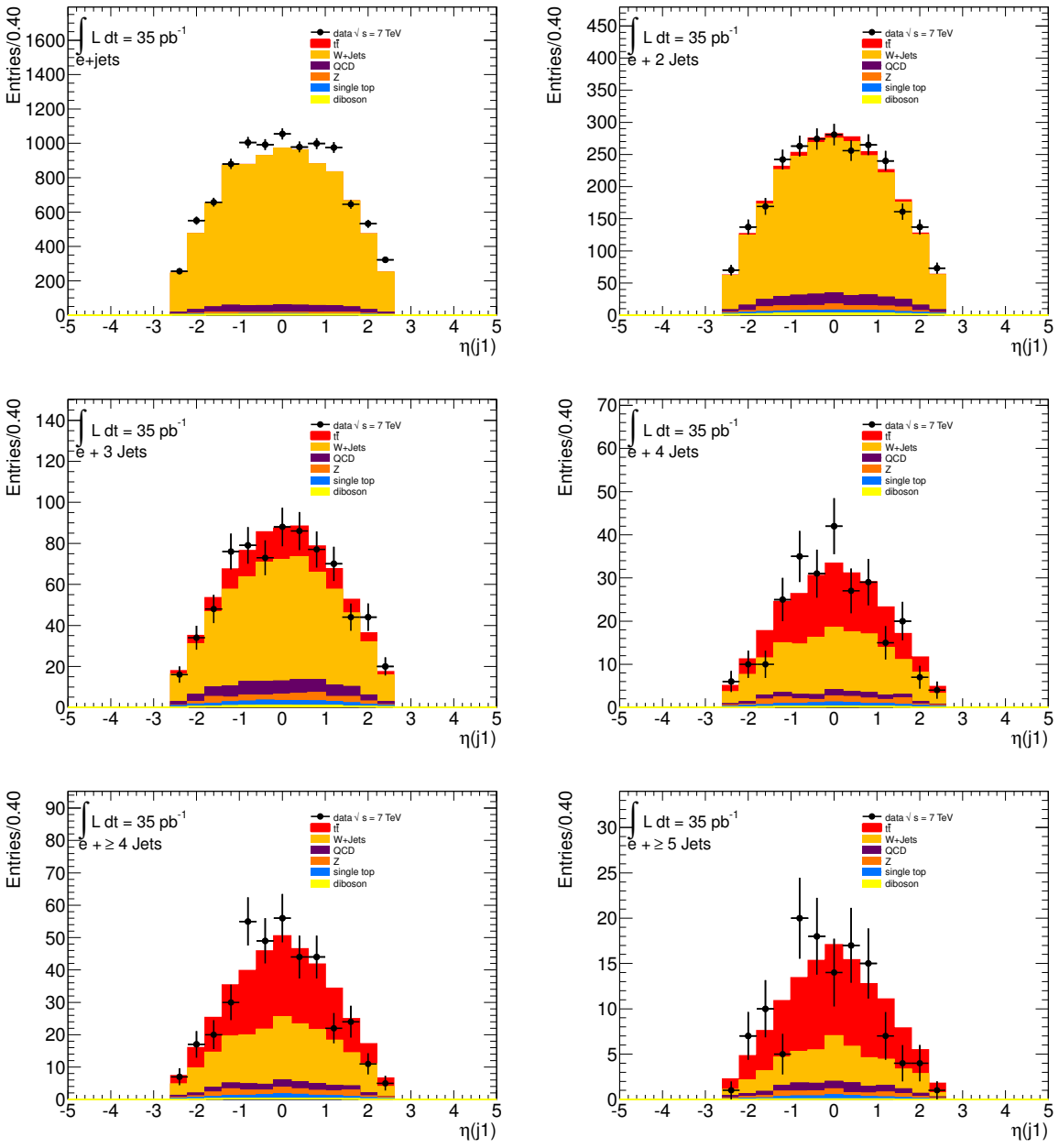

Figure C.2: Leading jet η in the e+jets channel.

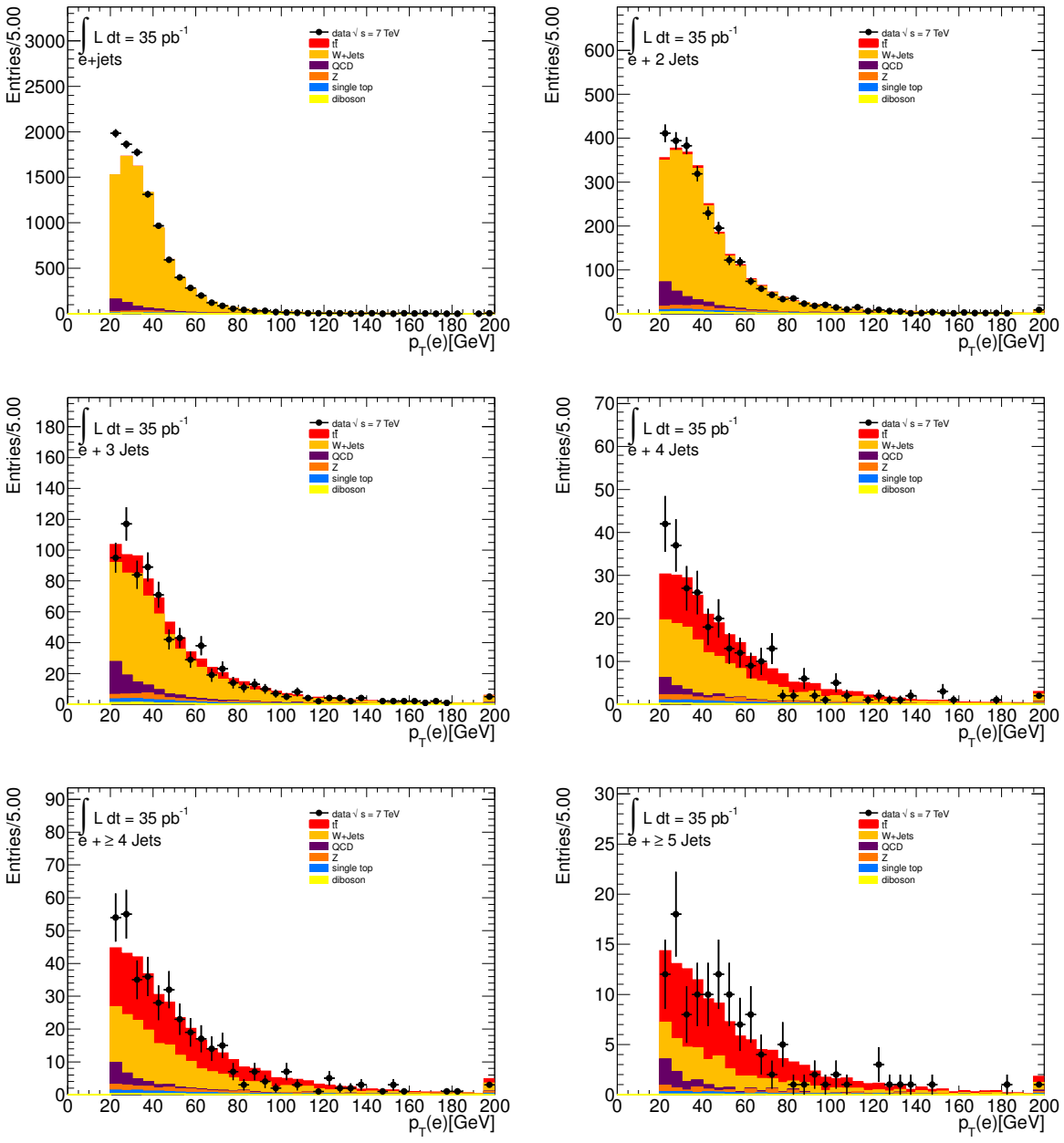

Figure C.3: Electron p_T.

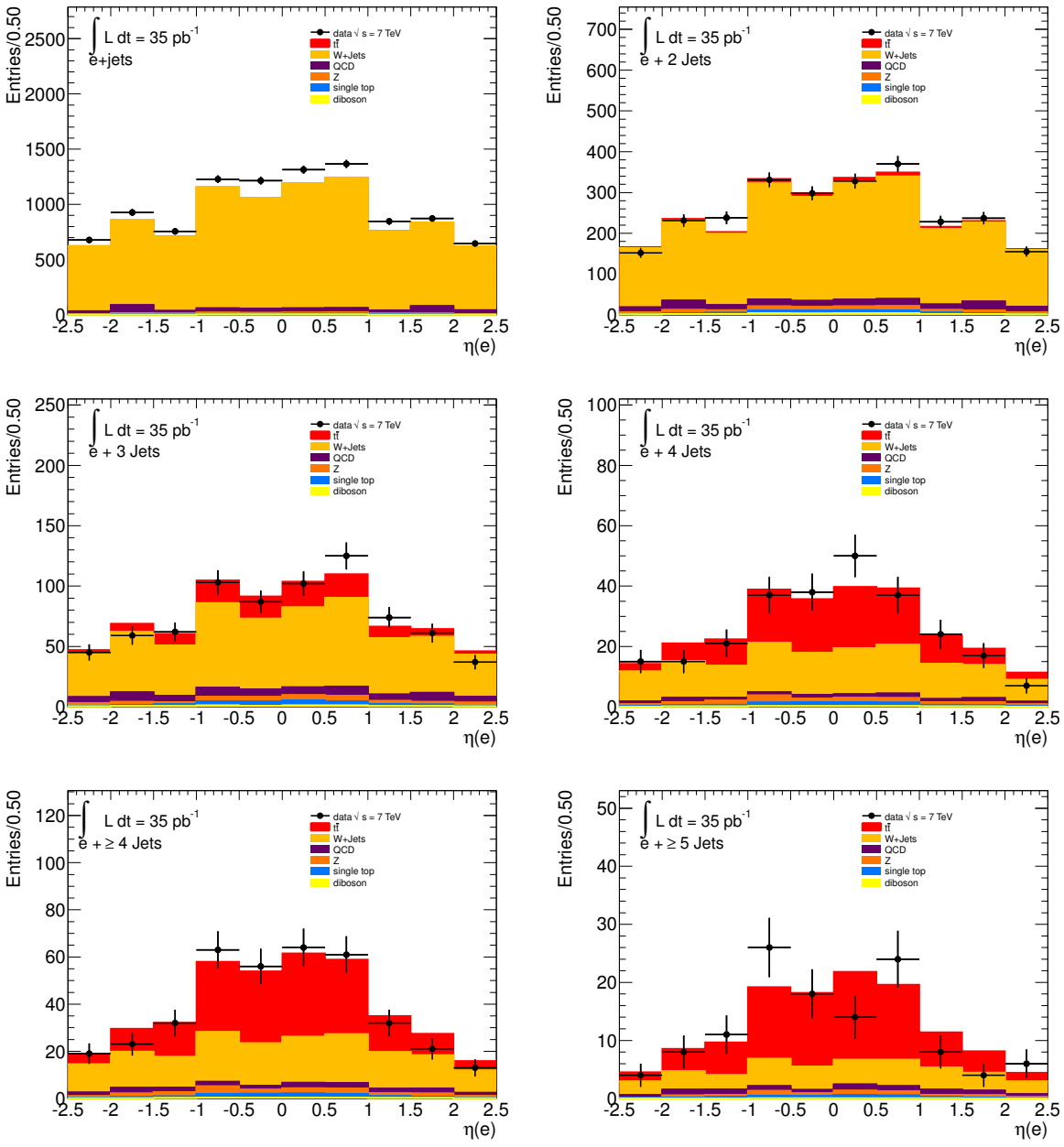

Figure C.4: Electron η.

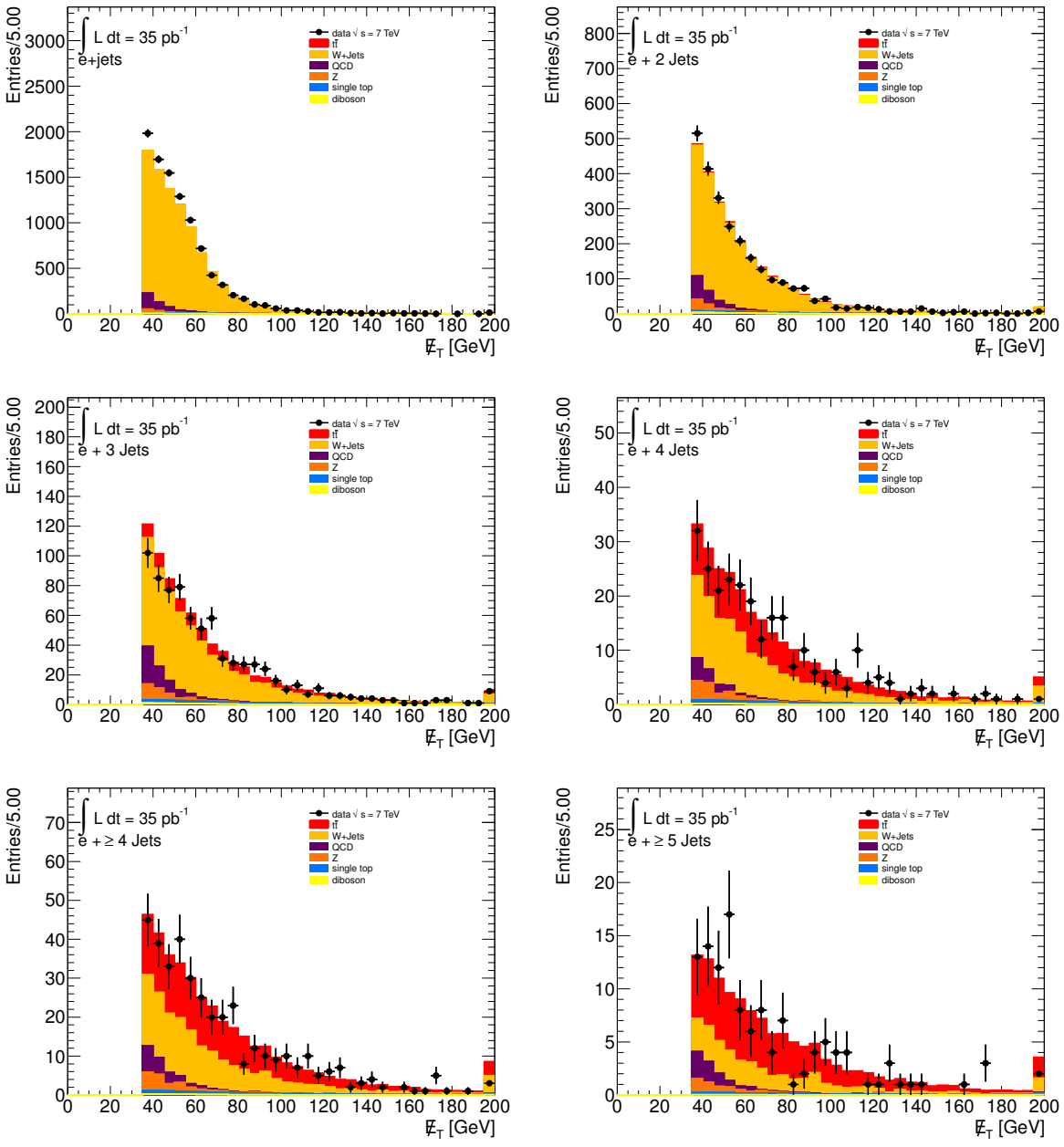

Figure C.5: $E_{\mathrm{T}}^{\mathrm{miss}}$ in the e+jets channel.

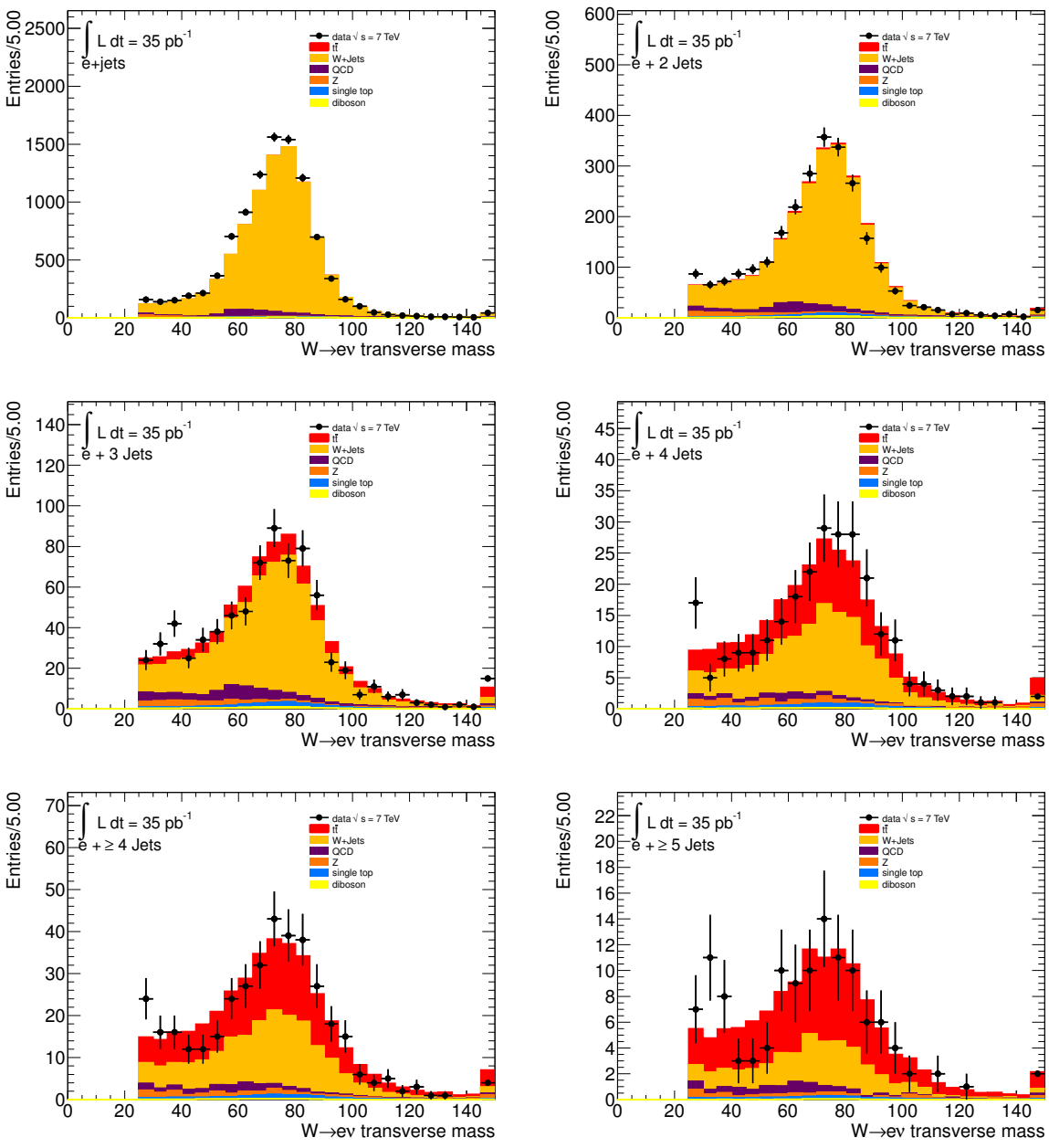

Figure C.6: $\mathrm{M_T^W}$ in the e+jets channel.

D Control Plots for the $\int \mathcal{L}\, dt = 0.7$ fb^{-1} Dataset

The expectations from MC simulation compared with observed data for the $\int \mathcal{L}\, dt = 0.7$ fb^{-1} dataset. All plots are shown for each jet multiplicity available, including the 4-jet bin, both inclusive and exclusive. The 5-jet bin is always inclusive. Both the e+jets channel and μ+jets channel are shown.

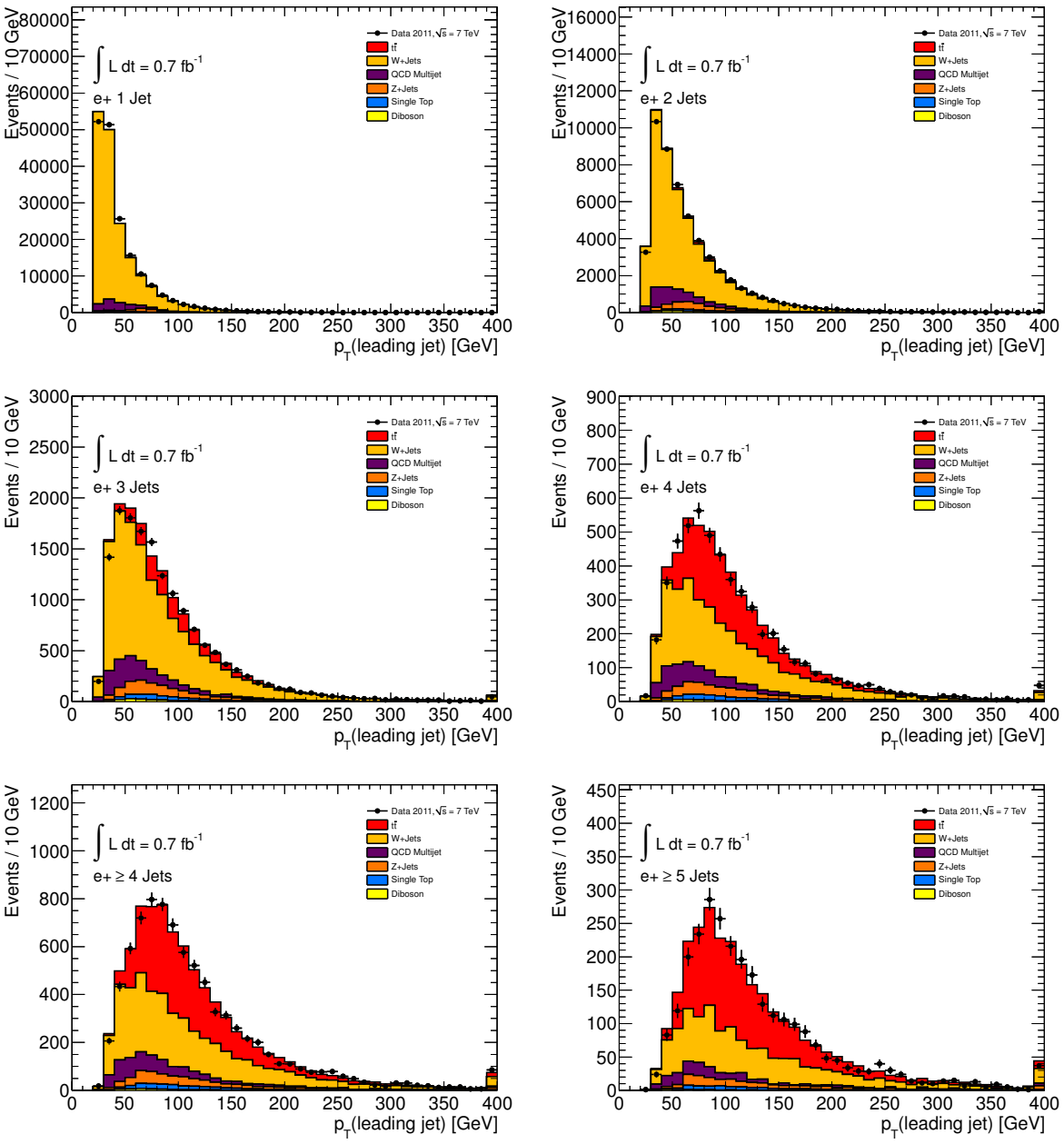

Figure D.1: Leading jet p_{T} in the e+jets channel.

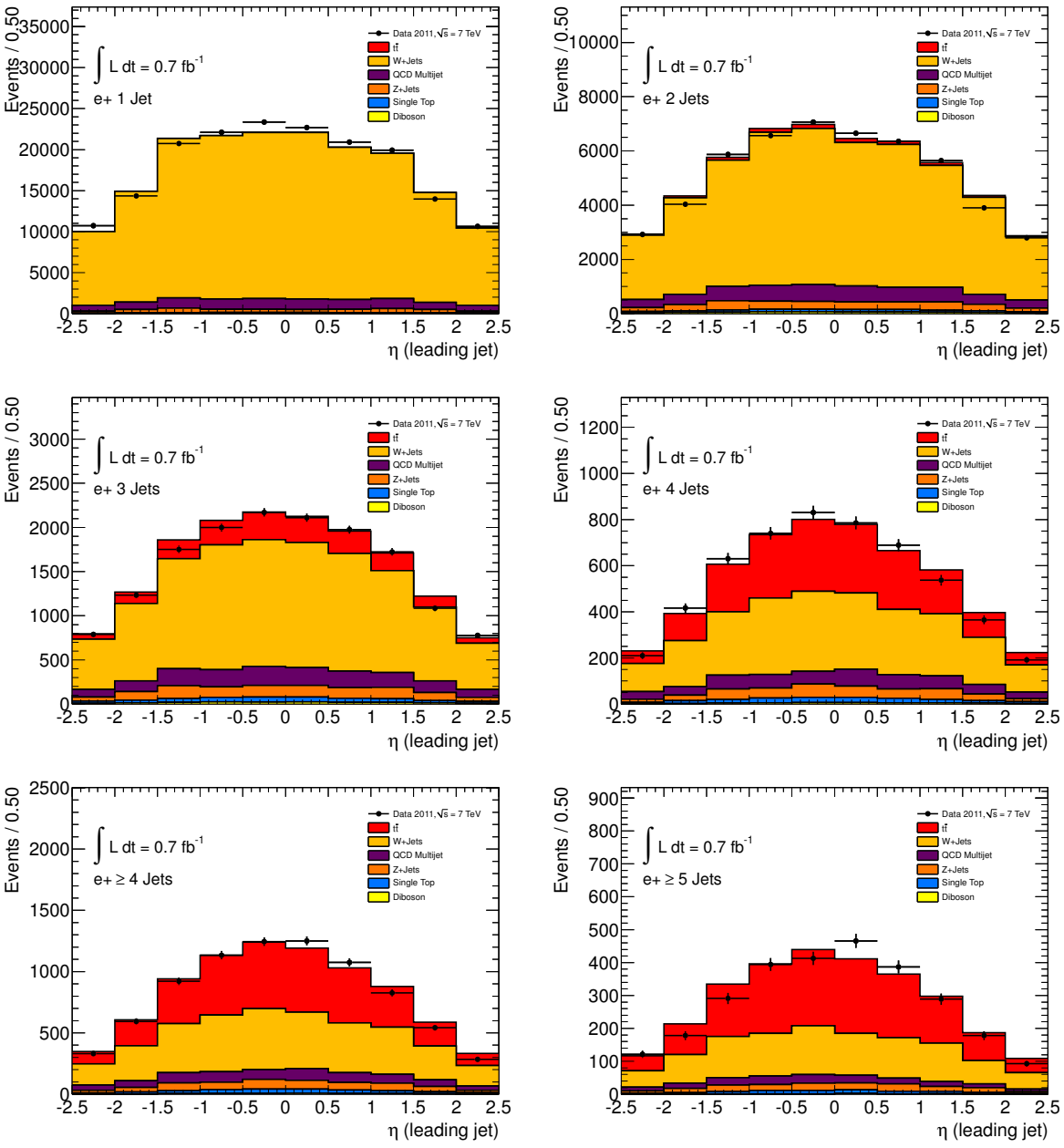

Figure D.2: Leading jet η in the e+jets channel.

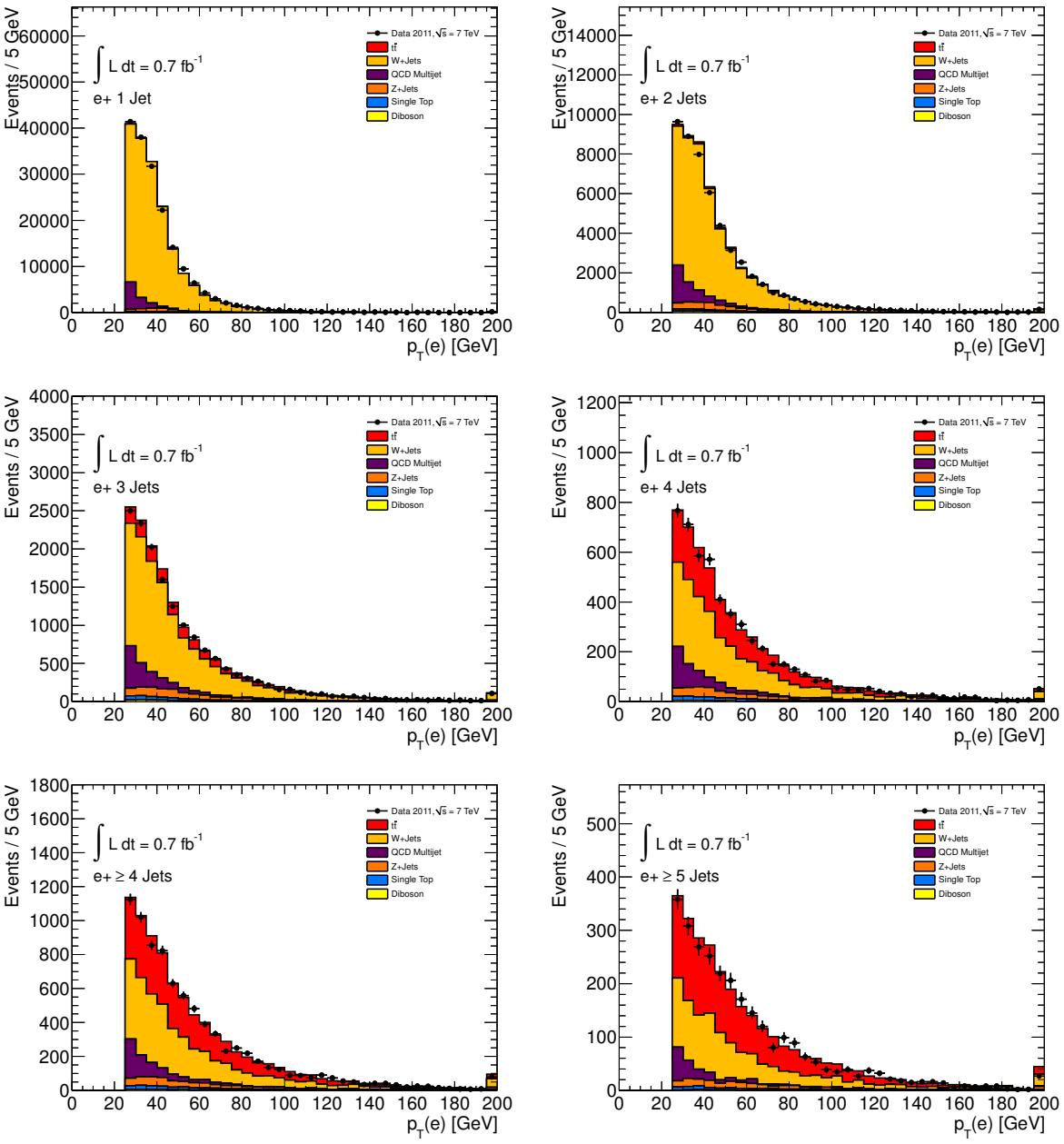

Figure D.3: Electron p_{T}.

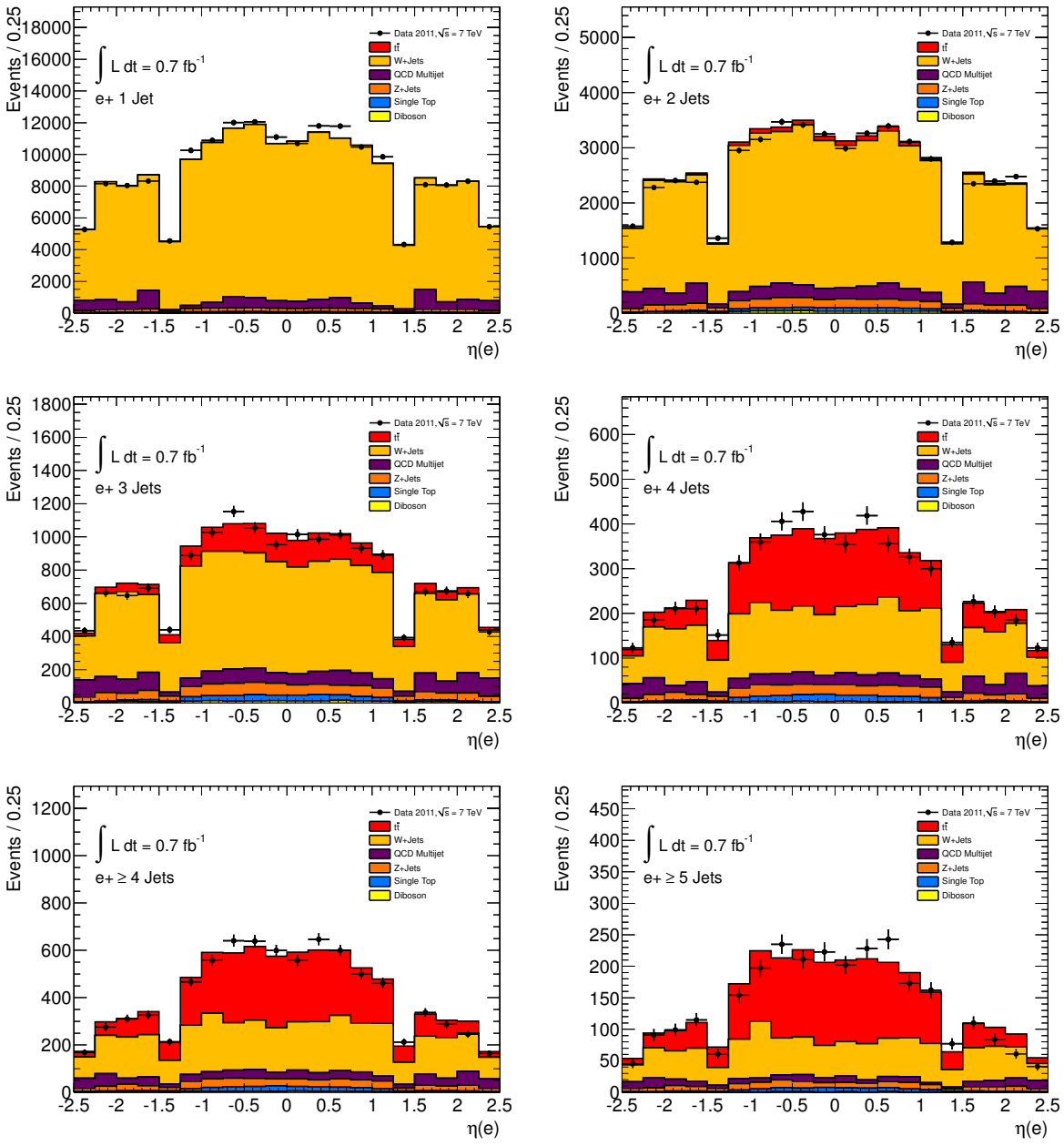

Figure D.4: Electron η.

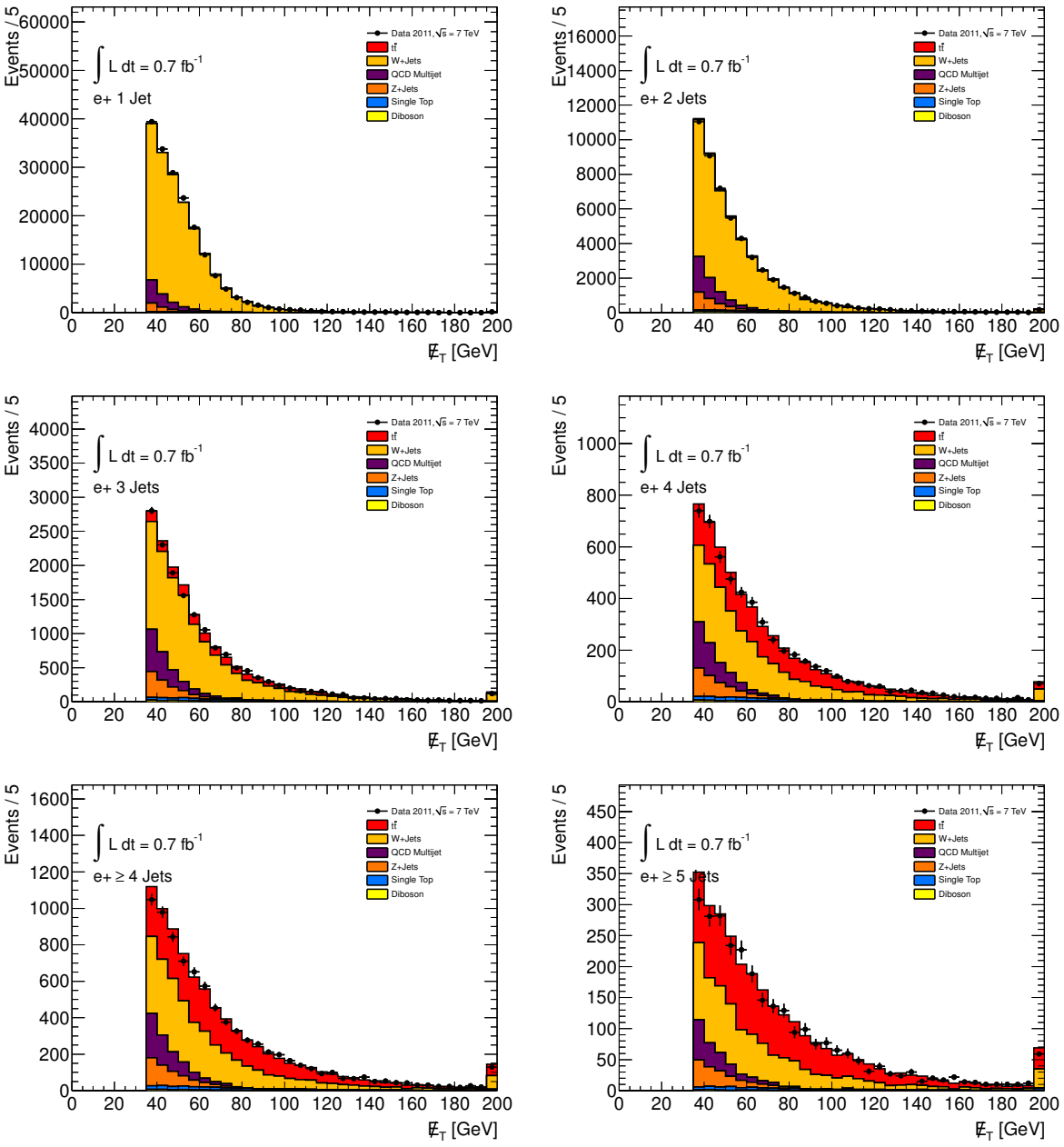

Figure D.5: $E_{\mathrm{T}}^{\mathrm{miss}}$ in the e+jets channel.

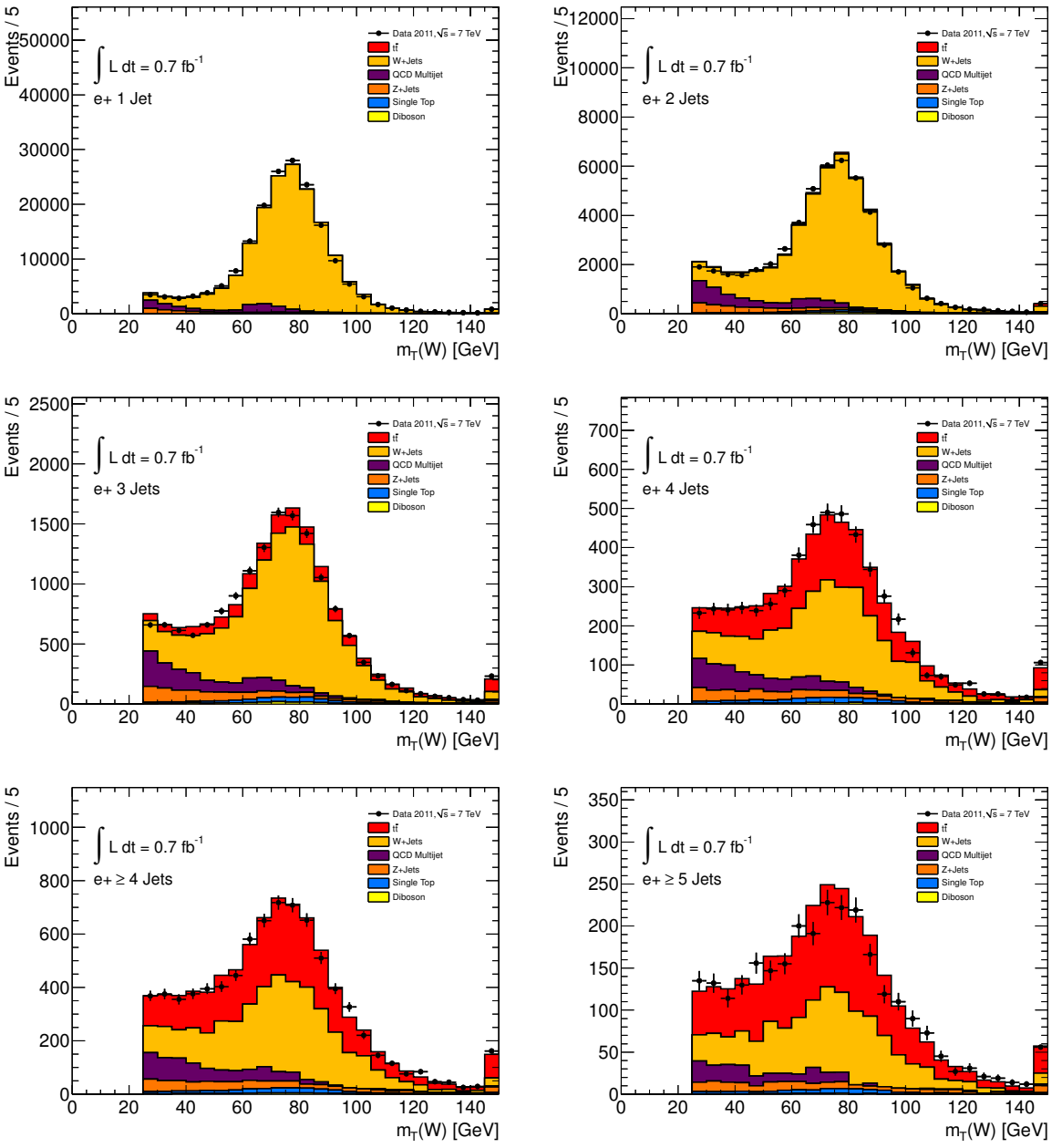

Figure D.6: $\mathrm{M_T^W}$ in the e+jets channel.

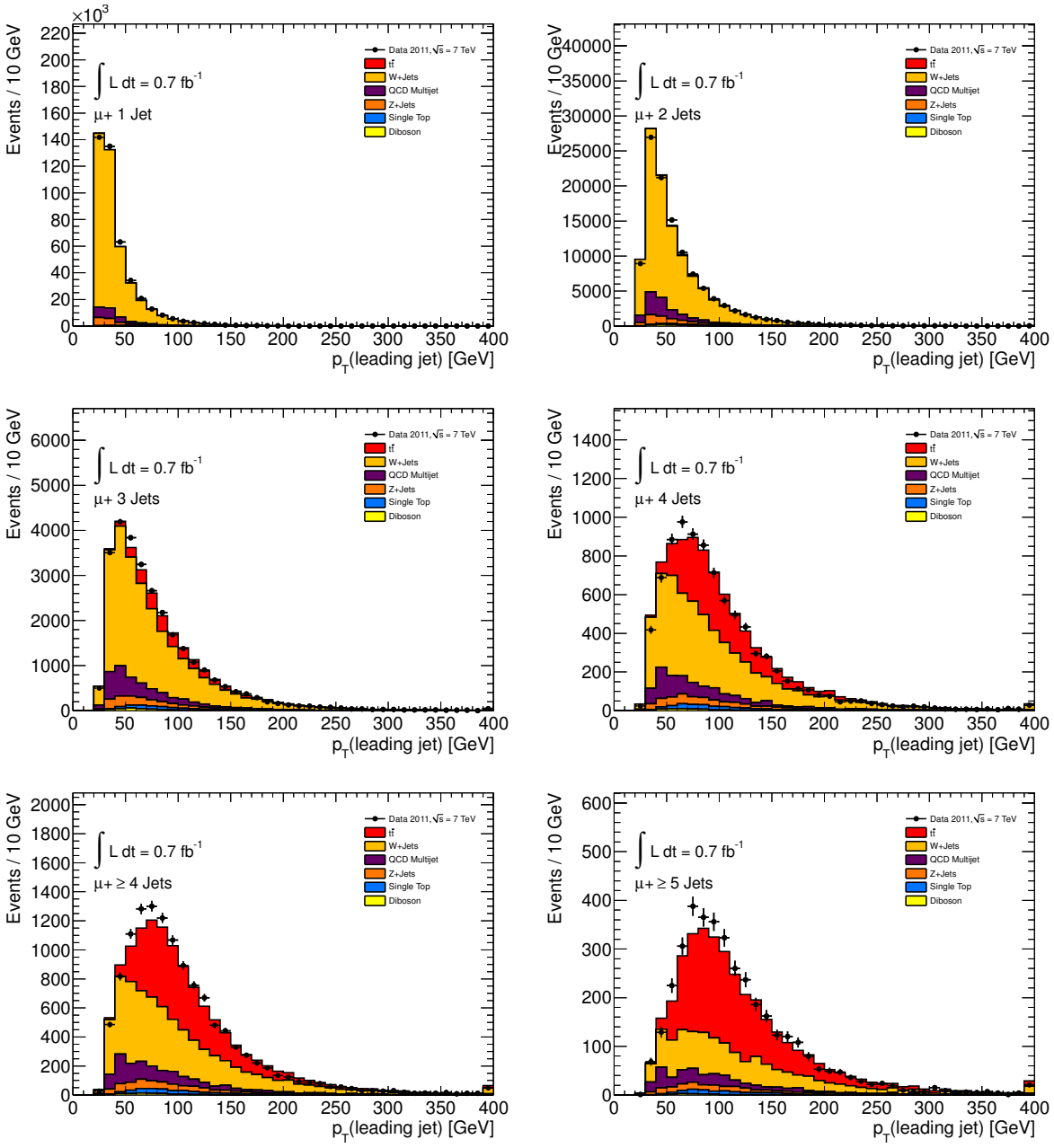

Figure D.7: Leading jet p_{T} in the μ+jets channel.

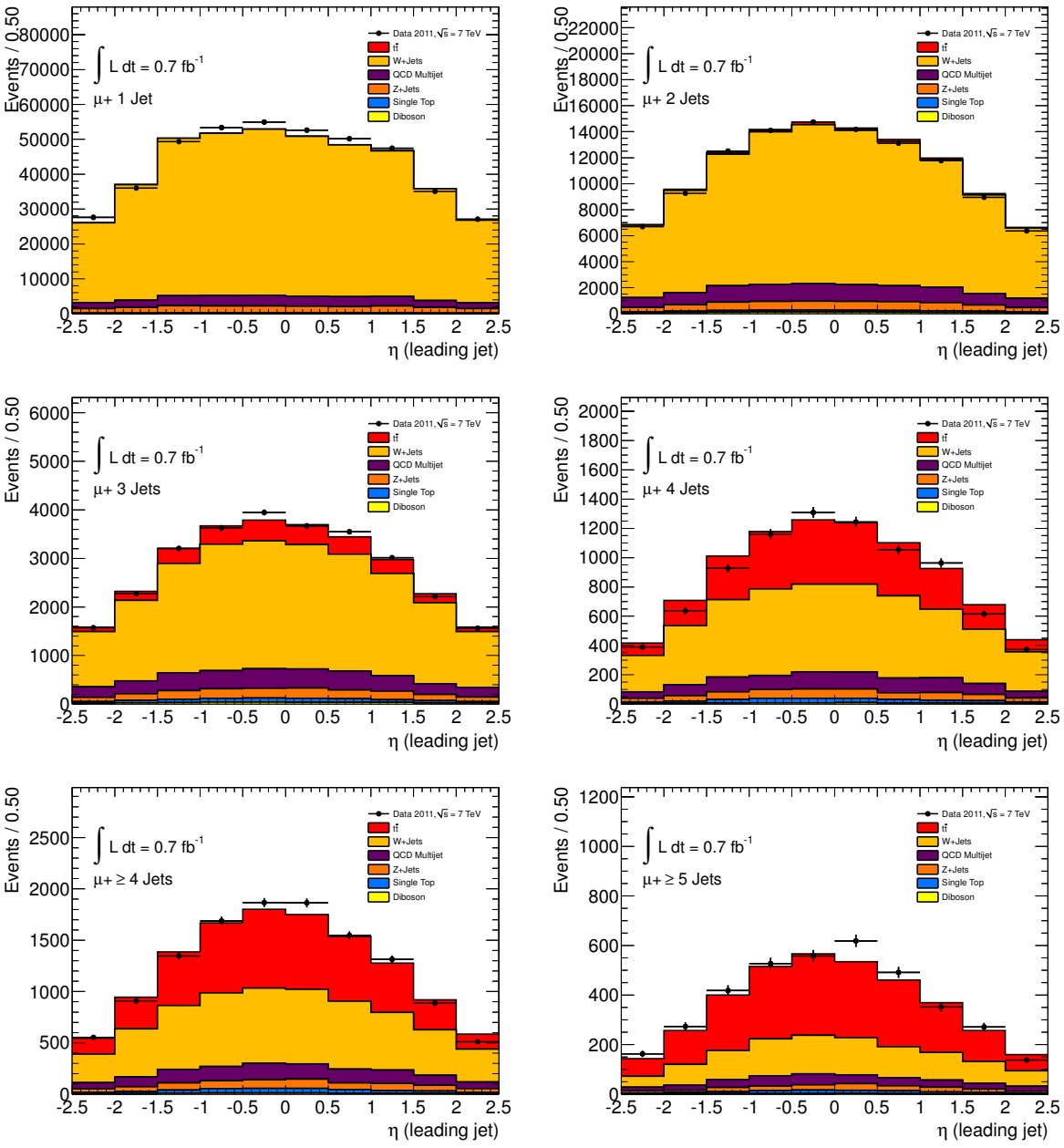

Figure D.8: Leading jet η in the μ+jets channel.

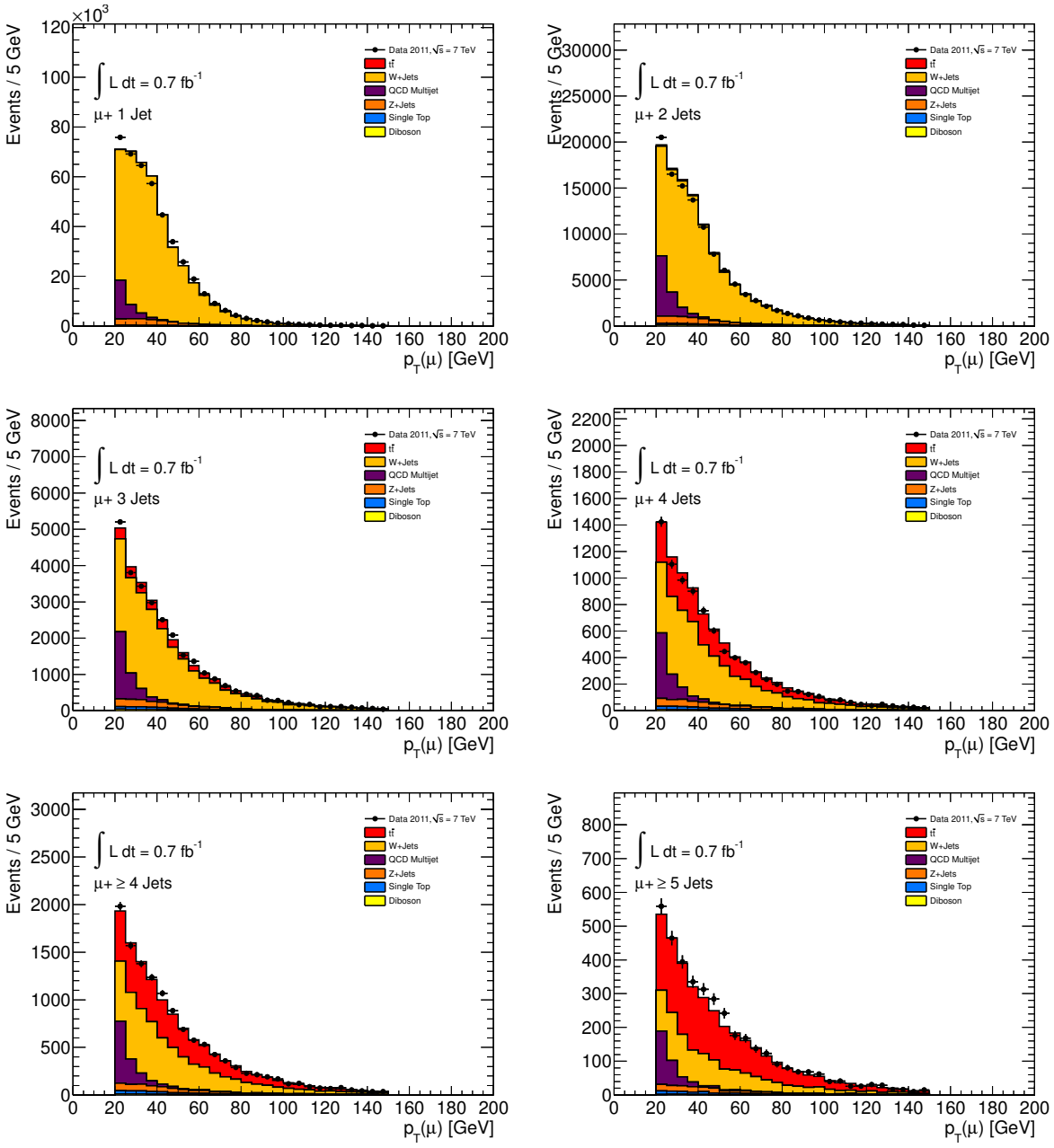

Figure D.9: Muon p_{T}.

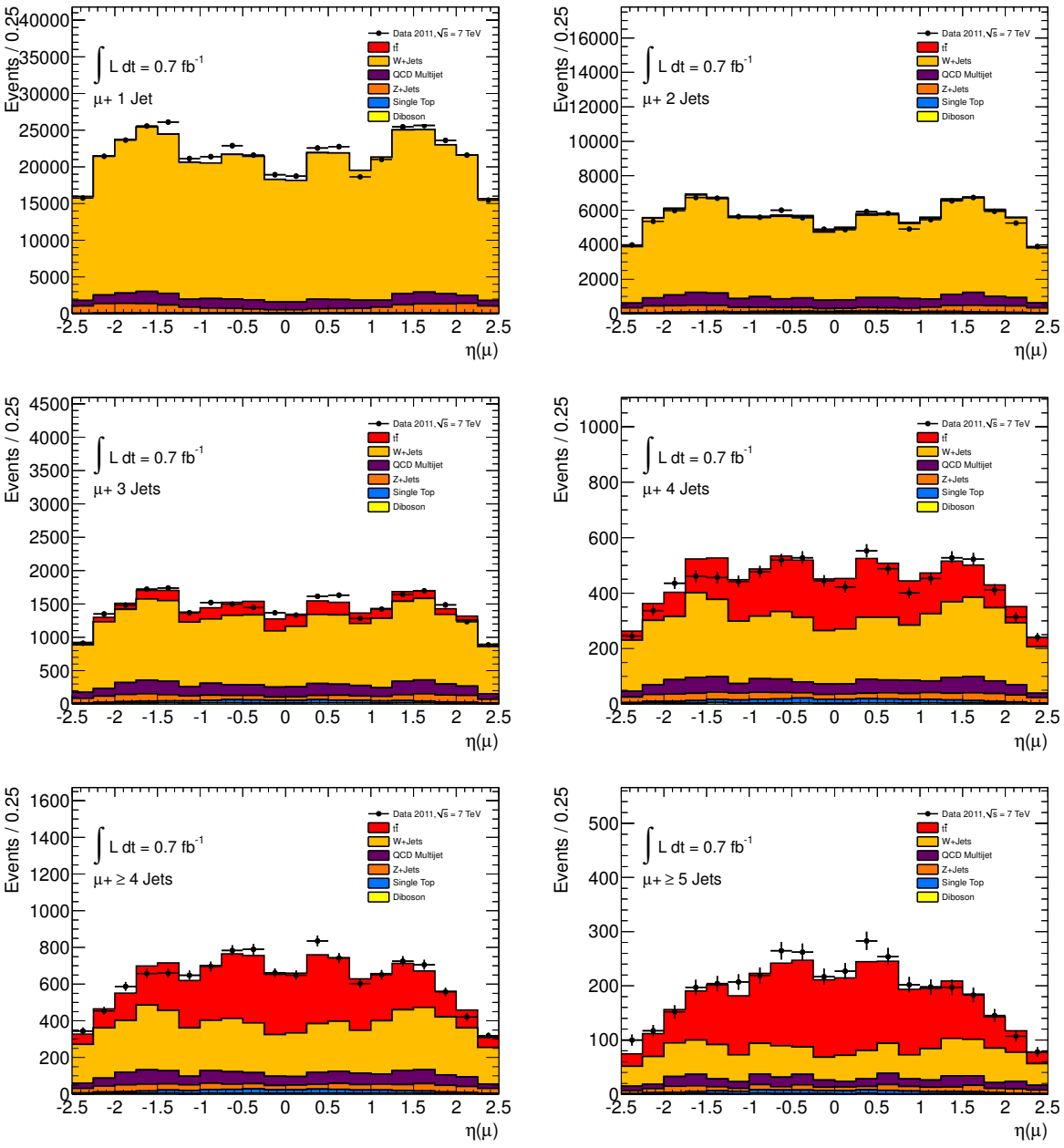

Figure D.10: Muon η.

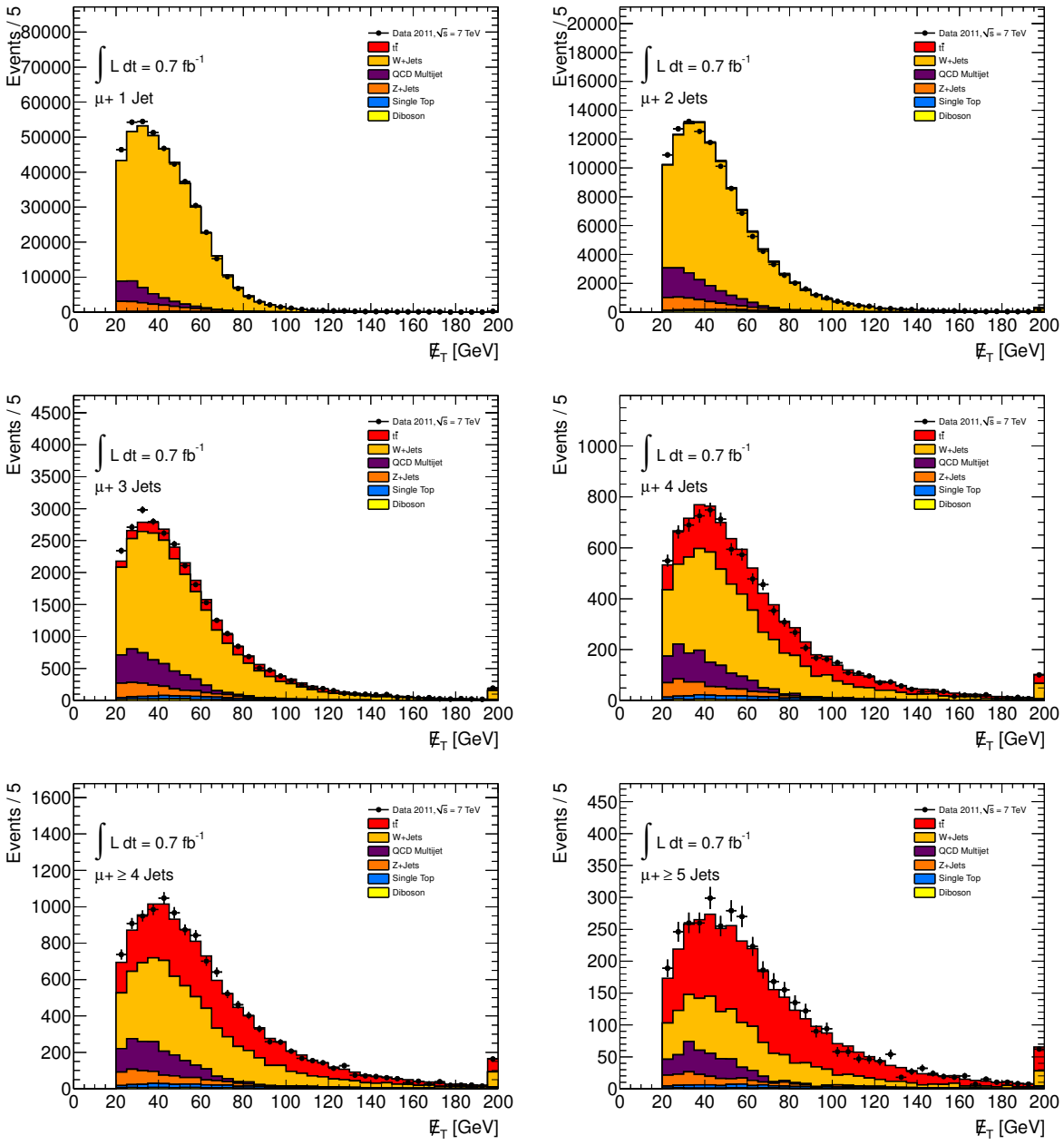

Figure D.11: $E_{\mathrm{T}}^{\mathrm{miss}}$ in the μ+jets channel.

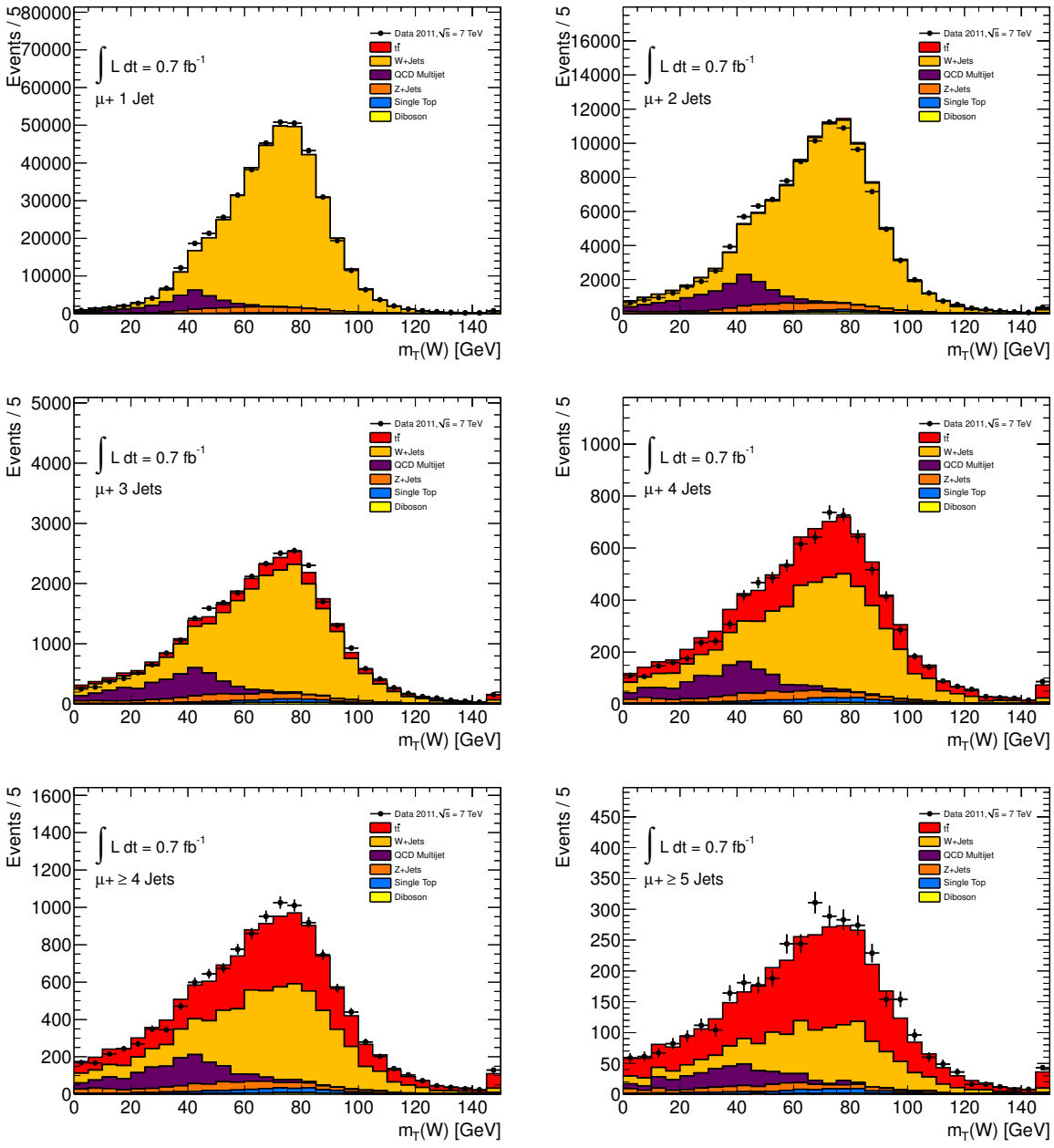

Figure D.12: $\mathrm{M_T^W}$ in the μ+jets channel.

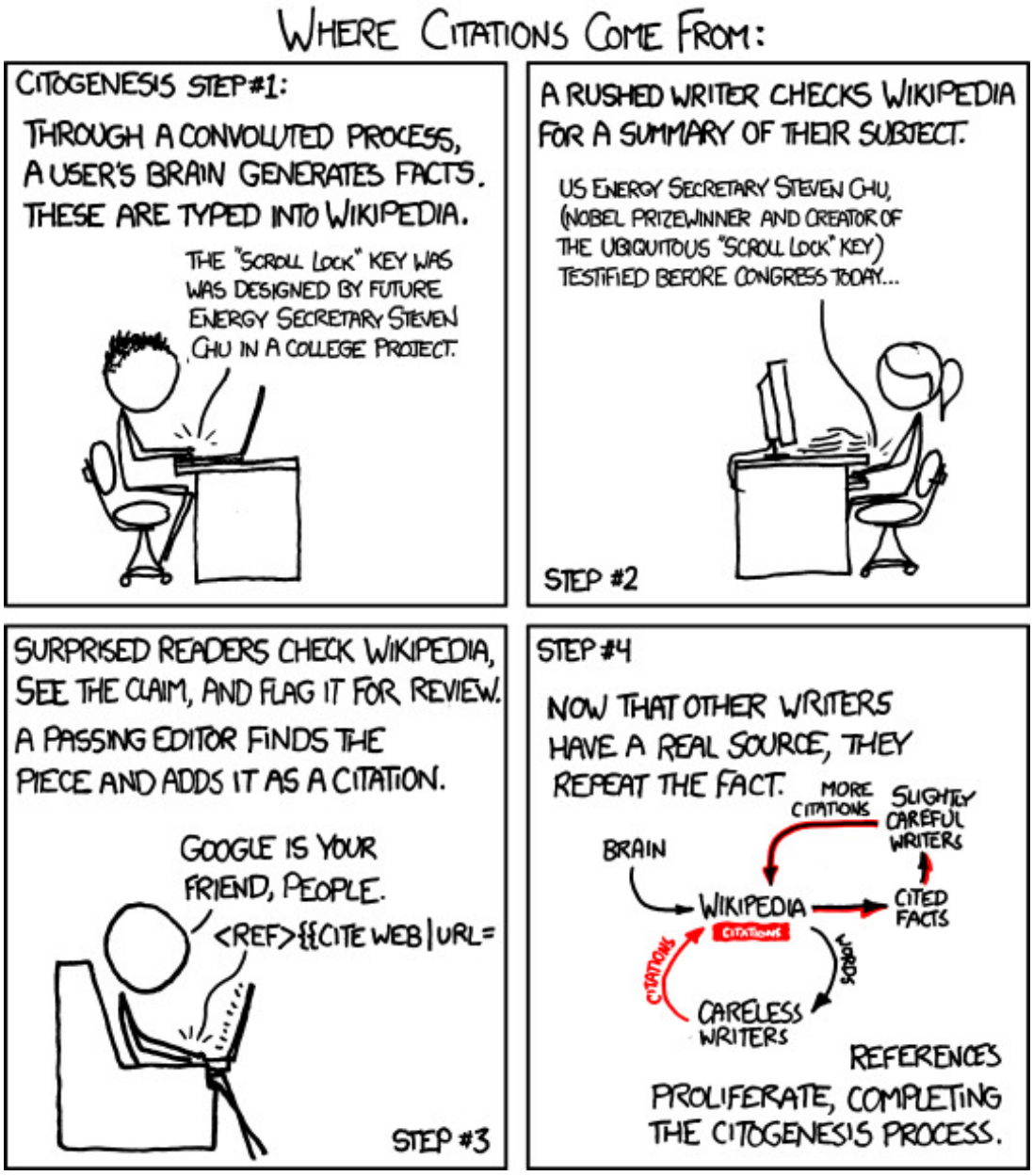

Citogenesis. "I just read a pop-science book by a respected author. One chapter, and much of the thesis, was based around wildly inaccurate data which traced back to...Wikipedia. To encourage people to be on their toes, I'm not going to say what book or author."[19]

Bibliography

[1] W. Pauli, *Pauli letter collection: letter to Lise Meitner*, Pauli Archives, CERN.

[2] H. Geiger and E. Marsden, *On a Diffuse Reflection of the α-Particles*, Proceedings of the Royal Society of London. Series A **82(557)** (1909) 495.

[3] E. Rutherford, *The scattering of α and β particles by matter and the structure of the atom*, Philosophical Magazine Series 6 **21(125)** (1911) 669.

[4] R. R. D. Ulam S, von Neumann J, *Statistical Methods in Neutron Diffusion*, Letter, April 9, 1947. LAMS-551.

[5] The Atlas Collaboration, G. Aad *et al.*, *Measurement of the top quark-pair production cross section with ATLAS in pp collisions at $\sqrt{s} = 7$ TeV*, Eur.Phys.J. **C71** (2011) 1577, hep-ph/1012.1792.

[6] The CMS Collaboration, V. Khachatryan *et al.*, *First Measurement of the Cross Section for Top-Quark Pair Production in Proton-Proton Collisions at $\sqrt{s} = 7$ TeV*, Phys.Lett. **B695** (2011) 424, hep-ph/1010.5994.

[7] P. Nason and B. Webber, *Next-to-Leading-Order Event Generators*, hep-ph/1202.1251.

[8] S. Frixione and B. R. Webber, *Matching NLO QCD computations and parton shower simulations*, JHEP **0206** (2002) 029, hep-ph/0204244.

[9] S. Frixione, P. Nason, and B. R. Webber, *Matching NLO QCD and parton showers in heavy flavor production*, JHEP **0308** (2003) 007, hep-ph/0305252.

[10] P. Nason, *A New method for combining NLO QCD with shower Monte Carlo algorithms*, JHEP **0411** (2004) 040, hep-ph/0409146.

[11] S. Hoeche, F. Krauss, M. Schonherr, and F. Siegert, *A critical appraisal of NLO+PS matching methods*, hep-ph/1111.1220.

[12] J. M. Campbell, K. R. Ellis, and C. Williams, *MCFM: A Monte Carlo for FeMtobarn processes at Hadron Colliders*, User's Guide, http://mcfm.fnal.gov/mcfm.pdf.

[13] M. Aliev *et al.*, *HATHOR: HAdronic Top and Heavy quarks crOss section calculatoR*, Comput.Phys.Commun. **182** (2011) 1034, hep-ph/1007.1327.

[14] V. Ferrara, A. Henrichs, U. Husemann, C. Lange, A. Quadt, A. Roe, E. Shabalina, and H. Zhu, *Measurement of the top quark cross-section in the semileptonic channel in pp collisions at $\sqrt{s}$=7 TeV using kinematic fits and b-tagging information*, ATL-COM-PHYS-2011-1012.

[15] V. Ahrens, M. Neubert, B. D. Pecjak, A. Ferroglia, and L. L. Yang, *Precision predictions for the $t\bar{t}$ production cross section at hadron colliders*, Phys.Lett. **B703** (2011) 135, 1105.5824.

[16] *Measurement of the ttbar production cross-section in pp collisions at $\sqrt{s}$ = 7 TeV using kinematic information of lepton+jets events.*

[17] The ATLAS Collaboration, G. Aad *et al.*, *Measurement of the top quark pair production cross-section with ATLAS in the single lepton channel*, `hep-ex/1201.1889`, Submitted to Phys. Lett. B 9 January 2012.

[18] A. D. Roeck, *Top Production at Hadron Colliders*, XXV International Symposium on Lepton Photon Interactions at High Energies. Mumbai, India, 22-27 August 2011. Proceedings not yet published.

[19] *XKCD*, Comic reprinted from xkcd.com, February 2012.

[20] P. A. M. Dirac, *The Quantum Theory of the Electron*, Proceedings of the Royal Society of London. Series A **117(778)** (1928) 610.

[21] K. Nakamura and P. D. Group, *Review of Particle Physics*, Journal of Physics G: Nuclear and Particle Physics (2010) 075021, Updated online in 2011, http://pdg.lbl.gov/.

[22] The Tevatron Electroweak Working Group, for the CDF and DØ Collaborations Collaboration, *Combination of CDF and DØ results on the mass of the top quark using up to 5.8fb^{-1} of data*, `hep-ph/1107.5255`.

[23] The Super-Kamiokande Collaboration, Y. Fukuda *et al.*, *Measurements of the solar neutrino flux from Super-Kamiokande's first 300 days*, Phys.Rev.Lett. **81** (1998) 1158, `hep-ex/9805021`.

[24] The MINOS Collaboration, D. Michael *et al.*, *Observation of muon neutrino disappearance with the MINOS detectors and the NuMI neutrino beam*, Phys.Rev.Lett. **97** (2006) 191801, `hep-ex/0607088`.

[25] The MINOS Collaboration, P. Adamson *et al.*, *Measurement of Neutrino Oscillations with the MINOS Detectors in the NuMI Beam*, Phys. Rev. Lett. **101** (2008) 131802, `hep-ph/0806.2237`.

[26] The K2K Collaboration, M. H. Ahn *et al.*, *Measurement of Neutrino Oscillation by the K2K Experiment*, Phys. Rev. **D74** (2006) 072003, `hep-ex/0606032`.

[27] The KamLAND Collaboration, T. Araki *et al.*, *Measurement of neutrino oscillation with KamLAND: Evidence of spectral distortion*, Phys.Rev.Lett. **94** (2005) 081801, `hep-ex/0406035`.

[28] E. K. Akhmedov, *Do charged leptons oscillate?*, JHEP **0709** (2007) 116, `hep-ph/0706.1216`.

[29] D. Griffiths, *Introduction to Elementary Particles*, John Wiley and Sons, Inc., (1987).

[30] C. S. Wu, E. Ambler, R. W. Hayward, D. D. Hoppes, and R. P. Hudson, *Experimental Test of Parity Conservation in Beta Decay*, Phys. Rev. **105** (Feb 1957) 1413.

[31] S. Weinberg, *A Model of Leptons*, Phys. Rev. Lett. **19** (1967) 1264.

[32] S. Glashow, *Partial Symmetries of Weak Interactions*, Nucl. Phys. **22** (1961) 579.

[33] A. Salam, *Weak and Electromagnetic Interactions*, in: *Elementary Particle Theory*, Stockholm, (1968), Almquist and Wiksell, 1968 p. 367.

[34] C. Quigg, *The Double Simplex*, `hep-ph/0509037`, 2005.

[35] P. Higgs, *Broken Symmetries, Massless Particles and Gauge Fields*, Phys. Lett. **12** (1964) 132.

[36] P. Higgs, *Broken Symmetries and the Masses of Gauge Bosons*, Phys. Rev. Lett. **13** (1964) 508.

[37] *Combination of Higgs Boson Searches with up to 4.9 fb^{-1} of pp Collisions Data Taken at a center-of-mass energy of 7 TeV with the ATLAS Experiment at the LHC*, ATLAS-CONF-2011-163.

[38] *Combination of SM Higgs Searches*, CMS-PAS-HIG-11-032.

[39] The Belle Collaboration, A. Bondar *et al.*, *Observation of two charged bottomonium-like resonances in Y(5S) decays*, `1110.2251`.

[40] V. Crede and C. Meyer, *The Experimental Status of Glueballs*, Prog.Part.Nucl.Phys. **63** (2009) 74, `hep-ph/0812.0600`.

[41] B. W. R. K. Ellis, W.J. Stirling, *QCD and Collider Physics*, Cambridge University Press, (2003), Cambridge Monographs on Particle Physics, Nuclear Physics and Cosmology: 8.

[42] K. G. Chetyrkin, B. A. Kniehl, and M. Steinhauser, *Strong Coupling Constant with Flavor Thresholds at Four Loops in the Modified Minimal-Subtraction Scheme*, Phys. Rev. Lett. **79** (Sep 1997) 2184.

[43] M. Czakon, *The Four-loop QCD beta-function and anomalous dimensions*, Nucl.Phys. **B710** (2005) 485, `hep-ph/0411261`.

[44] D. Politzer, *Reliable Perturbative Results for Strong Interactions?*, Phys. Rev. Lett. **30** (1973) 1346.

[45] D. Gross and F. Wilczek, *Ultraviolet Behaviour of Non-Abelian Gauge Theories*, Phys. Rev. Lett. **30** (1973) 1343.

[46] *The Nobel Prize in Physics 2004*, 15 January 2012, http://www.nobelprize.org/nobel_prizes/physics/laureates/2004/.

[47] *The Hamburger Postulate*, Season 1, Episode 5 of The Big Bang Theory. Directed by Andrew D. Weyman. First aired 22 October 2007.

[48] S. Bethke, *The 2009 World Average of alpha(s)*, Eur.Phys.J. **C64** (2009) 689, `hep-ph/0908.1135`.

[49] S. W. Herb *et al.*, *Observation of a Dimuon Resonance at 9.5 GeV in 400-GeV Proton-Nucleus Collisions*, Phys. Rev. Lett. **39** (Aug 1977) 252.

[50] M. Kobayashi and T. Maskawa, *CP Violation in the Renormalizable Theory of Weak Interaction*, Prog.Theor.Phys. **49** (1973) 652.

[51] *The Nobel Prize in Physics 2008*, 15 January 2012, http://www.nobelprize.org/nobel_prizes/physics/laureates/2008/.

[52] The ALEPH Collaboration, DELPHI Collaboration, L3 Collaboration, OPAL Collaboration, SLD Collaboration, LEP Electroweak Working Group, SLD Electroweak Group, SLD Heavy Flavour Group Collaboration, *Precision electroweak measurements on the Z resonance*, Phys.Rept. **427** (2006) 257, `hep-ex/0509008`.

[53] The DØ Collaboration, S. Abachi *et al.*, *Observation of the top quark*, Phys.Rev.Lett. **74** (1995) 2632, `hep-ex/9503003`.

[54] The CDF Collaboration, F. Abe *et al.*, *Observation of top quark production in anti-p p collisions*, Phys. Rev. Lett. **74** (1995) 2626, `hep-ex/9503002`.

[55] The DØ Collaboration, V. Abazov *et al.*, *Observation of Single Top Quark Production*, Phys.Rev.Lett. **103** (2009) 092001, `hep-ph/0903.0850`.

[56] The CDF Collaboration, T. Aaltonen *et al.*, *First Observation of Electroweak Single Top Quark Production*, Phys.Rev.Lett. **103** (2009) 092002, `hep-ph/0903.0885`.

[57] The DØ Collaboration, V. M. Abazov *et al.*, *Simultaneous Measurement of the Ratio* $R = \mathcal{B}(t \to Wb)/\mathcal{B}(t \to Wq)$ *and the Top-Quark Pair Production Cross Section with the DØ Detector at* $\sqrt{s} = 1.96$ *TeV*, Phys. Rev. Lett. **100** (May 2008) 192003.

[58] The CDF Collaboration, D. Acosta *et al.*, *Measurement of* $B(t \to Wb)/B(t \to Wq)$ *at the Collider Detector at Fermilab*, Phys.Rev.Lett. **95** (2005) 102002, `hep-ex/0505091`.

[59] The DØ Collaboration, V. M. Abazov *et al.*, *Determination of the Width of the Top Quark*, Phys. Rev. Lett. **106** (Jan 2011) 022001.

[60] W. Heisenberg, *Über den anschaulichen Inhalt der quantentheoretischen Kinematik und Mechanik*, Zeitschrift für Physik A Hadrons and Nuclei **43** (1927) 172, 10.1007/BF01397280.

[61] W. Bernreuther, A. Brandenburg, Z. Si, and P. Uwer, *Top quark pair production and decay at hadron colliders*, Nucl.Phys. **B690** (2004) 81, `hep-ph/0403035`.

[62] J. Pumplin, D. Stump, J. Huston, H. Lai, P. M. Nadolsky, *et al.*, *New generation of parton distributions with uncertainties from global QCD analysis*, JHEP **0207** (2002) 012, `hep-ph/0201195`.

[63] P. Nason, S. Dawson, and R. K. Ellis, *The Total Cross-Section for the Production of Heavy Quarks in Hadronic Collisions*, Nucl. Phys. **B303** (1988) 607.

[64] J. Aubert *et al.*, *Experimental Observation of a Heavy Particle J*, Phys. Rev. Lett. **33** (Dec 1974) 1404.

[65] J. E. Augustin *et al.*, *Discovery of a Narrow Resonance in* e^+e^- *Annihilation*, Phys. Rev. Lett. **33** (Dec 1974) 1406.

[66] M. Glück, J. F. Owens, and E. Reya, *Gluon contribution to hadronic* J/ψ *production*, Phys. Rev. D **17** (May 1978) 2324.

[67] B.L. and Combridge, *Associated production of heavy flavour states in pp and $p\bar{p}$ interactions: Some QCD estimates*, Nuclear Physics B **151(0)** (1979) 429 .

[68] S. Moch and P. Uwer, *Theoretical status and prospects for top-quark pair production at hadron colliders*, Phys. Rev. D **78** (Aug 2008) 034003.

[69] P. U. U. Langenfeld, S. Moch, *New results for $t\bar{t}$ production at hadron colliders*, Proc. XVII Int. Workshop on Deep-Inelastic Scattering and Related Topics, `hep-ph/0907.2527`.

[70] M. Beneke *et al.*, *Threshold expansion of the $gg(q\bar{q}) \to Q\bar{Q} + X$ cross section at $O(\alpha_s^4)$*, Phys. Lett. **B690** (2010) 483.

[71] *Combination of CDF top quark pair production cross section measurements with up to $4.6\,fb^{-1}$*, CDF note 9913.

[72] The DØ Collaboration, V. M. Abazov *et al.*, *Measurement of the $t\bar{t}$ production cross section using dilepton events in $p\bar{p}$ collisions*, Phys.Lett. **B704** (2011) 403, `hep-ph/1105.5384`.

[73] R. Kleiss and W. J. Stirling, *Spinor techniques for calculating $p\bar{p} \to W^{+/-}/Z^0$ + jets*, Nuclear Physics B **262** (Dec. 1985) 235.

[74] S. D. Ellis, R. Kleiss, and W. J. Stirling, *Missing transverse energy events and the standard model*, Physics Letters B **158** (Aug. 1985) 341.

[75] C. Berger *et al.*, *Precise Predictions for W + 4 Jet Production at the Large Hadron Collider*, Phys.Rev.Lett. **106** (2011) 092001, `hep-ph/1009.2338`.

[76] W. T. Giele, S. Keller, and E. Laenen, *QCD corrections to W boson plus heavy quark production at the Tevatron*, Phys.Lett. **B372** (1996) 141, `hep-ph/9511449`.

[77] U. Baur, F. Halzen, S. Keller, M. L. Mangano, and K. Riesselmann, *The Charm content of W + 1 jet events as a probe of the strange quark distribution function*, Phys.Lett. **B318** (1993) 544, `hep-ph/9308370`.

[78] The ATLAS Collaboration, G. Aad *et al.*, *Measurement of the cross section for the production of a W boson in association with b-jets in pp collisions at $\sqrt{s} = 7$ TeV with the ATLAS detector*, `hep-ph/1109.1470`.

[79] J. M. Campbell *et al.*, *Associated Production of a W Boson and One b Jet*, Phys.Rev. **D79** (2009) 034023, `hep-ph/0809.3003`.

[80] F. Febres Cordero, L. Reina, and D. Wackeroth, *NLO QCD corrections to W boson production with a massive b-quark jet pair at the Tevatron p anti-p collider*, Phys.Rev. **D74** (2006) 034007, `hep-ph/0606102`.

[81] R. Ellis and S. Veseli, *Strong radiative corrections to W b anti-b production in p anti-p collisions*, Phys.Rev. **D60** (1999) 011501, `hep-ph/9810489`.

[82] J. M. Campbell and R. Ellis, *Next-to-leading order corrections to W +2 jet and Z +2 jet production at hadron colliders*, Phys.Rev. **D65** (2002) 113007, `hep-ph/0202176`.

[83] M. L. Mangano, M. Moretti, F. Piccinini, R. Pittau, and A. D. Polosa, *ALPGEN, a generator for hard multiparton processes in hadronic collisions*, JHEP **0307** (2003) 001, `hep-ph/0206293`.

[84] M. L. Mangano, M. Moretti, and R. Pittau, *Multijet matrix elements and shower evolution in hadronic collisions: $Wb\bar{b}+n$ jets as a case study*, Nucl.Phys. **B632** (2002) 343, `hep-ph/0108069`.

[85] O. S. Bruning *et al.*, *LHC Design Report*, CERN, Geneva, (2004).

[86] P. Collier, *"LHC, Status and Performance"*, at the 107th LHCC Meeting, 21-22 September 2011. http://indico.cern.ch/conferenceDisplay.py?confId=153317.

[87] *CERN: The accelerator complex*, 2008, http://public.web.cern.ch/public/en/research/AccelComplex-en.html.

[88] *Approved ATLAS Event Displays from 2009 Collision Data*, ATLAS Experiment 2011 CERN, 15 January 2012, https://twiki.cern.ch/twiki/bin/view/AtlasPublic/EventDisplay2009PublicResults.

[89] *ATLAS Event Displays from the First LHC Collisions at 7 TeV Centre-of-Mass Energy*, ATLAS Experiment 2011 CERN, 15 January 2012, https://twiki.cern.ch/twiki/bin/view/AtlasPublic/EventDisplayFirstCollisions7TeV.

[90] *LuminosityPublicResults*, ATLAS Experiment 2011 CERN, 15 January 2012, https://twiki.cern.ch/twiki/bin/view/AtlasPublic/LuminosityPublicResults.

[91] The ATLAS Collaboration, G. Aad *et al.*, *Luminosity Determination in pp Collisions at $\sqrt{s}$=7 TeV Using the ATLAS Detector at the LHC*, Eur.Phys.J. **C71** (2011) 1630, `hep-ph/1101.2185`.

[92] *Updated Luminosity Determination in pp Collisions at $\sqrt{s}$=7 TeV using the ATLAS Detector*, 2011, ATLAS-CONF-2011-011.

[93] *ATLAS Detector and Physics Performance Technical Design Report, Vol. 1*, 1999.

[94] *ATLAS Detector and Physics Performance Technical Design Report, Vol. 2*, 1999.

[95] The ATLAS Collaboration Collaboration, G. Aad *et al.*, *The ATLAS Experiment at the CERN Large Hadron Collider*, JINST **3** (2008) S08003.

[96] The ATLAS Collaboration, G. Aad *et al.*, *A measurement of the material in the ATLAS inner detector using secondary hadronic interactions*, JINST **7** (2012) P01013, `hep-ex/1110.6191`.

[97] *Public Pixel Tracker Plots for Collision Data*, ATLAS Experiment 2011 CERN, 15 January 2012, https://twiki.cern.ch/twiki/bin/view/AtlasPublic/PixelPublicResults.

[98] *ATLAS calorimeter performance: Technical Design Report*, 1996.

[99] *Search for $t\bar{t}$ production in the all-hadronic channel in ATLAS with $\sqrt{s}$ = 7 TeV data*, 2011, ATL-CONF-2011-066.

[100] *ATLAS Monte Carlo tunes for MC09*, ATL-PHYS-PUB-2010-002.

[101] The ATLAS Collaboration, *First tuning of HERWIG/JIMMY to ATLAS data*, ATL-PHYS-PUB-2010-014.

[102] M. Cacciari, G. P. Salam, and G. Soyez, *The Anti-k(t) jet clustering algorithm*, JHEP **0804** (2008) 063, hep-ph/0802.1189.

[103] The ATLAS Collaboration, *Jet energy measurement with the ATLAS detector in proton-proton collisions at* $\sqrt{s} = 7$ *TeV*, hep-ph/1112.6426.

[104] *Jet energy resolution and selection efficiency relative to track jets from in-situ techniques with the ATLAS Detector Using Proton-Proton Collisions at a Center of Mass Energy* $\sqrt{s} = 7$ *TeV*, ATLAS-CONF-2010-054.

[105] W. Lampl *et al.*, *Calorimeter Clustering Algorithms: Description and Performance*, ATL-LARG-PUB-2008-002.

[106] The ATLAS Collaboration, G. Aad *et al.*, *Electron performance measurements with the ATLAS detector using the 2010 LHC proton-proton collision data*, hep-ph/1110.3174.

[107] *Muon Momentum Resolution in First Pass Reconstruction of pp Collision Data Recorded by ATLAS in 2010*, ATLAS-CONF-2011-046.

[108] *Combined Muon Performance Public Results*, 2011, https://twiki.cern.ch/twiki/bin/view/AtlasPublic/MuonPerformancePublicPlots.

[109] *Performance of Impact Parameter Based b-tagging Algorithms with the ATLAS Detector using Proton-Proton Collisions at* $\sqrt{s} = 7$ *TeV*, 2010, ATLAS-CONF-2010-091.

[110] *Commissioning of the ATLAS high-performance b-tagging algorithms in the 7 TeV collision data*, 2011, ATLAS-CONF-2011-102.

[111] R. E. Kalman, *A New Approach to Linear Filtering and Prediction Problems*, Transactions of the ASME–Journal of Basic Engineering **82(Series D)** (1960) 35.

[112] *Calibrating the b-Tag Efficiency and Mistag Rate in 35* pb^{-1} *of Data with the ATLAS Detector*, 2011, ATLAS-CONF-2011-089.

[113] G. Corcella *et al.*, *HERWIG 6.5: an event generator for Hadron Emission Reactions With Interfering Gluons (including supersymmetric processes)*, JHEP **01** (2001) 010, hep-ph/0011363.

[114] G. Corcella *et al.*, *HERWIG 6.5 release note*, hep-ph/0210213.

[115] A. Sherstnev and R. Thorne, *Parton Distributions for LO Generators*, Eur.Phys.J. **C55** (2008) 553, hep-ph/0711.2473.

[116] *ATLAS Monte Carlo Tunes for MC09*, 2010, ATL-PHYS-PUB-2010-002.

[117] T. Sjostrand, S. Mrenna, and P. Z. Skands, *PYTHIA 6.4 Physics and Manual*, JHEP **0605** (2006) 026, hep-ph/0603175.

[118] B. P. Kersevan and E. Richter-Was, *The Monte Carlo event generator AcerMC version 2.0 with interfaces to PYTHIA 6.2 and HERWIG 6.5*, hep-ph/0405247.

[119] M. Botje *et al.*, *The PDF4LHC Working Group Interim Recommendations*, hep-ph/1101.0538.

[120] F. Caravaglios, M. L. Mangano, M. Moretti, and R. Pittau, *A New approach to multijet calculations in hadron collisions*, Nucl.Phys. **B539** (1999) 215, hep-ph/9807570.

[121] *Monte Carlo samples used for top physics*, 2010, ATL-PHYS-INT-2010-132.

[122] *Measurement of the charge asymmetry in top quark pair production in pp collisions at $\sqrt{s}$ = 7 TeV using the ATLAS detector*, 2011, ATL-CONF-2011-106.

[123] T. Gleisberg, S. Hoeche, F. Krauss, M. Schonherr, S. Schumann, *et al.*, *Event generation with SHERPA 1.1*, JHEP **0902** (2009) 007, hep-ph/0811.4622.

[124] J. S. Conway, *Incorporating Nuisance Parameters in Likelihoods for Multisource Spectra*, ArXiv e-prints (Mar. 2011), hep-ex/1103.0354.

[125] F. Rademakers, M. Goto, P. Canal, and R. Brun, *ROOT Status and Future Developments*, CoRR **cs.SE/0306078** (2003), http://root.cern.ch.

[126] N. Metropolis, A. Rosenbluth, M. Rosenbluth, A. Teller, and E. Teller, *Equation of state calculations by fast computing machines*, J.Chem.Phys. **21** (1953) 1087.

[127] W. Hastings, *Monte Carlo Sampling Methods Using Markov Chains and Their Applications*, Biometrika **57** (1970) 97.

[128] A. Hoecker *et al.*, *TMVA 4 Users Guide, Toolkit for Multivariate Data Analysis with ROOT*, CERN-OPEN-2007-007, physics/0703039.

[129] *Measurement of the inclusive $t\bar{t}\gamma$ cross section with the ATLAS detector*, ATLAS-CONF-2011-153.

[130] *Reconstructed jet multiplicities from the top-quark pair decays and associated jets in pp collisions at $\sqrt{s}$ = 7 TeV measured with the ATLAS detector at the LHC*, ATLAS-CONF-2011-142.

[131] *Measurement of $t\bar{t}$ production in the all-hadronic channel in 1.02 fb^{-1} of pp collisions at $\sqrt{s} = 7$ TeV with the ATLAS detector*, ATLAS-CONF-2011-140.

[132] *Measurement of the charge asymmetry in top quark pair production in pp collisions at $\sqrt{s}$=7 TeV using the ATLAS detector*, ATLAS-CONF-2011-106.

[133] *Measurement of the t-channel Single Top-Quark Production Cross Section in 0.70 fb^{-1} of pp Collisions at $\sqrt{s}$ = 7 TeV with the ATLAS detector*, ATLAS-CONF-2011-101.

[134] *Measurement of the top quark mass from 2011 ATLAS data using the template method*, ATLAS-CONF-2011-120.

[135] *Measurement of the top quark charge in pp collisions at $\sqrt{s}$ =7 TeV in the ATLAS experiment.*, ATLAS-CONF-2011-141.

[136] The ATLAS Collaboration, G. Aad *et al.*, *Search for New Phenomena in $t\bar{t}$ Events With Large Missing Transverse Momentum in Proton-Proton Collisions at $\sqrt{s}$ = 7 TeV with the ATLAS Detector*, hep-ph/1109.4725.

[137] The ATLAS Collaboration, G. Aad *et al.*, *Measurement of the WW cross section in* $\sqrt{s}$ = *7 TeV pp collisions with ATLAS*, Phys.Rev.Lett. **107** (2011) 041802, `hep-ph/1104.5225`.

[138] The ATLAS Collaboration, G. Aad *et al.*, *Measurement of the WZ production cross section and limits on anomalous triple gauge couplings in proton-proton collisions at* $\sqrt{s}$ = *7 TeV with the ATLAS detector*, `hep-ph/1111.5570`.

[139] The ATLAS Collaboration, G. Aad *et al.*, *Measurement of the ZZ production cross section and limits on anomalous neutral triple gauge couplings in proton-proton collisions at* $\sqrt{s}$ = *7 TeV with the ATLAS detector*, `hep-ph/1110.5016`.

Acknowledgements

It's been quite an experience, this PhD thing. I've learned enourmously from the scientists I have worked with in the past few years, and I wouldn't have been able to do it without my friends and family to keep me sane. My advisor, Arnulf Quadt, has offered fine scientific gudiance and sometimes a good laugh to go with it. If we learn scienctific method from mimicry, I've learned it from Lisa Shabalina. I must thank Anna Henrichs, my officemate and scientific partner in crime, for putting up with me. A number of other postdocs in Göttignen, especially Kevin Kröninger and Jörg Meyer, were always helpful and kind. Oleg Brandt was both one of the first people I met in the field years ago at Fermilab and the last editor of my thesis. Thanks to Jörn Grosse-Knetter for being my second examiner, and for all the coffee. Lucie has been wonderful since day one. Many friends have helped me keep my feet on the ground over the past couple of years, Despoina more than anyone else, whose support and cigars helped me through the unbearable deadlines. The overtly academic physicist-classicist circle of friends that has grown over the last year here has been full of good times and conversation, down to middle of the night coffee break before printing out my thesis. Fabian has been everything from a friend to an editor. My months of writing have been greatly influenced by conversations with Leyla about the big-picture meaning of what we do and Erik about the details. These conversations have proved invaluable in clarifying my thoughts, and I am grateful that Sonderbar is open late enough to facilitate them. A number of people have helped me navigate and understand life on a big collaboration, amongst them Daniel Froidevaux and Alison Lister, while the impromptu student support groups that spring up in cafes in Geneva helped to overcome their often frustating reality. Speaking of cafes, the staff of R1 at CERN, the cafe in the physics department at Göttingen and a number of others around town have been indespensible in this process. My family has been nothing but supportive while I've been on the other side of the Atlantic from them, which I am grateful for.